MnO_2 Based Nanostructures for Supercapacitor Energy Storage Applications

Dissertation by

Wei Chen

In Partial Fulfillment of the Requirements

For the Degree of

Doctor of Philosophy

King Abdullah University of Science and Technology

Thuwal, Kingdom of Saudi Arabia

November 2013

The dissertation of Wei Chen is approved by the examination committee.

Dr. Aram Amassian		
Committee Member	Signature	Date
Dr. Osmar Bakr		
Committee Member	Signature	Date
Dr. Mohamed Eddaoudi		
Committee Member	Signature	Date
Dr. Yu Han		
Committee Member	Signature	Date
Dr. Husam Alshareef		
Committee Chair	Signature	Date

King Abdullah University of Science and Technology

2013

ABSTRACT

MnO_2 Based Nanostructures for Supercapacitor Energy Storage Applications

Wei Chen

Nanostructured materials provide new and exciting approaches to the development of supercapacitor electrodes for high-performance electrochemical energy storage applications. One of the biggest challenges in materials science and engineering, however, is to prepare the nanomaterials with desirable characteristics and to engineer the structures in proper ways. This dissertation presents the successful preparation and application of very promising materials in the area of supercapacitor energy storage, including manganese dioxide and its composites, polyaniline and activated carbons. Attention has been paid to understanding their growth process and performance in supercapacitor devices. The morphological and electrochemical cycling effects, which contribute to the understanding of the energy storage mechanism of MnO_2 based supercapacitors is thoroughly investigated. In addition, MnO_2 based binary (MnO_2-carbon nanocoils, MnO_2-graphene) and ternary (MnO_2-carbon nanotube-graphene) nanocomposites, as well as two novel electrodes (MnO_2-carbon nanotube-textile

and MnO_2-carbon nanotube-sponge) have been studied as supercapacitor electrode materials, showing much improved electrochemical storage performance with good energy and power densities. Furthermore, a general chemical route was introduced to synthesize different conducting polymers and activated carbons by taking the MnO_2 nanostructures as reactive templates. The electrochemical behaviors of the polyaniline and activated nanocarbon supercapacitors demonstrate the morphology-dependent enhancement of capacitance. Excellent energy and power densities were obtained from the template-derived polyaniline and activated carbon based supercapacitors, indicating the success of our proposed chemical route toward the preparation of high performance supercapacitor materials. The work discussed in this dissertation conclusively showed the significance of the preparation of desirable nanomaterials and the design of effective nanostructured electrodes for supercapacitor energy storage applications.

ACKNOWLEDGEMENTS

This dissertation would not have been possible without the generous help and guidance from my advisor, colleagues and collaborators, and unfaltering support from my family and friends. I am privileged for this opportunity to express my deeply-felt gratitude towards those individuals who have made significant contributions to my life during the past four years.

First of all, I would like to thank my advisor, Prof. Husam Alshareef, for his continuous encouragement, guidance, and support throughout my stay at KAUST. My study in Saudi Arabia was an adventure that I was excited to take as one of the pioneering PhD students who believed in the vision of KAUST. Looking back to the beginning years, I have endured several hardships, but with your thoughtful help and warm encouragement, I have overcome the obstacles and become stronger than ever. I appreciate all your help in further developing my communication skills, writing style and presentation techniques. Your dedication and hard work constantly inspired me to be the best in the research area and in my personal life.

I owe sincere gratitude to my dissertation committee, Prof. Aram Amassian, Prof. Osmar Bakr, Prof. Mohamed Eddaoudi and Prof. Yu Han. It is my great honor to have such an excellent group of people on my committee. Thanks for your time and patience to go through my dissertation and offering helpful feedback, which has been extremely helpful to shape this document.

I would also like to thank all my colleagues and collaborators. The Alshareef group provided a comfortable, helpful and inventive atmosphere, making my work always enjoyable and fun. Thanks to Dr. Rakhi Raghavan Baby for many fruitful discussions and collaborations on projects, and generous help in my life as a friend. I am also grateful to the previous and current members of the group: Dr. Sarath Kumar, Dr. Unnat Bhansali, Dr. Pradipta Nayak, Dr. Muhammad Shahid, Dr. Doddahalli Nagaraju, Alfonso Caraveo, Mohd Adnan Khan, Anas Abu-Taha, Nuha Al-Hebshi, Zhenwei Wang, Chuan Xia, Mahmoud Almadhoun, Yaocai Bai, and Nulati Yesibolati. My gratitude also goes to the people in the KAUST core labs who provided me with help and support: Qingxiao Wang, Dr. Lan Zhao, Dr. Yang Yang, Dr. Mohamed Nejib Hedhili and Dr. Hua Tan. I also want to especially thank Prof. Yi Cui at Stanford University for giving me the chance to do the summer research internship in his group, and for inspiring me to pursue very exciting research directions. Thanks to people in Cui group who helped me during my stay: Dr. Liangbing Hu, Dr. Hui Wu, Dr. Yan Yao, Xing Xie, Yuan Yang, Nian Liu and Shuang Wang.

Finally, I would like to dedicate this dissertation to my family, especially to my mother and my wife Liang Liu. I am grateful to my parents for giving me the freedom and support to do what I like in my life. To my wife Liang and my son Churui, I am so lucky to have you in my life. I cannot thank you more for your unconditional love, understanding and encouragement in my life.

TABLE OF CONTENTS

Page

LIST OF ABBREVIATIONS

AC	activated carbon
A-CNP	activated carbon nanoparticle
A-CNS	activated carbon nanosheet
A-CNT	activated carbon nanotube
BET	Brunauer-Emmett-Teller
BJH	Barret-Joyner-Halenda
CD	galvanostatic charge-discharge
CE	counter electrode
CNC	carbon nanocoils
CNP	carbon nanoparticle
CNS	carbon nanosheet
CNT	carbon nanotube
Co_3O_4	cobalt oxide
CPE	constant phase element

CV	cyclic voltammetry
DFT	density function theory
ECP	electrically conducting polymers
EDLC	electrochemical double layer capacitor
EDX	energy dispersive X-ray spectroscopy
EIS	electrochemical impedance spectroscopy
ESR	equivalent series resistance
FFT	fast Fourier transform
GN	graphene nanosheet
MnO_2	manganese dioxide
PAni	polyaniline
PAni-NF	polyaniline nanofiber
PAni-NS	polyaniline nanosphere
PAni-NT	polyaniline nanotube
PEDOT	poly(3,4-ethylenedioxythiophene)
PPy	polypyrrole

RE	reference electrode
rGO	reduced graphene oxides
RT	room temperature
SEM	scanning electron microscopy
SSA	specific surface area
STEM	scanning transmission electron microscopy
TEM	transmission electron microscopy
TMO	transition metal oxide
TGA	thermo gravimetric analysis
WE	working electrode
XRD	X-ray diffraction
XPS	X-ray photoelectron spectroscopy
0D	zero-dimensional
1D	one-dimensional
2D	two-dimensional
3D	three-dimensional

LIST OF SYMBOLS

Symbol	Definition
A	surface area of the interface
C	capacitance
C_s	specific capacitance
$C_{D.L}$	double layer capacitance
C_P	pseudocapacitance
D	thickness of the double layer
E	energy density
m	mass
P	power density
Q	electrical charge
R_{ct}	charge transfer resistance

R_s	solution resistance
t	time
V	voltage
V_{drop}	voltage drop/IR drop
ε_0	permittivity of vacuum
ε_r	relative dielectric constant

LIST OF ILLUSTRATIONS

LIST OF TABLES

Chapter 1

Introduction

1.1 General Properties of Supercapacitors

Supercapacitors, also known as ultracapacitors or electrochemical capacitors, are promising energy storage devices that bridge the gap between batteries and conventional capacitors, as shown in the so-called Ragone plot in Figure 1.1. Supercapacitors provide higher energy density than conventional capacitors and much higher power density than batteries.[1] They exhibit promising features of high power density, fast rates of charge-discharge, reliable cycling stability, and safe operation.[1-5] Moreover, they can deliver exceptionally low-temperature performance. As a result, supercapacitors are often used in stationary and mobile systems that require high-power pulses: car acceleration, tramways, cranes, forklifts, emergency and power back-up systems, consumer electronics, and so on.[2]

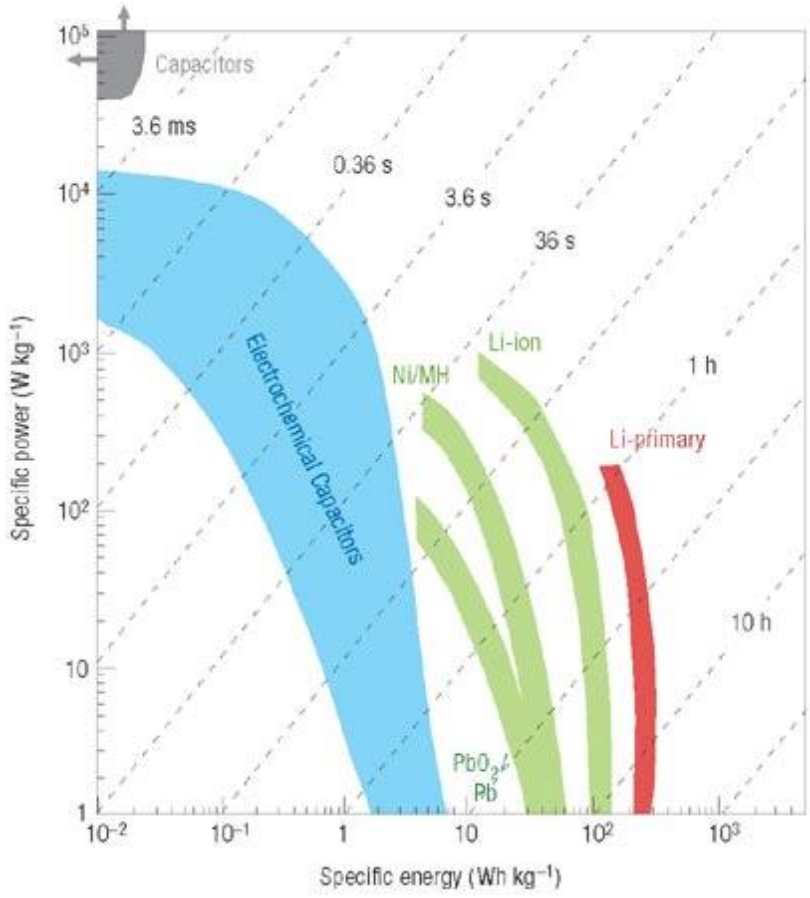

Figure 1.1: The Ragone plot shows different electrochemical energy storage devices, including conventional capacitors, supercapacitors and batteries.[2]

1.2 Classification of Capacitors

Depending on the choice of electrode and electrolyte, the capacitors can be classified into three major categories that are shown in Figure 1.2. They can be further divided into some subgroups according to the specific materials used as electrode and electrolyte.

1.2.1 Electrostatic Capacitors

A capacitor is a passive two-terminal electrical component used to store energy electrostatically in an electric field. The typical form of a practical electrostatic capacitor contains two electrical conductors (copper or aluminum) separated by an insulator (glass, air, mica, paper, polymer film or ceramic). The electrostatic capacitors can be operated at very high voltages for almost unlimited lifetime. Their gravimetric (energy per unit weight) and volumetric energy densities (energy per unit volume) are on the order of 1.5 mWh/kg and 2 mWh/L, respectively.

1.2.2 Electrolytic Capacitors

Unlike conventional electrostatic capacitors that utilize bulk insulators, the dielectric in electrolytic capacitors is made of a thin metal oxide layer. Take aluminum electrolytic capacitor for an example, the thin layer of insulating aluminum oxide on the surface of the aluminum film acts as the dielectric, which makes a relatively higher capacitance than the electrostatic capacitor. The electrolyte is typically boric acid or sodium borate in aqueous solution. Electrolytic capacitors have RC (resistance*capacitance) time constants on the order of milliseconds that are used in filtering applications. The voltage of the electrolytic capacitors is lower than that of the electrostatic capacitors, but their energy density is much higher due to their higher capacitance. Their gravimetric and volumetric energy densities are on the order of 30 mWh/kg and 120 mWh/L, respectively, which are much higher than that of the electrostatic capacitors.

1.2.3 Supercapacitors

Supercapacitors are electrochemical energy storage devices that store and release energy by nanoscopic charge separation at the interface between the electrode material and the electrolyte.[6] Generally, supercapacitors consist of two electrodes separated by a dielectric porous film called a separator, and impregnated by an electrolyte. The electrolyte contains a large amount of ions that based on aqueous or organic solvents. The electrode material is the most important component of the supercapacitor.

Supercapacitors can be divided into two categories based on the underlying energy storage mechanism.[1, 2, 5] One is electrochemical double layer capacitor (EDLC), where electrical energy is stored by electrostatic accumulation of charges.[1] EDLC can provide ultrahigh power and excellent cycle life due to the fast and non-degradation process between electrode active materials and electrolyte.[2] However, the energy stored in EDLCs is limited by the finite electrical charge separation at the interface of electrode materials and electrolyte, and the availability of electrode surface area.[4] The most widely studied materials for EDLCs are carbons, including activated carbons (ACs), carbon nanotubes (CNTs), graphene and so on. Among them, ACs are dominated in the commercially available supercapacitors due to their low cost, high availability, excellent electrical conductivity, stable electrochemical response and environmental benignity.[7, 8] CNTs have got superior material properties such as high chemical stability, aspect ratio, mechanical strength and activated

surface area and outstanding electrical properties, which make them widely accepted as supercapacitor electrode materials.[9-13] Graphene is a single layer of carbon sheet in the two-dimensional form. It is recently demonstrated as an excellent supercapacitor material with promising features of high specific surface area, a very high intrinsic electrical conductivity in plane as well as good mechanical strength and chemical stability.[6, 14]

Another type of supercapacitor is the so-called pseudocapacitor, in which the electrical charges are mainly stored by fast and reversible redox reactions.[1-3, 5] Because of the Faradaic process underpinning the energy stored in a pseudocapacitor, it has increased energy density but at the cost of power density and cycle life compared to EDLCs. The typical electrode materials used for pseudocapacitors are transition metal oxides/hydroxides and conducting polymers, such as manganese dioxide (MnO_2), cobalt oxide (Co_3O_4), polyaniline (PAni) and polypyrrole (PPy). Among the different transition metal oxides for supercapacitor, MnO_2 is of particular interest due to its high electrochemical activity, environmental compatibility, low cost, and abundant availability on earth.[15-18] The pseudocapacitive reaction of MnO_2 is a surface dominant reaction, only the surface or a very thin surface layer of the oxide can participate in this pseudocapacitive reaction.[19, 20] As the electrochemical performance of MnO_2 nanoparticles largely depends on their microstructure and surface area, the development of controlled synthesis of MnO_2 nanostructures with well-defined microstructure and high electrochemically active area is of great importance.

Hybrid supercapacitors that combine Faradaic and non-Faradaic charge storage mechanisms, resulting in improved device characteristics.[21-26] For example, a composite of graphene oxide supported by needle-like MnO_2 nanocrystals showed better electrochemical performance than that of MnO_2.[27] A rational design of ternary nanocomposite composed of MnO_2, CNT and conducting polymer exhibited outstanding electrochemical performance owing to the effective utilization of all the desired functions of each component.[28]

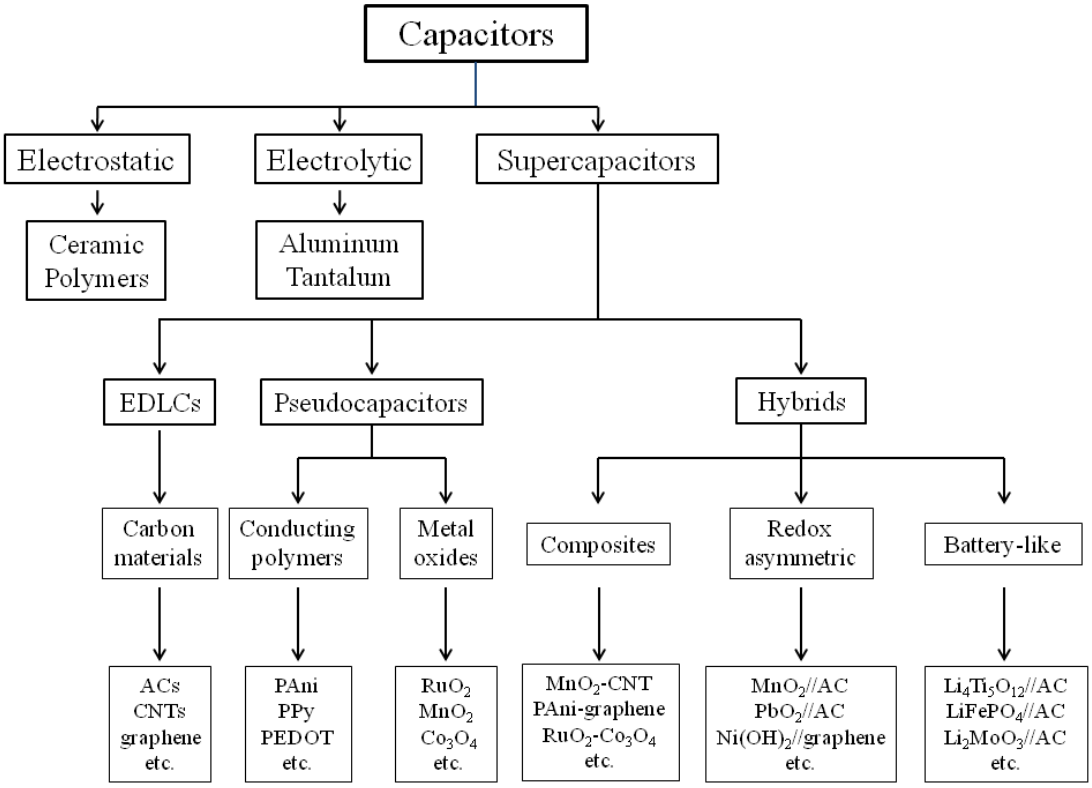

Figure 0.2: Classification of capacitors.

1.3 Electrochemical Techniques

1.3.1 Electrochemical Measurement System

Generally, the electrochemical system for measuring supercapacitor performance is composed of three main components: an electrochemical cell, an electrochemical workstation and a computer that used to control the workstation (Figure 1.3). The electrochemical workstation can be used to measure all the required electrochemical parameters of the supercapacitors.

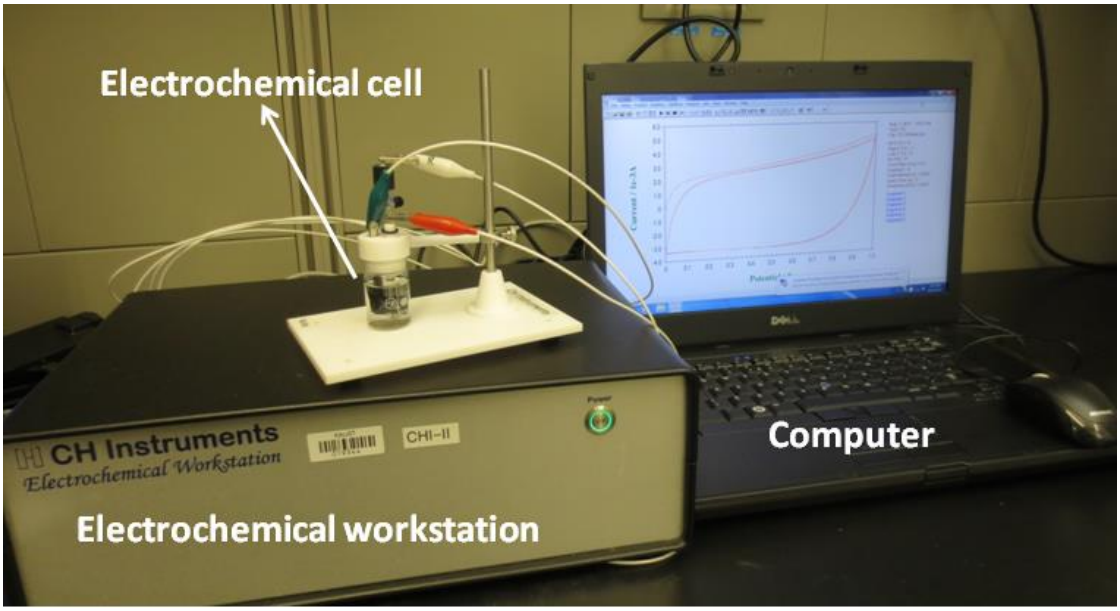

Figure 0.3: A typical electrochemical apparatus for the tests of supercapacitors.

1.3.2 Electrochemical Cells

To test an electrochemical cell, both three-electrode and two-electrode configurations can be performed as shown in Figure 1.4. Typically, the cells consist of three electrodes, including working electrode (WE), reference electrode (RE) and counter electrode (CE). The voltage is controlled between WE and RE, and the current flows through WE and CE. In the three-electrode configuration, the CE and RE are separated from each other to keep a constant voltage for the RE over a large range of currents (Figure 1.4a). While in the two-electrode set up, the CE and RE are shorted to work as a positive or negative electrode in contrast to the WE (Figure 1.4b). In this case, the measured voltage is the cell voltage of the full cell device. The insets of Figure 1.4a and b show the digital photographs of real three- and two-electrode setups. For the two-electrode coin cell shown in Figure 1.4b, it contains two identical electrode materials loaded on the conductive carbon substrates as working electrodes, sandwiched by a separator and assembled by adding electrolyte in between as well as the spaces, springs and cases included.

It was proposed by Ruoff et al. that the two-electrode configuration is better than the three-electrode one for the evaluation of energy storage capacity as real-world devices.[29] Although the three-electrode configuration is valuable for analyzing the redox reactions at a single electrode surface, the high sensitivity can lead to large errors when projecting the energy storage capacity of a single

electrode.[30] It is therefore encouraged to adopt the two-electrode configuration for the evaluation of supercapacitor performance for energy storage applications.

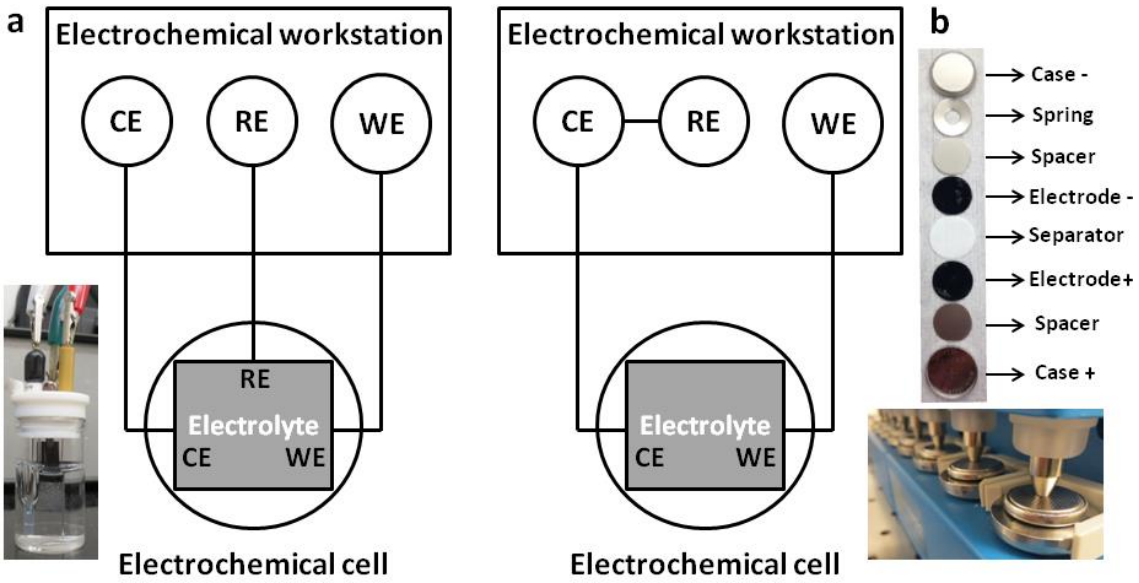

Figure 0.4: Illustration and photographs of electrochemical test configurations. (a) Three-electrode cell; (b) two-electrode cell and its components.

1.3.3 Electrochemical Techniques

Cyclic voltammetry (CV), galvanostatic charge-discharge (CD) and electrochemical impedance spectroscopy (EIS) are the most commonly used techniques for characterizing a supercapacitor in either a three-electrode cell (a supercapacitor electrode) or a two-electrode cell (a supercapacitor device).

1.3.3.1 Cyclic Voltammetry

CV and CD are two transient techniques that have been widely used by electrochemists.[30] The principle of the CV technique is to apply a linear voltage ramp to an electrode (or a device) within a set voltage range and to measure the resulting current. The CV is an accurate technique that enables.

- qualitative and pseudo-quantitative studies
- kinetic analysis by scanning a huge range of scan rates
- voltage window determination of the electrode or device

The CV technique is often used to evaluate the capacitance and cycling stability of a supercapacitor. However, the CD technique is considered to be better for those measurements.

1.3.3.2 Galvanostatic Charge-Discharge

The CD is the most accepted technique in the energy storage field due to its extendibility from a laboratory scale to an industrial one. Different from the CV technique, the current is accurately controlled and the voltage is measured accordingly in the CD technique. It is also called chronopotentiometry and gives access to different parameters such as capacitance, resistance and cycling stability.

1.3.3.3 Electrochemical Impedance Spectroscopy

The EIS is a stationary technique that allows acquisition times high enough to get accurate measurements. This technique can be conducted by controlling either the current or the voltage and thus measuring the voltage or current. The behavior of EIS for supercapacitors is strongly depended on their materials and electrolytes. Basically, the Nyquist plot (real impedance versus imaginary impedance) and the Bode plot (frequency versus impedance) are widely used to represent the behaviors of the supercapacitors, some of which will be discussed in detail in the following sections.

Above all, the electrochemical techniques introduced here are most widely used to characterize supercapacitors and to get important electrochemical parameters for determining the supercapacitor performance. The combination of these three techniques allows us to understand the electrochemical behaviors and will be discussed throughout the whole dissertation.

1.4 Supercapacitor Parameters

1.4.1 Capacitance

When charged by applying a voltage across the electrodes, a capacitor connected in a circuit will act as a voltage source for a short time. Its capacitor (*C*) is the ratio of electric charge on each electrode (*Q*) to the voltage (*V*) between them, thus:

$$C = \frac{Q}{V}$$

For a typical EDLC which stores the charges electrostatically by reversible adsorption and desorption of electrolyte ions onto and out of the high surface area carbonaceous active materials, *C* can also be represented as:

$$C = \frac{\varepsilon_0 \varepsilon_r A}{d}$$

where ε_0 is the permittivity of vacuum, ε_r is the relative dielectric constant of the electrolyte, *A* is the surface area of the interface and *d* is the effective thickness of the double layer.

Considering the measured electrochemical behaviors (CV or CD) of the supercapacitors, the capacitance can be calculated from the discharge part according to the following equation:

$$C = \frac{I}{dV/dt}$$

where *C* is the capacitance, *I* is the current, and *dV/dt* is the potential scan rate (for CV) or the slope of the discharge curve after voltage drop (for CD).

When two-electrode full cell is applied, the specific capacitance (C_s, with unit of F/g) can be expressed as:

$$C_s = \frac{4C}{M}$$

where *M* is the total mass of active materials on the two electrodes.

1.4.2 Energy and Power Density

Another two primary characteristics of supercapacitors are energy and power density, both of which can be expressed gravimetrically (the energy per unit weight) or volumetrically (the energy per unit volume). The maximum energy density is given by

$$E = \frac{1}{2}CV^2$$

where *E* is the energy (with unit of J), *C* is the capacitance (F) and *V* is the maximum voltage (V).

The power (*P*) is the rate of energy delivery per unit time. Generally, the resistance of the internal components of the supercapacitors (*e.g.* current collectors, electrode materials, electrolytes and separators) needs to be taken into account to determine the power of the supercapacitors, which is usually referred to as the equivalent series resistance (ESR). The ESR, obtained from a voltage drop (IR drop) during discharge, determines the maximum voltage and therefore limits the maximum energy and power density of the capacitors. The maximum power density is given by

$$P = \frac{V^2}{4ESR}$$

where *V* is the maximum cell voltage (V) and *P* is the maximum power (W). The *ESR* can be deduced from the voltage drop at the beginning of the discharge curve.

$$ESR = \frac{V_{drop}}{2I}$$

1.5 Challenges and Opportunities

During the past a few decades, much research and industrial efforts have been conducted on improving the supercapacitor performance through the following four distinguished and complementary axes to enable the merger of the energy storage systems: increase energy density, increase power density (i. e. decrease ESR), increase the lifetime and decrease the cost of the device. Only the device combing good electrochemical performance and low cost can be possible for the widespread applications.

In order to overcome the challenges in the supercapacitors, it is worth noting that the overall performance of a supercapacitor is largely determined by the active electrode materials, which define the capacitance and thus the storage capacity of the supercapacitor. Therefore, the opportunities in the field of supercapacitors could be the preparation of good electrode materials with low cost for excellent supercapacitor electrochemical performance. One effective strategy is to prepare low cost materials (such as manganese oxide, conducting polymers and activated carbons) with promising features for improved

supercapacitor performance. As mentioned in the previous section, MnO_2 as one of the most investigated materials for supercapacitors have very promising potential towards addressing the issues in the area of supercapacitors.

1.6 Literature Review of MnO_2

Ever since the pioneering work on MnO_2 as a good material for the supercapacitor in aqueous electrolytes that was published in 1999 by Lee and Goodenough, intensive work has been reported on the preparation and optimization of MnO_2 for improved supercapacitor energy storage performance.[31] As a transition metal element, manganese exists in a variety of stable oxides (MnO, Mn_3O_4, Mn_2O_3 and MnO_2). Among them, MnO_2 has been extensively investigated as an electrode material for high performance supercapacitors owing to its many good features of low cost, high theoretical capacity, environmental friendliness and natural abundance.[32] MnO_2 exists in polymorphs, such as α-, β-, γ- and ε-phases, which are different in the way on how the basic units of MnO_6 octahedra are linked, as shown in Figure 1.5 and Table 1.1.[33-35] The structural parameters are important in determining and optimizing the electrochemical behaviors of MnO_2 as supercapacitor materials. Additionally, various methods have been used to prepare MnO_2 nanostructures such as sol-gel, co-precipitation, hydrothermal reaction, and electrochemical deposition. In the meantime, a large variety of MnO_2 with different morphologies (such as

nanoparticles, nanocubes, nanorods, nanotubes, *etc.*) and different crystalline phases (such as α, β, γ, ε, δ, *etc.*) can be produced, as shown in Table 1.2.[36-43]

In general, MnO_2 exhibits specific capacitance within the range of 50-200 F/g in aqueous electrolyte, which is much lower than its theoretical capacitance value of 1370 F/g.[19] The capacitance of MnO_2 based supercapacitors is ultimately limited by the poor electrical conductivity of MnO_2. Therefore, two approaches have been applied to address this critical issue. One approach is to incorporate of other metal elements into MnO_2 compounds to enhance their electrical conductivity and charge storage capacity, which can be basically realized by mixing other transition metal oxides such as RuO_2, NiO, Co_3O_4 with MnO_2 to form the mixed metal oxides, or by the doping of other metallic elements such as Co, Fe, Sn, Ag and Au into the MnO_2 compounds.[44-52] The chemically modified MnO_2 showed enhanced electrical conductivity and the electrochemical properties have been improved accordingly, as shown in Table 1.3. Another approach to compensate for the poor electrical conductivity of MnO_2 can be achieved by the hybrid of MnO_2 with highly electrically conducting materials (such as carbon materials and conducting polymers) to form different composites. In this case, MnO_2 deposited on the conducting materials such as carbon nanotubes, graphene and PEDOT by different methods, including physical mixing of the components, thermal decomposition and electrochemical deposition, for enhancing supercapacitor performance with improved cycling stability.[53-57]

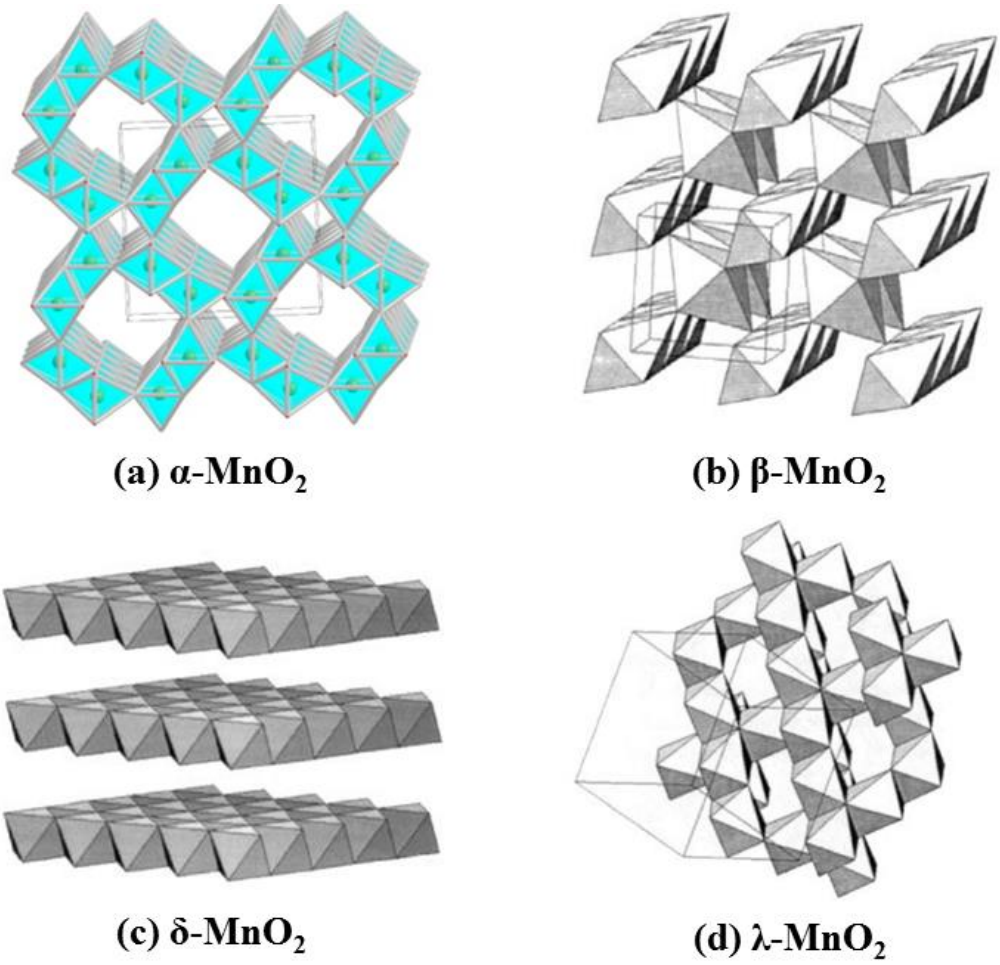

Figure 1.5: Schematic representation of the crystal structures of MnO_2. (a) α-MnO_2; (b) β-MnO_2; (c) δ-MnO_2; (d) λ-MnO_2.[33, 34]

Type	Crystal structure	Description
α-MnO_2 (psilomelane)	Monoclinic, *A*2/*m*	Cross-linking of double or triple chains of the MnO_6 octahedra, resulting in two-dimensional tunnels within the lattice.
β-MnO_2 (pyrolusite)	Rutile structure, *P*42/*mnm*	Rutile structure with an infinite chain of MnO_6 octahedra sharing opposite edges; each chain is corner-linked with four similar chains.
β-MnO_2 (ramsdellite)	*Pbnm*	Closely related to rutile except that the single chains of edge-sharing octahedra are replaced by double chains.
γ-MnO_2 (nsutite)		An irregular intergrowth of layers of pyrolusite and ramsdellite.
η-MnO_2		Different from γ-MnO_2 only in crystallite size and the concentration of microdomains of pyrolusite within the ramsdellite matrix.
δ-MnO_2 (phyllomanganate)	Birnessite, $R\bar{3}m$	Layered structure, containing infinite two-dimensional sheets of edge-shared MnO_6 octahedra.
ε-MnO_2	Defective NiAs, *P*63/*mmc*	Hexagonal close packing of anions, with Mn^{4+} statistically distributed over half the available octahedral interstices.

Table 1.1: Crystal structures of MnO_2.[32]

Technique	Synthesis conditions	Morphology	Structure	S_{BET} (m^2/g)	C_s (F/g)	Test conditions
Hydrothermal[36]	$MnSO_4$ + $KMnO_4$, 140 °C	Plate-like, nanorods	α-MnO_2	100-150	72-168	5 mV/s, 3-electrode setup
Hydrothermal[37]	$KMnO_4$ + HNO_3, 110 °C	Urchin-like	α-MnO_2	80-119	86-152	5 mV/s, 3-electrode setup
Hydrothermal[38]	$NaMnO_2$ + HNO_3, 120 °C	Lamellar	δ-MnO_2	---	241	2 mA/cm^2, 3-electrode setup
Room temperature precipitation[39]	$MnSO_4$ + $K_2S_2O_8$	Rod-shaped	δ-MnO_2	---	201	1 mV/s, 3-electrode setup
Low temperature reduction[40]	$KMnO_4$ or $NaMnO_4$ in acids, 20-100 °C	Layered	Rancieite structure	11-206	17-112	2 mV/s, 3-electrode setup
Sol–gel process[41]	Manganese acetate+ citric acid, 80 °C	Nanorods	γ-MnO_2	---	317	0.1 A/g, 3-electrode setup
Solution combustion[42]	$Mn(NO_3)_2$ + $C_2H_5NO_2$	Plate-like	ε-MnO_2	23-43	71-123	1 A/g, 3-electrode setup

Electro-deposition [43]	$MnSO_4$ (0.25M), pH=6.4	---	Amorphous	---	265-320	3-electrode setup

Table 1.2: Synthesis technique, conditions, morphology, crystal structures, BET surface area and subsequent specific capacitance of MnO_2.

Materials	Techniques	Synthesis conditions	C_s (F/g)	Test conditions
Ni-Mn oxide[44]	Anodic electrodeposition	10mM $MnCl_2$ + 100mM $NiCl_2$, 10 mV/s for 45 cycles	160	50 mV/s, 3-electrode setup
Ni-Mn oxide[45]	Potentiodynamic electrodeposition	0.4 M $MnSO_4$ + 0.1 M $NiCl_2$, pH=6, 200 mV/s for 300 cycles	621 (685)	10 mV/s (2 mA/cm^2), 3-electrode setup
Co-Mn oxide[45]	Potentiodynamic electrodeposition	0.4 M $MnSO_4$ + 0.1 M $CoCl_2$, pH=6, 200 mV/s for 300 cycles	498 (560)	10 mV/s (2 mA/cm^2), 3-electrode setup
Mo-Mn oxide[46]	Anodic electrodeposition	2 mM $MnSO_4$ + 20 mM Na_2MoO_4, 20 mV/s	190	5 mV/s, 3-electrode setup
Ru-Mn	Oxidative co-	$RuCl_3$ + $MnAc_2$ +	197-	2 mA, 3-electrode

oxide[47]	precipitation	$KMnO_4$	318	setup
Co-doped MnO_2[48]	Pulsed laser deposition	Laser fluency of 2-3 J/cm2, and repetition rate of 50 Hz	99	5 mV/s, 3-electrode setup
Fe-doped MnO_2[49]	Electrochemical deposition	0.1 M $MnSO_4$ + 0.1 M citric acid + 1M NaOH + $FeSO_4$, pH=10.5, 5 mA/cm^2	218	5 mV/s, 3-electrode setup
Sn-doped MnO_2[50]	Chemical co-precipitation	$KMnO_4$ + $MnCl_2$ + $SnCl_2$, pH=7	293	0.2 A/g, 3-electrode setup
Ag-doped MnO_2[51]	Cathodic electrochemical deposition	20 mM $KMnO_4$ + 0-2 mM $AgNO_3$, 1 mA/cm^2	770 (225)	2 mV/s, mass loading of 50 $\mu g/cm^2$ (160 $\mu g/cm^2$), 3-electrode setup
Au-doped MnO_2[52]	Electrochemical deposition of MnO_2; Physical vapor deposition of Au-doping	0.2 M $MnAc_2$ + 0.2 M Na_2SO_4, 0.4 V for 5s and 0.45 V for 10s, last for 5 min; Sputtering current of 40 mA, deposition rate of ~ 0.62 $\mu g\ s^{-1}\ cm^{-2}$	626	5 mV/s, mass loading of ~100 $\mu g/cm^2$, 3-electrode setup

Table 1.3: Electrochemical performance of the mixed metal oxides (MnO_2 with other transition metal oxides), and the doped MnO_2 compounds by other metallic elements.

1.7 Objective of the Dissertation

The objective of this dissertation is to prepare MnO_2 based nanostructures in order to improve supercapacitor electrochemical performance. We will achieve the objective from the following strategies:

1. The preparation of MnO_2 nanostructures with desirable morphological and crystalline structures, and the detailed understanding of their electrochemical performance as supercapacitor materials.
2. The fabrication of MnO_2 with different forms of carbon nanomaterials for MnO_2 based nanocomposites to improve the electrode conductivity and energy storage density.
3. The design and fabrication of novel MnO_2-based electrodes for low-cost and scalable supercapacitors with excellent electrochemical performance.
4. The preparation of other supercapacitive materials (conducting polymers and carbons) based on the MnO_2 nanostructures as templates.

Chapter 2

MnO_2 Based Supercapacitor Electrodes

2.1 MnO_2 Nanostructures

2.1.1 Introduction

Manganese dioxide (MnO_2) is considered to be one of the most promising materials for energy storage systems including batteries and supercapacitors.[32, 58-61] Compared to batteries, supercapacitors have much higher power density (10-100 times higher than batteries), fast charge rate (charge a supercapacitor takes only a few seconds to minutes) and excellent cycling stability (cycle number of more than 1 million cycles). This makes supercapacitors ideal devices for many critical applications such as consumer electronics, hybrid electric vehicles, and smart grid storage.[2, 62] However, their relatively lower energy density (~10 times lower than that of batteries) has thus far limited their wide-spread application as energy storage devices.[5] Carbon based supercapacitors show low charge storage capacity due to the limited electrolyte ion adsorption and desorption on the surface of the carbon. Therefore, replacing carbon materials in commercial supercapacitors by high capacity materials like MnO_2 can be an effective strategy to increase the energy density of supercapacitors, thus paving the way for their adoption in a variety of applications. However, oxide

electrodes have the fatal disadvantage of poor cycling performance, an issue that so far has not been sufficiently investigated.

Various synthesis methods and a large variety of MnO_2 with different morphologies and crystalline phases have been reported to prepare MnO_2 nanostructures.[63-71] However, a systematic study focused on studying the effect of MnO_2 nanoscale morphology and crystal phase and its cycling performance on supercapacitor capacity has not been performed. One of the very first studies conducted by Belanger *et al.* revealed the energy storage mechanism of MnO_2 electrode in aqueous electrolyte by cyclic voltammetry and X-ray photoelectron spectroscopy techniques.[72] They found that the MnO_2 electrode with thick layer underwent no change of the Mn oxidation state because only a very thin layer of the material contributed to the energy storage process.[72] Afterwards, Wei *et al.* carried out a study of the influence of MnO_2 morphology on the electrochemical properties by controlling the material synthesis conditions.[36] The electrochemical tests demonstrated that the storage capacity of MnO_2 electrodes is highly related to its morphology, nanostructure, and surface area, but the study did not provide very detailed material analysis to elucidate the factors that control electrochemical performance of the devices.[36] In order to achieve the best energy storage performance of MnO_2 and better understand the energy storage mechanism, it is very important to study not only the general shape or nanostructure of MnO_2 but also the evolution of the nanostructures with electrochemical cycling to the supercapacitor performance.

We report a comprehensive study on investigating the energy storage mechanism of nanostructured MnO_2 by a systematic route using multiple techniques that have not been utilized to study MnO_2 based supercapacitors previously. Firstly, we prepared different MnO_2 nanostructures with well-controlled morphology and crystallinity by a facile hydrothermal reaction. In addition to many conventional characterization methods, three-dimensional scanning transmission electron microscopy tomography is used, for the first time, to explain the growth mechanism of the MnO_2 and the corresponding cycling performance of the supercapacitors. Furthermore, the electrochemical performance of the MnO_2 nanostructures was studied in detail and we revealed the energy storage mechanism of MnO_2 by direct observation of the evolution of material structure during long-term cycling tests.

2.1.2 Experimental Section

2.1.2.1 Preparation of MnO_2 Nanostructures

MnO_2 nanostructures with controlled morphologies were prepared from a facile hydrothermal route. In a typical procedure, $KMnO_4$ (0.263 g, 1.66 mmol) were dissolved in water (30 mL) with agitation at room temperature, followed by adding concentrated HCl (37%, 1 mL). After stirring for 5 min in air, the solution was transferred to a Teflon-lined stainless steel autoclave (capacity of 45 mL) and heated to 140 °C in an electric oven. In order to get designed morphology, the reaction of the solution was kept for different periods (1h, 1.5h, 2h, 4h, 8h,

12h), and the autoclave was then cooled naturally to room temperature. The resulting products were filtered, washed by water and absolute ethanol repeatedly to remove any possible residual reactants. Finally, the products were dried in an oven at 80 °C.

2.1.2.2 Materials Characterization

The microstructure and morphology of MnO_2 were characterized by scanning electron microscopy (SEM, Nova Nano 630, FEI), and transmission electron microscopy (TEM, T12 and Titan 80-300 kV (ST) TEM, FEI). The crystallographic structure of the samples was tested by X-ray diffraction (XRD, D8 Advance bulk power XRD, Bruker). Surface area and pore size distribution measurement (ASAP 2420, surface area and pore size analyzer, Micromeritics) was carried out by nitrogen adsorption and desorption at bath temperature of -195.85 °C. The X-ray photoelectron spectroscopy (XPS) analysis was conducted on a Kratos AXIS Ultra DLD spectrometer. A FEI Titan Super Twin 80-300 operated at 300 kV, equipped with a Fischione Dual-Axis tomography holder (Model 2040), was used to acquire the TEM images and scanning transmission electron microscopy (STEM) tomography tilt series. Fischione Annular Dark Field (ADF) detector (Model 3000) was used to acquire HAADF STEM images. The semi-convergence angle (alpha) of the probe is 10 mrad and HAADF STEM images was acquired at the detector inner and outer collection angles of 58 mrad and 200 mrad. The total data acquisition time was ~3h which included the operation of tracking and focusing in manual mode. The tilt series were acquired

at the range from -70 degree to +70 degree in Xplore 3D software (FEI Company) with the tilt increment of 2 degree. Inspect3D software (FEI Company) was used to process the tilt series using a cross correlation method for image shift and tilt alignments, and the 3D reconstruction was performed by simultaneous iterative reconstruction technique (SIRT) with 30 iterations. The visualization of the 3D datasets was performed by using isosurface and volume rendering in Avizo Fire software.

2.1.2.3 Electrochemical Measurements

All electrochemical tests in this study were conducted at room temperature in a three-electrode configuration, with Pt wire used as counter electrode, Ag/AgCl as reference electrode, and MnO_2 coated on carbon paper as working electrode. MnO_2 with different morphologies acting as active material was each mixed with acetylene black and polytetrafluoroethylene (PTFE) binder with a ratio of 80:10:10 in ethanol to form homogenous electrode slurry. The electrodes of supercapacitors were prepared by drop casting of the slurry onto graphitized carbon papers. Then the electrodes were vacuum dried at 100 °C for 12 hours. The mass of the materials on the electrode was determined by a microbalance (Mettler Toledo XP26, resolution of 1 μg) using the mass difference before and after materials loading. The typical mass loading of the electrodes is 2 ~ 3 mg/cm^2. The electrolyte used in this study is 1 M Na_2SO_4. The electrochemical performance was tested in a VMP3 multi-channel electrochemical workstation (Bio-Logic) by the techniques of electrochemical impedance spectroscopy (EIS),

cyclic voltammetry (CV) and galvanostatic charge-discharge (CD). The EIS was measured with frequency range between 100 kHz and 100 mHz. The CV was tested from scan rate of 5 mV/s to 100 mV/s with voltage window from 0 to 0.8 V vs. Ag/AgCl. The CD measurement was conducted from current density of 0.5 A/g to 10 A/g with the same voltage window as the CV tests. The capacitance values were calculated from galvanostatic charge-discharge curves according to the equation mentioned in the chapter 1. The galvanostatic charge and discharge technique was used to determine the cycling performance for all samples.

2.1.3 General Characterization of MnO_2 Nanostructures

Different morphologies of MnO_2 nanostructures were prepared by a hydrothermal reaction between $KMnO_4$ and HCl in aqueous solution. The reaction periods were chosen to engineer the morphology of the MnO_2 electrodes, and included reaction times of 1 h, 1.5 h, 2 h, 4 h, 8 h and 12 h. As shown in Figure 2.1, after a reaction of 1h, the mixed solution of $KMnO_4$ and HCl aqueous medium results in the nucleation and growth of porous nanospheres (inset in Figure 2.1a). The nanospheres are comprised of many wrinkled nanosheets, which are self-assembled perpendicular to the outer surface of the nanospheres (Figure 2.1a). The porous nanospheres have typical diameters ranging from a few hundred nanometers to several micrometers, and the gaps between the nanosheets vary from 50 nm to 300 nm. When the reaction time is increased to 1.5 h, short nanofibers begin to emerge between the nanosheets, as marked by the red arrows in Figure 2.1b. However, the porous sphere-like

morphology persists, and the nanosheets are still dominant over nanofibers. When the hydrothermal reaction is further prolonged to 2h (Figure 2.1c), more nanofibers grow from the nanosheets and the diameter of the nanofibers also increases, compared to the sample in Figure 2.1b. It is interesting to note that the nanosheets inside the nanospheres disappear completely when the reaction time extends to 4h (Figure 2.1d), and instead of forming more nanofibers, a large number of nanotubes are formed. The nanotubes formation can be seen from their end tips (Figure 2.1d), and will be confirmed later in the manuscript. The nanotubes replace the original nanosheets, but the overall sphere-like morphology is retained, where each nanosphere now consists of MnO_2 nanotube bundles. When the reaction time reaches 8 h (Figure 2.1e), the nanotubes still exist but the overall morphology of MnO_2 has changed to hollow urchin-like structure, which is less agglomerated as compared to the morphology in Figure 2.1d. Finally, after reaction time of 12h, the individual nanotubes disperse well in the reaction solution and the nanosphere morphology disappears (Figure 2.1f).

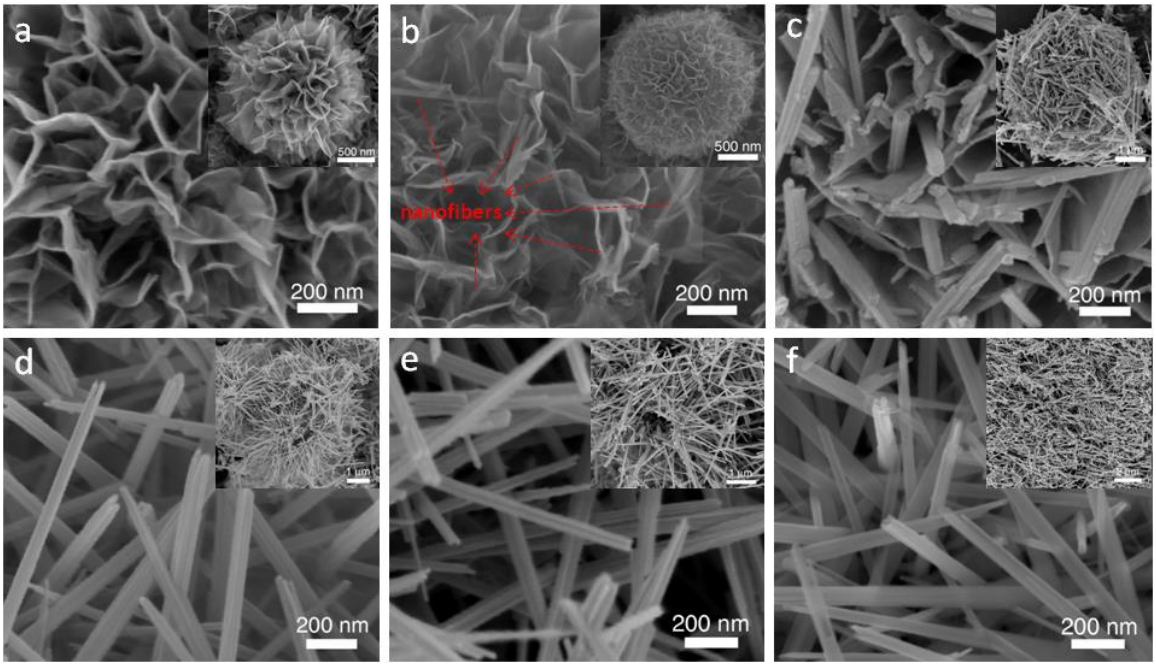

Figure 0.1: SEM images of the MnO_2 nanostructures obtained at different hydrothermal reaction times. (a) MnO_2-1h; (b) 1.5h; (c) 2h; (d) 4h; (e) 8h; (f) 12h.

XRD was carried out to investigate the crystal structure and phase purity of the as-prepared MnO_2 nanostructures with different morphologies. It is found that the MnO_2 can be classified into two different crystalline structures, depending on the hydrothermal reaction time. When the hydrothermal reaction is less than 2 h, the diffraction peaks of the MnO_2 shown in Figure 2.2 can be indexed to K-Birnessite δ-MnO_2 (JCPDS 01-080-1098, base-centered monoclinic with a=5.149Å, b=2.843Å, c=7.176Å and β=100.76°).[73] The broad and low intensity XRD peaks indicate a poor or polycrystalline feature of the layered δ-MnO_2. While for the MnO_2 obtained at hydrothermal reaction of more than 2 h, the sharp and high intensity peaks correspond to α-MnO_2 (JCPDS 00-044-0141,

body-centered tetragonal with a=9.78 Å and c=2.86 Å), indicating the high crystallinity and high purity of the MnO_2 prepared by the facile hydrothermal method.[74] Therefore, the crystal phase and morphology of the MnO_2 nanostructures can be controlled very well by the reaction time.

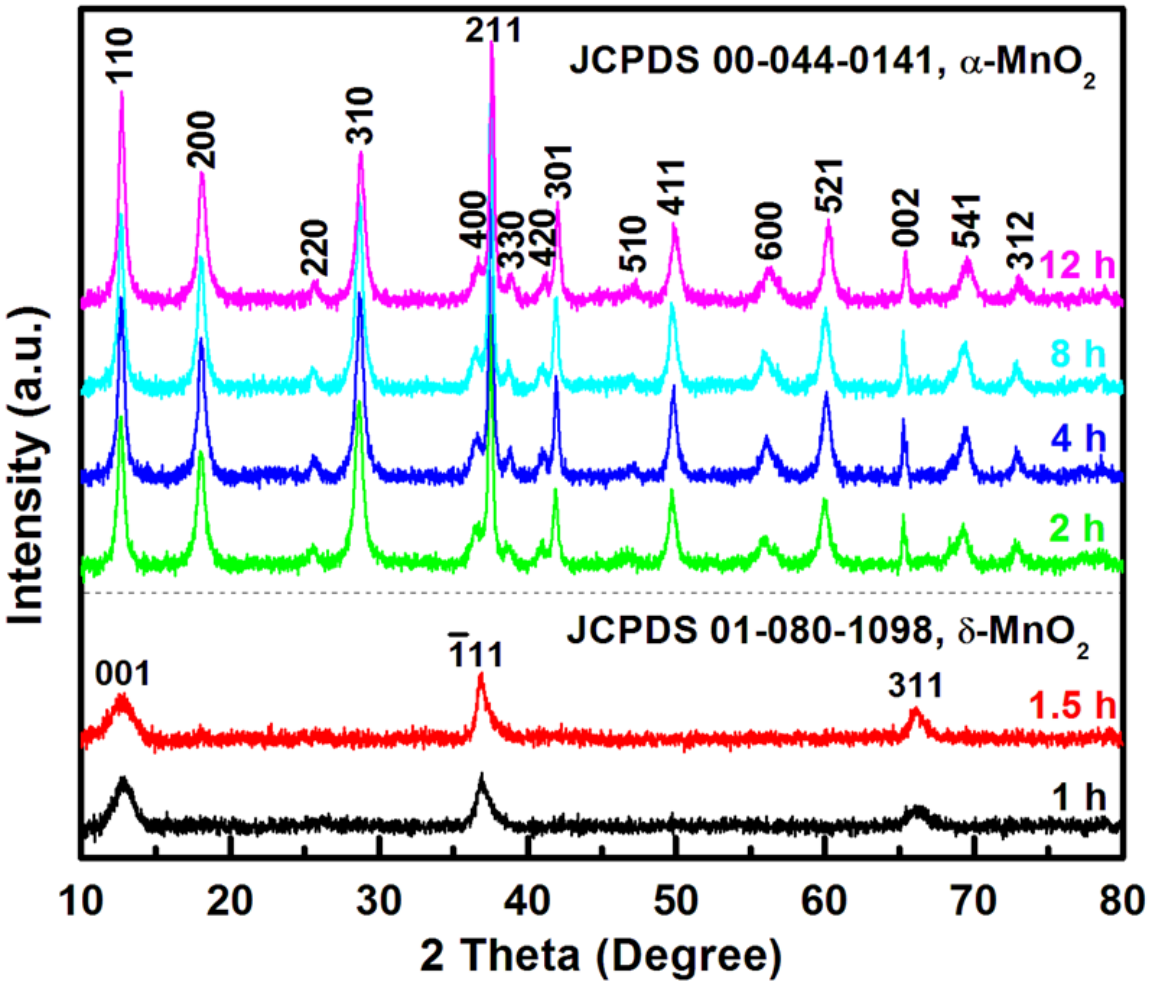

Figure 0.2: XRD patterns of the MnO_2 nanostructures obtained at different hydrothermal reaction times, ranged from 1h to 12h.

TEM was used to characterize the interior of the MnO_2 nanostructures with different morphologies. Figure 2.3a shows folded MnO_2 nanosheets that self-assembled into porous nanospheres (inset of Figure 2.3a), corresponding to the MnO_2 morphology observed in the SEM in Figure 2.1a. Furthermore, the TEM images in Figure 2.3b confirm that the nanofibers start to appear from the surface of the nanosheets within the nanospheres, as was demonstrated by the SEM in Figure 2.1b. It is also observed in Figure 2.3b that the nanofibers are polycrystalline. The lattice fringes show d-spacings of 0.24 nm and 0.31 nm, corresponding to the d values of (211) and (310) planes of α-MnO_2, respectively. This indicates that the δ-MnO_2 nanosheets convert to polycrystalline α-MnO_2 nanofibers in the initial phase of nanofiber formation. The lattice fringe with spacing of 0.49 nm corresponds to d value of (200) plane of α-MnO_2. Figure 2.3c shows the TEM image of MnO_2 nanostructure formed at a 2h hydrothermal reaction time. The overall morphology in the inset of Figure 2.3c shows that the nanospheres are composed a number of nanofibers. Enlarged image of selected region in Figure 2.3c inset (marked by the red square) exhibits the coexistence of MnO_2 nanosheets and nanofibers, which agrees well with the morphology observed by SEM in Figure 2.1c. The nanofibers have their one end embedded in the nanosheets, indicating that the growth of MnO_2 nanofibers originates from the nanosheets themselves.[70] Figure 2.3d shows the hollow urchin-like MnO_2 sphere, consisting of a bundle of nanotubes obtained at reaction time of 4h. Most of the nanotubes in this stage are not completely hollow tubes, with only the

outer end part of the tubes becoming hollow (Figure 2.3d). However, the end tips of the MnO_2 nanotubes have become rough and irregular, different from the smooth and neat shape of the nanofibers (Figure 2.3b). The tubular morphology of individual MnO_2 remained with increasing reaction time, as shown in Figure 2.3e (reaction time of 8h) and Figure 2.3f (reaction time of 12h). However, at these long reaction times (8 and 12 h), the overall morphology of MnO_2 evolved to rather hollow spheres (Inset of Figure 2.3e) and well-dispersed nanotubes (Inset of Figure 2.3f). The evolution of the MnO_2 nanostructure and morphology is summarized in Table 1.

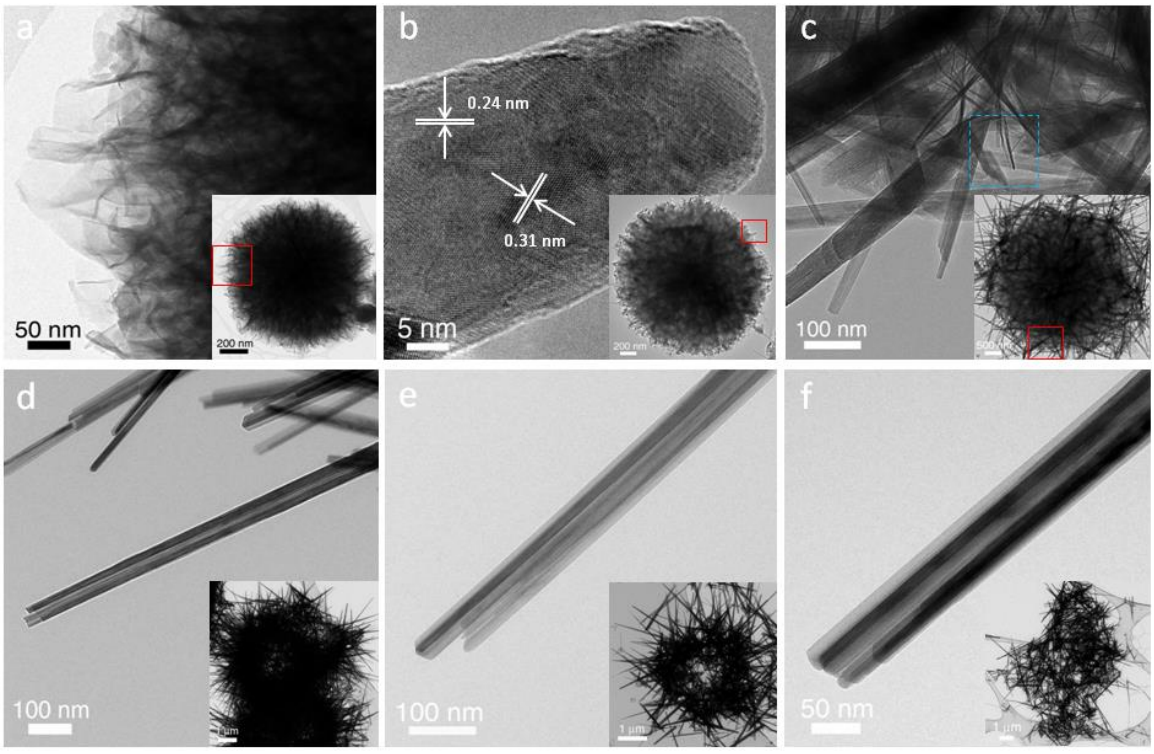

Figure 0.3: TEM images of the MnO_2 nanostructures obtained at different hydrothermal reaction times. (a) MnO_2-1h; (b) 1.5h; (c) 2h; (d) 4h; (e) 8h; (f) 12h.

Reaction time (h)	1	1.5	2	4	8	12
Morphology	spheres consisting of sheets	sheets + fibers	sheets (less) + fibers (more)	tubes	tubes	tubes
Crystallinity	poly-crystalline δ-MnO_2 sheets	polycrystalline δ-MnO_2 sheets and polycrystalline α-MnO_2 fibers	polycrystalline δ-MnO_2 sheets and polycrystalline α-MnO_2 fibers	single crystalline α-MnO_2 tubes	single crystalline α-MnO_2 tubes	single crystalline α-MnO_2 tubes
BET surface area (m^2/g)	201.65	156.35	55.62	44.99	41.58	40.58

Table 2.1: The summary of MnO_2 nanostructures in terms of morphology, crystallinity and BET surface area.

Additional HRTEM and selected area electron diffraction (SAED) were performed on MnO_2. Figure 2.4a shows a folded nanosheet in one of the MnO_2 nanospheres. By careful inspection, it can be seen that the nanosheet consists of many small domains with different orientations, confirming its polycrystalline nature. The observed fringes with spacing of 0.7 nm and 0.24 nm correspond to the d value of (001) and $(\bar{1}11)$ planes of δ-MnO_2. The SAED pattern taken in approximately the same region as Figure 2.4a displays two characteristic rings that correspond to (311) and $(\bar{1}11)$ planes of δ-MnO_2 (Figure 2.4b). The appearance of (311) plane in the SAED pattern is not observed in the HRTEM image due to the limited spatial resolution of the TEM. Nevertheless, the HRTEM together with its SAED pattern confirm that the MnO_2 nanospheres are δ-MnO_2 with polycrystalline nature for short hydrothermal reaction time (1h). In contrast, the MnO_2 nanotubes formed after long hydrothermal reaction time (12h)

demonstrate the typical hollow structure with irregular open tips (Figure 2.4c). The highly crystalline lattice fringes in the HRTEM image (Figure 2.4c) indicate the single crystalline characteristic of the MnO_2 nanotubes, as confirmed by the corresponding SAED pattern (inset of Figure 2.4c). The growth direction of the nanotubes is [001], which can be determined from its SAED pattern and further confirmed by the cross-sectional TEM image of MnO_2 nanotube and its corresponding SAED pattern (Figure 2.4d).

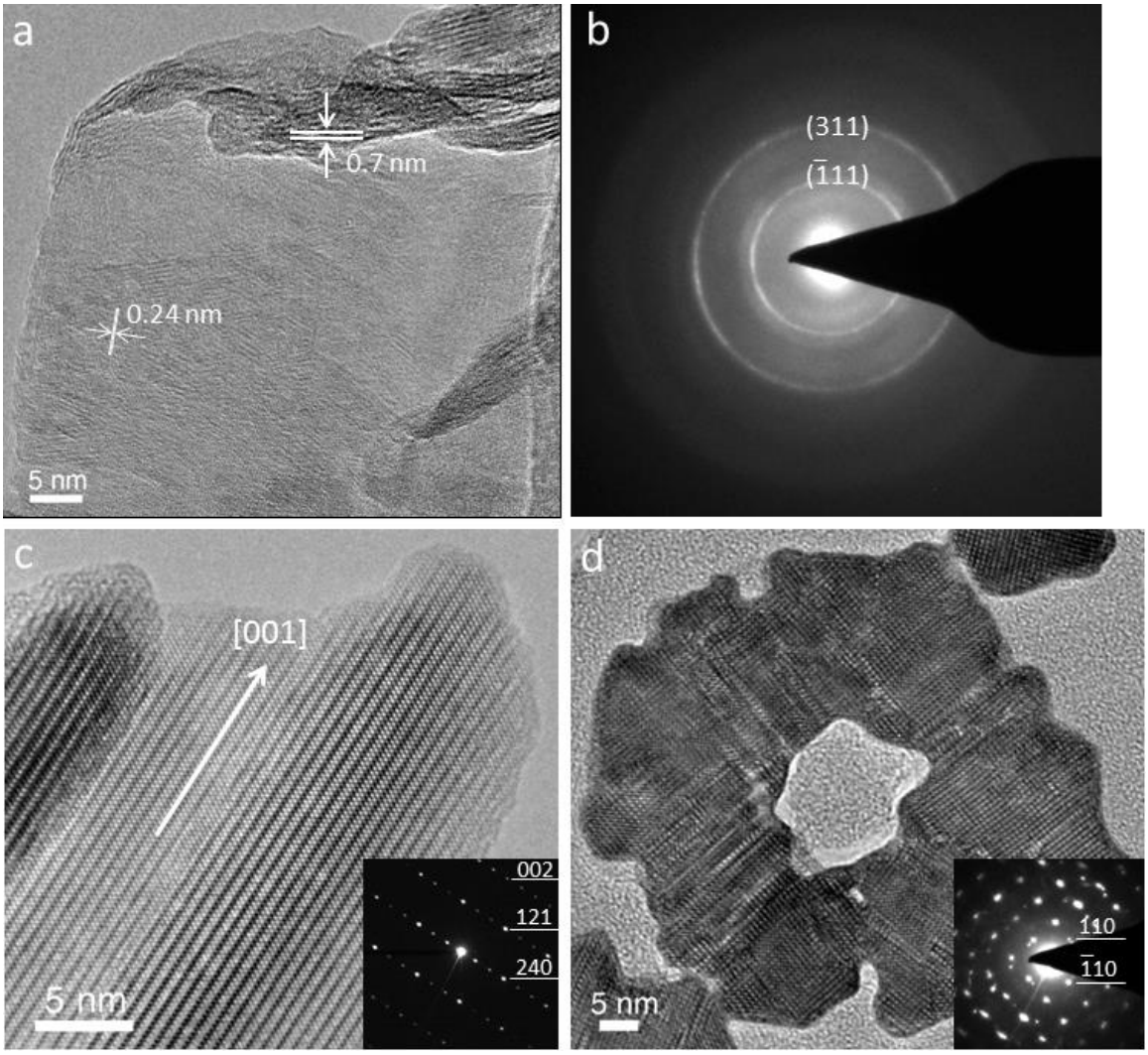

Figure 0.4: HRTEM images of (a) the MnO_2 nanosheets (MnO_2-1h) and (b) the corresponding SAED pattern; (c) MnO_2 nanotubes (MnO_2-12h) and (d) the corresponding SAED pattern.

2.1.4 3D Electron Tomography of MnO_2

Although the morphological and crystalline characteristics of MnO_2 nanostructures can be identified from 2D TEM images, some important

information on the material may still be difficult to detect due to the limitation of 2D projection in the TEM technique.[75] We therefore used 3D electron tomography to visualize the 3D morphological evolution of the various MnO_2 nanostructures to better understand the growth mechanism and the corresponding electrochemical performance of MnO_2 electrodes.[76] Three different morphologies of the 1D MnO_2 were selected for study using 3D electron tomography: (i) nanofibers obtained at hydrothermal reaction time of 2h, nanotubes obtained at hydrothermal reaction time of (ii) 4h, and (iii) 12h. We understand that it is difficult to cover all the different morphologies, but the selected three morphologies are enough to show the evolution of the 1D MnO_2 nanostructures. As depicted in Figure 2.5, the reconstructed 3D images and their cross sectional slices exhibit the overall morphology and interior structure of MnO_2, information that is not available by conventional TEM images, but is extremely important to explain the growth mechanism and electrochemical performance of MnO_2. Take the MnO_2 nanofiber (MnO_2-2h) as an example, the constructed 3D image in Figure 2.5a shows a nanofiber with smooth outer surface. Figure 2.5b shows that the inside of the nanofiber is completely solid without any voids or defects. However, some areas on the tip of the nanofiber are rough, as illustrated by the red circles in Figure 2.5a and b. This roughness is probably caused by the acid etching effect in the reaction solution, indicating that the etching process preferably takes place on side surfaces of the nanofibers. The cross-sectional slice shown in Figure 2.5b is irregularly shaped indicating

that one side of the outer surface is also corroded by acid etching. All this information confirms the solid interior of the nanofibers without internal openings. As for the MnO_2 nanotubes (MnO_2-4h), their outer surfaces are quite rough and irregular (Figure 2.5d-f), which is a result of being seriously etched by the acids. The 3D reconstruction of the nanotube shows clearly the formation of the voids. It is further revealed that these voids are preferable to grow laterally along the nanotubes as labeled by the red rectangles in Figure 2.5e, which are caused by the recrystallization during the Ostwald ripening process (discussed in the next section). The irregular nanotube was formed as a result of further growth of the central voids that run the entire length of the structure, as confirmed by the cross sectional images taken at the two ends of the nanotube. In the case of MnO_2 nanotubes obtained at a reaction time of 12h (MnO_2-12h), the structure has been further corroded by the acid etching, forming larger hollow openings and even rupturing the walls of the nanotubes, as indicated by the red arrows in Figure 2.5g and h. It is a combined result that dominated by the ripening and etching processes (Figure 2.5I).

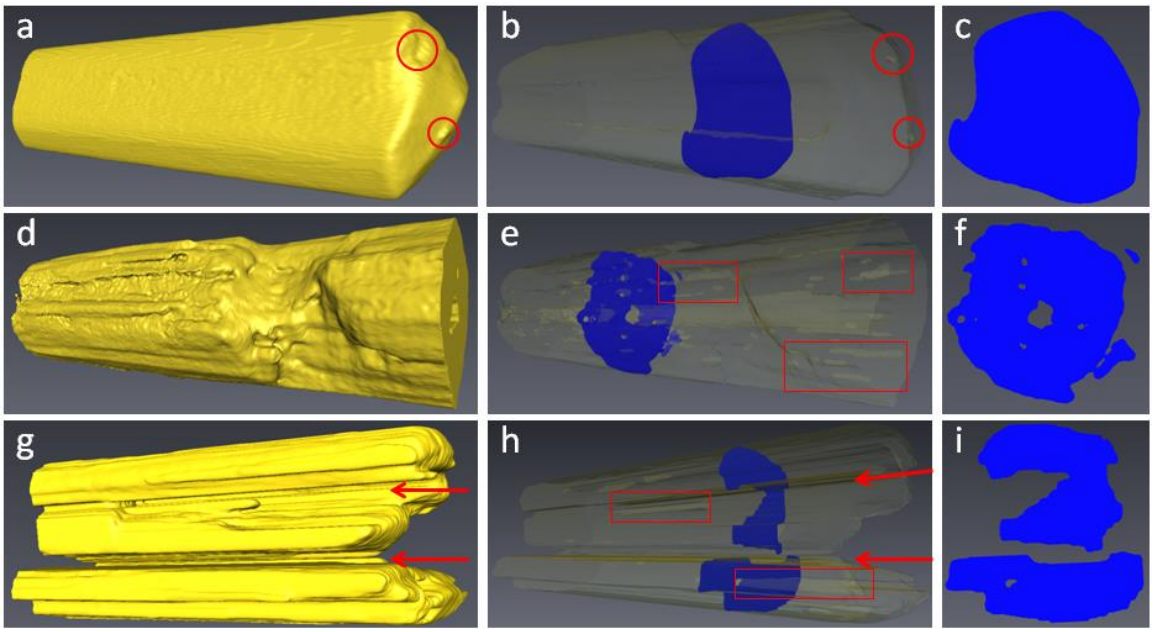

Figure 0.5: Electron tomography of 1D MnO_2 nanostructures. 3D reconstruction, semi-transparent reconstruction and the cross sectional slice for (a-c) MnO_2 nanofiber (MnO_2-2h), (d-f) MnO_2 nanotube (MnO_2-4h), (g-i) MnO_2 nanotube (MnO_2-12h), respectively.

2.1.5 Growth Mechanism of MnO_2 Nanostructures

In order to get the desired morphology and crystal phase for specific applications, it is important to understand the growth mechanism of the MnO_2 nanostructures. Several growth mechanisms of the hydrothermally synthesized MnO_2 have been proposed in the previous reports. Wang *et al.* proposed a rolling mechanism to explain the formation of one-dimensional MnO_2 from lamellar structure of MnO_2.[77] Luo *et al.* suggested that the formation of MnO_2 nanotube is a result of the acid etching process in the reaction solution.[74] Recently, Li *et al.*

provided an “oriented attachment” mechanism to illustrate the convention of MnO_2 nanotubes from nanorods.[78] Truong *et al.* proposed the diffusion of nanosheets and the anisotropic growth of nanowires, followed by an Ostwald ripening process to form MnO_2 nanotubes.[70] However, none of these hypotheses are obtained based on direct observation of the evidence. We believe that it is important to support the proposed growth mechanisms of MnO_2 nanostructures by direct observation. Taking the 3D reconstruction of the nanostructures by electron tomography and combining with the results obtained from XRD, SEM and TEM, we are able to provide vivid insight into the internal structures of the materials, and to explain the growth mechanism of MnO_2 nanostructures during hydrothermal synthesis.[76]. Figure 2.6 summarizes our view of the growth process of MnO_2 nanostructures. As shown in Figure 2.6a, the rose-like MnO_2 nanoflower consists of numerous nanosheets that form rapidly once the reaction solution has reached the target temperature. The observation of this very first step in our experiment agrees well with the previous reports.[67, 70] The formation of the MnO_2 nanospheres is a result of the following reactions:

$$2MnO_4^- + 8H^+ + 6Cl^- \rightarrow 2MnO_2 + 3Cl_2 + 4H_2O \quad (1)$$

$$4MnO_4^- + 4H^+ \rightarrow 4MnO_2 + 3O_2 + 2H_2O \quad (2)$$

The MnO_2 nanosheets are determined to be δ-MnO_2, as revealed by XRD and TEM, which is a layered structure that is composed of edge-shared MnO_6

octahedral units.[77] However, the layered δ-MnO_2 nanosheets are in a metastable state and tend to be curled at elevated temperature and pressure, resulting in the conversion from nanosheets to nanofibers as illustrated in Figure 2.6b. The short nanofibers inherit the polycrystalline nature of the nanosheets of MnO_2, but their crystalline phase changes from δ-MnO_2 to α-MnO_2 as the MnO_2 one-dimensional structures is formed. This phase change is driven by an overall reduction of the free energy of the system as the α-MnO_2 is a 2×2 tunneled structure with higher crystallinity, and is thermodynamically more stable than the δ-MnO_2.[68 78] These observations agree with the growth mechanism that has been proposed by Truong *et al.* for the formation of 1D nanostructures from 2D nanosheets.[70] With increasing reaction time, more energy is introduced into the system. The δ-MnO_2 nanosheets continue to diffuse until completely consumed while the α-MnO_2 nanofibers continue to grow, finally resulting in α-MnO_2 nanofibers (Inset of Figure 2.6c). In the meantime, some of the α-MnO_2 nanofibers start to undergo an Ostwald ripening process that converts the polycrystalline α-MnO_2 nanofibers to single crystalline phase. Due to the direct contact of the outer surface with the reaction solution, the nanofiber outer surface can firstly become highly crystalline, while the ripening process in its interior is much slower owing to their different activities of the polycrystalline nanodomains (Figure 2.6c). As the hydrothermal reaction time is further increased, the conversion of nanosheets to nanofibers is completed and some partially hollow nanotubes are formed (Figure 2.6d). The formation of nanotubes from nanofibers was confirmed earlier by 3D

electron tomography. As discussed in the previous section, the nanofibers are easily converted to irregular nanotubes under the high temperature and strong acid conditions, which is dominated by the ripening process as well as the acid etching process. The effect of the acid etching process is favored on the outer surfaces of the nanofibers, because the side surfaces can access the surrounding acid more easily than the materials inside the nanofibers, inducing the concave side surfaces and even large openings that observed by the 3D electron tomography. Longer hydrothermal reaction times make the nanotubes more hollow and more crystalline, while individual nanotube starts to disperse more uniformly in the solution (Figure 2.6e and f), slowly losing the overall spherical/urchin-like morphology.

In summary, our detailed analysis suggests that the nucleation and growth process of the MnO_2 nanostructures formed by the hydrothermal reaction proceed as flows: (a) nucleation and self-assembly of MnO_2 nanosheets into of 3D nanospheres, (b) the formation of 1D nanofibers that nucleate out of the nanosheets, and subsequent conversion of the nanosheets to short nanofibers, (c) growth of the nanofibers in size and length, along with continued conversion of nanosheets to nanofibers, (d) complete conversion of nanosheets to nanofibers, and formation of nanotubes from nanofibers, (e) continued formation of nanotubes with more hollow interior. In the meantime, the crystal phase of MnO_2 transforms from polycrystalline δ-MnO_2 nanosheets to polycrystalline α-

MnO_2 nanofibers, and then to single crystalline α-MnO_2 nanofibers and nanotubes.

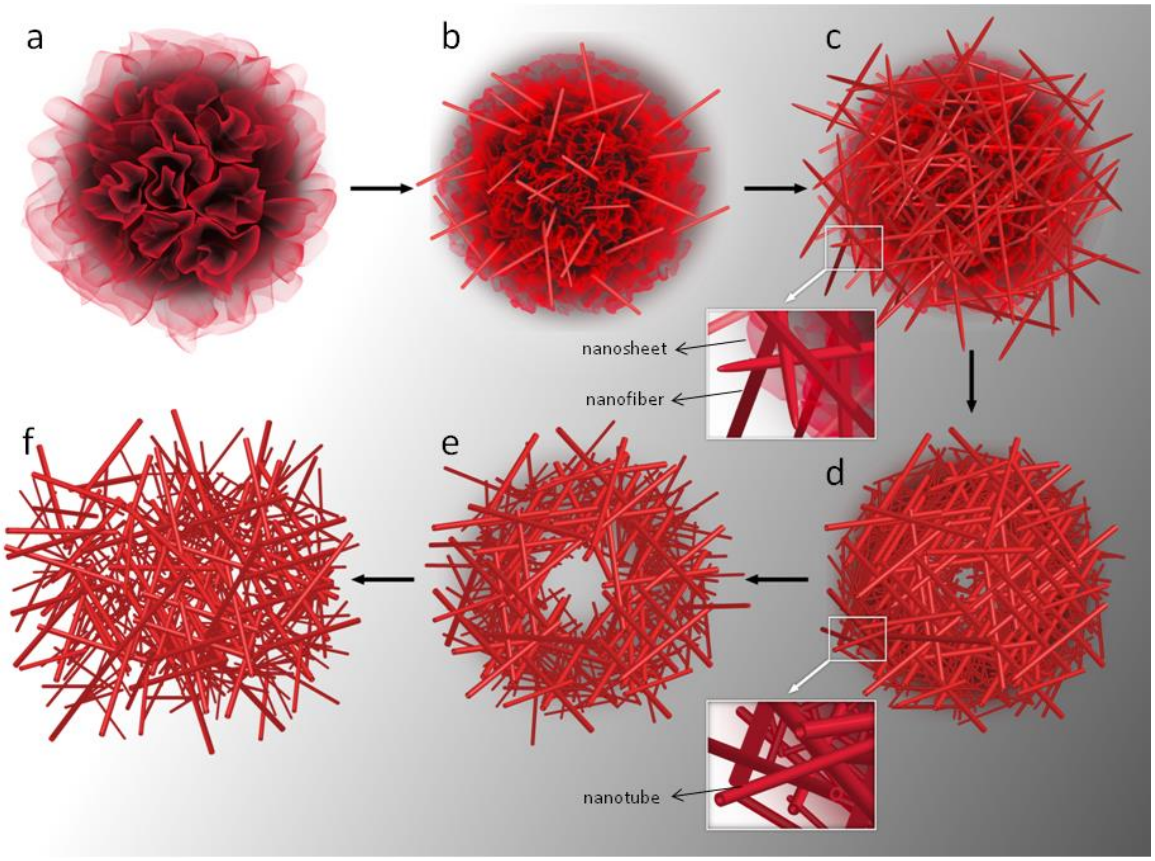

Figure 0.6: Schematic illustrations of the growth process of MnO_2 nanostructures controlled by the hydrothermal reaction time. (a) MnO_2-1h; (b) 1.5h; (c) 2h; (d) 4h; (e) 8h; (f) 12h.

2.1.6 Electrochemical Performance of MnO_2 Nanostructures

2.1.6.1 Morphological Effect

The electrochemical properties of nanostructured MnO_2 as electrode material for supercapacitors were studied in a three-electrode configuration by means of cyclic voltammetry (CV), galvanostatic charge-discharge (CD) and electrochemical impedance spectroscopy (EIS). The purpose of the electrochemical study is to understand the impact of the structural variation on the energy storage mechanism of MnO_2. The MnO_2 nanostructures with different morphologies and crystal phases obtained at different hydrothermal reaction periods were all systematically studied as supercapacitor electrode materials, and their electrochemical behaviors are summarized in Figure 2.7. Figure 2.7a and b show the CV curves at the same scan rate of 10 mV/s and CD at the same current density of 1 A/g for all samples before cycling tests. All CV curves show nearly rectangular shapes (Figure 2.7a), corresponding to the highly symmetrical charge and discharge curves (Figure 2.7b), which all indicate good supercapacitor characteristics that agree well with the previous reports.[25, 79]. At the same scan rate, the measured current density of the MnO_2 nanostructures decreases with the hydrothermal reaction time. This results in the decrease of area under the CV loops with the reaction time. Similarly, under the same applied current density of 1 A/g, the charge and discharge time becomes shorter as the hydrothermal reaction time increases, suggesting the decrease in capacitance

with the reaction time. As a result, the sample of MnO_2-1h shows the highest values of specific capacitance, while the sample of MnO_2-12h shows the lowest ones (Figure 2.7c). It is worth noting that the capacitance of MnO_2-1.5h is only slightly lower than that of MnO_2-1h, but the values of other samples (MnO_2-2h, 4h, 8h and 12h) are much lower than that of MnO_2-1h. The capacitances of MnO_2-2h, 4h, 8h and 12h are in a relatively low range between 10 F/g and 30 F/g, while the range for MnO_2-1h and 1.5h is between 50 F/g and 110 F/g.

It is known that the electrochemical performance of supercapacitive materials is highly dependent to their surface area for both electrochemical double layer storage mechanism and pseudocapacitive storage mechanism.[2] The morphological evolution of the MnO_2 from nanosheets to nanofibers and finally nanotubes, together with the crystallinity change from polycrystalline to single crystalline resulted in a huge difference in the surface area of the MnO_2 nanostructures used in this study. As shown in Figure 2.8, the nitrogen adsorption and desorption isotherm curves demonstrate typical type IV curves for all MnO_2 nanostructures, indicating the mesoporous nature of the materials. The calculated specific surface area (SSA) based on BET model for all MnO_2 is presented in Table 2.1. The SSA changes with the hydrothermal reaction time over a wide range (Figure 2.7d). Specifically, the SSA of the samples of MnO_2-1h (201.65 m^2/g) and MnO_2-1.5h (156.35 m^2/g) are three to four-fold higher than that of MnO_2-2h (55.62 m^2/g), MnO_2-4h (44.99 m^2/g), MnO_2-8h (41.58 m^2/g), and MnO_2-12h (40.58 m^2/g). The dramatic decrease of the SSA is caused by the

conversion of MnO_2 nanosheets to nanofibers/nanotubes, accompanied by the transformation of poor crystalline lamellar structured δ-MnO_2 to highly crystalline tunnel structured α-MnO_2. The decrease of the SSA with the reaction time decreases the capacitance of the devices as shown in Figure 2.7d, which agrees well with the reports.[80, 81] Some previous studies also showed that the amorphous/poor crystalline MnO_2 with higher SSA is preferable as supercapacitor material.[82-84] The pore size distribution of the MnO_2 nanostructures (Figure 2.8b) shows a relatively narrow pore size distribution of the materials (average pore size between 7 and 13 nm), indicating the uniform pores of our MnO_2 nanostructures.

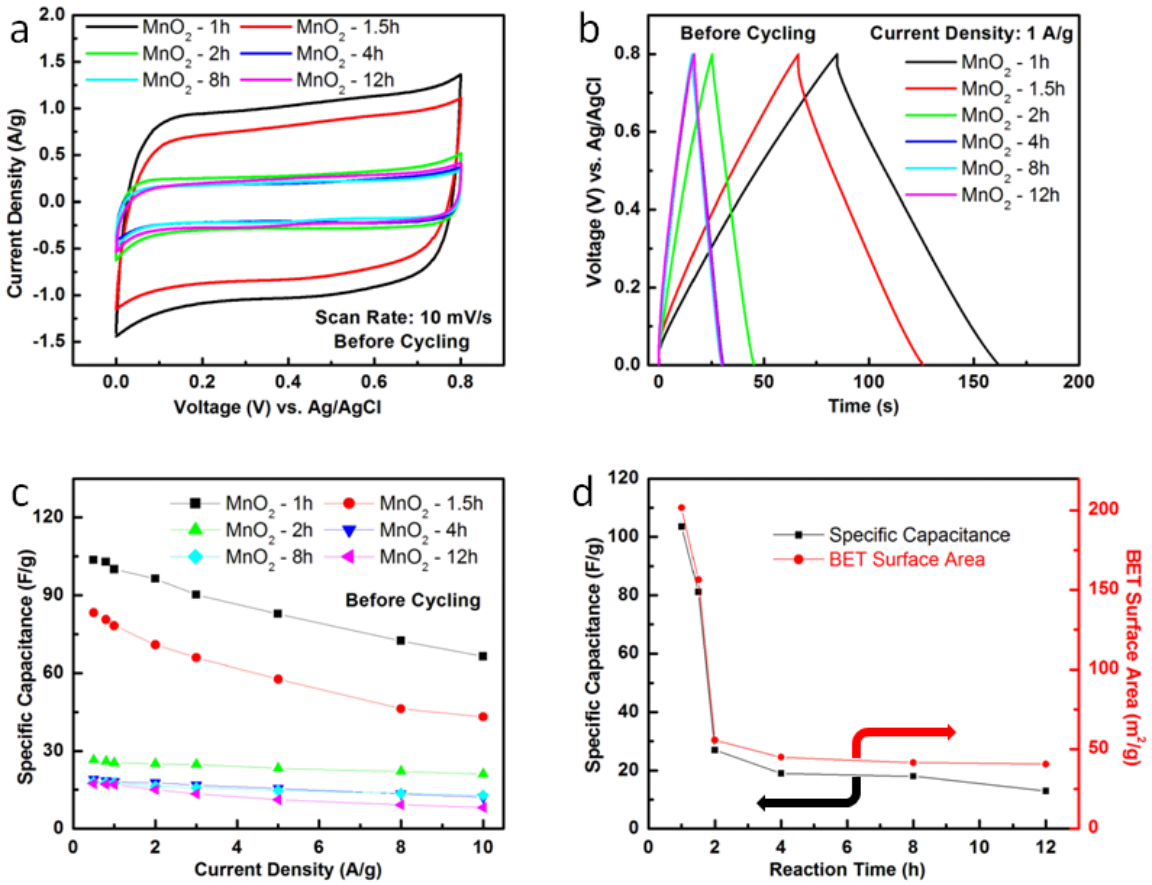

Figure 0.7: Electrochemical performance of all MnO_2 nanostructures as supercapacitor electrode materials before cycling tests. (a) Cyclic voltammetry at scan rate of 10 mV/s; (b) Galvanostatic charge-discharge at current density of 1 A/g; (c) Specific capacitance vs. current density; (d) The change of specific capacitance (at 0.5 A/g) and BET specific surface area with the reaction time.

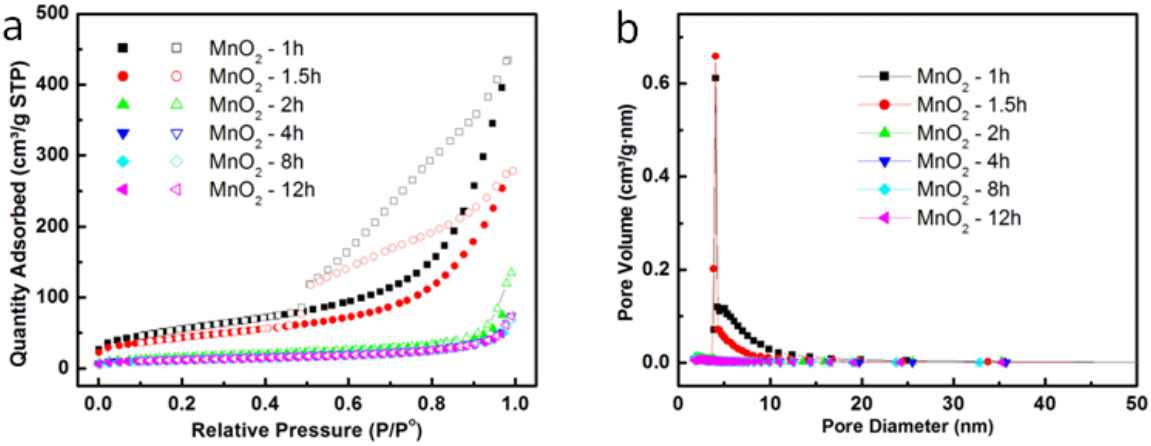

Figure 0.8: (a) Nitrogen adsorption and desorption isotherms and (b) pore size distribution of the as-prepared MnO_2 nanostructures.

2.1.6.2 Electrochemical Cycling Effect

We then studied the electrochemical cycling effect on the performance of all the MnO_2 nanostructures. We picked up the sample of MnO_2-1h as an example. Figure 2.9 shows the electrochemical performance of MnO_2-1h sample before and after 5000 cycles. The MnO_2-1h electrode shows nearly rectangular CV curves (Figure 2.9a) as demonstrated previously. The CD curves in Figure 2.9b show very symmetrical charge-discharge behaviors, consistent with the CV curves in Figure 2.9a. It is interesting to note that the capacitance increases steadily during the 5000 cycles, showing a 20% increase after 5000 cycles (Figure 2.9c). The CV curves of the MnO_2-1h sample also show that higher capacitance can be obtained after cycling test, as revealed by the larger CV loop area in Figure 2.9a. Similarly, the prolonged charge and discharge periods of the

same sample indicate increased capacitance upon cycling (Figure 2.9b). The capacitance change with current density (Figure 2.9d) demonstrates that the specific capacitance increases with cycling over a range of current densities. A specific capacitance of 103.5 F/g at current density of 0.5 A/g is a typical value for MnO_2 prepared by the hydrothermal method.[36, 85, 86] The capacitance increase of about 20% after cycling at 1 A/g is in good agreement with the cycling performance. Even at a high current density of 10 A/g, the capacitance of the sample after cycling is 93.7 F/g, which is higher than the value of 66 F/g before cycling. The rate capability of the sample after cycling tests (a ratio of capacitance at 10 A/g to 0.5 A/g) increased from 64% to 75%. EIS curve exhibits a lower equivalent series resistance after the cycling test, further demonstrating better electrochemical performance upon cycling.

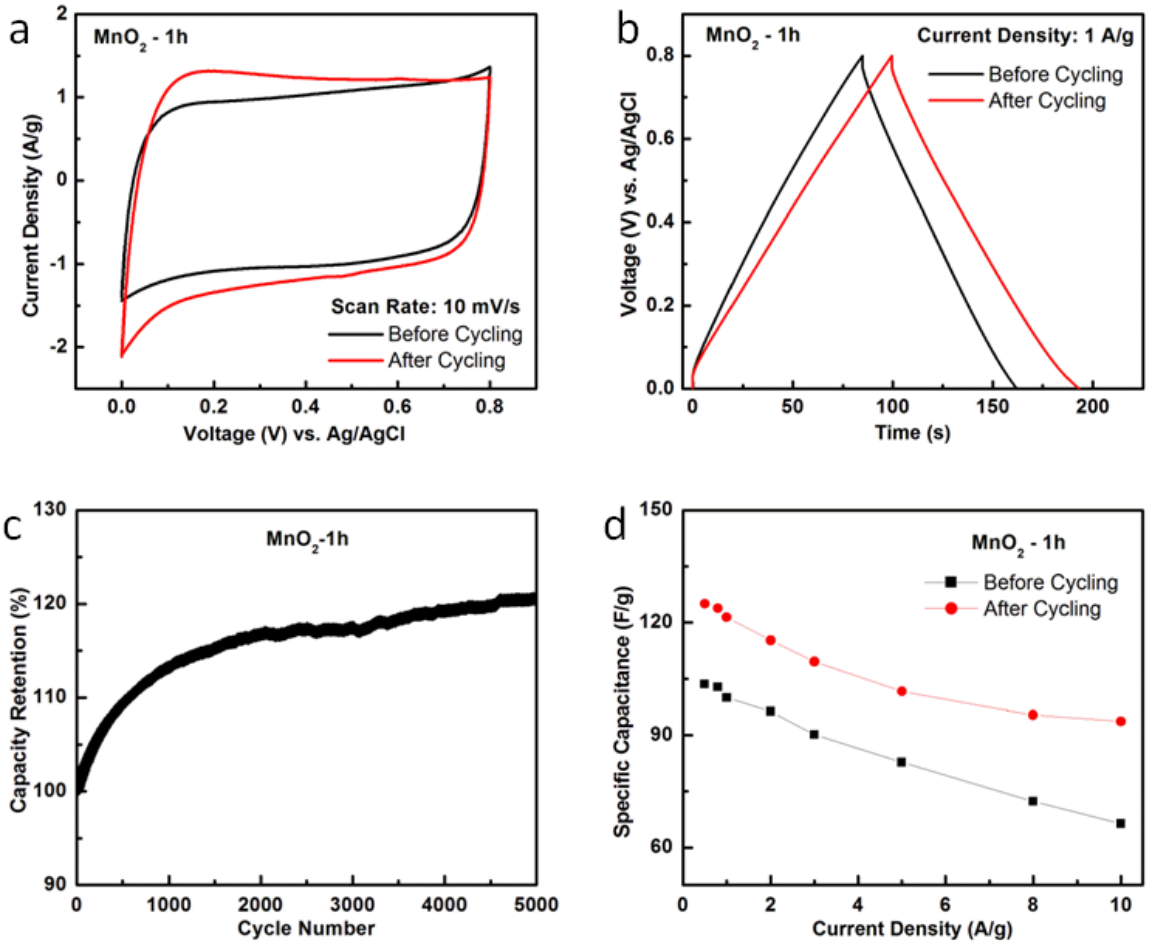

Figure 0.9: Comparison of electrochemical performance of MnO_2 nanospheres (MnO_2-1h) as supercapacitor electrode materials before and after 5000 cycles. (a) Cyclic voltammetry at scan rate of 10 mV/s; (b) Galvanostatic charge-discharge at current density of 1 A/g; (c) The cycling stability over 5000 cycles; (d) The change of specific capacitance with current density.

All the MnO_2 samples after cycling tests exhibit excellent electrochemical properties in terms of rectangular shapes of CV curves (Figure 2.10a) and highly symmetrical CD curves (Figure 2.10b), which are similar to the behaviors of the samples before cycling tests. As summarized in Figure 2.10c, the specific capacitances after cycling are still highly dependent on the morphology and crystal phase of MnO_2. Additionally, the values of MnO_2-1h and 1.5h are still higher than that of the other samples. The specific capacitance of the MnO_2-1h and 1.5h increased to a range between 70 F/g and 130 F/g, and the numbers of MnO_2-2h, 4h, 8h and 12h are in a range of 20 F/g to 50 F/g. Further investigations demonstrate that the percentage increase of specific capacitance (the ratio of capacitance increase to the initial capacitance) of all the samples upon cycling is in the order of the hydrothermal reaction time. For example, the capacitance increased by about 20% for the sample of MnO_2-1h after 5000 cycles (the value for MnO_2-1.5h is 23.9%, MnO_2-2h (39%), MnO_2-4h (50.5%), MnO_2-8h (65%)), while the increase rate for MnO_2-12h is as high as 76%. Consequently, the specific capacitances of MnO_2 nanostructures have increased to a higher level upon cycling, depending on the specific morphology and crystal phase of the MnO_2 nanostructures. It is also found that the capacitance of MnO_2-1.5h is close to that of MnO_2-1h at low current densities and the capacitance values of MnO_2-2h, 4 h, 8h and 12h are still almost in the same range after the cycling tests.

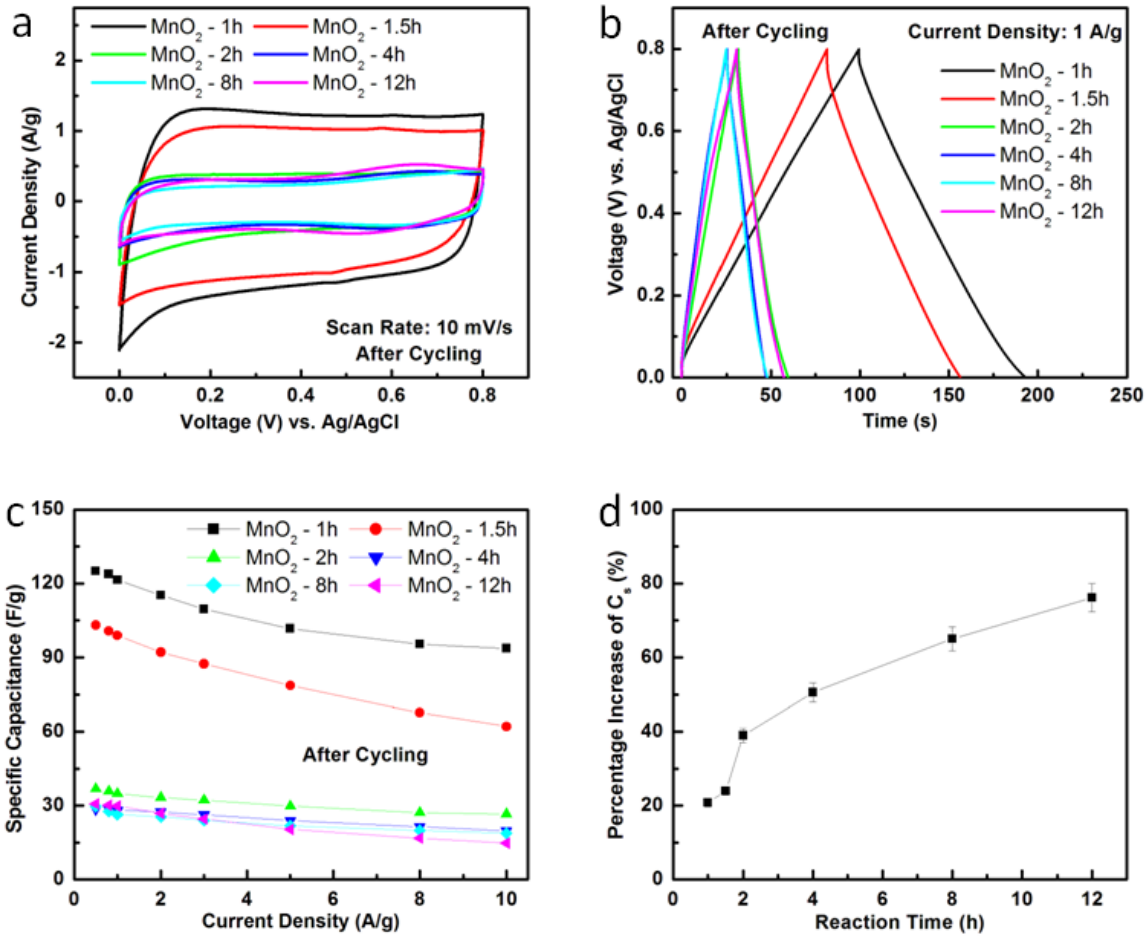

Figure 0.10: Electrochemical performance of all MnO_2 nanostructures as supercapacitor electrode materials after 5000 cycles. (a) Cyclic voltammetry at scan rate of 10 mV/s; (b) Galvanostatic charge-discharge curves at current density of 1 A/g; (c) Specific capacitance vs. current density; (d) The percentage increase of specific capacitance (0.5A/g) with the reaction time.

2.1.7 Mechanism of Capacity Change with Cycling

While the effect of morphology, crystal phase, and cycling on the supercapacitive performance of MnO_2 nanostructures have been discussed

previously, extensive analysis of the material properties driving these changes is still lacking.[36, 87-90] We firstly conducted SEM and TEM studies to investigate any possible changes of the materials on morphology and microstructures caused by the long term cycling tests. We focused on samples with two extreme reaction times: MnO_2-1h and MnO_2-12h. Figure 2.11 shows the morphology of these two electrodes after 5000 cycles by SEM. It is interesting that the MnO_2 nanospheres on the electrode of MnO_2-1h became highly porous after the cycling tests, while keeping their initial morphological features. Many “blooming nanoflowers” are deposited closely on the surface of the electrode, and the nanosheets of the MnO_2 nanospheres tend to face toward the electrode surface (Figure 2.11a). The gaps between the nanosheets of the MnO_2-1h electrode after cycling tests became slightly larger (Figure 2.11b). These changes are probably caused by the repeated electrolyte ions insertion and extraction upon the cycling tests. The nanosheets are forced to be vertical to the electrode surface in order to shorten the electrolyte ion transportation path, while the pores tend to become larger to facilitate more electrolyte accesses for ion adsorption/desorption or redox reactions between the electrode materials and electrolytes. However, the changes for the electrode of MnO_2-12h upon cycling tests are not obvious from its SEM image (Figure 2.11c). MnO_2 nanotubes with random orientations are still heavily deposited on surface of the electrode even after the cycling tests (Figure 2.11c, d). Therefore, it is necessary to employ TEM for the investigation of the microstructures. We are surprised to observe that many small defective or

“disordered” regions are formed on some parts of the MnO_2 nanosheets (Figure 2.12) and nanotubes (Figure 2.13) after the cycling tests. As for the MnO_2 nanosheets (MnO_2-1h), the materials generally kept their good porous feature and the folded nanosheets assembled to nanospheres (Figure 2.12a). Looking closely at some portions of the MnO_2 nanosheets (Red square area in Figure 2.12a), we can see that some defective or disordered regions have been formed on the nanosheets (Figure 2.12b). This is totally different from the morphology of the smooth MnO_2 nanosheets before electrochemical cycling (Figure 2.3a and Figure 2.4a). The size of these regions, some of which may have become pores on the MnO_2 nanosheets, ranges from 2 nm to 7 nm, which is in the mesoporous range (2-50 nm). Enlarged view of the area with large sizes of the defective regions is shown in Figure 2.12c (Left red square area in Figure 2.12b) indicates that the crystallinity of the regions became very poor as the lattice fringes tend to be disordered (labeled by the red circles). The defective regions with small sizes, shown in Figure 2.12d (Right red square area in Figure 2.12b), demonstrate the disappearance of the crystalline fringes (labeled by the small red circles), similar to the change observed in the larger disordered regions in Figure 2.12c.

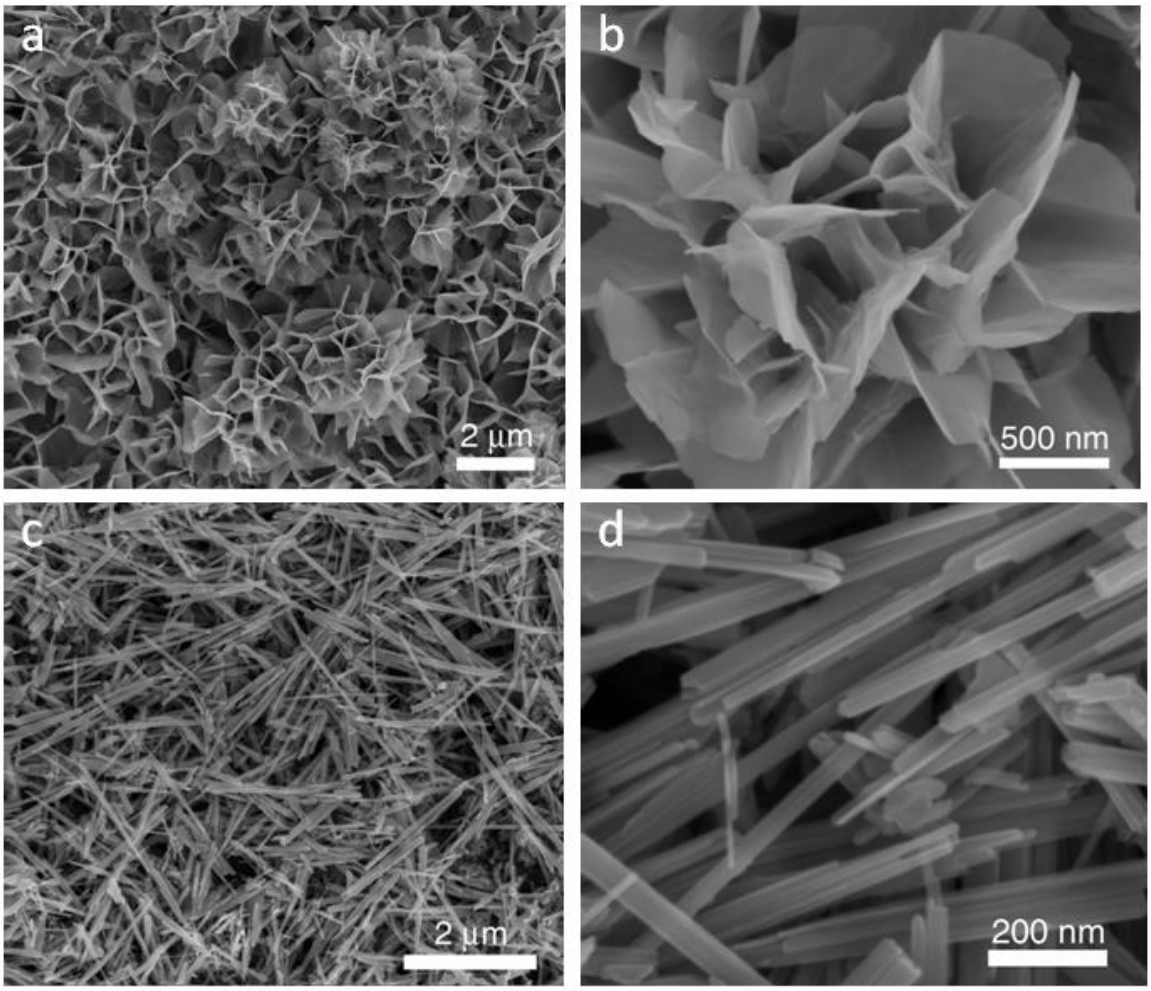

Figure 0.11: SEM images of (a, b) MnO_2 nanoflowers (MnO_2-1h) and (c, d) MnO_2 nanotubes (MnO_2-12h) after 5000 cycling testes at different magnifications.

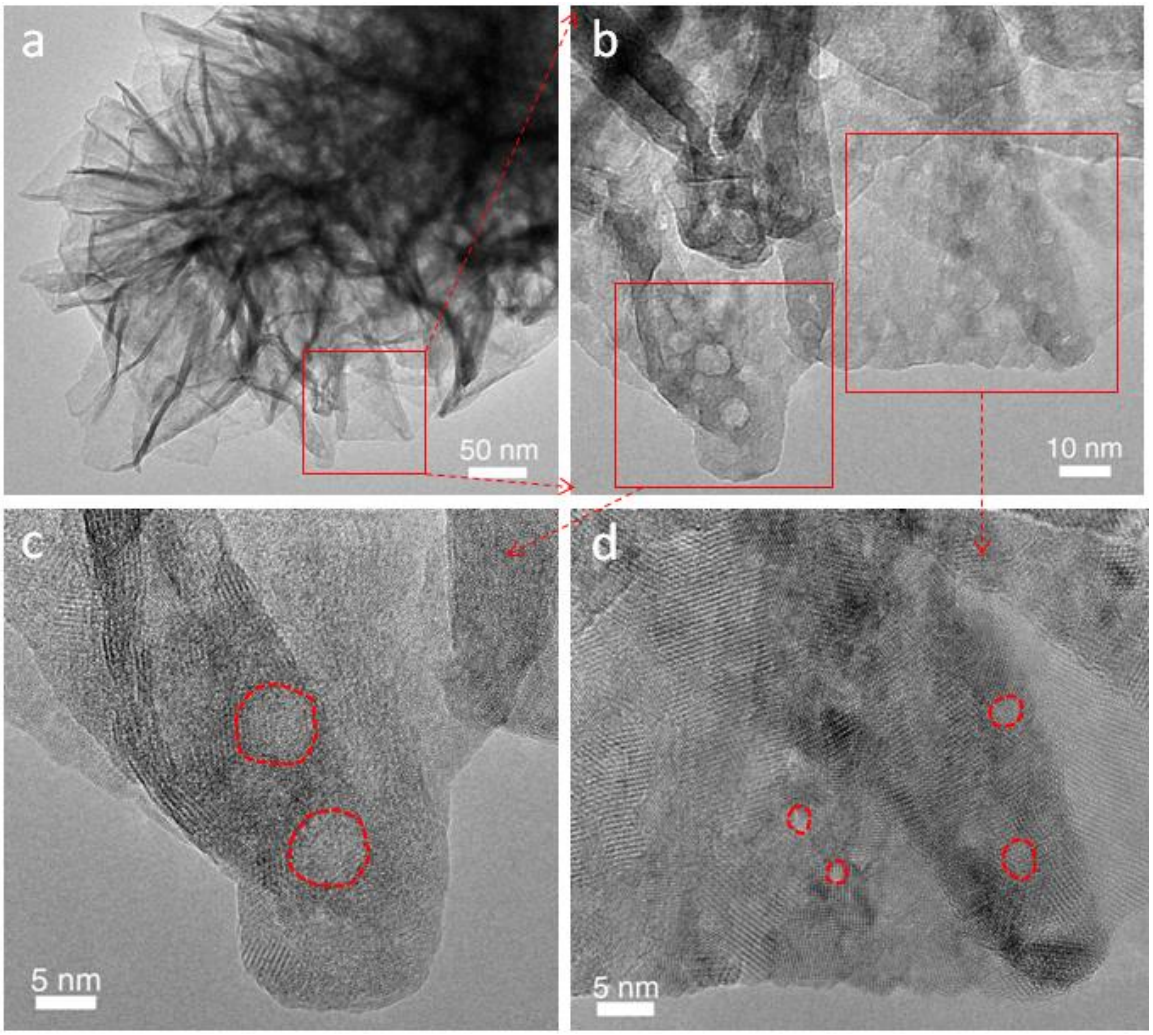

Figure 0.12: TEM images of MnO_2 nanoflowers (MnO_2-1h) after 5000 cycling testes at different magnifications.

In the case of MnO_2 nanotube (MnO_2-12h) after cycling tests, we found even more of these disordered regions are formed on the nanotube, making the whole nanotube highly porous (Figure 2.13a). Enlarged view of the tube in its central part (Figure 2.13b, the left red square area in Figure 2.13a) clearly shows a number of small defective sites throughout the whole tube. The size of the

small defective or disordered regions is between 2 nm and 5 nm. The high resolution TEM image near the tip portion of the MnO_2 nanotube indicates that apart from the long gaps formed by the acid etching in the hydrothermal process (labeled by the red arrow in Figure 2.13c), there are also small defective sites formed on the tube. It is worth pointing out that although some voids are formed on MnO_2 nanotubes during the hydrothermal reaction by the strong acid etching, these voids are different in size and shape from the disordered regions formed after long-term electrochemical cycling tests.

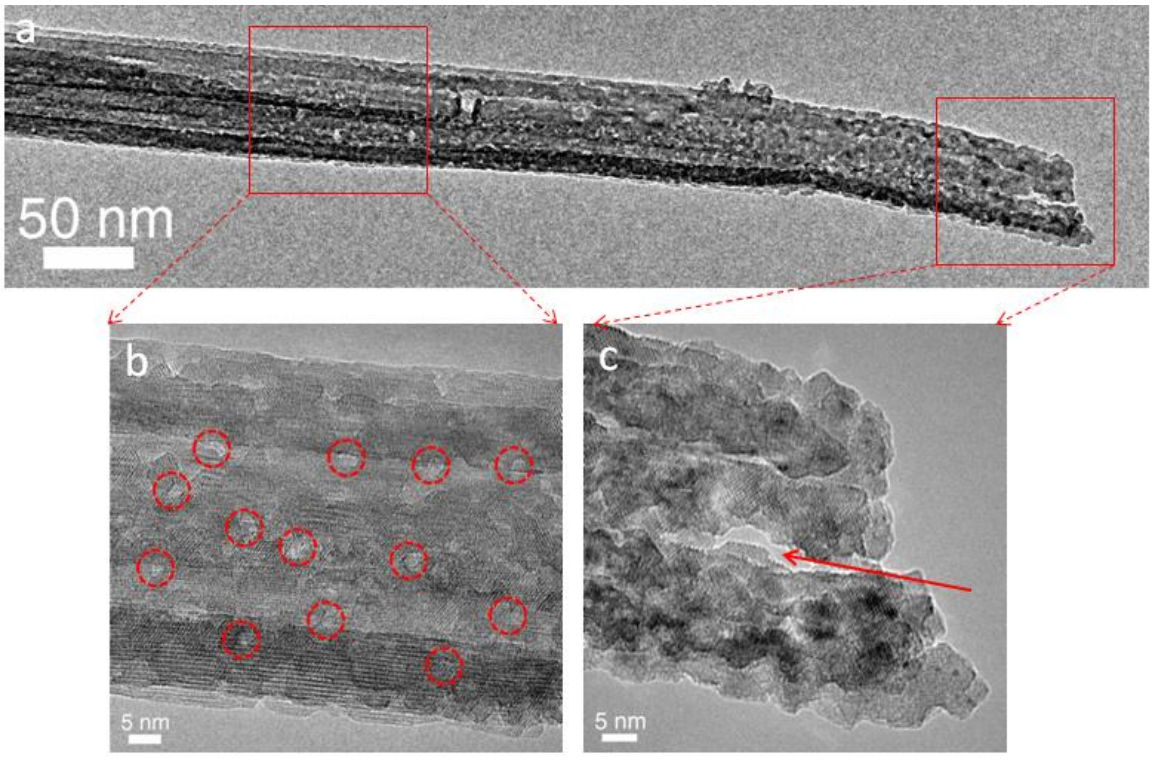

Figure 0.13: TEM images of MnO_2 nanotubes (MnO_2-12h) after 5000 cycling testes at different magnifications.

The formation of the defective regions within the MnO_2 nanostructures upon cycling is attributed to the repeated insertion/extraction of the electrolyte ions into/out of the MnO_2 electrode materials. The Na^+ ions from the electrolyte are expected to interact with MnO_2 on some active sites of the surface by either physisorption or fast and reversible redox reactions as shown in the following equation.

$$MnO_2 + xNa^+ + xe^- \leftrightarrow Na_xMnO_2$$

The porous structure induced by the electrochemical cycling tests contributes to the increase of the interaction due to the increased access of the electrolyte ions to the electrode materials. Hence the capacitance increases after electrochemical cycling tests. Due to the different MnO_2 electrode morphologies, the cycling-induced formation of defective/disordered regions differs from sample to sample. This fact results in varying degrees of capacitance increase after cycling (Figure 2.10d).

In order to identify the chemical and bonding states of the electrode material after cycling, we have conducted XPS analysis. As shown in Figure 2.14a, the prepared MnO_2 nanostructures are actually potassium doped MnO_2, which is introduced by $KMnO_4$ in the raw materials. The comparison between the MnO_2 samples before and after 5000 cycles clearly shows the appearance of the sodium peaks in the spectra for the sample after cycling tests, which indicates that Na interacts with the MnO_2 electrodes during cycling tests (Figure 2.14a).

Quantitative analysis further reveals that the ratio of Na to Mn in the cycled electrode material is about 0.05. Therefore, we can denote the final compounds as $Na_{0.05}MnO_2$. The Mn 2p spectra exhibit characteristic peaks of Mn $2p_{3/2}$ (641.9 eV) and Mn $2p_{1/2}$ (653.5 eV), indicating the oxidation state is Mn^{4+}, which agrees well with the previous reports (Figure 2.14b).[72] For the sample of MnO_2-1h, no obvious changes of the Mn oxidation state can be observed from the Mn 2p spectra after the long term cycling, suggesting that the MnO_2 underwent no chemical changes during the cycling tests.

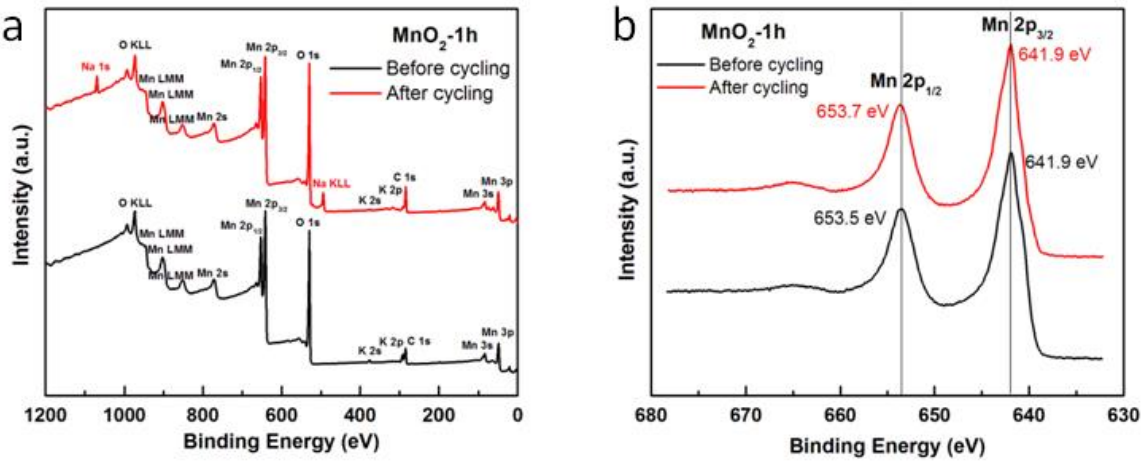

Figure 0.14: XPS of MnO_2 nanoflowers (MnO_2-1h) before and after 5000 cycling testes. (a) Survey scan; (b) Mn 2p core level spectra.

Based on the above observations, we can make the following conclusions to explain the electrochemical energy storage mechanism of MnO_2 in neutral Na_2SO_4 aqueous electrolyte. Firstly, the MnO_2 electrode tends to become more porous during cycling due to repeated Na^+ insertion/extraction into/out of the

electrode material. This effect enhances the porosity of the MnO_2 electrode and hence increases storage capacity during cycling. Secondly, the MnO_2 interacts with Na^+ to form Na doped MnO_2. However, only a small portion of the materials are involved in the interaction, giving limited doping level of the Na ions to the MnO_2, indicating that only a thin layer of the MnO_2 electrode has contributed to the energy storage, and the MnO_2 undergoes no chemical changes. This is consistent with the energy storage mechanism of MnO_2 proposed earlier by Toupin et al.[72] Thirdly, the interaction of the MnO_2 with Na^+ introduced a lot of defective/disordered regions in some parts of the MnO_2, further increasing the surface area and therefore the storage capacity of MnO_2.

In summary, we have reported in this section a comprehensive study on the growth process, electrochemical supercapacitor performance, and cycling stability of hydrothermally-derived MnO_2 electrodes. It is proposed that the growth of different MnO_2 nanostructures is controlled by two steps: the conversion of MnO_2 nanosheets to nanofibers by a diffusion and crystallization process and the formation of MnO_2 nanotubes from nanofibers by a combined Ostwald ripening and acid etching processes. The morphological evolution of nanostructured MnO_2 was extensively studied and explained with the help of 3D electron tomography, revealing the vivid formation process from nanofibers to nanotubes. The electrochemical performance of MnO_2 supercapacitors was revealed to be highly correlated to their surface area, determined by their morphology and crystallinity, as well as their cycling performance, determined by

their defective regions formation during cycling. The often observed unusual increase in specific capacitance with cycling was studied and correlated not only with MnO_2 electrode morphology, but also with its structural and chemical state, including the formation of defective regions on the materials and the interaction of the materials with the electrolyte. Our detailed study provides significant insight into the growth mechanism, electrochemical performance, and cycling stability of nanostructured MnO_2.

2.2 MnO_2 Based Nanocomposites

While MnO_2 is a promising material for pseudocapacitor applications due to its high specific capacity and low cost, MnO_2 electrodes suffer from their low electrical and ionic conductivities. One effective approach to address this problem is to make MnO_2 composites, where the conductivity and accessibility of the MnO_2 can be effectively enhanced. In this section, we will study MnO_2 based nanocomposites for supercapacitor electrodes, including binary MnO_2-carbon nanocoils (CNCs) and MnO_2-graphene nanocomposites, ternary MnO_2-CNT-graphene nanocomposites.

2.2.1 MnO_2 Based Binary Nanocomposites

2.2.1.1 MnO_2-CNC Nanocomposite

Different forms of graphitic nanostructured materials, such as carbon nanotubes[91,92], carbon nanofibers[93], graphene nanoplatelets[94], etc. have been recognized as potential electrode materials for supercapacitors because of their unique properties such as mesoporous character, chemical stability and good electrical conductivity.[95] Recently, carbon nanocoils (CNCs), which are vapor-grown helical carbon nanofibers, have attracted significant research interest because of their helical morphologies, excellent conductivity, corrosion or oxidation resistance nature and high porosity that minimizes the diffusion resistances of various reactants.[96] Yu *et al.* [97]and Jian *et al.*[98] have reported synthesis and growth mechanism of CNCs. Ever since their discovery[99], detailed studies on various properties of CNCs such as mechanical, field emission, EM wave absorption, thermal and electrical properties, and so forth have been reported.[100,101,102] Use of pristine CNCs as supercapacitor electrode materials with a maximum specific capacitance of 40 F/g[103] has been reported by Wang, *et al*. In another work they have shown that by purification and activation, specific capacitance of CNCs can be increased to 107 F/g.[104] However, these values are still low. A hybrid of CNCs and MnO_2 could be a better candidate for a supercapacitor electrode with high specific capacitance and energy density.

MnO_2-CNC nanocomposites were prepared through an easy and efficient solution based method.[25] Specifically, 200 mg of functionalized CNCs were dispersed in 35 mL of an aqueous solution, containing 10 mM of $MnSO_4$, by ultrasonication for 5 min. In order to allow impregnation of the carbon by $MnSO_4$, the suspension was then maintained at a controlled temperature of 80 ºC for 20 min under magnetic stirring. A 150 mL aqueous solution containing 33 mmol of $KMnO_4$, previously heated at controlled 80 ºC, was then gradually added to the agitated suspension. This mixture was maintained at 80 ºC under agitation for 15 min and then washed, filtered and dried at 100 ºC for approximately 10 h.

Figure 2.15a shows the powder XRD pattern of functionalized CNCs. The peaks are indexed to the reflections of hexagonal graphite (JCPDS card No. 75-1621). In addition to the graphitic peaks, XRD pattern of MnO_2-CNCs (Figure 2.15b) show four weak broad peaks from MnO_2 situated at 2θ values approximately 11.8º, 25.5º, 36.9º and 65.7º can be attributed to the (110), (220), (400), and (002) diffraction of α-MnO_2, which has tetragonal symmetry with a space group of I4/m (JCPDS Card, No. 44-0141). Absence of peaks with high diffraction intensities (such as (200) and (310)) together with the presence of other crystalline peaks in the XRD diffraction pattern indicates coexistence of α-phase and amorphous MnO_2 structure in the composite. A more amorphous structure has been considered to be beneficial in increasing the specific capacitance of the oxide electrode for the supercapacitor.[105] The highly amorphous structure is expected to favor the electrolyte insertion into (or

expulsion out of) the oxide matrix, which can increase the contact between electrolyte and the electrode material and improve the utilization ratio of the material.

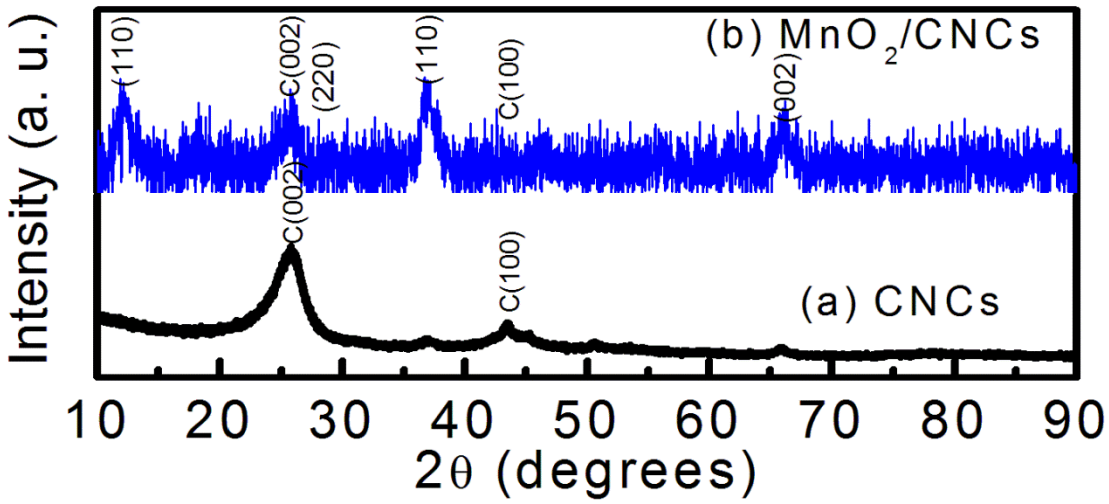

Figure 0.15: Powder XRD of (a) CNCs and (b) MnO_2-CNCs.

Figure 2.16a shows the typical SEM image of CNCs along with some straight carbon nanofibers. The CNCs are single helical coils with twisted forms similar to a-helix proteins.[106] Absence of hollow structure in Figure 2.16c indicates that CNCs are not coiled multiwalled carbon nanotubes (MWCNTs), instead these are coiled nanofibers with an average coil diameter of 80-100 nm. SEM of MnO_2-CNCs (Figure 2.16b) shows the presence of MnO_2 nanowhiskers on the surface of CNCs, which is confirmed by the TEM image shown in Figure 2.16d. Xia et al. reported the detailed growth mechanism of these MnO_2 nanflakes as a function of reaction temperature.[107] MnO_2 nanoflakes are

expected to be promising as electrode materials for supercapacitors due to their porous structure, large surface area, and short diffusion length for protons or alkali cations.[108]

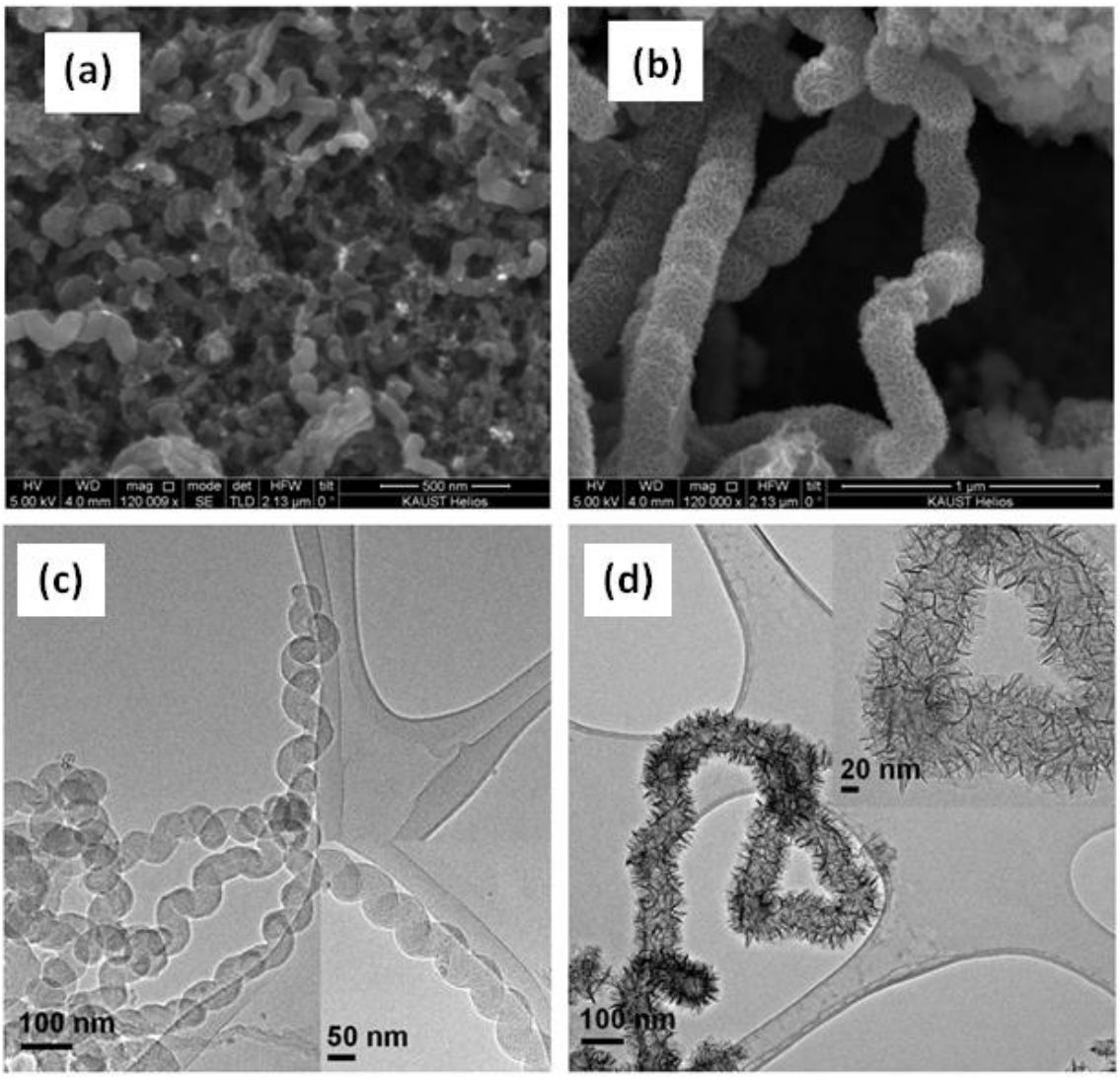

Figure 0.16: SEM and TEM images of (a, c) CNCs and (b, d) MnO_2-CNCs, respectively.

The CV curves of the symmetric supercapacitors based on MnO_2-CNCs exhibit nearly rectangular shape (Figure 2.17a), consistent with their galvanostatic charge-discharge behavior (Figure 2.17b). Specific capacitance obtained for CNCs and MnO_2-CNCs from the discharge curves are 121 and 213 F/g respectively. The enhancement in the specific capacitance of MnO_2 dispersed CNCs from that of functionalized CNCs is due to the progressive redox reactions occurring at the surface and bulk of transition metal oxides through Faradaic charge transfer. There is a considerable increase in the specific capacitance value for MnO_2-CNCs nanocomposite as compared to pure CNCs. This is due to the fact that, anchoring of whisker-shaped α-MnO_2 nanocrystallites on the surface of CNCs can increase the effective contact of the electrolyte and the active materials. Moreover, CNCs in the nanocomposite can provide highly effective conductive pathway to provide more effective electrical transport from the active materials to the current collector.[25]

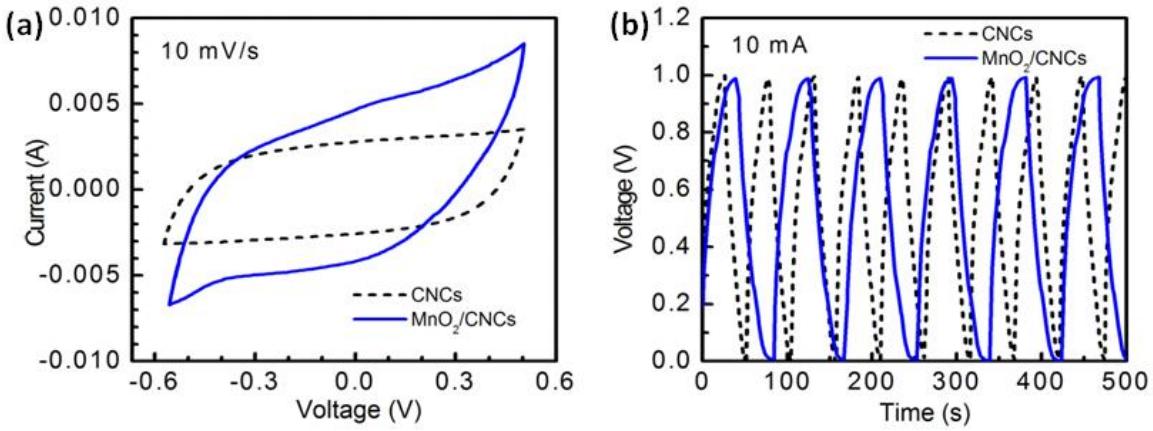

Figure 0.17: (a) Cyclic voltammetry and (b) galvanostatic charge-discharge curves of CNCs and MnO_2-CNCs supercapacitors in 30 wt% KOH electrolytes.

2.2.1.2 MnO_2-Graphene Nanocomposite

Graphene, with its outstanding properties including high theoretical surface area of over 2600 m^2/g, good electrical conductivity, thermal stability, chemical tolerance, and a broad electrochemical window can be considered as an ideal candidate for EDLC electrode material.[109] Recently, promising results on the electrochemical performance of graphene nanosheets (GNs) have been reported following the progress in the large scale synthesis of GNs.[110] In 2008, Stoller *et al*. demonstrated the use of chemically modified GNs as electrode material for supercapacitors with specific capacitances of 135 F/g and 99 F/g in aqueous KOH and organic electrolytes respectively.[6] In 2010, Liu et al. reported fabrication and performance studies of symmetric supercapacitors based on

curved GNs electrodes, capable of operation at a high voltage (4 V) in ionic liquid electrolyte 1-ethyl-3-methylimidazolium tetrafluoroborate with an exceptional high energy density of 85.6 Wh/kg at 1 A/g.[111] However, in the drying process during electrode preparation, GNs tend to aggregate and stack to multilayers due to van der Waals interactions, inducing inferior physical and chemical properties than that in their exfoliated monolayer state.[112] The agglomeration adversely affects supercapacitor performance by preventing electrolyte penetration into layers, and can be avoided by the introduction of spacers into the graphene layers.[113, 114] Transition metal oxide (TMO) nanoparticles are widely used as the spacers into the interlayers of GNs to prevent them from aggregating.[115] These nanoparticles help in increasing the interplanar spacing and making both sides of the GNs accessible to the electrolyte. Moreover, the resultant composite exhibits superior capacitive performance as compared to its components, as TMO nanoparticles can contribute pseudocapacitance to the total capacitance apart from the double-layer capacitance from GNs.[116]

Figure 2.18a and b show the typical SEM images of GNs and MnO_2-GNs respectively. It can be seen that the GNs structure is retained after introducing MnO_2 nanoparticles. However, the surfaces of the GNs become much rougher than pure GNs, indicating the growth of MnO_2 nanoparticles on the surfaces. These particles were densely and homogeneously deposited, as confirmed by the TEM image shown in Figure 2.18d. In contrast, the TEM image (Figure 2.18c) exhibits thin layers of GNs with smooth surfaces. The growth of MnO_2 is

preferred near the edges of graphene layer (marked by arrows) with the size of 5-10 nm. Many remained oxygen-containing functionalities (hydroxyl, carbonyl and carboxyl groups) on the edges of graphene are vulnerable to oxidation and direct electron transfer from sheet defects to MnO_4^- results in easy MnO_2 precipitation near the defect sites. MnO_2 nanocrystals with particle size nearly 2 nm with the interlayer spacing of 0.7 nm and very thin amorphous MnO_2 coatings are also formed away from the edges of sheets resulted from the reaction of MnO_4^- with less active carbon.

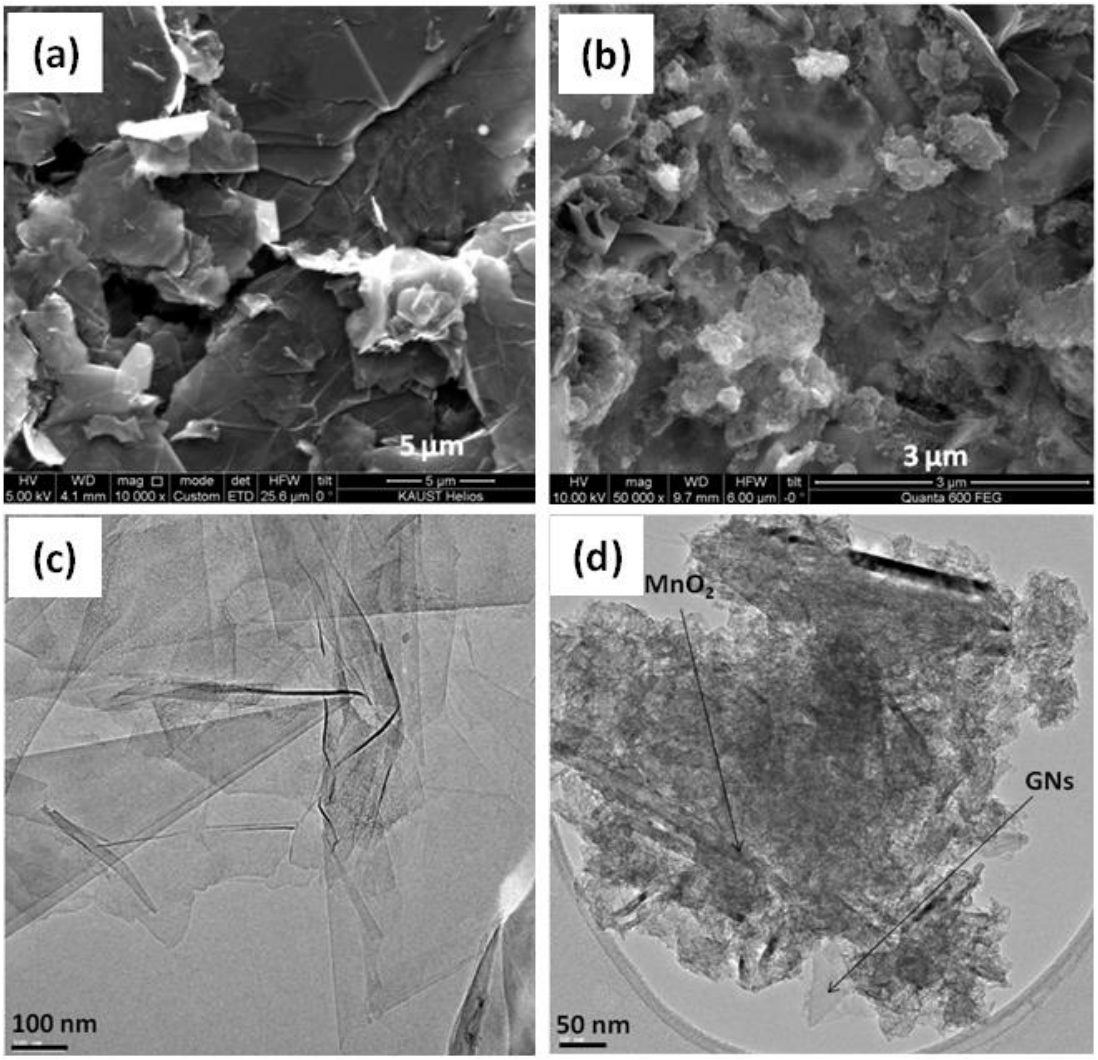

Figure 0.18: SEM and TEM images of (a, c) GNs and (b, d) MnO_2-GNs, respectively.

The CV loops for symmetric supercapacitors are quasi-rectangular in nature (Figure 2.19a). The specific capacitances of GNs and MnO_2-GNs based symmetric supercapacitors obtained from CV loops at 20 mV/s are 150 and 235 F/g respectively (Figure 2.19b). Meanwhile, the capacitance of MnO_2-GNs

composites based supercapacitors is much higher than that of GNs supercapacitors over a large range of scan rates (5-200 mV/s). It can be seen from charge-discharge curves (Figure 2.19c and d) that they are nearly linear and symmetrical. Voltage drop is observed to be very small, which indicates that the electrodes have low internal resistance. In addition, the charge-discharge duration for MnO_2-GNs composites are greater than that of GNs, indicating higher specific capacitance for MnO_2-GNs composites based supercapacitors. The enhancement in the specific capacitance of MnO_2 dispersed GNs from that of functionalized GNs are mainly due to the spacer effect of nanoparticles leading to the increase in accessible surface area of the electrolyte and the progressive redox reactions occurring at the surface and bulk of MnO_2 through Faradaic reactions.[117]

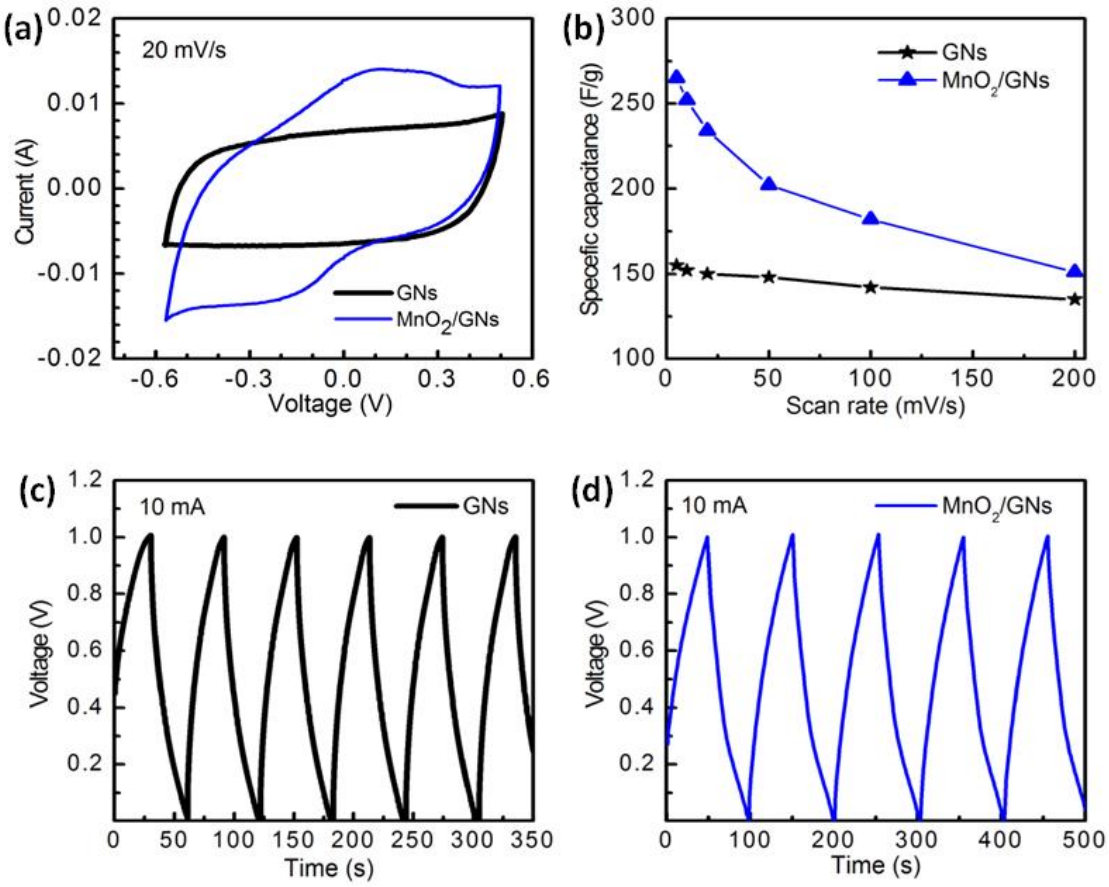

Figure 0.19: (a) CV of GNs and MnO_2-GNs based supercapacitors at scan rate of 20 mV/s. (b) Specific capacitance vs scan rate for GNs and MnO2/GNs based supercapacitors. (c, d) CD curves of GNs and MnO_2-GNs based supercapacitors under a constant current of 10 mA, respectively.

2.2.2 MnO_2 Based Ternary Nanocomposites: MnO_2-CNT-Graphene

Effective surface area of graphene as supercapacitor electrode material depends highly on the number of graphene layers.[118] Therefore, single or few layered graphene with less agglomeration should be expected to exhibit higher effective surface area and thus better supercapacitor performance. However, as

we showed previously, during the drying process in electrode preparation, GNs naturally aggregate and stack to multilayers, inducing inferior physical and chemical properties than that in their exfoliated monolayer state.[119] The agglomeration can be avoided by the introduction of spacers into the graphene layers. Both nanocarbon materials and pseudocapacitance materials are currently being designed to be introduced into the interlayers of GNs to prevent them from aggregating.[120-124] These spacers are intended to enlarge the interplanar spacing, maintain the high surface area of GNs, and make both sides of the nanosheets accessible to the electrolyte. Spacers ensure high electrochemical utilization of graphene layers as well as contribute to the total capacitance of the system.[125]

In the present work CNTs loaded with high surface area γ-MnO_2 nanoflakes prepared by chemical methods are used as spacers in GNs and the resultant nanocomposite coated on flexible carbon cloth substrates are used as efficient flexible electrodes for supercapacitors. The incorporation of γ-MnO_2/CNTs into GNs is expected to improve electrolyte-electrode accessibility and electrode conductivity by reducing the agglomeration of GNs. Symmetric supercapacitors are fabricated using GNs-(γ-MnO_2/CNTs) nanocomposite electrode materials and the electrochemical performance are evaluated using two-electrode configuration in 30% KOH electrolyte. Figure 2.20a shows the schematic of GNs-(γ-MnO_2/CNTs) nanocomposite prepared by ultrasonication of chemically functionalized GNs and γ-MnO_2/CNTs. The latter is expected to act as

an effective spacer between different layers of GNs, thereby preventing agglomeration of GNs. Schematic of the symmetric supercapacitor assembly is shown in Figure 2.21b.

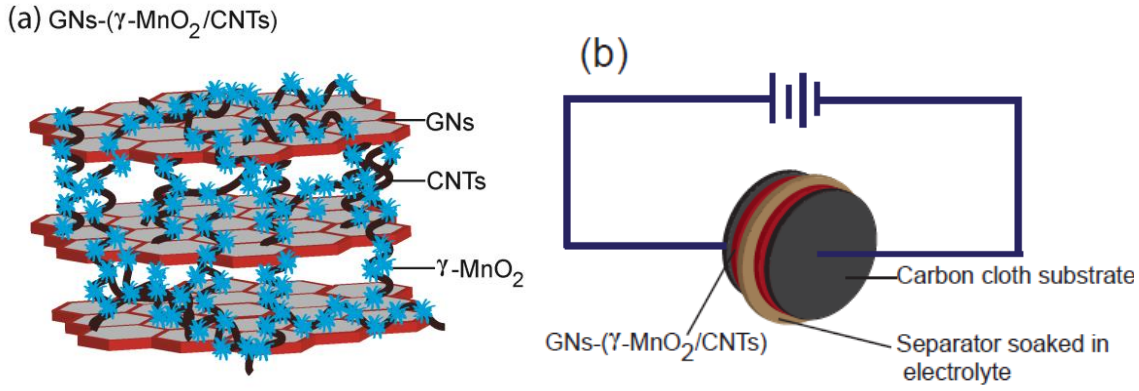

Figure 0.20: Schematic of (a) GNs-(γ-MnO_2/CNTs) nanocomposite and (b) symmetric supercapacitor test cell.

Powder XRD pattern of MnO_2/CNTs is shown in Figure 2.21a. XRD pattern has a peak around 25.9°, which is the characteristic peak corresponding to the reflections of hexagonal graphite (JCPDS card No. 75-1621) and should arise from CNTs. According to the XRD standard card, JCPDS 14-644, the rest of the peaks on the pattern demonstrate the deposit exist as γ-MnO_2. The peaks of γ-MnO_2 are assigned as (120), (131), (300), (160) and (003) appearing respectively at 22.2°, 36.6°, 41.7°, 55.6° and 66.1°. γ-MnO_2 is a ramsdellite (2.3 Å×4.6 Å tunnel structure) matrix with randomly distributed intergrowth micro domains of pyrolusite (2.3 Å × 2.3 Å tunnel structure), which are made of MnO_6 subunits with either edge or corner sharing.[126] The pyrolusite and ramsdellite

structures have similar arrangements along the *a* and *c* axes and infinite strings of MnO_6 can only grow along the *b* axis.[127] γ-MnO_2 hexagon-based structures consist of ε-MnO_2 (space group of *P63/mmc*), β-MnO_2 (space group of *$P4_2$/mnm)* and ramsdellite (space group of *Pbnm*) which indicates that MnO_2 exists in different crystalline phases.[126] To investigate the oxidation state of Mn in γ-MnO_2/CNT nanocomposite, the sample was further characterized by XPS. XPS survey spectra for as-prepared γ-MnO_2/CNTs showed the peaks of Mn ($2p_{3/2}$, $2p_{1/2,}$ 3s, 3p), O 1s, C 1s and small amount of potassium. Figure 2.21b shows the Mn 2p spectrum, with two peaks located at 642.1 and 653.8 eV (with a spin-energy separation of 11.7 eV) which can be attributed to Mn $2p_{3/2}$ and Mn $2p_{1/2}$, respectively. The peak values agree well with those reported for MnO_2, indicating the oxidation state of Mn^{4+}.[128] Deconvoluted O 1s spectrum of the γ-MnO_2/CNT nanocomposite is shown in Figure 2.21c, in which 3 peaks (one sharp peak located at 529.8 eV and two broad peaks located at 531.1 and 532.4 eV) can be observed. This is in good agreement with literature reports of 529.3-530.3 eV for oxide, 530.5–531.5 eV for hydroxide, and 531.8–532.8 eV for water.[129] Chemical compositions of as-prepared γ-MnO_2/CNT nanocomposites are determined using thermo gravimetric analysis (TGA). TGA curve (Figure 2.21d) of γ-MnO_2/CNTs shows 6% weight loss below 250 ˚C, which corresponds to a loss of water and trace amount of oxygen. Weight loss of about 30% between 400˚C and 700˚C is due to the oxidation of the CNTs in air.[129] From TGA analysis it is clear that the γ-MnO_2/CNT nanocomposite contains ~30% of CNTs. Hence the GNs-(γ-

MnO_2/CNTs) obtained by mixing of 80% of GNs and 20% of (γ-MnO_2/CNTs) contains 80% GNs, nearly 12% MnO_2, 6% CNTs and remaing 2% of water and traces of Potassium (K).

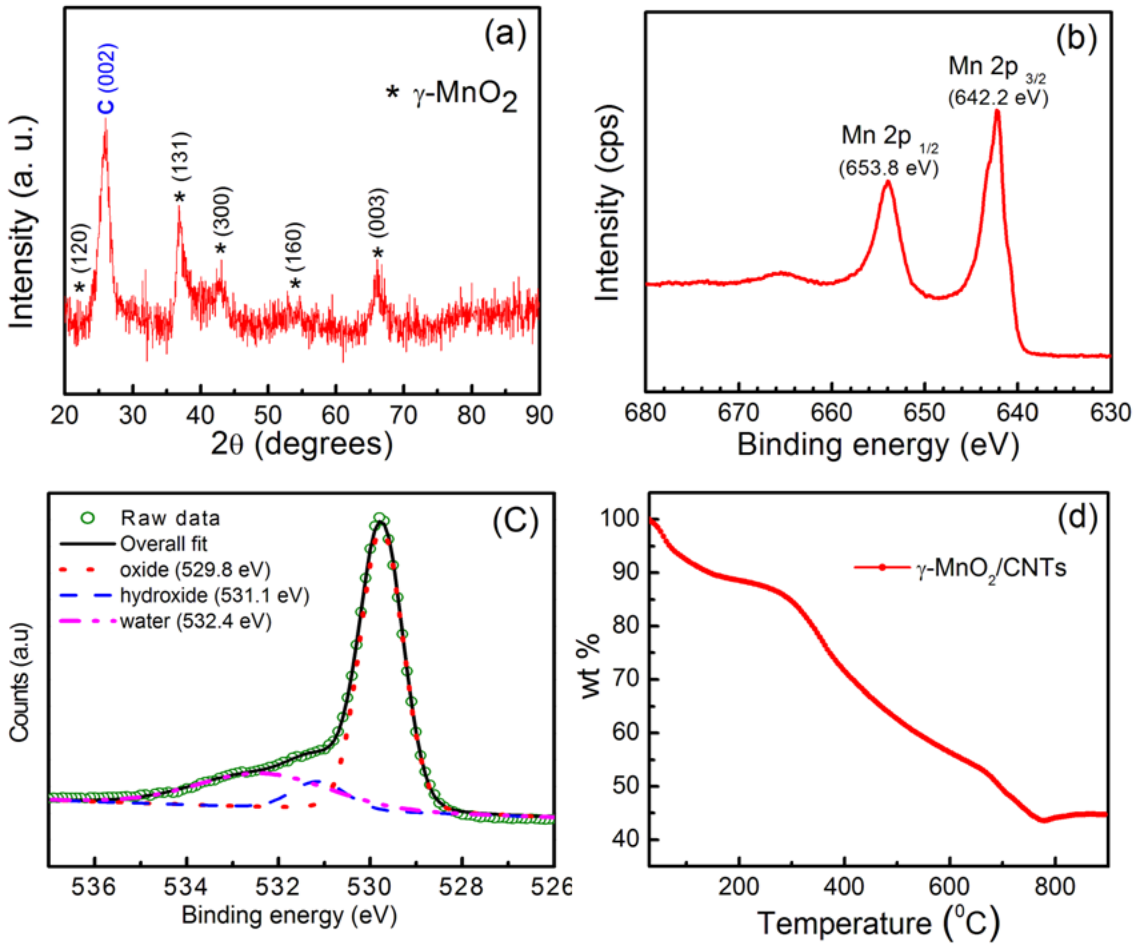

Figure 0.21: (a) Powder XRD pattern, (b) XPS narrow scan spectra of Mn 2p and (c) O 1s, (d) TGA curve of the γ-MnO_2/CNTs.

The nitrogen adsorption and desorption isotherms of the CNTs, γ-MnO_2/CNTs, GNs and GNs-(γ-MnO_2/CNTs) are shown in Figure 2.22a**,** using

which the Brunauer-Emmett-Teller (BET) surface area values are calculated as 108.36, 144.89, 153.09 and 317.35 m^2/g respectively. Based on the density function theory (DFT) model, pore volumes are calculated as 0.18, 0.88, 0.25 and 0.52 cm^3/g respectively for CNTs, γ-MnO_2/CNTs, GNs and GNs-(γ-MnO_2/CNTs). It is worth noting that the BET specific surface area of GNs dispersed with metal oxide loaded CNTs are much higher than that of GNs, which can be explained on the basis of spacer effect of γ-MnO_2/CNTs in between different GNs layers. The increase in surface area is favorable for better supercapacitive performance of the composites. The pore size distributions of the samples calculated by desorption isotherms using Barret-Joyner-Halenda (BJH) method are shown in Figure 2.22b. BJH Desorption cumulative volume of pores between 1.7 nm and 300 nm diameter for CNTs, γ-MnO_2/CNTs, GNs and GNs-(γ-MnO_2/CNTs) are 0.18, 0.92, 0.27 and 0.51 cm^3/g respectively.

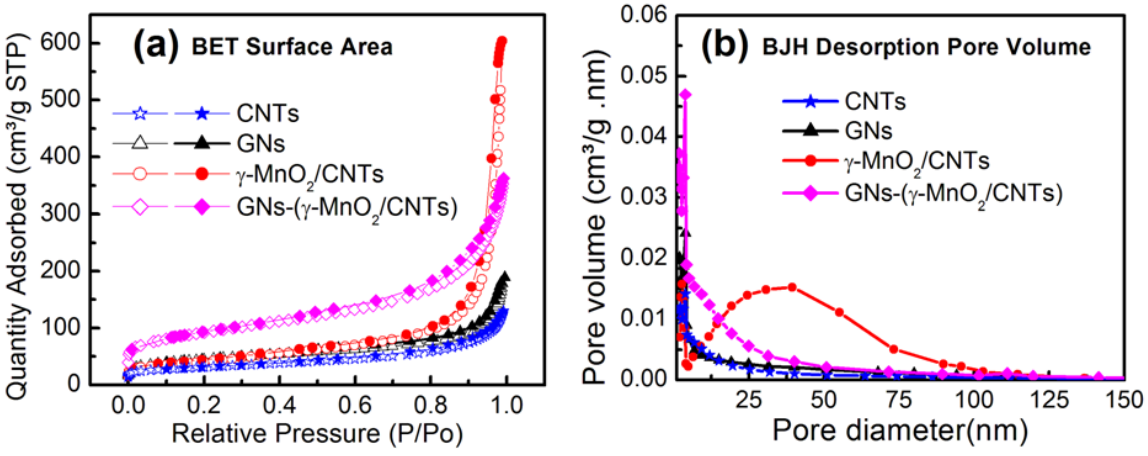

Figure 0.22: (a) Nitrogen adsorption and desorption isotherms and (b) pore size distributions of CNTs, GNs, γ-MnO_2/CNTs and GNs-(γ-MnO_2/CNTs).

The morphology of CNTs, γ-MnO_2/CNTs, GNs and GNs-(γ-MnO_2/CNTs) are analyzed using SEM, TEM and HRTEM. SEM image of CNTs (Figure 2.23a) shows that their packing density is high. Entangled nanotubes with an average outer diameter of 30 nm and length of several micrometers can be seen. Figure 2.23b shows SEM image of MnO_2 nanoflowers loaded over CNTs. The MnO_2 nanostructures synthesized here may have preferably grown on the energetically favorable sites under the temperature control, resulting in a highly porous structure that promotes efficient contacts between the active material and the electrolyte, providing more active sites for electrochemical reactions. Some portions of CNTs which are not loaded with MnO_2 are also visible. Figure 2.23c and d respectively shows SEM images of GNs and GNs-(γ-MnO_2/CNTs). Presence of GNs, MnO_2 nanostructures and CNTs in the nanocomposite are evident from Figure 2.23d.

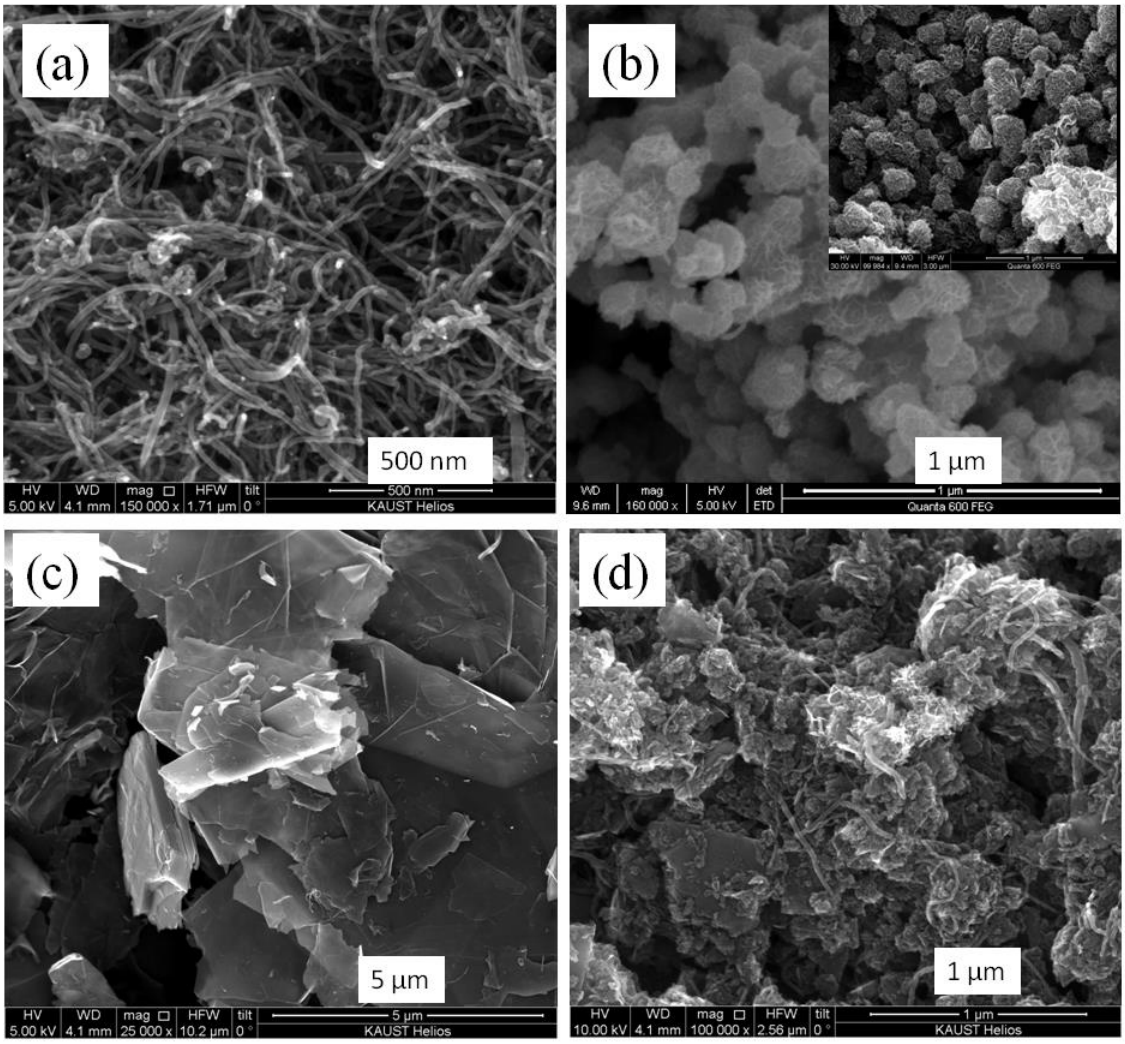

Figure 0.23: SEM images of (a) CNTs, (b) γ-MnO_2/CNTs, (c) GNs and (d) GNs-(γ-MnO_2/CNTs).

TEM images of CNTs, γ-MnO_2/CNTs, GNs and GNs-(γ-MnO_2/CNTs) are shown in Figure 2.24a-d respectively. CNTs are having an average inner diameter of 10 nm and an outer diameter of 30 nm and an average length in the range of 10-30 µm (Figure 2.24a). Figure 2.24b suggests the partial coverage of

the MnO_2 nanoflowers on the surface of CNTs. MnO_2 nanoflowers on the surface of CNTs formed whisker-like microstructures with the length of 80-100 nm. Thin transparent layers of GNs can be clearly seen from Figure 2.24c. TEM image of GNs-(γ-MnO_2/CNTs) (Figure 2.24d) shows the presence of CNTs and MnO_2 nanoflowers over the surface of GNs. γ-MnO_2 structures with porosity and interconnectivity can supply additional accessible space for ions while maintaining sufficient conductivity for solid-state electronic transfer.

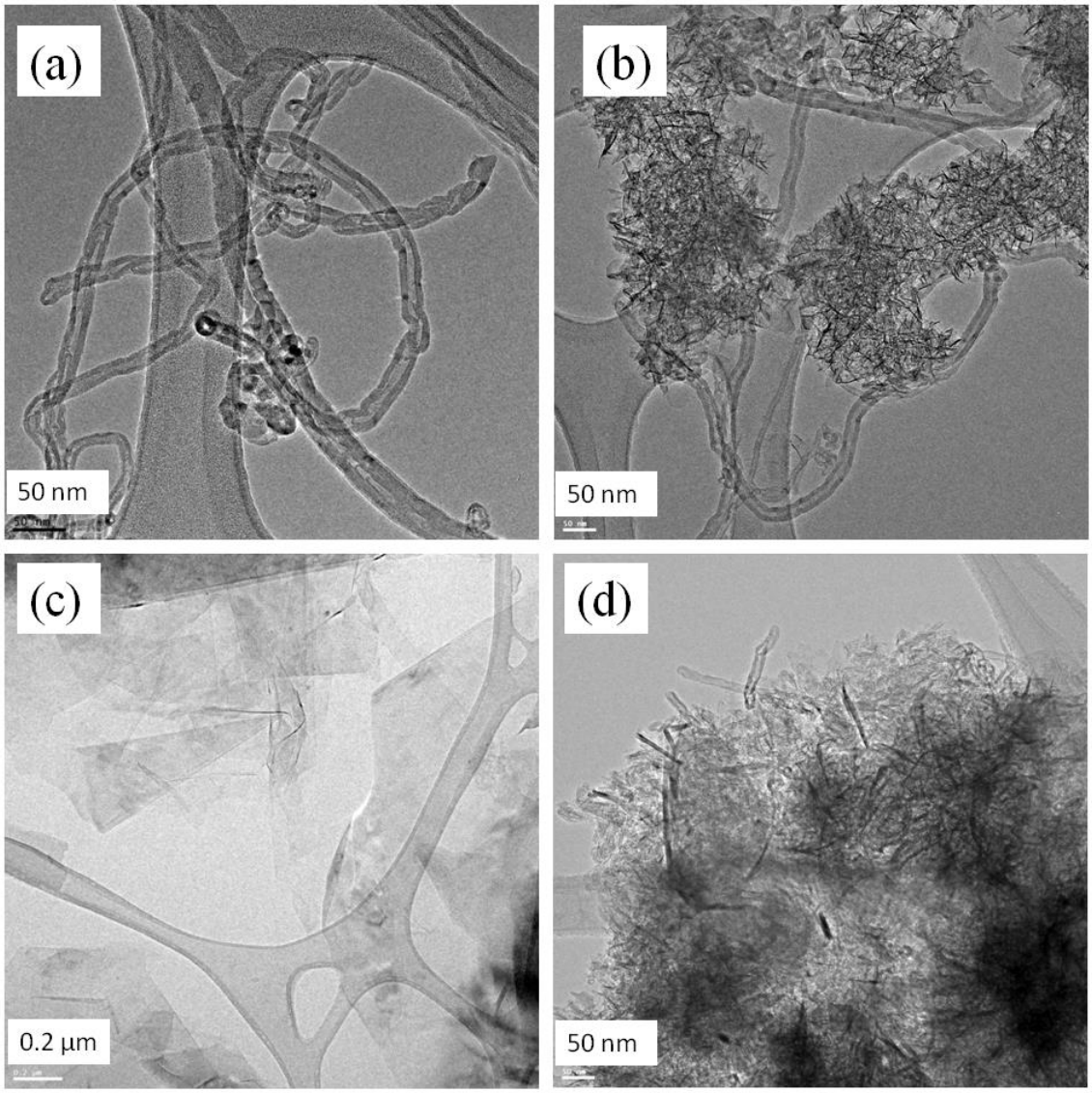

Figure 0.24: TEM images of (a) CNTs, (b) γ-MnO_2/CNTs, (c) GNs and (d) GNs-(γ-MnO_2/CNTs).

HRTEM offers further insight into the morphology and microstructure of these nanomaterials. HRTEM images of CNCs, GNs-(γ-MnO_2/CNTs) and γ-MnO_2 nanoflowers are shown in Figure 2.25a-d respectively. Figure 2.25a shows

the high crystallinity of CNT with an average interlayer spacing of 0.34 nm. CNT has an inner diameter of 10 nm and an outer diameter of 30 nm. Nanocrystalline MnO_2 whiskers have an average length of 60-80 nm are clearly visible in Figure 2.25b. Figure 2.25c shows that γ-MnO_2/CNTs occupy the surface of GNs. From Figure 2.25b and d it is clear that the MnO_2 nanoflowers are polycrystalline in nature and γ-MnO_2/CNTs are expected to provide short diffusion path lengths to both ions and electrons and also sufficient porosity for electrolyte penetration giving rise to high charging and discharging rates of the supercapacitors.

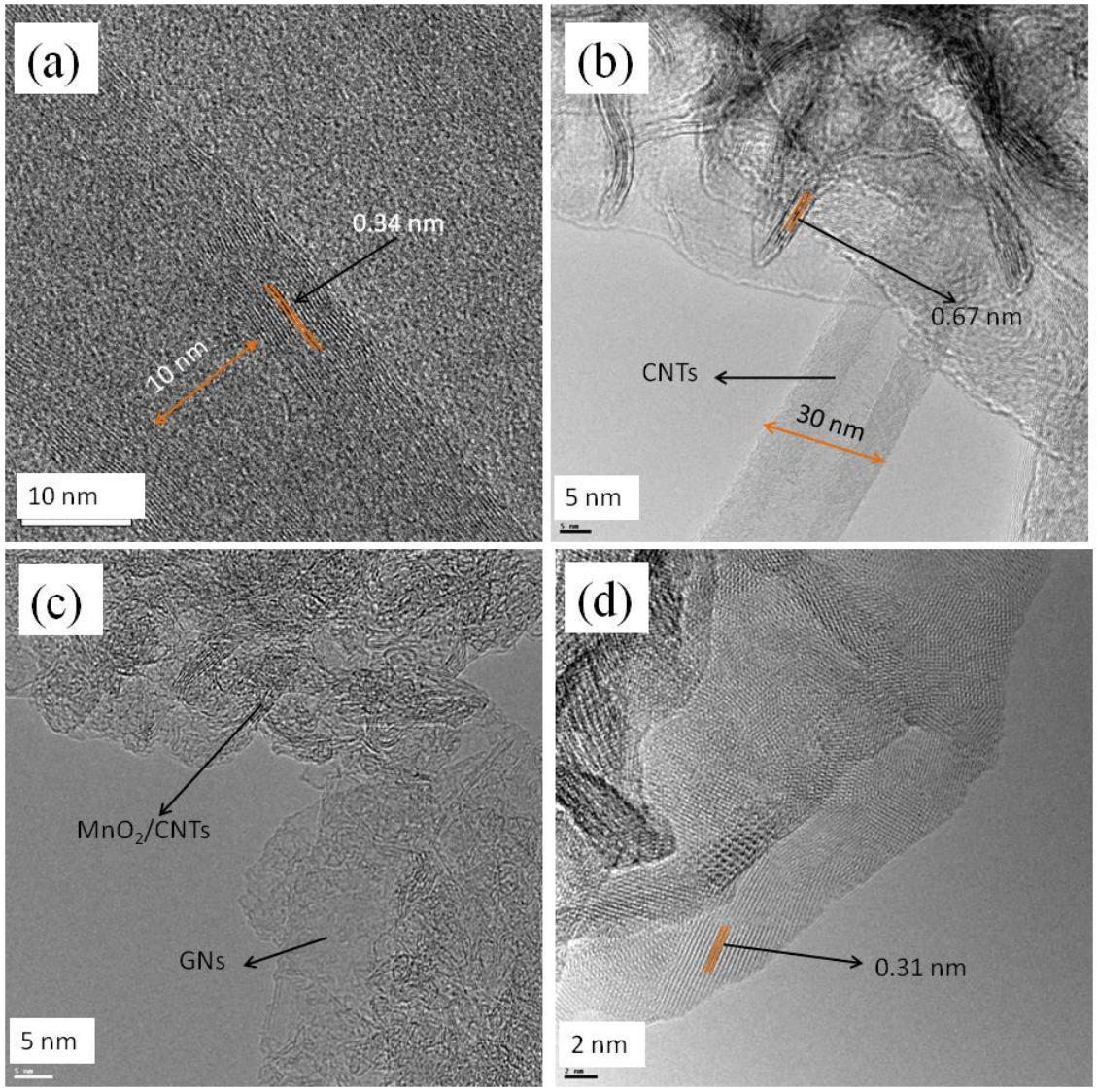

Figure 0.25: HRTEM images of (a) CNTs, (b) and (c) GNs-(γ-MnO_2/CNTs) and (d) γ-MnO_2.

Figure 2.26a and b respectively shows CV loops of the γ-MnO_2/CNTs and GNs-(γ-MnO_2/CNTs) based symmetric supercapacitors. For γ-MnO_2/CNTs nearly rectangular CV loops are obtained only up to a scan rate of 50 mV/s, whereas,

GNs-(γ-MnO_2/CNTs) based symmetric supercapacitor retains rectangular CV loops, which are characteristics for supercapacitors with low contact resistance, up to a scan rate of 300 mV/s, indicating an excellent capacitor behavior and low contact resistance. Absence of any oxidation or reduction peaks in the CV loops of the latter denotes the good capacitive characteristics of the GNs-(γ-MnO_2/CNTs) composite based symmetric supercapacitors. A comparison of CV loops of carbon cloth substrate, GNs, GNs/CNTs, γ-MnO_2/CNTs and GNs-(γ-MnO_2/CNTs) composite based supercapacitors at a scan rate of 20 mV/s is shown in Figure 2.26c. The CV loops of GNs, GNs/CNTs and GNs-(γ-MnO_2/CNTs) symmetric supercapacitors are rectangular in nature as well. Among them, GNs-(γ-MnO_2/CNTs) composite materials show higher capacitive performance than GNs, GNs/CNTs or γ-MnO_2/CNTs as supercapacitor electrodes. The specific capacitances of GNs, γ-MnO_2/CNTs, GNs/CNTs and GNs-(γ-MnO_2/CNTs) symmetric supercapacitors obtained from CV loops are 150, 204, 217 and 308 F/g respectively. Figure 2.26d shows the variation in the specific capacitance as a function of scan rate. It can be seen that the specific capacitance decreases with the increase of scan rate from 5 to 200 mV/s. It is also observed that the specific capacitance of GNs/(γ-MnO_2/CNTs) supercapacitors is much higher than that of GNS or γ-MnO_2/CNTs based supercapacitor at the same scan rate.

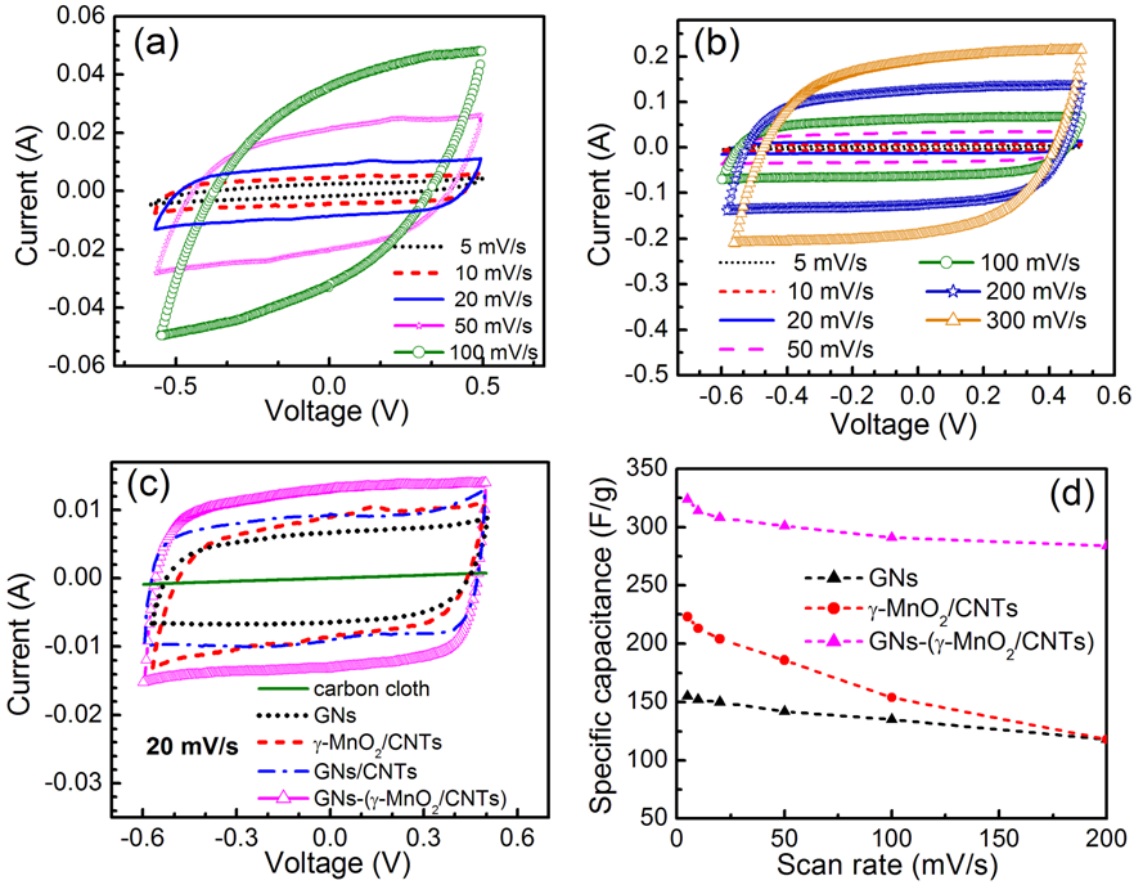

Figure 0.26: Cyclic voltammograms of (a) γ-MnO_2/CNTs and (b) GNs-(γ-MnO_2/CNTs) based symmetric supercapacitors at different scan rates, (c) comparison of cyclic voltammograms of carbon cloth substrate, GNs and metal oxide dispersed GNs composite based supercapacitor devices at the same scan rate of 20 mV/s and (d) specific capacitance change as a function of scan rate.

Galvanostatic charge-discharge curves of GNs, γ-MnO_2/CNTs and GNs-(γ-MnO_2/CNTs) symmetric supercapacitors at a constant current of 10 mA in the potential range between 0 and 1 V are shown in Figure 2.27a. It can be seen that the curves are nearly linear and symmetrical, which is another typical

characteristic of an ideal capacitor. Voltage drop is observed to be very small, which indicates that the electrodes have low internal resistance. In addition, the charge-discharge duration for GNs-(γ-MnO_2/CNTs) composite is greater than that of GNs, indicating a high specific capacitance of 310 F/g for GNs-(γ-MnO_2/CNTs) composite. The specific capacitance is obtained as 153 F/g and 205 F/g for GNs and γ-MnO_2/CNTs based supercapacitors, respectively. Specific capacitances at constant currents from 20 to 50 mA are also calculated, however, the results remain practically invariant. For practical applications, supercapacitors must have long-term cycle stability. The stability of the supercapacitor devices is evaluated by conducting galvanostatic charge-discharge measurements for 5000 cycles at a constant current of 10 mA. The specific capacitance as a function of cycle number is presented in Figure 2.27b. The specific capacitance of γ-MnO_2/CNTs rapidly drops to 80% after 2500 cycles and after that it remains almost stable and then gradually decreases to 74% at the end of 5000 cycles. Both GNs and GNs-(γ-MnO_2/CNTs) symmetric supercapacitors are found to exhibit excellent cycle life over the entire cycle numbers. After 5000 cycles, GNs and GNs-(γ-MnO_2/CNTs) symmetric supercapacitors retain 94% and 90%, respectively, of their initial specific capacitance indicating that both the electrode materials have excellent cycle stability and very high degree of reversibility in the repetitive charge-discharge cycling.

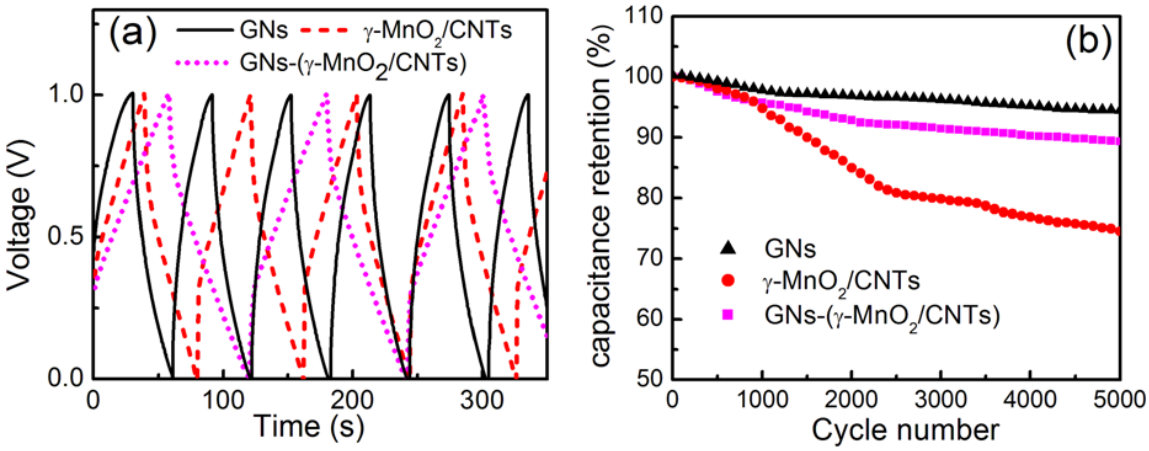

Figure 0.27: (a) Galvanostatic charge-discharge curves of GNs and MnO_2 dispersed GNs composite based supercapacitors at a constant current density of 10 mA, and (b) the specific capacitance retention at a constant current of 10 mA as a function of cycle number.

Impedance spectra of the GNs and GNs-(γ-MnO_2/CNTs) electrodes are presented in Figure 2.28a. The spectra can be divided into two regions by the so-called knee frequency, with a semicircle arc in the high frequency region and a straight line in the low frequency region. The equivalent circuit for GNs-(γ-MnO_2/CNTs) based ideal symmetric supercapacitor cell is illustrated in Figure 2.28b. In the equivalent circuit, a solution resistance (R_S) is connected in series with a double layer capacitance ($C_{D.L}$), and the C_{DL} is connected in parallel with the charge transfer resistance (R_{ct}) and pseudo-capacitance (C_P). The solution resistance refers to the resistance from the electrolyte, and the charge transfer resistance corresponds to the total resistance at the interface between the

electrode and the electrolyte. This equivalent circuit gives a theoretical Nyquist plot consisting of a semi-circle at high-frequency region followed by a vertical line within the low frequency region. The parallel R_{ct} and C_{DL} configuration accounts for the semi-circle feature, while C_P for the steep line.

Nyquist plot obtained for GNs-(γ-MnO_2/CNTs) electrodes is largely consistent with the proposed model. The deviation from this model can be attributed to the porous nature of the electrode. The real axis intercept at high frequency corresponds to the uncompensated resistance of the bulk electrolyte solution (R_s) and it is also known as equivalent series resistance (ESR). Experimental results show that the magnitude of ESR obtained from the *x*-intercept of the Impedance spectra for GNs and GNs-(γ-MnO_2/CNTs) composite based electrodes are insensitive to the surface condition of the electrode, and it is consistent with a value of around 1.2 Ω for the both devices.[130-132] R_{ct} is a surface property of the porous electrode which is related to the electroactive surface area. It is a combination of electrolyte accessible area and electrical conductivity of the electrode material. The larger the electroactive surface area, the lower the charge-transfer resistance. For pure GNs based system, the radius of the semicircle arc in the nyquist plot is large, which indicates the charge transfer resistance of GNs is high. This may be due to fact that the tendency of pure GNs layers to agglomerate decreases electrolyte accessible electro active surface area. For GNs based system, the specific capacitance value obtained in the very low frequency region is consistent with the specific capacitance values

obtained from cyclic voltammograms at lower scan rates. R_{ct} of the nanocomposite electrode is very small and this implies good electronic conductivity at the nanocomposite electrode/electrolyte interface. This also indicates that γ-MnO_2/CNTs act as efficient spacers between different GNs thereby providing more electrolyte accessible electroactive surface area.

C_p arises from the pseudocapacitance of γ-MnO_2. The equivalent circuit model shown in Figure 2.28b cannot as such explain either the deviation from vertical behavior or the existence of a short curved region in the Nyquist plots between the semicircle arc and the steep line in the low frequency region. This behavior may arise from the granular and porous nature of the electrode which can be accounted for by a transmission line model that contains distributed RC network as schematically shown in Figure 2.28c. In the generalized sense of the model, the resistances sum up the pore resistances and the electric resistances along the solid conductive matrix over different segments within an electrode.[133] The electric resistance is determined to a greater extent by contact resistances between the grains than by the bulk resistances within the grains. For the RC network having infinite numbers of equal-valued resistances and capacitances, the line has a theoretical inclination of 45°. On the other hand, it can readily be demonstrated that the angle deviates (changes slope from 45° to nearly 90°) from the ideal value for varied resistances and capacitors.

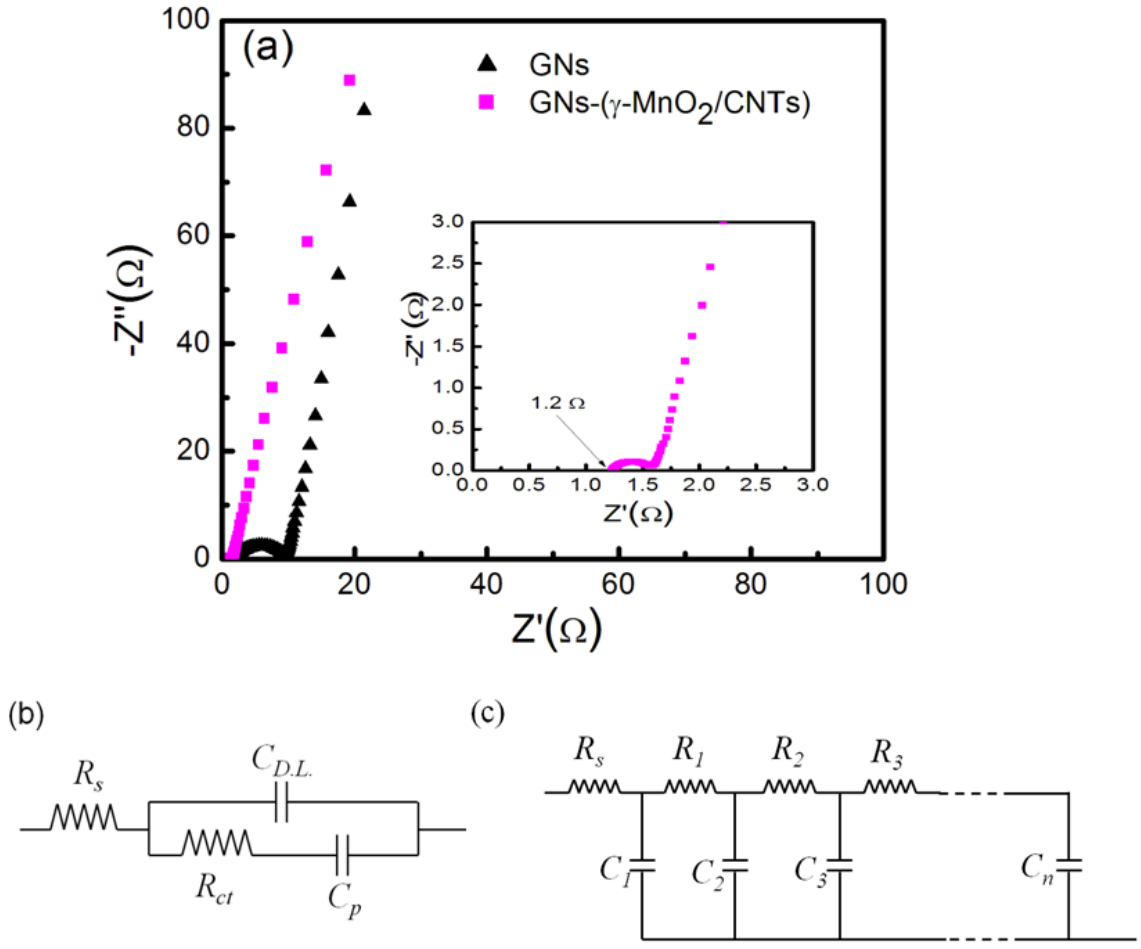

Figure 0.28: (a) Nyquist plots for GNs and GNs-(γ-MnO_2/CNTs) composite based supercapacitors with the at a dc bias of 0 V with sinusoidal signal of 10 mV over the frequency range from 100 kHz and 1 mHz. (*Z'*: real impedance. *Z"*: imaginary impedance). Inset shows an enlarged scale (b) Equivalent circuit for GNs-(γ-MnO_2/CNTs) composite based supercapacitor and (c) transmission model for porous electrode.

Specific capacitance value obtained for chemically modified GNs based supercapacitor in the present study is comparable to that reported by Liu *et al.* for

curved GNs based supercapacitors (154.1 F/g at 1 A/g) with ionic electrolyte in two electrode configuration.[134] For CB spacer dispersed GNs supercapacitor electrodes, a maximum specific capacitance of 175 F/g has been reported in 6M aqueous KOH electrolyte.[120] The use of CNT spacers in polymer modified GNs reported to give an average specific capacitance of 120 F/g in 1M H_2SO_4 electrolyte.[125] Supercapacitor performance of the GNs-(γ-MnO_2/CNTs) composite we report here is superior to GNs/CB or GNs/CNTs composites.[120, 125] For MnO_2(78%)/GNs in three electrode configurations, Yan *et al.* reported a specific capacitance value of 310 F/g at a scan rate of 2 mV/s.[20] In the present study, with lower loading of MnO_2, we could achieve 308 F/g at a higher scan rate of 20 mV/s in the two-electrode configuration.[135] But, it is well known that the three-electrode configuration yields larger specific capacitance values than that for the same materials in two electrode configuration. From that aspect the values obtained in the present study, with two electrode configuration, are highly encouraging. In the present study, using symmetric two electrode configuration we could achieve a specific capacitance of 310 F/g with 12% of MnO_2 loading, at a constant charge discharge current of 10 mA. Hence, GNs-(γ-MnO_2/CNTs) composite with a maximum specific capacitance of 310 F/g, energy density of 43 Wh/kg and power density of 26 kW/kg can be considered as a promising electrode material for high performance supercapacitors. Moreover, the flexible nature of the carbon fabric substrate is an extra advantage which opens up new

possibilities for incorporating these kinds of composite electrodes in flexible energy storage devices.

2.3 MnO_2 Based Novel Electrodes

2.3.1 MnO_2-CNT-Textile

We designed a new nanostructure based on a conductive CNT-textile fiber network, which provides an effective three-dimensional (3D) framework for the electrodeposition of nanoscale MnO_2. Such a 3D network allows for a large mass loading of MnO_2 without any mechanical peeling problems. The processes for fabricating conductive textiles and depositing MnO_2 are scalable. The MnO_2 shows much stronger binding with CNT-textile fibers than metal substrates, which is beneficial for stable cycling performance.[136]

Conductive textiles were fabricated with a conformal coating of CNTs on the surface of polyester fibers.[137] Due to the high flexibility of CNTs and the large Van der Waals forces between CNTs and polyester fibers, an excellent overcoating is observed.[137] Figure 2.29a illustrates the structure of the pseudocapacitor electrode, where MnO_2 is conformally electrodeposited onto the highly conductive polyester fibers. CNTs have -COOH groups on the surface which promote the nucleation of MnO_2 and bonding with the conductive textile. Figure 2.29b shows the final device structure with the MnO_2-CNT-textile as a

positive electrode, reduced MnO_2-CNT-textile (R-MnO_2-CNT-textile) as a negative electrode and 0.5 M Na_2SO_4 in water with pH=10 as the electrolyte. The advantages of such a pseudocapacitor are: (1) the conductive textile is much lighter than metal foil as a current collector, which reduces the total weight of the pseudocapacitor; (2) the highly macroporous structure of the textiles allows for a large mass loading of MnO_2, much larger than that on flat metal substrate on the same projection area; (3) the strong binding between MnO_2 and CNT-coated polyester fibers is beneficial for achieving stable performance; (4) the material and the process could lead to low cost pseudocapacitors. Although the cost of CNTs is relatively high, the areal mass loading of CNTs is low (less than 0.2 mg/cm^2). Also, the cost of CNTs is projected to drop in the future with further commercialization efforts. Other conductive nanomaterials with potential low costs such as graphene and conductive polymers can replace CNT in our pseudocapacitors.

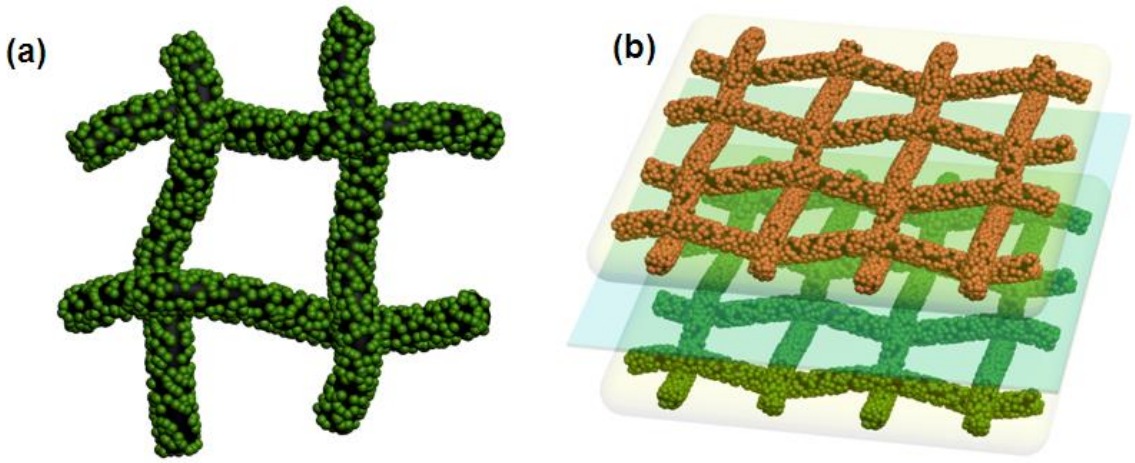

Figure 0.29: (a) Schematic of conformal coating of MnO_2 on CNT-wrapped polyester fibers. Black, CNT-polyester fibers; Green, MnO_2 nanoflowers. (b) Schematic of pseudocapacitor based on MnO_2-CNT-textile. The positive electrode (bottom) is MnO_2, the negative electrode (top) is reduced MnO_2, and the electrolyte is 0.5 M Na_2SO_4 in water at pH of 10.

After washing away the surfactant thoroughly with deionized (DI) water, the conductive textile is hydrophobic. To ensure conformal coating of MnO_2 over the entire textile surface including the fibers inside, textiles are soaked in 4 M HNO_3 for 4 hours to generate -COOH groups on CNTs, taken out and dried in air for one hour.[138] The textile is cut with a size of 1 cm by 3 cm, where 1 cm by 1 cm is immersed into aqueous solution with 100 mM Na_2SO_4 and 10 mM $MnSO_4$. MnO_2 is electrodeposited onto the conductive textile with a three electrode setup, where a conductive textile with a sheet resistance of ~ 10 Ω/□ is used as the working electrode, platinum (Pt) as the counter electrode and Ag/AgCl as the

reference electrode. A small piece of Pt is used to connect the textile and the alligator clip to avoid side reactions. Impedance spectra in the frequency range of 0.1 Hz-100 kHz are recorded before the electrodeposition to check the connections. Typical resistance at high frequency (~100 kHz) is ~20 Ω. The MnO_2 is electrodeposited with a galvanostatic technique by applying a small current, 500 μA, to ensure a conformal coating of MnO_2.

Figure 2.30a shows the conductive textiles after MnO_2 deposition. The bottom surface becomes darker as the deposition time increases, which indicates more materials were deposited. Figure 2.30b shows the mass loading versus the deposition time. Due to the highly porous structure of the textile, a larger mass loading of MnO_2 is achieved by increasing the deposition time. 8.3 mg/cm^2 of MnO_2 is readily achieved, where the textile structure is still highly porous. Pseudocapacitors based on MnO_2 typically have small mass densities (<0.5 mg/cm^2) due to its low proton diffusion constant (~ 10^{-13} cm^2/s) and low electrical conductivity (~10^{-5} S/cm).[19] We found that the MnO_2 nanoflowers are polycrystalline, which is consistent with the literature (Figure 2.30c and d). The strong signals at 642 and 653 eV in XPS in Figure 2.30e correspond to the binding energies of Mn $2p_{3/2}$ and $2p_{1/2}$, respectively.[82] The well-resolved peak at 37.1° *etc.* in X-ray diffraction (XRD) pattern marked by the arrows (Figure 2.30f) are attributed to MnO_2,[139] and the other peaks are from textiles or CNTs.[128]

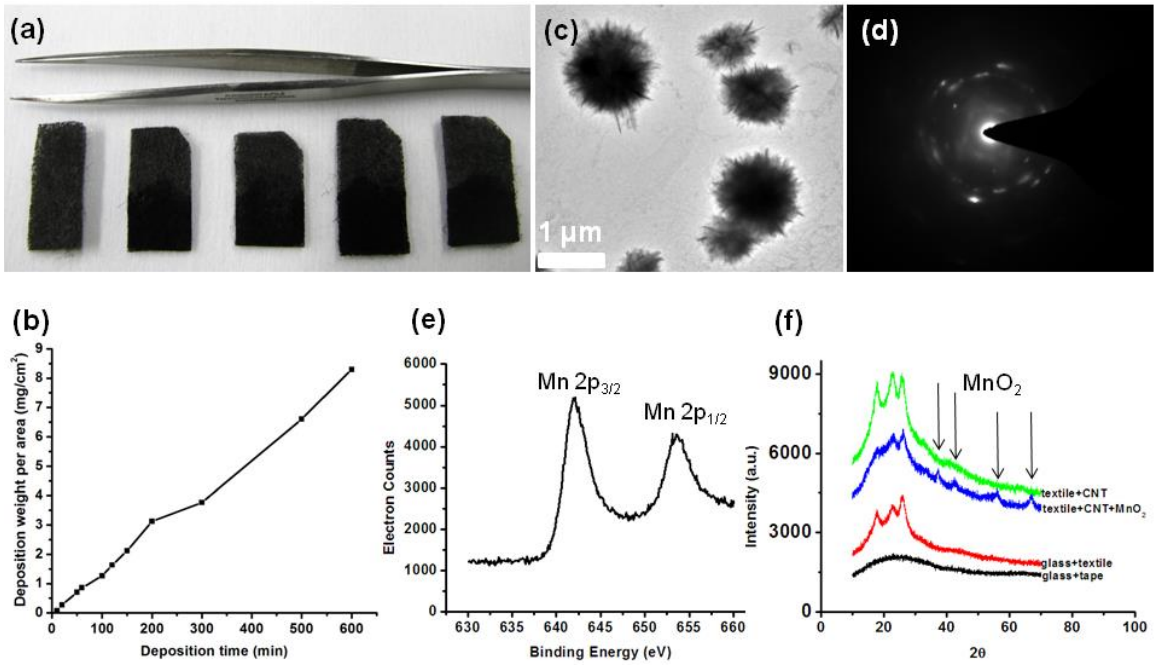

Figure 0.30: (a) MnO_2 deposited on conductive textiles with different areal masses. The MnO_2 mass increases from left to right (0.06, 0.3, 0.8, 2.1, 3.8 mg/cm^2). (b) MnO_2 weight *versus* deposition time. (c) TEM image of MnO_2 nanoflowers by electrodeposition. (d) TEM diffraction pattern of MnO_2 nanoflowers. (e) XPS of MnO_2-CNT-textile. (f) XRD patterns of textile, CNT-textile and MnO_2-CNT-textile.

Figure 2.31 shows SEM images of the MnO_2 deposited on conductive textile with different electrodeposition times. MnO_2 forms nanoflower structures which is consistent with previous studies. MnO_2 nanoflowers and CNTs can be clearly identified (Figure 2.31a and b). As the deposition time increases, the sizes of the nanoflowers increase until a continuous, thick MnO_2 layer is formed on the textile fibers (Figure 2.31c and d). Even for a large mass loading, ~ 8.3 mg/cm^2,

the 3D textile fiber structure is still maintained without merging into a film. Such a highly porous structure with a large mass loading is excellent for pseudocapacitor applications. During the experiment, we found that the treatment of the conductive textile is crucial for achieving such a uniform coating. The conductive textile was washed with HNO_3 to remove surfactants and generated -COOH groups.[138] The washed textile was dried in air for an hour before MnO_2 deposition. A longer drying time in air makes the conductive textile highly hydrophobic which prohibits electrolyte penetration and the deposition of MnO_2 inside the structure. A shorter drying time leads to a highly hydrophilic textile which allows the water to climb along the fibers and cause corrosion on the metal connector during the electrodeposition process.

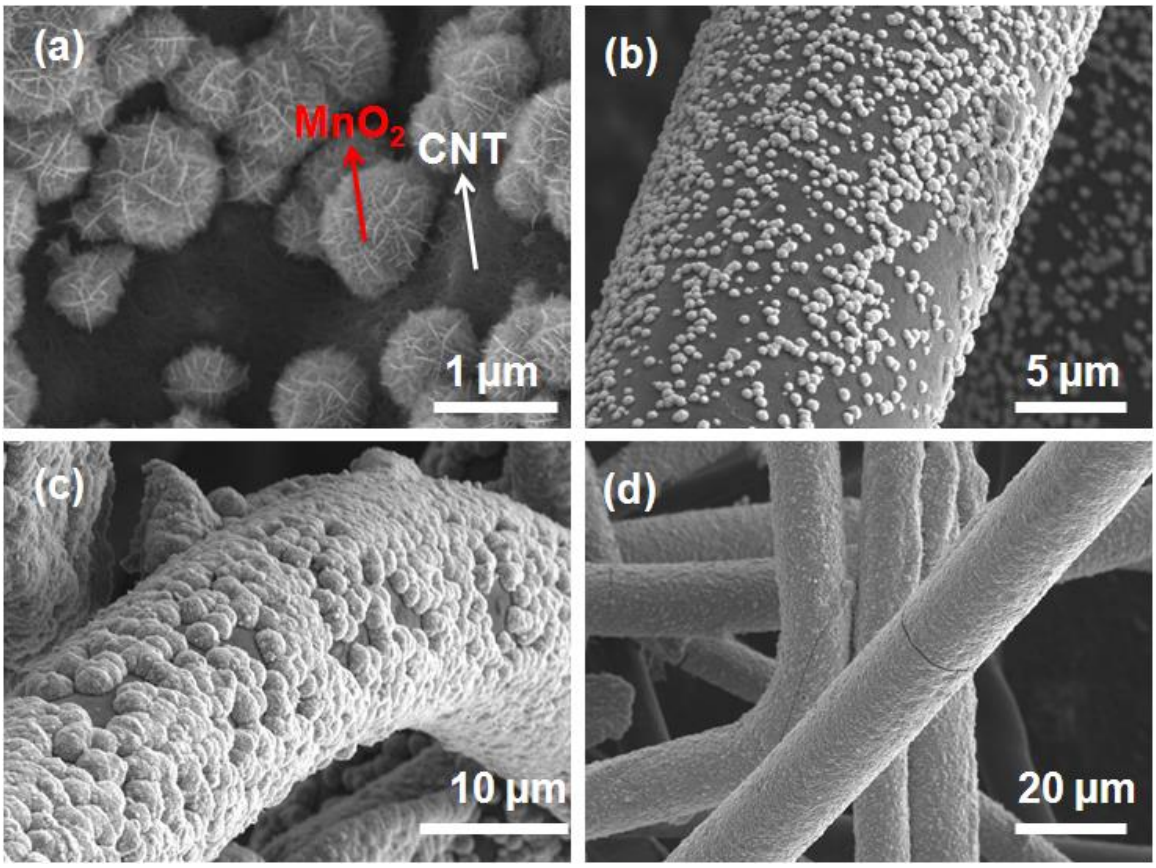

Figure 0.31: (a)-(b) SEM of MnO_2-CNT-texitle after a 10-minute deposition. (c) and (d) SEM of MnO_2-CNT-texitle after 120-minute and 300-minute depositions, respectively.

Impedance of the half cells with a three-electrode setup is tested over a frequency range of 100 kHz ~ 0.1 Hz with MnO_2-CNT-textile as the working electrode, Pt as the counter electrode and Ag/AgCl as the reference electrode (Figure 2.32a). 0.5 M Na_2SO_4 in DI water was used as the electrolyte. Impedance of flat Pt without MnO_2 deposition was tested as a control experiment, which reflects the contribution from the electrolyte (~7 Ω) between the working

electrode and the counter electrode in our setup. The impedance at a high frequency (100 kHz) for MnO_2-CNT-textile reflects the combination of electrolyte resistance and textile electrode resistance. For example, the total resistance of MnO_2-CNT-textile with a 20-minute deposition at 100 kHz is 20.4 Ω (Figure 2.32a). 13.4 Ω is contributed by the textile electrode and 7 Ω by the electrolyte.

To illustrate the advantages of the 3D porous textile electrode based pseudocapacitors, a comparison study of MnO_2 pseudocapacitor with a flat Pt substrate was conducted. The MnO_2 deposition time is 60 minutes for both the Pt substrate and conductive textile. The areal mass is approximately 0.8 mg/cm^2. The coating is uniform on both sides of the Pt plate immersed into the electrolyte solution. After drying in air, the MnO_2 film on Pt is fragile and easily cracks into pieces. Electrochemical performance was evaluated for MnO_2-Pt and MnO_2-CNT-textile, where MnO_2-Pt is not dried to avoid cracking. The voltage range is chosen according to the Pourbaix diagram of MnO_2. Figure 2.32b and c show the CV comparisons between MnO_2-Pt and MnO_2-CNT-textile at scan rates of 5 mV/s and 50 mV/s, respectively. With the same mass density of 0.8 mg/cm^2, the capacitance for the MnO_2-CNT-textile is much higher than that for MnO_2-Pt. As shown in Figure 2.32d, a specific capacitance of 185 F/g is achieved for CNT-textile based device, while only 18 F/g for Pt based device. The specific capacitance is based on the mass of MnO_2 on the substrates. This 10-fold difference in specific capacitance with respect to the mass of MnO_2 at the same scan rate must be due to the kinetics of ions and electrons in the electrode

materials. For the same mass loading, the thickness of MnO_2 on textile fibers is much smaller than that on the Pt substrate, which largely facilitates the ion and electron transport in the electrode materials. As the scan rate increases, the specific capacitance decreases for both substrates. This study clearly illustrates that the 3D CNT-textile fiber is better than a flat metal current collector for pseudocapacitor applications.

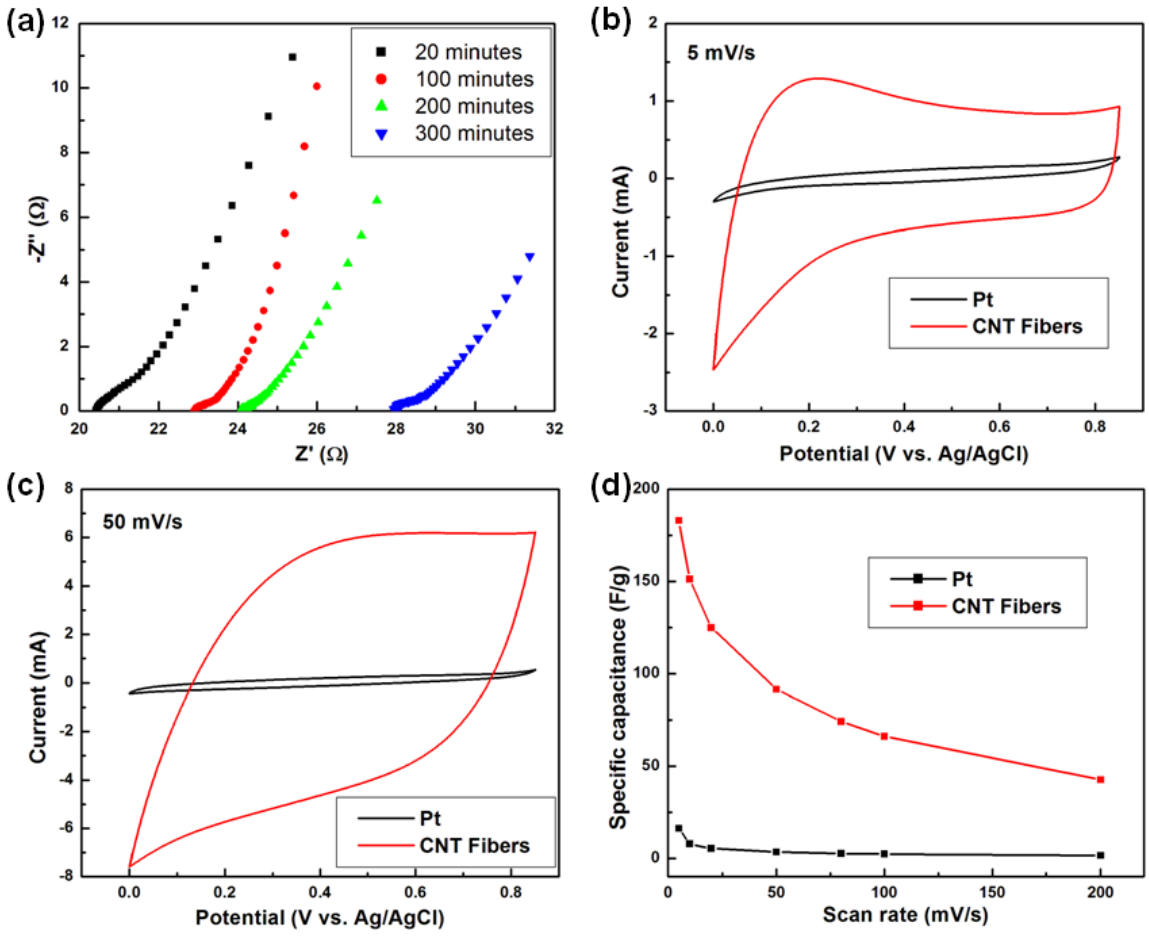

Figure 0.32: (a) Impedance of MnO_2-CNT-textiles with different MnO_2 deposition times. The frequency range is 100 kHz~0.1 Hz. (b,c) CV scan comparison of

MnO_2-CNT-textile and MnO_2-Pt at scan rates of 5 mV/s and 50 mV/s, respectively. (d) Specific capacitance comparison between MnO_2-CNT-textile and MnO_2-Pt, The mass density of MnO_2 for both substrates is 0.8 mg/cm^2.

To achieve the highest specific capacitance with respect to MnO_2 mass, the thickness needs to be infinitely small, and the scan rate needs to be infinitely slow to enhance the transport of electrons and ions in the electrode materials. However, high power performance at the device level depends on the total mass which includes all the components in a device (electrolyte, current collectors, electrodes, separator, packaging, *etc.*). Therefore, the optimization of MnO_2 mass percentage with respect to the total mass is important. We have carried out a detailed study of changing the mass loading and the scan rate in a large range to identify a trend, which will be useful for designing practical pseudocapacitors based on conductive textiles. First, we performed CV scans of a MnO_2-CNT-textile with a large range of MnO_2 deposition times on conductive textile (from 5 to 600 min). The MnO_2 mass varies from 60 μg to 8.3 mg per cm^2 accordingly. The electrochemical performance of MnO_2-CNT-textiles was tested with two different scan rates (5 and 50 mV/s). As the MnO_2 mass increases, the total capacitance increases at the same scan rate, as indicated by the increases of the current (Figure 2.33a and b). As the scan rate increases from 5 to 50 mV/s, the overpotentials lead to large resistance and the RC time constant causes the curves to deviate from those of an ideal capacitor (Figure 2.33b). Second, we varied the scan rate from 5 to 200 mV/s for MnO_2-CNT-textiles. The CV scan of

the 0.8 mg/cm^2 sample is shown in Figure 2.33c. As the scan rate increases, the peak current increases but the shape deviates from that of an ideal capacitor. The specific capacitance with respect to the electrode mass versus the scan rates are shown in Figure 2.33d. As the scan rate increases, the capacitance decreases dramatically for MnO_2-CNT-textile. The highest specific capacitance is 410 F/g for the sample with a mass density of 0.06 mg/cm^2 at a scan rate of 5 mV/s. As the thickness increases, the specific capacitance decreases due to the kinetics of ion transport in MnO_2 with its low ion diffusion constants. The low electrical conductivity and the low diffusion constant limit the pseudocapacitor performance.

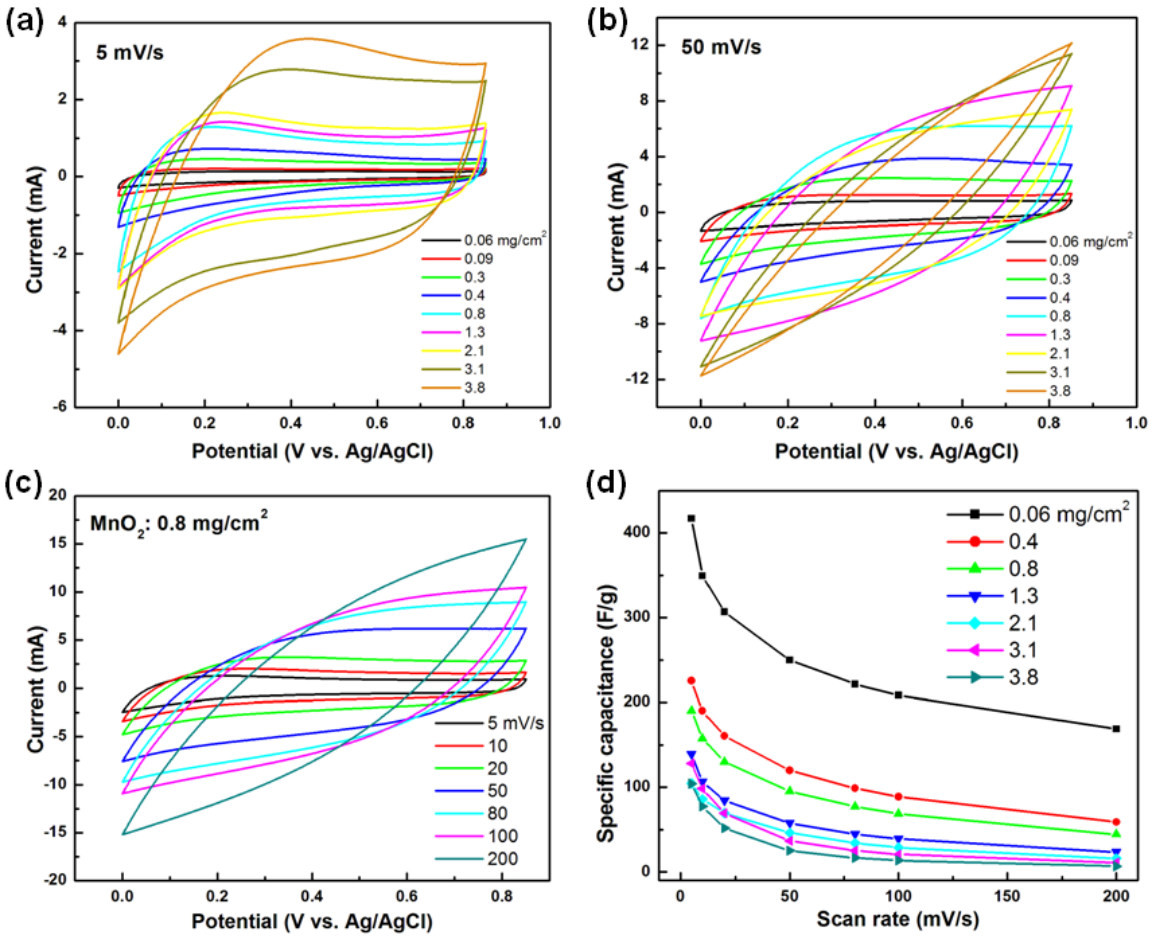

Figure 0.33: (a, b) CV of MnO_2-CNT-textile electrode with different areal mass densities for MnO_2. The scan rate is (a) 5 mV/s and (b) 50 mV/s. (c) CV of MnO_2-CNT-textile with different scan rates. The areal mass for MnO_2 is 0.8 mg/cm^2. (d) Specific capacitance vs. scan rate for samples with different areal mass densities for MnO_2.

It is worthwhile to point out that the mass loading per area is important for battery or pseudocapacitor devices. It is considered a good practice to report the values of the electrode mass.[29] The areal capacitance versus MnO_2 with different

mass loadings is plotted in Figure 2.34a. At a fixed rate of 200 mV/s, the areal capacitance increases with the mass until a saturation value is reached at a deposition time of approximately 60 min (mass loading of 0.8 mg/cm^2). At this fixed scan rate, the capacitance increases with MnO_2 thickness or mass until a critical value is reached. The critical MnO_2 thickness should be close to the Na^+ diffusion length at this rate. The critical mass loading at a fixed scan rate is helpful for device designs. As the scan rate decreases, the ion diffusion length in MnO_2 increases and more of electrode material contributes to the energy storage. For example, at the scan rate of 20 mV/s, the critical areal mass of MnO_2 is 3.8 mg/cm^2 (300 min of electrodeposition of MnO_2). For 5 mV/s, no saturation was observed in the range of measurement and all of the MnO_2 contributes to the energy storage. The highly porous structures of conductive textiles allow for the demonstration of pseudocapacitors with extremely high areal capacitances. Figure 2.34b shows areal capacitance versus scan rate for MnO_2-CNT-textile electrodes with a mass loading of 8.3 mg/cm^2. Such high areal mass loadings are not reported in the literature, and 2.8 F/cm^2 at slow a scan rate of 0.05 mV/s is demonstrated.

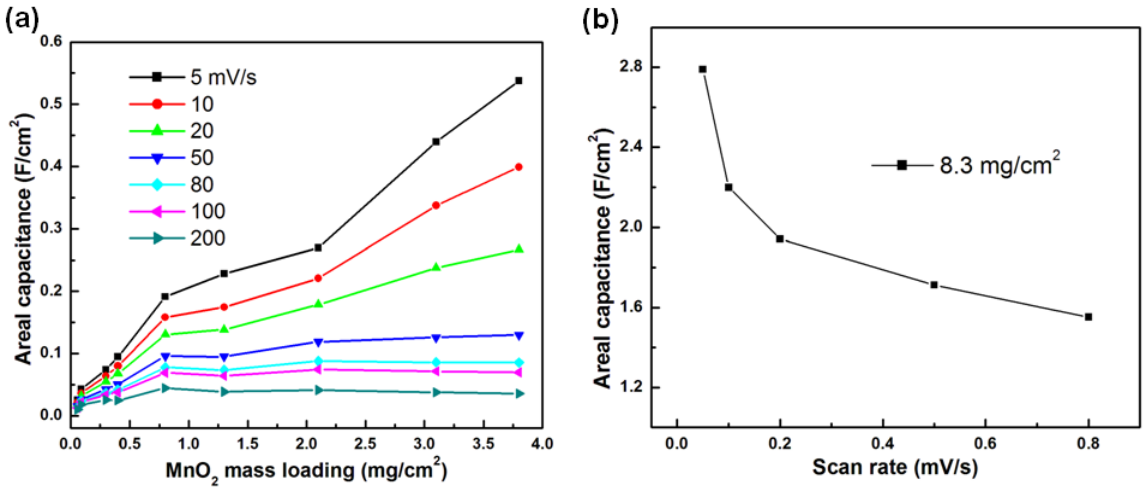

Figure 0.34: (a) Areal capacitance of MnO_2-CNT-textile versus MnO_2 mass loading. (b) Areal capacitance versus scan rate for a sample with 8.3 mg/cm^2 of MnO_2.

2.3.2 MnO_2-CNT-Sponge

Different from the textile in the previous section, here we will exploit sponge as the substrate for supercapacitors.[21] Sponges, with a hierarchical macroporous nature, have been widely used in our daily life as cleaning tools and can be found everywhere. Sponges are made up of many small cellulose or polyester fibers, which make them highly porous and strong absorbing media with significant internal surface area. A commercial sponge has been employed into this study, which has a high water absorption capacity. A simple experiment showed that it can absorb 45 times more water than its own weight. This indicates the good accessibility and compatibility of sponge to water and aqueous solutions. Sponges offer novel exciting characteristics different from

paper and textile that we demonstrated previously: first, sponge has much more uniform size of macropores. The pore size can be in the range of 100-500 μm. Second, the cellulose or polyester fibers are interconnected virtually free of junctions. Therefore, continuous coating of conducting nanomaterials is much easier since there are no boundaries to cross.

We suggest to design and fabricate high performance supercapacitors using a simple and scalable method. The fabrication process consisted of four simple steps, as illustrated in Figure 2.35. A piece of commercially available sponge (pore sizes 100-500 μm) was cleaned by water and acetone for several times (Figure 2.35a). After drying completely in a vacuum oven, the sponge was cut into small ribbons with thickness of 1 mm and area of 1×2 cm^2. The sponge ribbons were subsequently coated with CNTs using a simple “dipping and drying” process in CNT ink suspension (Figure 2.35b). The next step was to electrodeposit MnO_2 nanoparticles on the CNT-coated sponge by galvanostatic electrochemical deposition (Figure 2.35c). A very small current density (500 $\mu A/cm^2$) was required to obtain the desired nanostructure of MnO_2. To study the dependence of supercapacitor performance on MnO_2 deposition time, we deposited MnO_2 on CNT-sponge for different times: ranging from 3 to 40 min. The deposition area of each sample was 1×1 cm^2. In the last step (Figure 2.35d), two identical MnO_2-CNT-sponges were sandwiched with a piece of polymer separator dipped in 1 M Na_2SO_4 electrolyte inserted in between, and sealed in a coin cell to complete the symmetrical two electrode assembly.

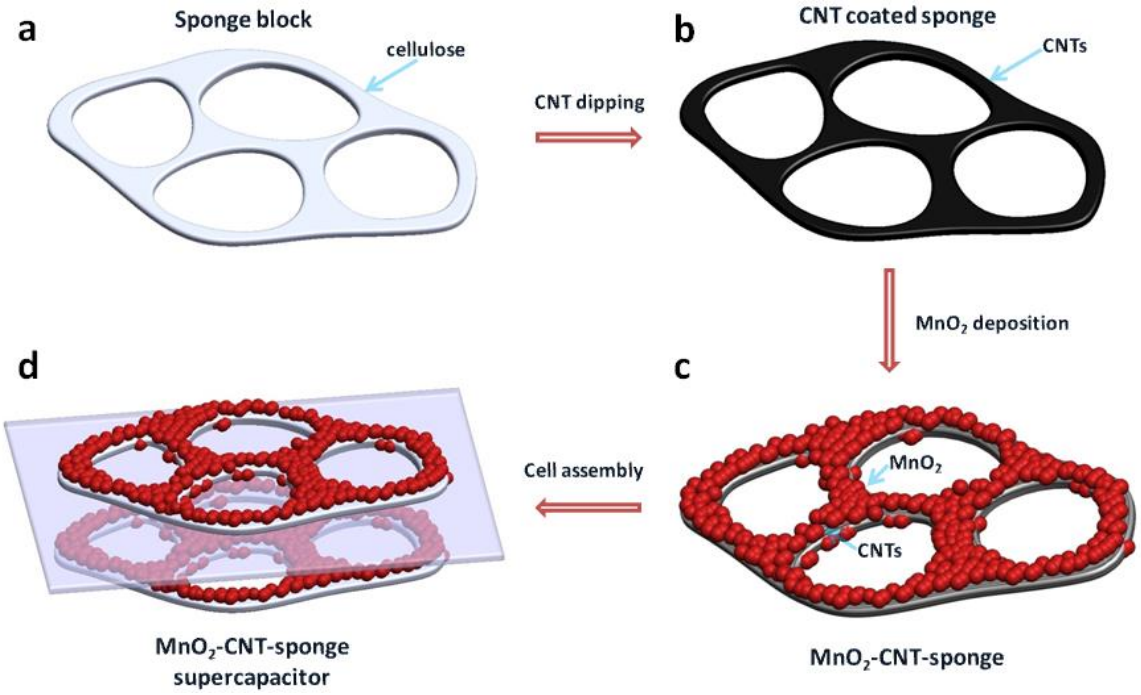

Figure 0.35: Fabrication process of MnO_2-CNT-sponge supercapacitors: (a) A piece of sponge is cleaned and cut into small ribbons; (b) CNTs are coated onto the skeleton of the sponge by a “dipping and drying” method; (c) nanostructured MnO_2 is electrodeposited onto the conductive CNT-sponge skeleton; (d) two pieces of MnO_2-CNT-sponge electrodes were assembled into coin cell to form a MnO_2-CNT-sponge supercapacitor.

The weight of a clean 1×2 cm^2 sponge is about 10 mg, which is much lighter than the rigid metal and other flexible substrates with the same area.[45, 105, 140] Due to the mechanical flexibility of CNTs and strong van der Waals interactions between the macroporous sponge cellulose and CNTs, the CNTs can be easily coated onto the skeleton of a sponge, rendering the insulating

sponge highly conductive by a simple dipping and drying process.[141] The mass of CNT on the CNT-sponge is ~0.24 mg/cm^2 after two times of dipping and drying. After conformal coating of CNTs onto the skeleton of the sponge, it still maintained hierarchical macroporous nature where its intricate assembly of pores remained open to allow the flow of electrolyte. The CNTs coated on the sponge have formed a thin layer of CNT network wrapped around the skeleton of sponge. The amount of CNTs coating on sponge can be readily controlled by the dipping time and ink concentration. In this section, we optimized the dipping time to maximize the amount of CNTs coated on the sponge but without blocking its pores. Undercoating degrades the conductivity of the CNT-sponge electrode while overcoating closes the pores of the sponge and prevents the movement of the electrolyte ions. The mechanical resilience of the CNT-sponge skeleton was tested by folding, twisting, and stretching it repeatedly. After all the mechanical tests, the CNT-sponge always reverted to its original shape without any permanent deformation.

SEM images of the MnO_2-CNT-sponge showed clearly the 3D hierarchical macroporous open-pore structure (Figure 2.36a). Flower-like MnO_2 nanoparticles were uniformly deposited onto the conductive CNT-sponge skeleton, even at the edges (Figure 2.36b and c). This further confirms that CNTs have been conformably coated on the sponge. Figure 2.36a also shows an exciting point: the backbone of sponge is free of junctions and promotes the continuous coating of CNT to form excellent conducting pathways in the whole structure. After

deposition of MnO_2, the highly porous nanostructure remained, which is good for the fast transportation of electrons and ions in the supercapacitor devices. The deposition mass of MnO_2 can be well controlled by adjusting the deposition time. We found that the surface of the CNT-sponge can be fully covered by MnO_2 after 10-minute of electrodeposition. Increasing the deposition time will increase the mass loading and the thickness of MnO_2. If the electrodeposition is run for one hour, a very thick film of MnO_2 with some cracks can be observed due to the large thickness. TEM images revealed that the nanostructure of MnO_2 is highly porous and includes many small nanoplates (Figure 2.36d). The average pore size of the MnO_2 is around 3.2 nm and it has a BET specific surface area of 174 m^2/g. An HRTEM image together with SAED pattern demonstrated that the deposited MnO_2 are polycrystalline (Figure 2.36e and inset). We further confirmed that the polycrystalline MnO_2 nanoparticles belong to ε-MnO_2 by XRD (JCPDS 00-030-0820) (Figure 2.36f). The flower-like MnO_2 nanoparticles on macroporous CNT-sponge essentially form a so-called double porous nanostructure.[141] This unique structure provides outstanding performance for the intercalation/de-intercalation of electrolyte cations into electrode materials, and we therefore expect a high performance supercapacitor.

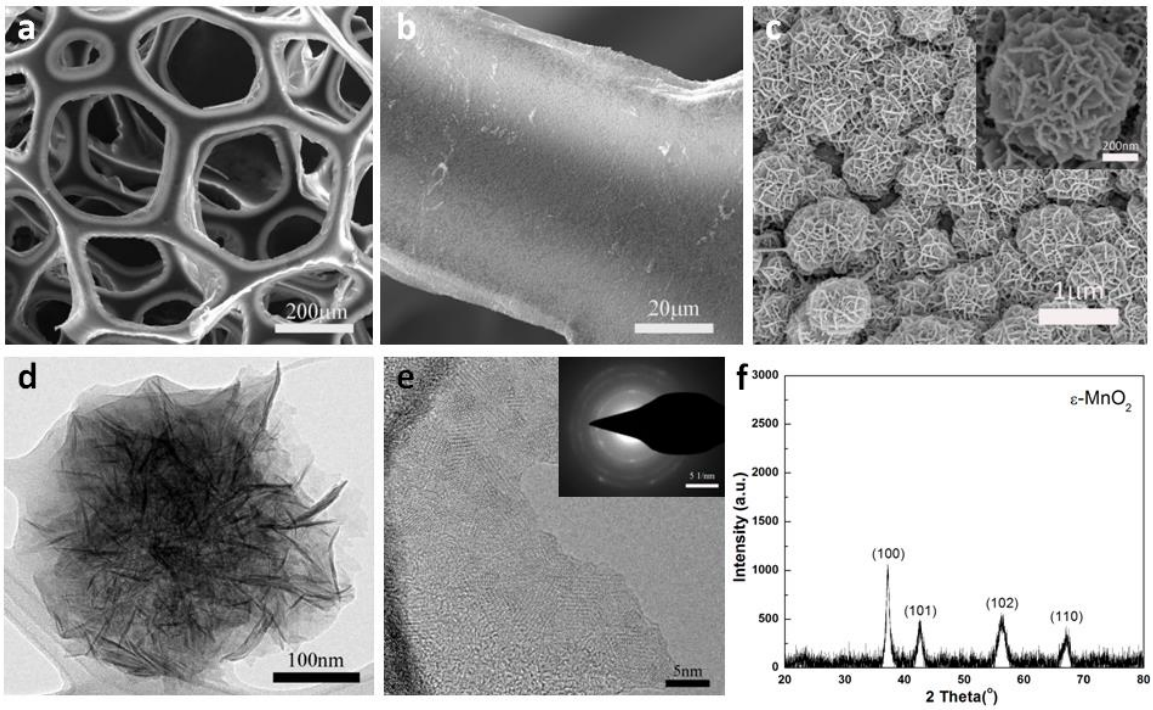

Figure 0.36: Characterizations of MnO_2-CNT-sponge electrodes: (a) an overall view of 3D macroporous hierarchical MnO_2-CNT-sponge electrode; (b) MnO_2 uniformly deposited on the skeleton of CNT-sponge; (c) high magnification of porous MnO_2 nanoparticles on CNT-sponge, inset shows morphology of an individual MnO_2 flower-like particle; (d) a TEM image of MnO_2 shows highly porous structure; (e) high resolution TEM (HRTEM) image and the inset SAED pattern of porous MnO_2 showing the polycrystalline nature of MnO_2; (f) XRD of the as-synthesized structure showing the ε-MnO_2 phase.

The electrochemical performance of CNT-sponge substrate was tested using a two-electrode coin cell configuration. Two pieces of symmetrical CNT-sponge, one piece of separator and 1 M Na_2SO_4 have been used as electrodes,

separator and electrolyte, respectively. All measurements have been conducted at room temperature. As shown in Figure 2.37a and b, the CNT-sponge devices (without MnO_2 deposition) can be operated over a wide range of scan rates: from 0.001 up to 200 V/s. The cyclic voltammograms retain the rectangular shape (which is characteristic of the ideal electrochemical double layer capacitive behavior) even at a high scan rate of 20 V/s. As expected, the currents increase with the applied scan rates, but surprisingly the CNT-sponge devices operates at the highest reported scan rate for aqueous electrolyte supercpacitors.[19, 22, 45, 82, 105, 140, 142] We can therefore conclude that ultrahigh power can be obtained from this kind of device.[143] Another good feature of the CNT-sponge device is its good electrochemical behavior even at an extremely high scan rate of 200 V/s, which is comparable to micro-supercapacitors built on rigid silicone substrates.[143, 144] Furthermore, a linear dependence of the discharge current on the scan rate up to 8 V/s can be observed from Figure 2.37c. The deviation of the linear dependence after 8 V/s is due to the diffusion limit of electrolyte ions to the electrode materials. The discharge currents are calculated from the discharge scan with an average over the whole voltage range at specific scan rates.[143, 144] A mean areal capacitance of 0.36 mF/cm^2 can be obtained from the slope of Figure 2.37c, which is comparable to the value of carbon materials based micro-supercapacitors.[144] A maximal value of 0.9 mF/cm^2 can also be obtained at a scan rate of 1 mV/s, but this value can be improved if more CNTs have been coated on the sponge. Figure 2.37d illustrates the charge-discharge behavior of

the CNT-sponge device. The figure shows ultrafast charge-discharge rate and linear dependence on voltage and time, with very small voltage drop at a specific current of 10 A/g. These results indicate that the CNT-sponge substrates used in the present work exhibit excellent supercapacitor performance. More importantly, these results coupled with other promising features of the CNT-sponge (such as ease of fabrication, low cost, light weight and flexibility) make it a highly promising energy storage substrate.

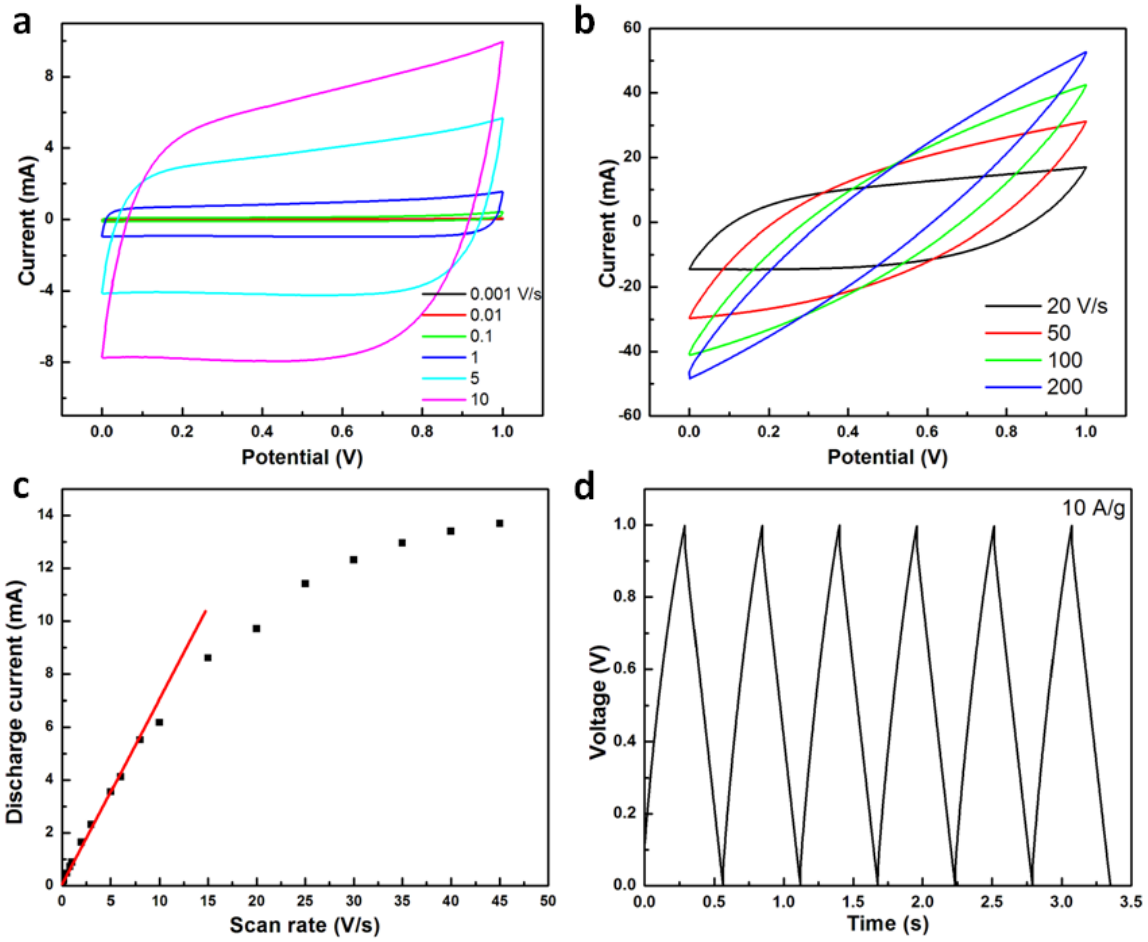

Figure 0.37: Electrochemical behaviors of CNT-sponge substrates: (a and b) cyclic voltammetry scan from 0.001 to 10 V/s and from 20 to 200 V/s, respectively; (c) discharge currents as a function of scan rates (linear relation is obtained up to scan rate of 8 V/s); (d) galvanostatic charge-discharge curves at a specific current of 10 A/g. The mass of CNT on CNT-sponge substrate is ~0.24 mg/cm^2.

Figure 2.38e shows the digital photograph of the MnO_2-CNT-sponge electrodes prepared by electrochemical deposition of MnO_2 onto conductive

CNT-sponge. The amount of MnO_2 was controlled by the deposition time. Here, we varied the deposition time from 3 to 40 min. It was observed that as the deposition time increased, the mass loading of MnO_2 increased accordingly. This can be observed from the increased darkness of the sponge as shown in Figure 2.38b. The first ribbon on the left in Figure 2.38b is a bare sponge, and the second one from the left is a CNT-sponge without MnO_2 on it. The remaining samples from left to right are MnO_2-CNT-sponge with deposition time from 3 to 40 min. The color of the bottom part of the CNT-sponge becomes darker with increased electrodeposition time, which means more MnO_2 has been deposited on the sponge. This can be further confirmed by plotting the change of MnO_2 content and MnO_2 mass loading *versus* deposition time (Figure 4a). As can be seen from Figure 2.38a, the MnO_2 content (the weight percentage of MnO_2 in MnO_2-CNT composite) and its mass loading increased with the deposition time. Each data point in Figure 2.38a is an average value of at least 10 samples. At low deposition time, *e.g.*, 10 min, the MnO_2 mass loading is around 0.1 mg/cm^2 and its content in the MnO_2-CNT composite is nearly 30% by weight. These values are higher than the values obtained from rigid metal substrates such as platinum at the same deposition time due to the large surface area of the sponge. When the electrodeposition time increased to 40 min, the mass loading of MnO_2 increased to 0.5 mg/cm^2, which is more than twice of CNT loading on the sponge, and the corresponding MnO_2 content in the MnO_2-CNT composite is as high as 67% by weight. For long deposition times, *e.g.*, 20 hours, the mass

loading of MnO_2 can go up to 12.8 mg/cm^2, which is twice of the weight than the CNT-sponge itself. To reveal the good adhesion between MnO_2 and CNT-sponge, a simple Scotch tape adhesion test was performed comparing the MnO_2-CNT-sponge and MnO_2-platinum electrodes. It can be seen clearly from Figure 2.38c that superior adhesion performance is observed for the MnO_2-CNT-sponge: no peeling was observed in the case of MnO_2-CNT-sponge (Figure 2.38c), while significant peeling was observed in the case of the rigid Pt foil (Figure 2.38d). Another result that demonstrates the superior electrochemical performance of the MnO_2-CNT-sponge electrodes is comparing its cyclic voltammetry behavior to the flat MnO_2-Pt substrate. A three-electrode configuration has been setup to test the electrochemical performances by cyclic voltammogram. At scan rate of 50 mV/s (Figure 2.38f), the electrochemical performance of MnO_2-CNT-sponge outperforms that of MnO_2-Pt electrode in terms of wider voltage range and higher capacitance. At a 5 min electrodeposition of MnO_2, a specific capacitance of 1230 F/g based on MnO_2 mass can be achieved from MnO_2-CNT-sponge electrode at scan rate of 1 mV/s. However, the value is just 155 F/g for MnO_2-Pt electrode under the same condition (Figure 2.38g). This controlled experiment further confirms the outstanding electrochemical performance of MnO_2-CNT-sponge electrode.

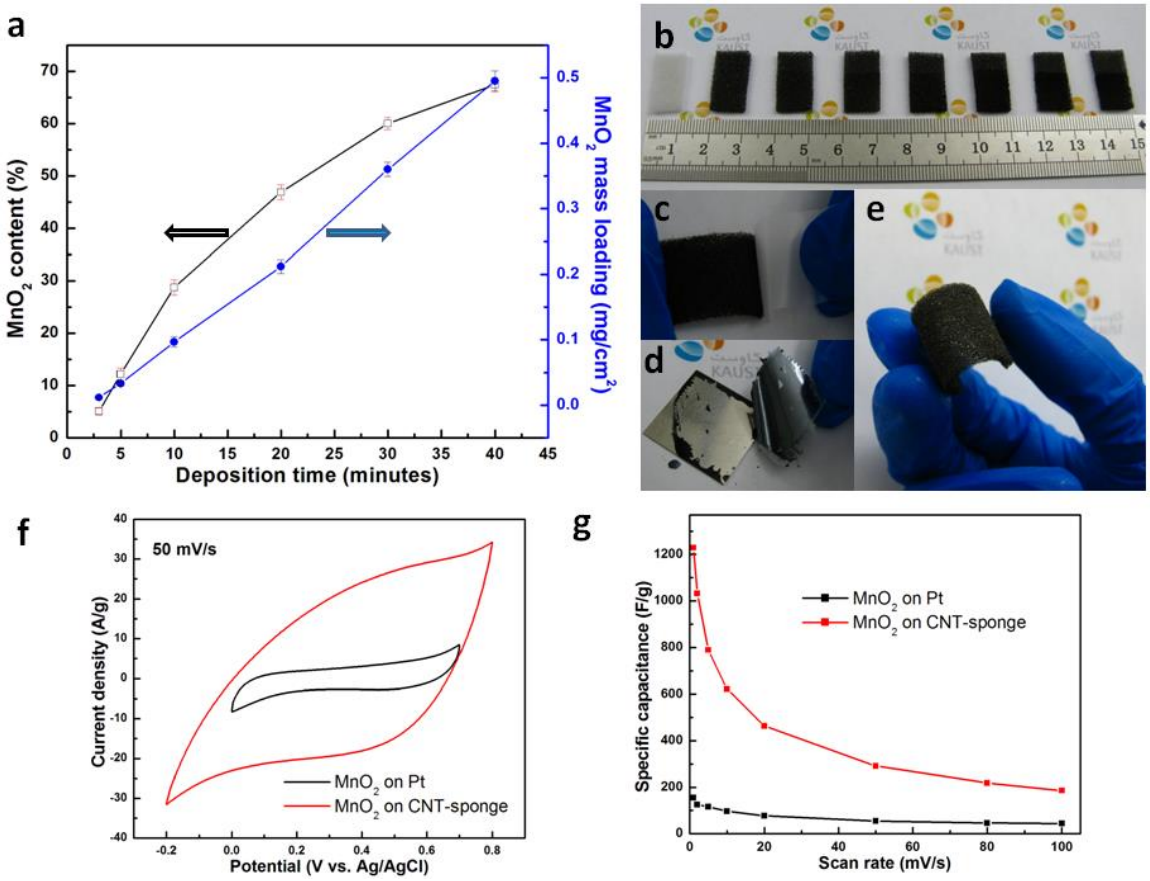

Figure 0.38: MnO_2-CNT-sponge supercapacitor electrodes: (a) MnO_2 content and mass loading *vs* elctrodeposition time from 3 to 40 min; (b) photograph of MnO_2-CNT-sponge electrodes array, the samples from left to right are corresponding to bare sponge, CNT-sponge, MnO_2 deposition on CNT-sponge for 3, 5, 10, 20, 30 and 40 min; (c and d) photograph of Scotch tape tests of MnO_2-CNT-sponge and MnO_2-Pt electrode, respectively; (e) photograph of a MnO_2-CNT-sponge electrode; (f) cyclic voltammogram of MnO_2 on Pt *vs* MnO_2 on CNT-sponge at 50 mV/s after 5 min deposition of MnO_2; (g) specific capacitance comparison between MnO_2-Pt and MnO_2-CNT-sponge (all based on the mass of MnO_2).

To completely investigate the electrochemical performances of MnO_2-CNT-sponge supercapacitors, a typical two-electrode configuration has been employed in this work.[29, 145] The MnO_2-CNT-sponge serves as electrode as well as current collector, and the integrated binder-free structure provides highly porous and conductive channels for the full access of electrolyte ions to the active electrode material in supercapacitors. As shown in Figure 2.39a and b, the full cell has been studied by cyclic voltammograms over a wide range of scan rates: from 0.001 to 10 V/s. Take the 5 min MnO_2 deposition sample as an example. The CV shapes are almost rectangular at scan rates below 2 V/s and remain quasi-rectangular at scan rate up to 10 V/s (Figure 2.39b), indicating the excellent charge storage characteristics and ultrafast response of the electrodes. The high scan rate of 10 V/s is 1 to 2 orders of magnitude higher than the rate used in most of the literature for the MnO_2/CNT composite electrodes with aqueous electrolyte.[22, 23, 28, 82, 146] The voltages versus time profiles were obtained by galvanostatic charge-discharge measurements (Figure 2.39c). The device can be steadily operated over a wide range of applied specific current, from 1 to 100 A/g. The internal resistances[29, 147] (including the electrical resistances of electrodes, the ions diffusion resistances and the interfacial resistance between the electrode and electrolyte) derived from the voltage drop are consistent with the values calculated from impedance electrochemical spectroscopy. The cyclic voltammetry response of different samples under different deposition times have been demonstrated in Figure 2.39d and e, at specific scan rate of 20 and 200

mV/s, respectively. The corresponding current increases with MnO_2 content on the electrodes for both scan rates, suggesting that more materials contributed to charge storage. When the scan rate changed from 20 to 200 mV/s, the CV shapes remained nearly rectangular, with only a few deviations for samples with high mass loading. This clearly shows the excellent electrochemical performance of the MnO_2-CNT-sponge supercapacitors. The specific capacitances with respect to the mass of MnO_2 have been derived from CVs and plotted in Figure 2.39f, which are comparable with the values calculated from galvanostatic charge-discharge curves. A specific capacitance of 1000 F/g can be obtained based on the mass of MnO_2 at scan rate of 1 mV/s. The specific capacitances of MnO_2-CNT-sponge supercapacitor are competitive with literature values.[28, 45, 105, 140, 142, 146, 148] The specific capacitance decreases with the scan rates and MnO_2 deposition times, but remains constant at scan rates higher than 100 mV/s. The measured specific capacitance depends strongly on scan rate for low mass loading devices, but depends weakly on scan rate for high mass loading devices. For example, the specific capacitance decreased from 1000 F/g at 1 mV/s to 581 F/g at 100 mV/s for the 3 min electrodeposition device. In comparison, it decreased from 444 F/g at 1 mV/s to 295 F/g at 100 mV/s for the 10 min electrodeposition device. For higher mass loading devices, such as 30 and 40 min MnO_2 depositions, negligible change in specific capacitance was observed, especially at high scan rates. This is mainly due to the limited conductivity of high mass loading samples and the limited utilization of MnO_2 at high scan rates. At

low mass loading of MnO_2, the highly conductive double porous electrodes provide good opportunity for electron transportation and ions accessibility, maximizing the utilization of MnO_2 materials. At even lower deposition time, the theoretical specific capacitance can be possibly achieved in this unique structure.

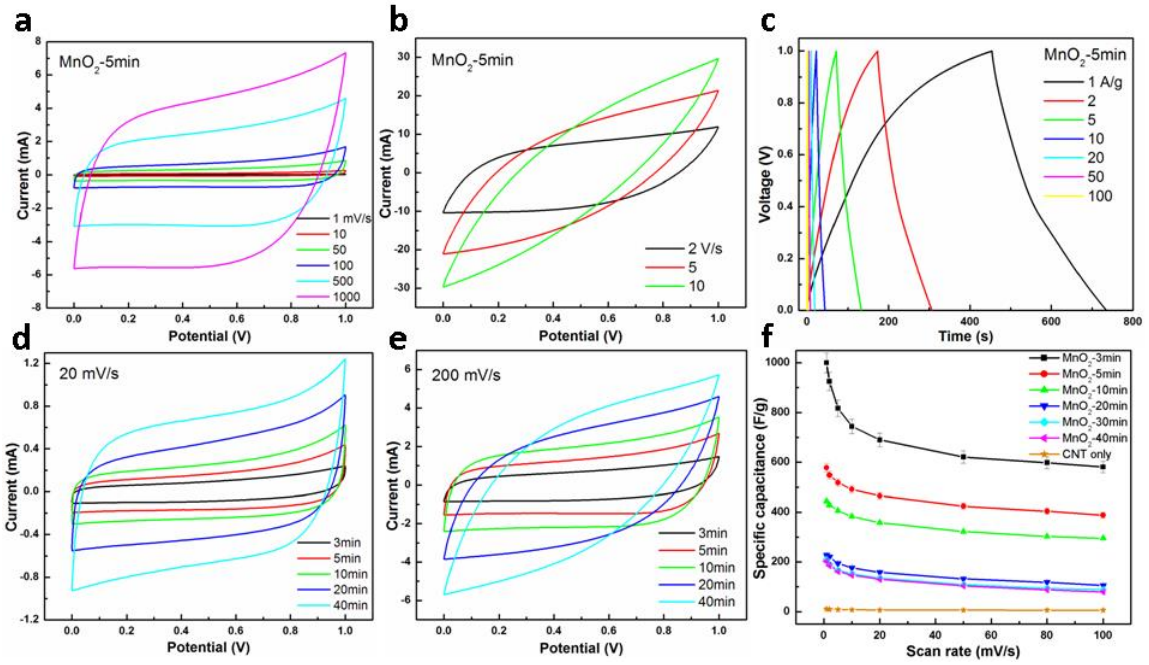

Figure 0.39: Electrochemical performance of MnO_2-CNT-sponge supercapacitors: (a and b) cyclic voltammograms of a 5 min MnO_2 deposition device at low and high scan rates, respectively; (c) galvanostatic charge-discharge of a 5 min MnO_2 deposition device under different current densities: (d and e) cyclic voltammograms of device with different MnO_2 deposition times at scan rate of 20 and 200 mV/s, respectively; (f) specific capacitance *vs* scan rate for devices with different MnO_2 deposition time, ranging from 0 to 40 min. The capacitance

contribution of CNT-sponge has been subtracted from all MnO_2-CNT-sponge devices. All data are taken in a 1 M Na_2SO_4 full cell at room temperature.

Looking into the charge storage mechanisms of MnO_2-CNT-sponge supercapacitors, a possible electrochemical reaction can be proposed as the following:

$$MnO_2 + xH^+ + yNa^+ + (x+y)e^- \text{<---> } MnOOH_xNa_y$$

The energy storage contributions come from both surface adsorption/desorption of electrolyte cations (Na^+) to the surface of CNTs and MnO_2, and the fast, reversible redox reactions by means of intercalation/extraction of protons into/out of MnO_2.[2, 149] The conductive double porous structure facilitates the adsorption/desorption of Na^+ and the transportation of electrons and protons, allowing full access of the electrolyte to electrode materials and maximizing the utilization of MnO_2. Therefore, the cyclic voltammograms exhibit the ideal rectangular shapes and a specific capacitance of 1000 F/g can be obtained based on the mass of MnO_2.

Electrochemical impedance spectroscopy (EIS) and long time cycling stability are two important parameters to determine the performances of supercapacitors. Figure 2.40a and inset show the Nyquist plots in the frequency range from 100 kHz to 0.01 Hz, which can be represented by the equivalent circuit and the corresponding model for ideal supercapacitors, as shown in Figure

2.40b. In the equivalent circuit, a solution resistance (R_S) connects in series with a constant phase element (CPE), and the CPE connects in parallel with the charge transfer resistance (R_{CT}) and pseudo-capacitance (C_P). The solution resistance refers to the resistance from the electrolyte, the CPE accounts for the double-layer capacitance, and the charge transfer resistance (also called Faraday resistance) corresponds to the total resistance at the interface between the electrode and the electrolyte.[132] Experimental results show that R_S is insensitive to the surface condition of the electrode, and it is consistent with a value of around 1.5 Ω for all our devices. However, R_{CT} increases with the mass loading of MnO_2 on the surface of the CNT-sponge, from 4.5 Ω at 3 min MnO_2 electrodeposition to 28 Ω at 40 min deposition (Figure 2.40a). Typically, the Nyquist plot can be divided by the so-called knee frequency into a high frequency semicircle and a low frequency vertical line,[132] as schematically illustrated in Figure 2.40b. The semi-circle intersection with the abscissa depends on the internal resistance and the vertical line implies good capacitive behaviors of supercapacitors. The internal resistances (including R_S, R_{CT} and other resistances) of all samples are consistent with those derived from the voltage drop of charge-discharge curves. This result clearly indicates that the internal resistance increases with the MnO_2 deposition time due to increased mass loading of semiconducting MnO_2, making the MnO_2-CNT-sponge electrode less conductive. A long time charge-discharge cycling up to 100000 cycles has been performed on CNT-sponge devices using a scan rate of 10 V/s. The results,

shown in Figure 2.40c, indicate that 98% of the initial capacitance was retained. In comparison, the cycling stability of MnO_2-CNT-sponge supercapacitors was also investigated up to 10000 charge-discharge cycles using a specific current of 5 A/g. It is seen that 96% of the initial capacitance has been retained after 10000 cycles (Figure 2.40c inset) for the 40 min MnO_2 deposition device. These results demonstrate good stability of both CNT-sponge and MnO_2-CNT-sponge supercapacitors. Figure 2.40d shows a Ragone plot of MnO_2-CNT-sponge supercapacitors. Although it is challenging to compare accurately the performance of all types of supercapacitor due to a large number of variables such as materials mass loadings, charge-discharge rates and testing configurations, the rough comparison can still be made. The Ragone plot shows that the specific energy and specific power values of our sponge supercapacitors are very competitive compared to the ones reported in the literature[10, 146, 148-152], with maximum specific energy of 31 Wh/kg and specific power of 63 kW/kg. All the specific energy and power values were calculated from the galvanostatic charge-discharge curves. These values demonstrate the outstanding capability of CNT-sponge and MnO_2-CNT-sponge supercapacitors as high-power and high-energy storage systems.

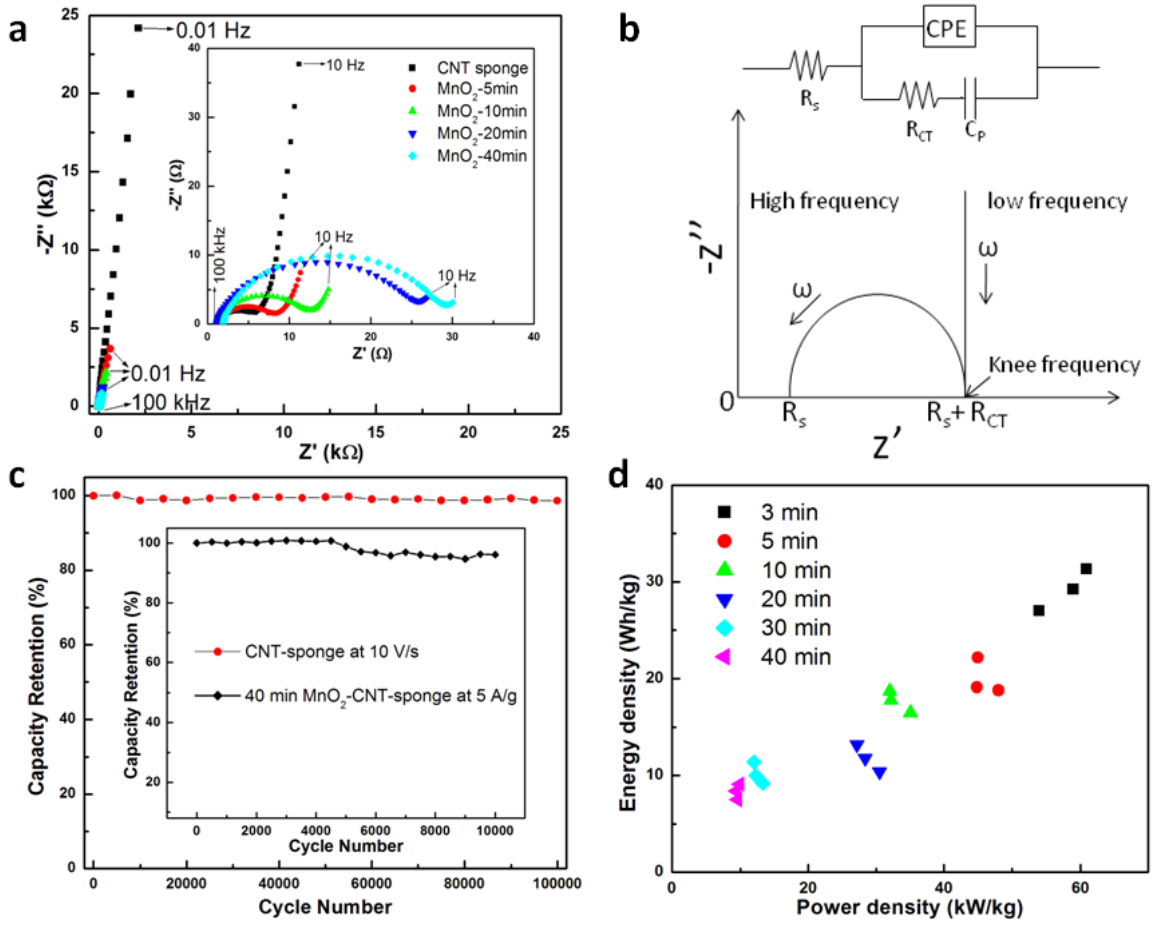

Figure 0.40: Nyquist plot, equivalent circuit model, long time cycling and Ragone plot of MnO_2-CNT-sponge supercapacitors: (a) Nyquist plot of supercapacitor devices with different MnO_2 deposition times, ranging from 0 to 40 min. (b) equivalent circuit model of the device; (c) capacity retention *vs* cycle number for CNT-sponge device up to 100000 cycles at a high scan rate of 10 V/s and 40 min MnO_2-CNT-sponge supercapacitors under 10000 cycles at a specific current of 5 A/g, respectively; (d) Ragone plot of MnO_2-CNT-sponge supercapacitors under different mass loadings of MnO_2.

In summary, novel sponge supercapacitors have been fabricated using a simple method while providing remarkable performance. The macroporous nature of the sponge along with the porous nature of the electrodeposited MnO_2 nanoparticles provided a double porous electrode structure giving good conductivity and full accessibility of electrolyte to MnO_2, improving the performances of MnO_2-CNT-sponge supercapacitors dramatically. The MnO_2-CNT-sponge supercapacitor exhibits high specific capacitance, ultrafast charge-discharge rate, excellent cycling stability as well as good energy and power density, making it a promising electrode for high-performance large-scale energy storage systems.

2.4 Conclusions

In this chapter, we have explored MnO_2 based nanomaterials and nanostructures as supercapacitor electrodes for energy storage applications. We focused on studying the MnO_2 and its nanocomposites, including binary systems of MnO_2-CNC and MnO_2-graphene, ternary system of MnO_2-CNT-graphene, as well as two novel electrodes of MnO_2-CNT-textile and MnO_2-CNT-graphene, as good candidates for high-performance supercapacitors. These studies vary from fundamental understanding of the materials synthesis and rational designs of the structures to the real applications of the device systems will make a huge potential to direct the high-performance supercapacitors in the future.

Chapter 3

MnO_2 as Templates for Conducting Polymers and Activated Nanocarbons

3.1 Conducting Polymers

3.1.1 Introduction of Conducting Polymers

Electrically conducting polymers (ECPs) are referred to a class of organic polymers that conduct electricity. Different from traditional polymers that have low electrical mobility due to the bounded valence electrons in sp^3 hybridized covalent bonds, the ECPs have a conjugated π-system that is formed by the overlap of carbon p_z orbitals. This leads to a contiguous backbone of sp^2 hybridized carbon centers. An unpaired valence electron on each sp^2 center resides in p_z orbitals and forms a bonding π band and corresponding antibonding π* band. When the conducting polymer is properly oxidized, an electron can be removed from this band and the remaining electrons within this partially emptied band become more mobile, and thus conductive. The ECPs store charges by fast doping and dedoping processes.[153] ECPs can be p-doped (an ion insertion process that raises the redox state and electronic conductivity of the polymer) with anions when oxidized and n-doped (adding of an electron to an unfilled band) with cations when reduced, as shown in Figure 3.1. The mainly investigated

conducting polymers as supercapacitor electrode materials are polyaniline (PAni), polypyrrole (PPy), polythiophene (PTh) and derivatives of PTh.

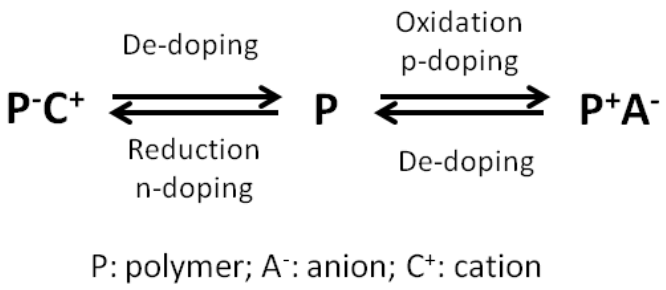

Figure 0.1: The doping and dedoping processes of ECPs.

3.1.2 Polyaniline

PAni, as an electrical conducting polymer, is known to be a good pseudocapacitor material owing to its many promising characteristics, including high doping level, good electrical conductivity (0.1-5 S/cm), low cost, high theoretical capacitance and excellent electrochemical response.[154, 155] Although PAni has a theoretical capacitance of as high as 2000 F/g, this theoretical value is hard to achieve due to the limited reactive sites available in the material that the electrolytes can access.[156] Therefore, a number of studies have been conducted on the preparation of different nanostructured PAni in supercapacitor devices for the improvement of capacitance.[157-160] It was also revealed that the electrochemical performance of PAni is highly dependent upon its shapes when its dimension goes down to nanoscale. However, distinguished from inorganic nanomaterials, it is difficult to manipulate the shapes of nanostructured

conducting polymers. Recently, Park *et al.* reported anisotropic growth of PAni nanostructures with three different morphology (*i.e.* nanospheres, nanorods and nanofibers) and the specific capacitances of the pseudocapacitors based on these PAni are in the order of PAni nanospheres<nanorods<nanofibers.[161] However, the obtained specific capacitance in this report (4~55 F/g for full cells) are much lower than that of most of PAni pseudocapacitors (100~400 F/g for full cells). Thus, it is a good opportunity to develop a robust route to prepare nanostructured PAni with well-controlled morphology and enhanced electrochemical performance for pseudocapacitor energy storage applications.

We proposed a general approach in which oxide templates can be used to create novel morphologies of conducting polymers, and will take an specific example of using MnO_2 as reactive template to produce PAni in this section.[162] Three different morphologies of nanostructured PAni (*i.e.* nanofibers, nanospheres and nanotubes) were synthesized using MnO_2 with tunable morphologies as the reactive templates. MnO_2 was chosen as the reactive template in this study due to its low cost, facile fabrication of a variety of morphologies and easy availability of different crystallographic forms as discussed in the previous chapters.[163] The oxide template-guided PAni have much higher surface area, resulting in much improved capacitance than the PAni without using the template. The growth mechanism of the template-guided PAni with different morphologies was also discussed. Furthermore, the electrochemical properties of nanostructured PAni pseudocapacitors were

investigated and the performance is highly dependent to the morphology of the PAni, highlighting the importance of the morphology controlled process.

The morphology-dependent polyanilines were prepared by a reactive-template technique using different morphologies of MnO_2 as sacrificial templates.[163] Typically, 50 mg of MnO_2 nanospheres or nanotubes were dispersed in 30 mL of water and bath sonicated for 30 min before transferring to ice bath. A solution containing 100 µL of aniline dissolved in 20 mL H_2SO_4 (2.8 mL of concentrated H_2SO_4 in 17.2 mL of water) cooled also in ice bath previously was rapidly poured into the MnO_2 solution under stirring. Subsequently, the mixture was stirred in the ice bath for 6 h, and the resulting product was filtered, washed by water and ethanol for several times. Finally, the product was dried under vacuum at 60 °C for 12 h. The preparation of polyaniline nanofibers was conducted using a method without any templates.[160, 164]

3.1.3 Polyaniline Characterization

Three different morphologies of PAni nanostructures (*i.e.* nanofibers, nanospheres and nanotubes) were prepared by a facile chemical polymerization process. Among them, PAni nanofibers were obtained without any templates while the PAni nanospheres and nanotubes were synthesized using different morphologies of MnO_2 nanostructures as the sacrificial templates.[163, 164] The different morphologies of MnO_2 can be easily tuned by controlling the reaction time in a one-pot hydrothermal reaction as discussed in Chapter 2. The resulting

PAni nanostructures mimic of the starting MnO_2 template, producing various morphologies of PAni. As shown in Figure 3.2, the shapes of PAni nanospheres (Figure 3.2b) or nanotubes (Figure 3.2d) were similar to those of MnO_2 nanospheres (Figure 3.2a) or nanotubes (Figure 3.2c) respectively, indicating the successful preparation of PAni by using MnO_2 as sacrificial templates. The porous structures of MnO_2 nanospheres have been retained well in PAni nanospheres (Figure 3.2b), and the tubular nature of MnO_2 nanotubes have also been kept in PAni nanotubes, as shown in Figure 3.2d. It is noticed that compared to MnO_2 templates, the surface of the PAni became relatively rough, as some particles formed and attached to the surface of PAni nanospheres whereas some nanofibers also formed and mixed with the PAni nanotubes during the preparation of PAni nanotubes. The PAni nanotubes became curved and entangled to each other because of the high flexibility of polymer chains as compared to rigid MnO_2 nanotubes. In contrast, the PAni nanofibers prepared without the MnO_2 templates connect more easily and form dense networks of PAni nanofibers, as indicated by the SEM images in Figure 3.2e and f.

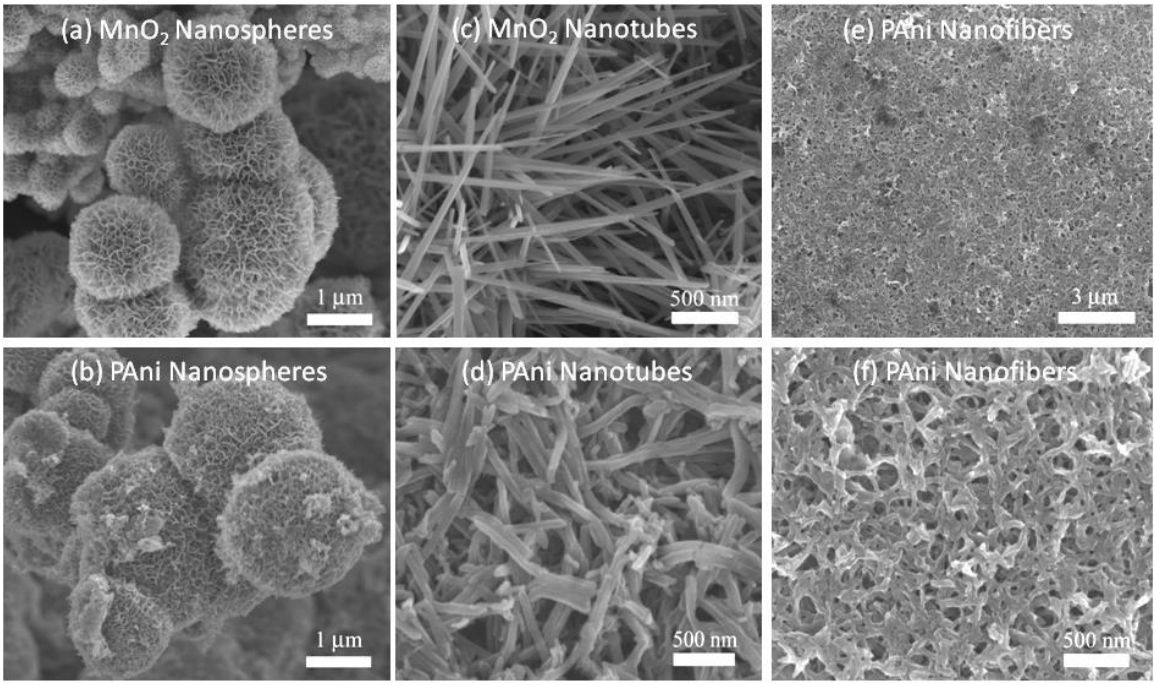

Figure 0.2: SEM images of nanospheres of (a) MnO_2 and (b) PAni, nanotubes of (c) MnO_2 and (d) PAni, and (e) low and (f) high magnification SEM images of PAni nanofibers.

Figure 3.3 shows the TEM images of the three different nanostructured PAni morphologies. Figure 3.3a shows PAni nanosphere with a diameter of 3.5 µm. These spheres are characterized by a porous surface, where multiple PAni nanosheets are stacked as shown in the zoom-in image in Figure 3.3b. Figure 3.3c depicts the typical morphology of the PAni nanotubes. It is worth pointing out that the wall of the nanotube consists of multiple layers, an observation that will be discussed in the next session. As labeled in Figure 3.3c, layer 2 is the original wall derived from the MnO_2 nanotube. Layer 1 (outer layer) and layer 3

(inner layer) are the PAni layers that grow on the surface of the MnO_2 templates outwards and inwards respectively, resulting in larger outer diameter and smaller inner diameter than the MnO_2 templates. Layer 4 is the hollow area of the PAni nanotubes. Figure 3.3d shows the interconnected PAni nanofibers network, corresponding to the SEM image shown in Figure 3.2f.

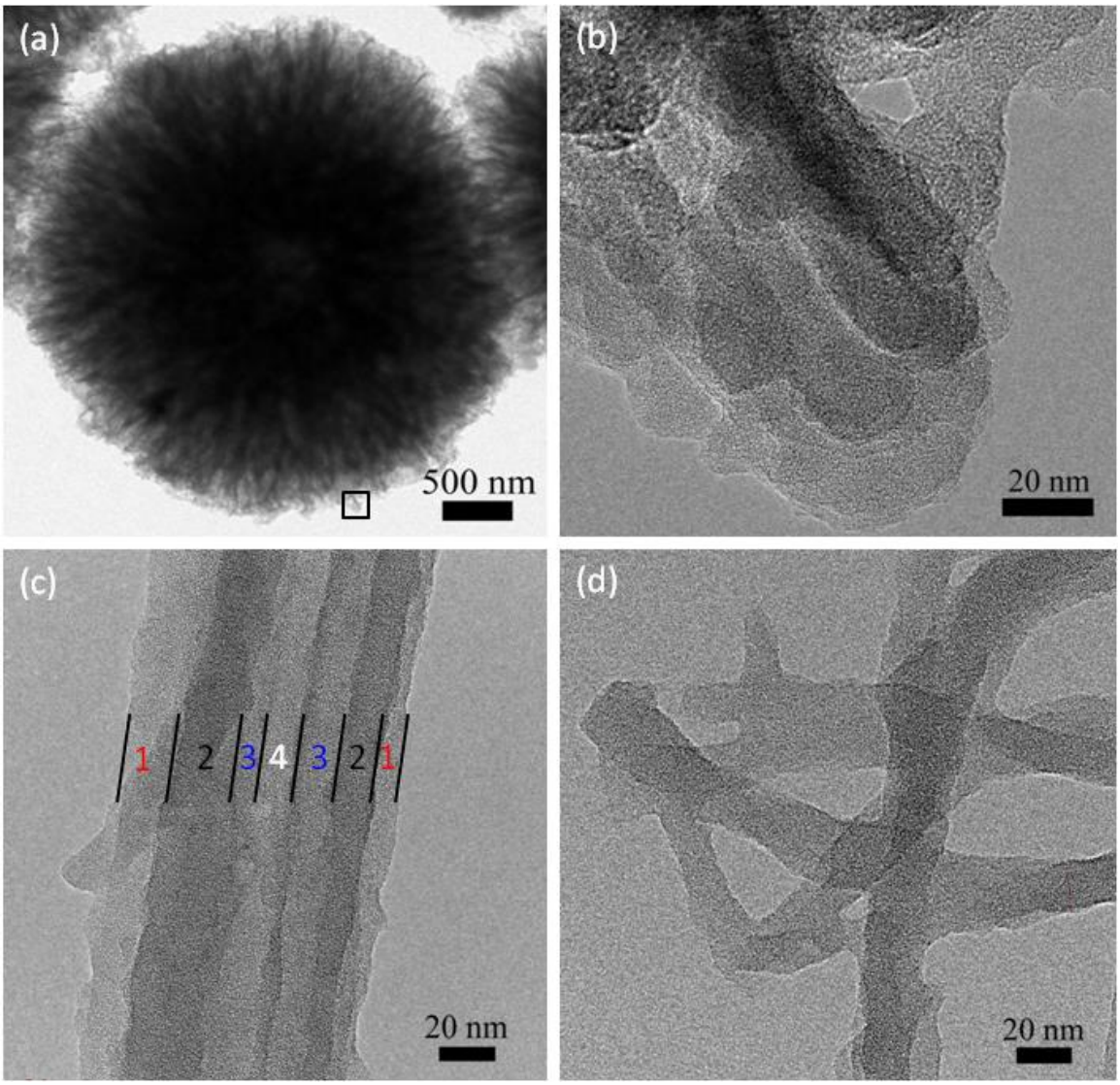

Figure 0.3: TEM images of PAni nanostructures. (a) Low and (b) high magnification TEM images of PAni nanosphere, where (b) is the zoom in image of the rectangular area in (a). (c) TEM of PAni nanotubes, where the wall of the nanotubes contains three layers of PAni, indicated as (1) outer layer, (2) original MnO_2 layer and (3) inner layer, whereas (4) is the hollow area of the nanotubes. (d) TEM of PAni nanofibers.

The energy dispersive X-ray spectroscopy (EDX) of MnO_2 and the resulting PAni nanostructures are shown in Figure 3.4. As a comparison, it is easy to observe that the EDX spectra of PAni nanospheres and nanotubes are very similar (Figure 3.4b and d), which are totally different from that of MnO_2 nanospheres and nanotubes (Figure 3.4a and c). Importantly, the disappearance of Mn peaks in the spectra of PAni confirmed the successful preparation of high purity PAni nanostructures using MnO_2 as sacrificial templates. The carbon and nitrogen peaks in the EDX spectra of polyaniline originate from the polyaniline backbones, whereas the peak of sulfur comes from the sulfuric acid used in the preparation of polyanilines, indicating the resulting PAni nanostructures are H_2SO_4 doped PAni.

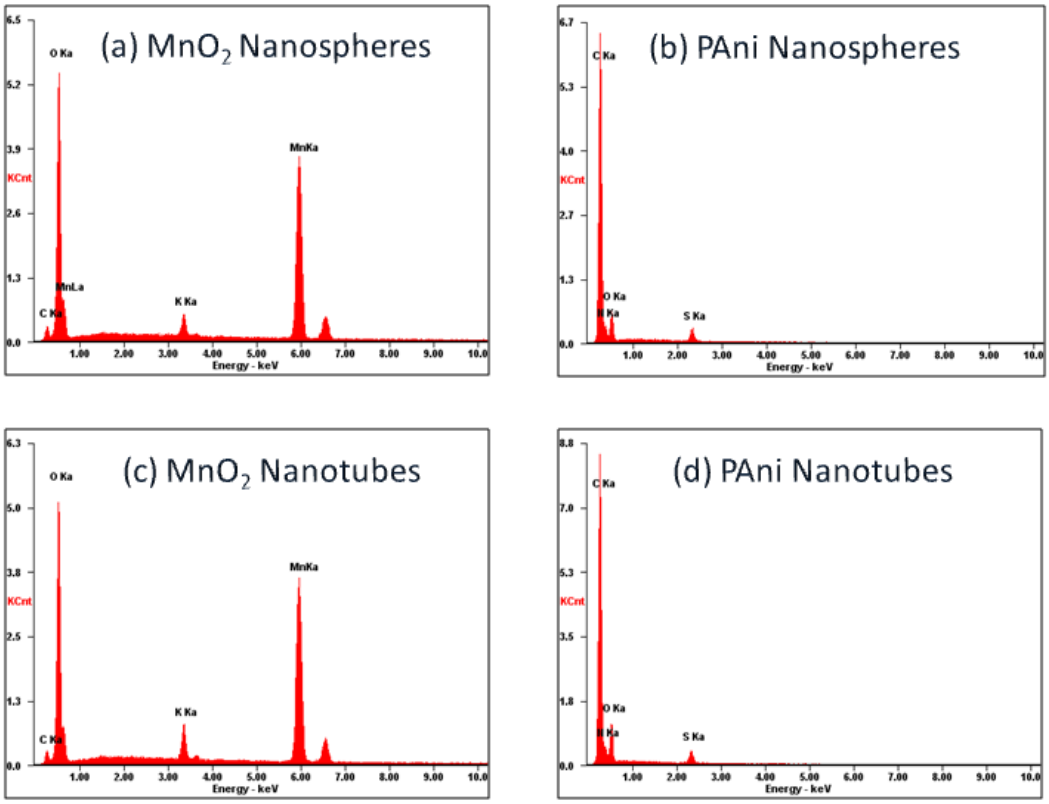

Figure 0.4: SEM-EDX of (a) MnO_2 nanospheres, (c) MnO_2 nanotubes, and (b) PAni nanospheres and (d) PAni nanotubes.

XRD and Raman analyses were carried out to further characterize the PAni nanostructures. As shown in Figure 3.5a, the XRD patterns of the three PAni nanostructures display typical emeraldine salt forms of amorphous PAni, which agrees well with the reported literature.[163, 165] Compared to PAni nanofibers, the XRD peaks of PAni nanospheres shifted to lower angles, which may be related to the conductivity of the PAni nanospheres.[166] Moreover, the intensity of the peaks at around 16° and 20° for PAni nanospheres are higher than that of PAni

nanofibers, suggesting the appearance of a relatively ordered structure and the decrease of the polymer chain distance.[167] This is due to the ordered pore structure in PAni nanospheres as shown in their SEM image (Figure 3.5b) and TEM image (Figure 3.4a). In contrast, the intensity of the peaks centered at around 16° and 20° for PAni nanotubes are lower than that of PAni nanofibers, indicating the decrease of the ordered structure and the increase of the distance in the polymer chains.[167] The Raman spectra show very similar characteristic peaks for the three different morphologies of PAni nanostructures, which also agree with the PAni prepared by chemical polymerization in the reported study (Figure 3.5b).[168] For example, the bands at 1165 cm^{-1} can be assigned to C-H bending of the benzenoid ring.[168] The band located at 1218 cm^{-1} is attributed to C-N stretching mode of the single bonds.[169] The band at 1335 cm^{-1} corresponds to the semiquinone radical structure of the PAni.[170] The band situated at 1471-1505 cm^{-1} corresponds to C=N stretching mode of the quinoid units, and the one at 1593 cm^{-1} is contributed to C=C stretching of the quinoid ring.[168]

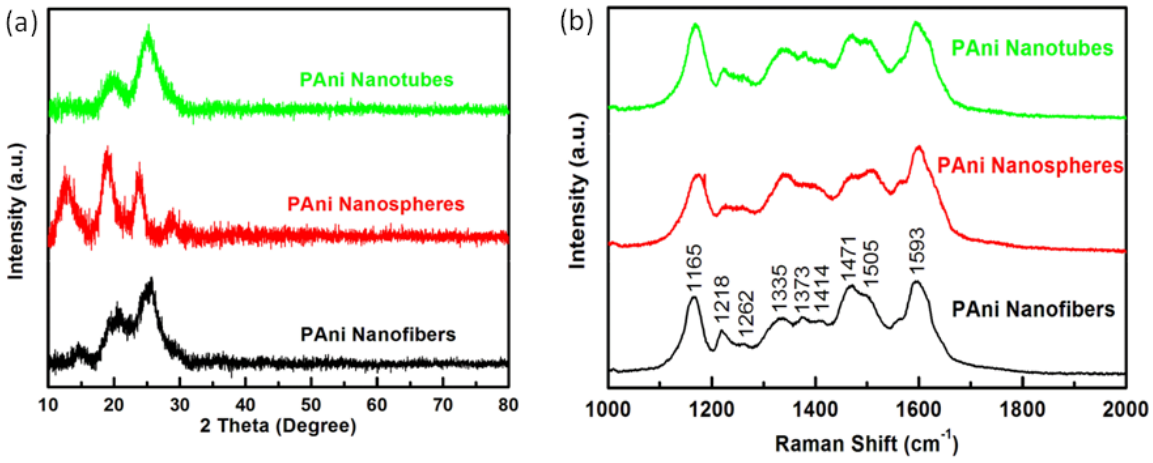

Figure 0.5: (a) XRD patterns and (b) Raman spectra of PAni nanostructures, respectively.

We further conducted nitrogen adsorption-desorption analysis to demonstrate the increased surface area of PAni nanospheres and nanotubes compared to the PAni nanofibers. As shown in Figure 3.6a, the BET surface areas of PAni nanosphere (67.9 m^2/g) and PAni nanotubes (77.1 m^2/g) are much higher than that of PAni nanofibers (30.9 m^2/g), highlighting the advantages of the PAni nanomaterials prepared by the MnO_2 sacrificial templates. The much increased surface areas of our PAni nanospeheres and nanotubes are attributed from their porous nature and the values are among the highest reported to date for PAni nanostructures by chemical methods. For example, Huang *et al.* prepared different acids doped PAni nanofibers by interfacial polymerization method, and the obtained surface areas ranged from 37.2 m^2/g to 54.6 m^2/g.[171] Qin *et al.* synthesized PAni naoparticles with surface area of 53.1 m^2/g.[172] Pan *et al.*

reported PAni hydrogel with surface area of 41.6 m^2/g.[165] The average pore size of PAni nanospheres (11.5 nm) and nanotubes (18 nm) are comparable to that of PAni nanofibers (16.3 nm), which are all much larger than the size of the electrolyte ions used in the supercapacitor fabrication and will allow fast flow of the electrolyte ions into the PAni electrode materials (Figure 3.6b).

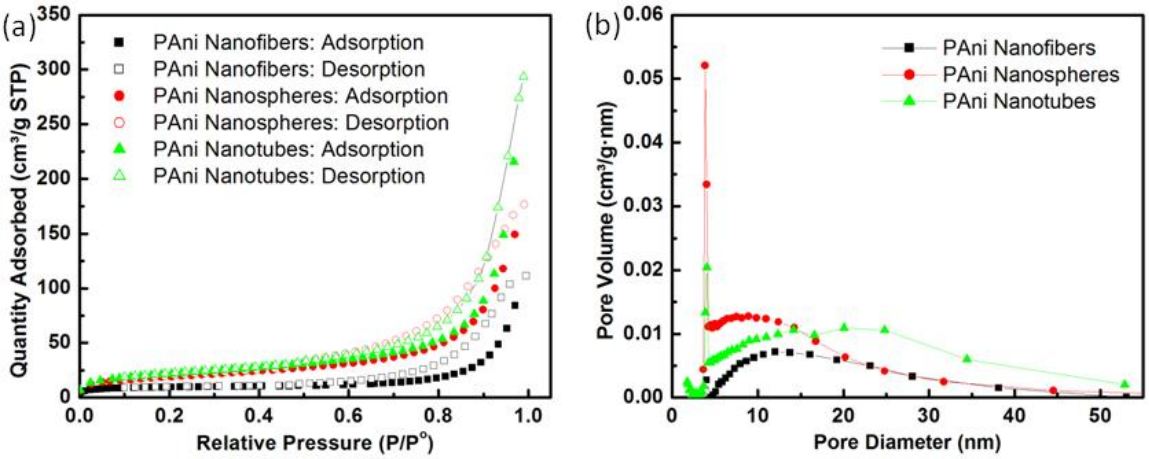

Figure 0.6: (a) BET surface area and (b) pore size distribution of the three different morphologies of PAni nanostructures, respectively.

3.1.4 Growth Mechanism of Polyaniline Nanostructures

The growth mechanism of the two different morphologies of PAni nanostructures (*i.e.* nanospheres and nanotubes) using corresponding morphologies of MnO_2 as the sacrificial templates can be explained as following.[163, 173] MnO_2 was found to be a strong oxidant in acidic medium with an electrochemical potential of 1.23 V according to the half reaction of MnO_2 in acidic conditions[173]:

$$MnO_2 + 4H^+ + 2e \rightarrow Mn^{2+} + 2H_2O \ (E^0 = 1.23\ V)$$

Because of the higher potential of MnO_2 than that of the aniline polymerization (the oxidation potential of dimer aniline is 0.5 V), MnO_2 is able to oxidize aniline and produce polyaniline in acidic environment. As shown in the schematic illustration in Figure 3.7, initially, MnO_2 with different morphologies (nanospheres and nanotubes) are dispersed well in aqueous solution separately (Figure 3.7a). Once aniline in acidic solution is mixed with the MnO_2 templates, the aniline monomers are oxidatively polymerized on the surface of the MnO_2 templates, forming the heterogeneous MnO_2-PAni core-shell structures (Figure 3.7b).[163, 164] The redox reactions are spontaneously accelerated in the heterogeneous systems, leading to further polymerization of aniline at the interface between the MnO_2 and aniline acidic aqueous solution.[173] The MnO_2 templates accept two electrons to be reduced to water-soluble Mn^{2+} ions, while aniline monomers lose electrons to be oxidatively polymerized to PAni. Finally, the redox reactions using different morphologies of MnO_2 as the reactive templates as well as oxidants in acidic conditions result in complete replication of MnO_2 by PAni, forming different morphologies of PAni nanostructures (Figure 3.7c). In the preparation of PAni nanotubes, the redox reactions take place on the exposed surfaces of the MnO_2 nanotubes (both inner and outer surfaces as shown in the zoom-in picture in Figure 3.7b) and form thin films of PAni covering on the both surfaces, which also applied to the synthesis of PAni nanospheres. With the MnO_2 nanotubes

gradually consumed, another layer of PAni can be formed on the original site of the wall of MnO_2 nanotubes (zoom-in part in Figure 3.7c). This leads to the unique PAni nanotube structures with three layers of shell, larger outer diameter, and smaller inner diameter than the MnO_2 nanotube templates as demonstrated in the TEM image (Figure 3.3c).

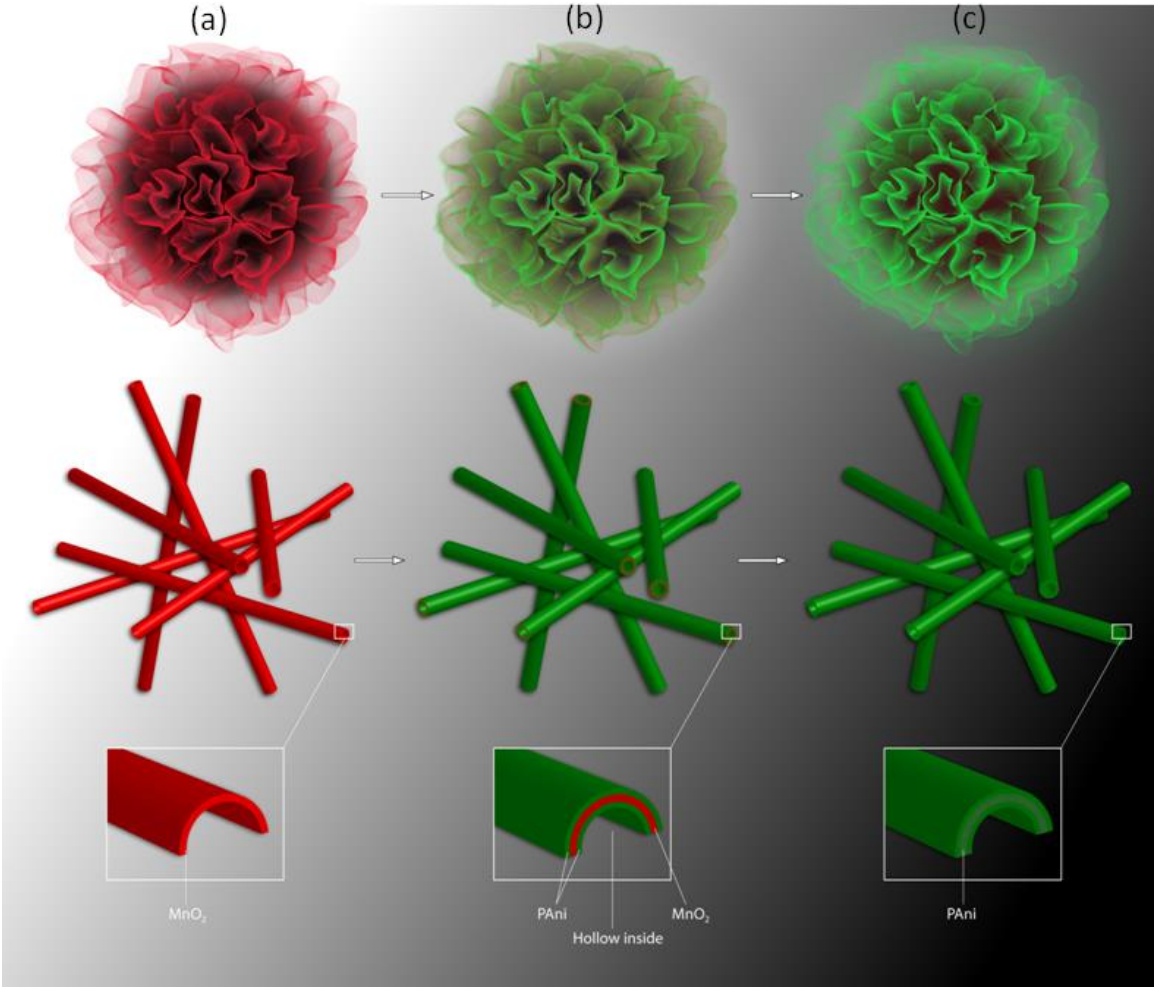

Figure 0.7: Growth mechanism of PAni nanostructures by taking the tunable morphology of MnO_2 as reactive templates. (a) Schematics of MnO_2 nanosphere

and nanotubes, (b) PAni coated MnO_2 hybrid structures, and (c) PAni nanosphere and nanotubes obtained by removing the MnO_2 reactive templates automatically in the aqueous solution.

3.1.5 Electrochemical Performance

The electrochemical properties of the three different morphologies of PAni nanostructures were studied by CV, CD and EIS in classical two-electrode full cell supercapacitors, which consistent with the best practical method for the evaluation of supercapacitor performance.[29] Figure 3.8 shows the CV and corresponding CD curves for the three different of PAni morphologies used as electrode materials in aqueous H_2SO_4 electrolyte. The PAni nanofibers (PAni-NF) based pseudocapacitors show nearly rectangular CV shapes at different scan rates (Figure 3.8a), corresponding to the linearly symmetrical CD curves under different current densities (Figure 3.8b). However, the CV behavior of PAni nanospheres (PAni-NS) based pseudocapacitors deviated from rectangular shape and a pair of typical redox reaction peaks appears in the anodic and cathodic process (Figure 3.8c). The CD curves of the PAni-NS based pseudocapacitors are not as symmetrical as the PAni-NF ones, also indicating the redox reaction peaks in the charge and discharge process (Figure 3.8d). In the case of PAni nanotubes (PAni-NT) based pseudocapacitors, a pair of redox reaction peaks can be found in quasi-rectangular CV curves (Figure 3.8e), making the corresponding CD curves also quasi-symmetrical (Figure 3.8f). The redox peaks are induced by Faradaic transformation of emeraldine-pernigraniline

form of polyaniline during the charge and discharge process of the pseudocapacitors. The intensity of the redox peaks indicates that the electrochemical response of the PAni to the electrolyte. Among the three different morphologies of PAni nanostrucutres, PAni-NT pseudocapacitors exhibit extensive redox peaks than the other two ones, suggesting better electrochemical performance of the PAni-NT pseudocapacitors.

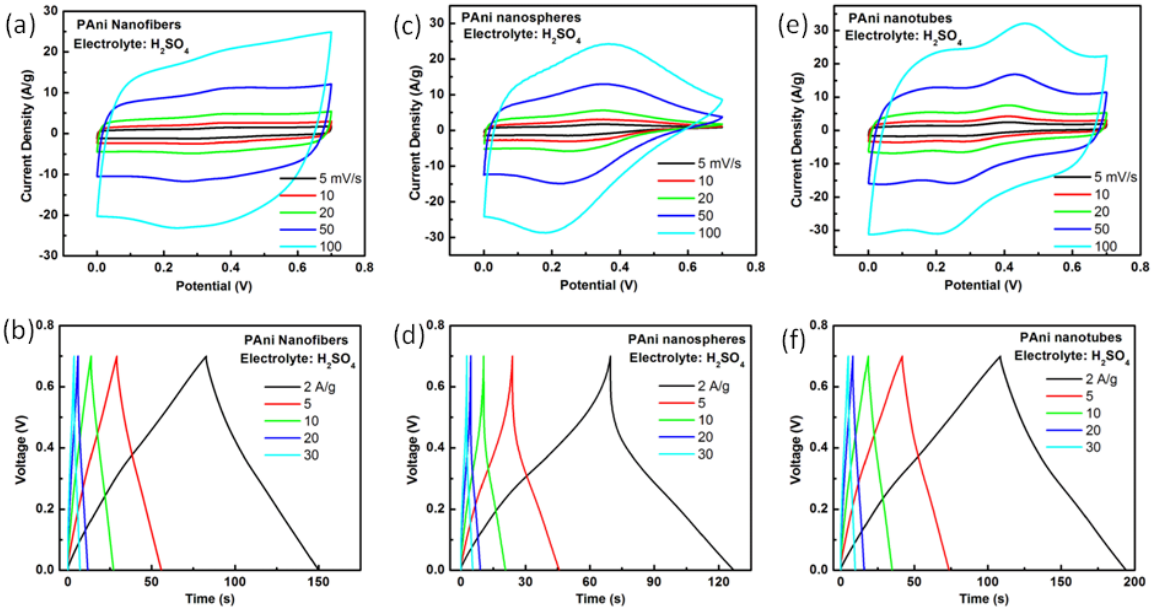

Figure 0.8: Electrochemical performance of three different morphology of PAni nanostructures as pseudocapacitor materials in aqueous H_2SO_4 electrolyte. Cyclic voltammetry and galvanostatic charge-discharge curves of (a, b) PAni nanofibers, (c, d) PAni nanospheres and (e, f) PAni nanotubes, respectively.

The comparison of electrochemical performance of the pseudocapacitors based on the three different morphologies of PAni nanostructures is summarized

in Figure 3.9. At the same scan rate of 50 mV/s, the CVs vary with different PAni morphologies. The integrated area of the CV loops increases in the following order: PAni-NS<PAni-NF<PAni-NT (Figure 3.9a). This agrees well with the behaviors of the CD curves, where the charge and discharge time increases in the same order (Figure 3.9b). The change of the calculated specific capacitance derived from the charge-discharge curves with the current density is summarized in Figure 3.9c. It is found that the specific capacitances of PAni-NT pseudocapacitors are higher than that of the other two morphologies and the capacitance values vary in the order of PAni-NS<PAni-NF<PAni-NT, confirming the behaviors of the CV and CD. For example, at the same current density of 10 A/g, the specific capacitance for PAni-NT based pseudocapacitors (477 F/g) is higher than that of PAni-NS based pseudocapacitors (315 F/g) and PAni-NF based pseudocapacitors (385 F/g). The highest specific capacitance obtained at low current density of 1 A/g is 502 F/g for the PAni-NT pseudocapacitors, 345 F/g for PAni-NS pseudocapacitors, and 404 F/g for PAni-NF pseudocapacitors. The enhancement of specific capacitance of PAni pseudocapacitors based on different morphology is as high as 51% (comparison of PAni-NT *vs.* PAni-NS at current density of 10 A/g). This finding suggests that the electrochemical performance of PAni pseudocapacitors is highly morphology dependent and it is crucial to optimize the morphology of PAni for the best performance. It is interesting that although PAni-NS has higher surface area than the PAni-NF, its capacitance is lower. This is probably due to the limited diffusion and

transportation of the electrolyte ions to the entire parts of the big PAni spherical particles, especially their condensed central parts, preventing the full utilization of the inner surface of the PAni spheres. In contrast, the much increased surface area of PAni-NT over PAni-NF contributed largely to their energy storage capacity, as the hollow nanostructures provide more exposed surface for electrochemical reaction to take place. From another point of view, the structure tortuosity (a parameter used to bridge the pore structure and the permeability of the materials) of PAni nanostructures varies with their morphology, porosity, pore size and its distribution, which may also have effect on the electrochemical performance of the PAni pseudocapacitors. The relative high tortuosity of PAni-NS makes the electrolyte ions difficult to diffuse to the whole particles, resulting in modest electrochemical response and capacitance values. While the lower structure tortuosity of PAni-NF and NT contributes to easier and faster access of electrolyte ions to the materials, giving better electrochemical response and higher capacitance values. Nevertheless, the specific capacitance values of our PAni-based pseudocapacitors are slightly higher than the reported ones (in two-electrode configuration).[161, 174, 175] Ryu *et al.* reported PAni symmetrical supercapacitor with a specific capacitance of 107 F/g.[174] Meng *et al.* reported a flexible and solid-state PAni-carbon nanotube supercapacitor with a high specific capacitance of 360 F/g at 1 A/g.[175] The specific capacitances of the pseudocapacitors based on the anisotropic growth of three different morphologies of polyaniline nanostructures (*i.e.* nanospheres, nanorods and

nanofibers) are in the order of PAni nanospheres<nanorods<nanofibers, agrees with the behavior of our PAni pseudocapacitors. However, the reported specific capacitance in this report (4~55 F/g for full cells) are much lower than that of our PAni pseudocapacitors (300~500 F/g for full cells), demonstrating the superb electrochemical performance of our PAni nanostructures by facile morphology control.[161] The Nyquist plot in Figure 3.9d shows low impedance of the PAni pseudocapacitors (<1 Ω), indicating good electrical conductivity of the devices.

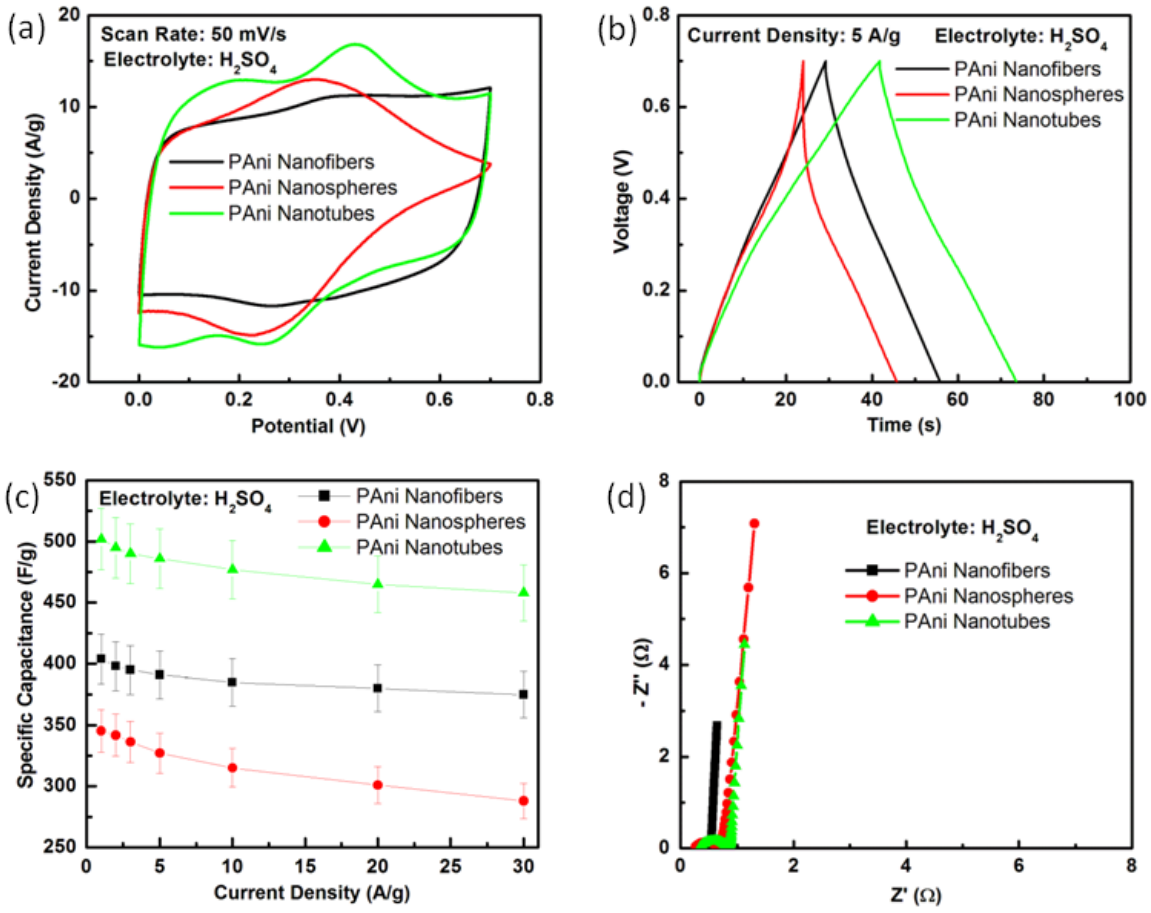

Figure 0.9: Comparison of electrochemical performance of three different morphologies of PAni nanostructures as pseudocapacitor materials in aqueous H_2SO_4 electrolyte. (a) Cyclic voltammetry at scan rate of 50 mV/s; (b) galvanostatic charge-discharge at current density of 5 A/g; (c) specific capacitance vs. current density; and (d) electrochemical impedance spectroscopy.

As an important parameter to determine the overall performance of supercapacitors, the long term cycling of our pseudocapacitors with the three

different morphologies of PAni have been tested and presented in Figure 3.10. It shows gradual degradation of the capacitance with the cycle number. However, the overall capacitance of PAni-NT cell is higher than the other two, when tested under the same current density of 10 A/g. Even after 5000 cycles, the specific capacitance value of PAni-NT cell is still as high as 314 F/g, much higher than the PAni-NS cell (182 F/g) and PAni-NF one (234 F/g). This further demonstrated the advantages of the PAni-NT and the morphologies dependent electrochemical properties of PAni nanostructures.

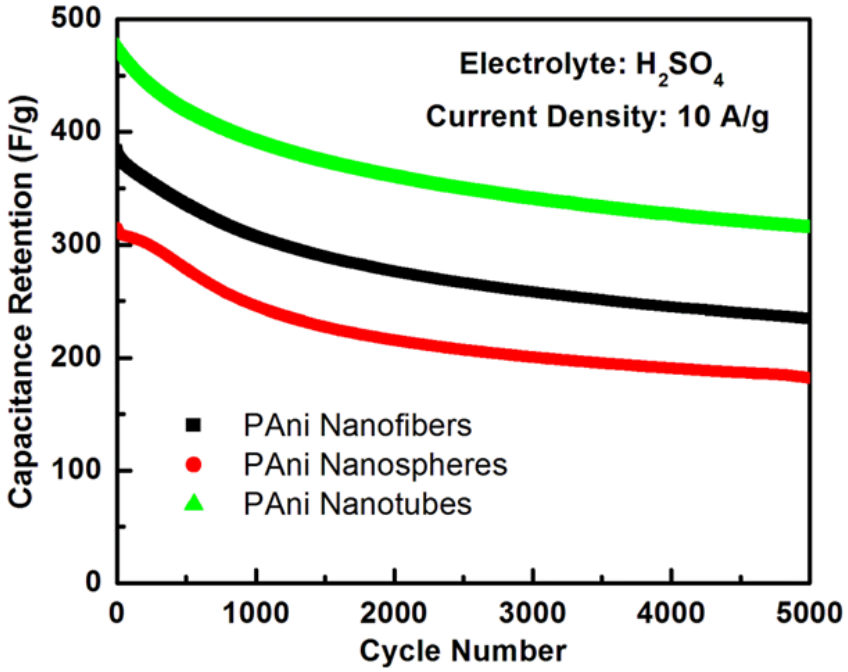

Figure 0.10: Cycling performance of three different morphologies of PAni nanostructures as pseudocapacitor materials in aqueous H_2SO_4 electrolyte with current density of 10 A/g.

3.2 Activated Nanocarbons

3.2.1 Introduction

To date, carbon based materials are dominant in the commercial available supercapacitors.[176] The electrical charges in the supercapacitors are stored electrostatically by the formation of electrochemical double layers on the interfaces of the carbon based electrode materials and the electrolytes.[177] The supercapacitor energy storage capacity is largely determined by the capability of

the electrolyte ion adsorption and desorption with the high surface area carbon materials. Different forms of carbon materials, such as 1D carbon nanotubes, 2D graphene nanosheets, 3D carbon aerogels are all investigated as efficient materials for supercapacitors.[7, 118, 178-181] Unfortunately, the preparation processes of some of those nanocarbons are relatively costly due to the specific requirements of the instruments and conditions, which largely prevent their widespread applications as materials for low-cost supercapacitors. Activated carbon, however, is the most widely used material for supercapacitors (including the commercial ones).[7, 8] The yield of the activated carbon is usually in the scale of tons in industry.[182] However, the commercial activated carbon materials are typically in the form of big bulks, lacking in flexibility in specific dimensionalities or morphologies. It was demonstrated that the electrochemical performance of the carbon based supercapacitors is strongly related to their dimensionality, morphology, surface area, porosity and heteroatom doping level.[183] Therefore, carbon based materials with desirable morphology and high surface area are preferable for high-performance supercapacitors. Although different forms of nanocarbons are available by some individual preparation processes, it is still a great challenge to prepare activated nanocarbons with controlled dimensionality and morphology in a systematical route.

We demonstrate in this section a facile carbonization and activation process toward the preparation of porous activated nanocarbons with well controlled dimensionality and morphology, including 0D activated carbon

nanoparticles (A-CNP), 1D activated carbon nanotubes (A-CNT) and 2D activated carbon nanosheets (A-CNS). The resulting functionalized nanocarbons with large surface areas (1332 m^2 g^{-1} – 2005 m^2 g^{-1} depending on the specific morphology), good electrical conductivity, and highly porous nanoarchitectures were applied as supercapacitor materials with excellent electrochemical performance. The supercapacitors with the three different nanocarbons showed morphology dependent electrochemical performance. Among them, the A-CNT based supercapacitors showed the best electrochemical performance due to their higher surface area, opened porous structures and better electrical conductivity. The porous nanocarbons based supercapacitors present high specific capacitances, excellent rate capability, and superior long-term cycling stability in both aqueous and ionic liquid electrolytes. A very high energy density of 50.5 Wh kg^{-1} with power density of 17.4 kW kg^{-1} can be obtained from A-CNT based supercapacitors in ionic liquid electrolyte (with charge time of ~ 10 s), making the nanocarbons very promising for high-performance energy storage devices.

3.2.2 The Preparation of Three Different Nanocarbons

Figure 3.11 shows the process flow used to prepare the nanocarbons directly derived from polyaniline nanostructures by the carbonization and activation process. Although Figure 3.11 only shows two types of structures, all the three structures (A-CNP, A-CNS, and A-CNT) were prepared using the same process. The starting polyaniline nanostructures with different morphologies were

obtained by a one-step chemical polymerization process using tunable morphologies of MnO_2 as reactive templates as was described in the previous section.[162] Among them, A-CNP is derived from polyaniline nanofibers, while A-CNS and A-CNT are derived respectively from polyaniline nanosheets and nanotubes (Figure 3.11). The one-step chemical polymerization process carried out using metal oxides as reactive templates provides a general approach to prepare conducting polymer nanostructures with different morphologies. Moreover, the subsequent carbonization and KOH activation process produces different nanocarbons with well-controlled morphologies.[162] Meanwhile, the KOH activation process produces many nanopores on the activated nanocarbons surface, as shown in the zoom in images in Figure 3.11. It will be shown that these activated nanocarbons with increased surface areas contributed to the supercapacitors with largely improved energy storage performance.

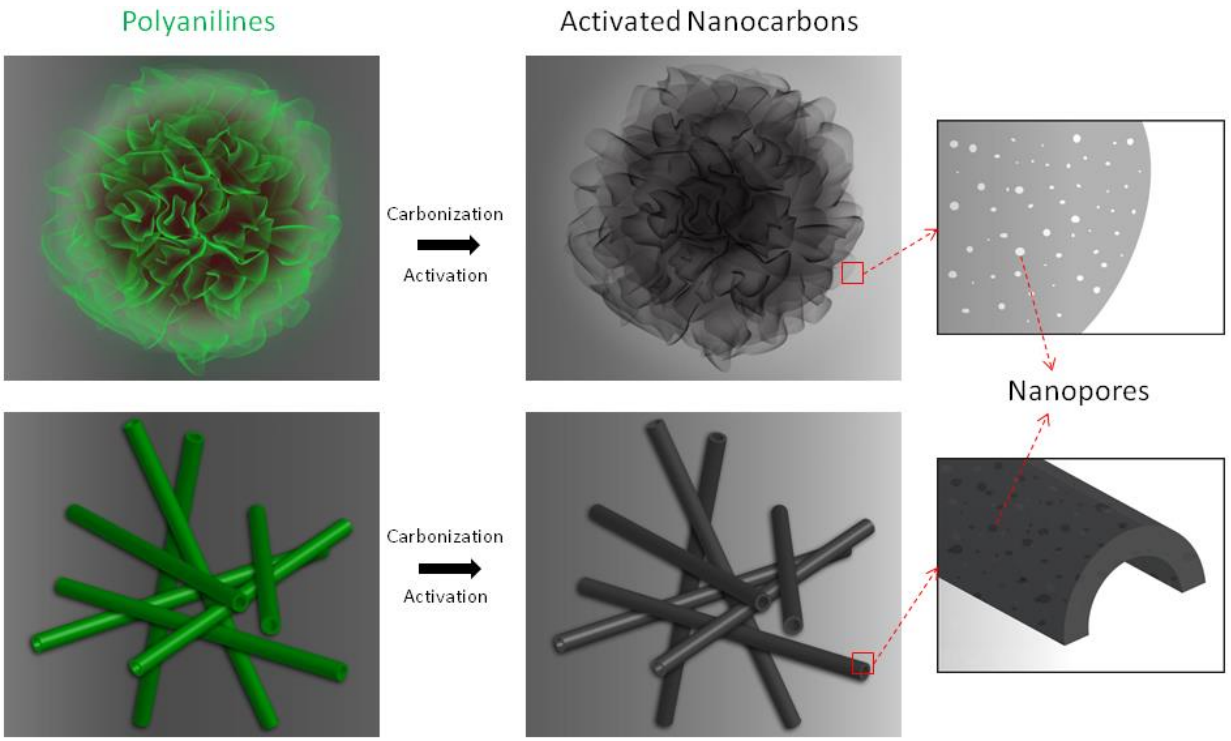

Figure 0.11: Schematic illustration of the preparation of activated nanocarbons derived from polyaniline nanostructures with different morphologies.

3.2.3 Characterization of the Nanocarbons

Figure 3.12 shows the morphological and microstructural features of the as-prepared activated nanocarbons. It can be seen that the high temperature carbonization process does not significantly alter the overall morphology of the starting polyanilines. However, the polyaniline nanofibers underwent high temperature treatment tend to break into some small carbon nanoparticles that aggregated together (not shown here). In contrast, the carbon nanosheets and nanotubes kept their original morphologies well. The KOH activation process has

a great impact on the microstructures of the nanocarbons. For instance, the surface of the activated nanocarbons becomes very rough (Figure 3.12) compared to the relatively smooth surface of the unactivated nanocarbons (not shown here). Furthermore, the activation process makes the nanocarbons highly porous and produces many nanopores on the nanocarbons. It is clearly shown that many nanopores are formed on the A-CNS (inset of Figure 3.12b) and A-CNT (Figure 3.12c).

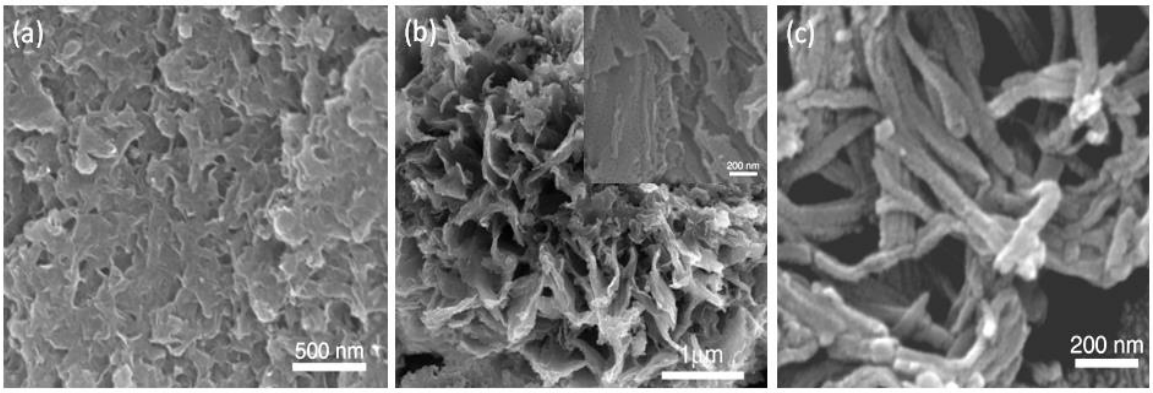

Figure 12: SEM images of the three different activated nanocarbons: (a) activated carbon nanoparticles, (b) activated carbon nanosheets, and (c) activated carbon nanotubes.

The microstructures of the activated nanocarbons were further investigated by TEM. Figure 3.13a shows that the agglomerated A-CNP consists of small nanoparticles with uniform size of about 12-18 nm, and Figure 3.13b shows the porous nature of the A-CNP, where many micropores can be found on its surface. In the structure of the A-CNS, the A-CNS retained the flower-like morphology which is comprised of self-assembled carbon nanosheets (Figure 3.13c). One can easily identify numerous pores on the carbon nanosheets surface as well (Figure 3.13d). The pores on the nanosheets were further characterized that apart from most of the micropores (<2 nm), there are also some mesopores (2-50 nm) formed on the nanosheets. The surface of the A-CNT also became rather rough after activation, but individual nanotubes are separated from each other (Figure 3.13e). HRTEM (Figure 3.13f) also indicates its highly porous feature with many micropores on the nanotube. The introduction of the pores on the carbon materials by the KOH activation is a well-known technique that has been applied to graphene nanosheets, carbon nanotubes, and carbon nanofibers.[14, 184, 185] The activation process introduced pores on the carbon structures and significantly improved the surface area of the carbon materials.

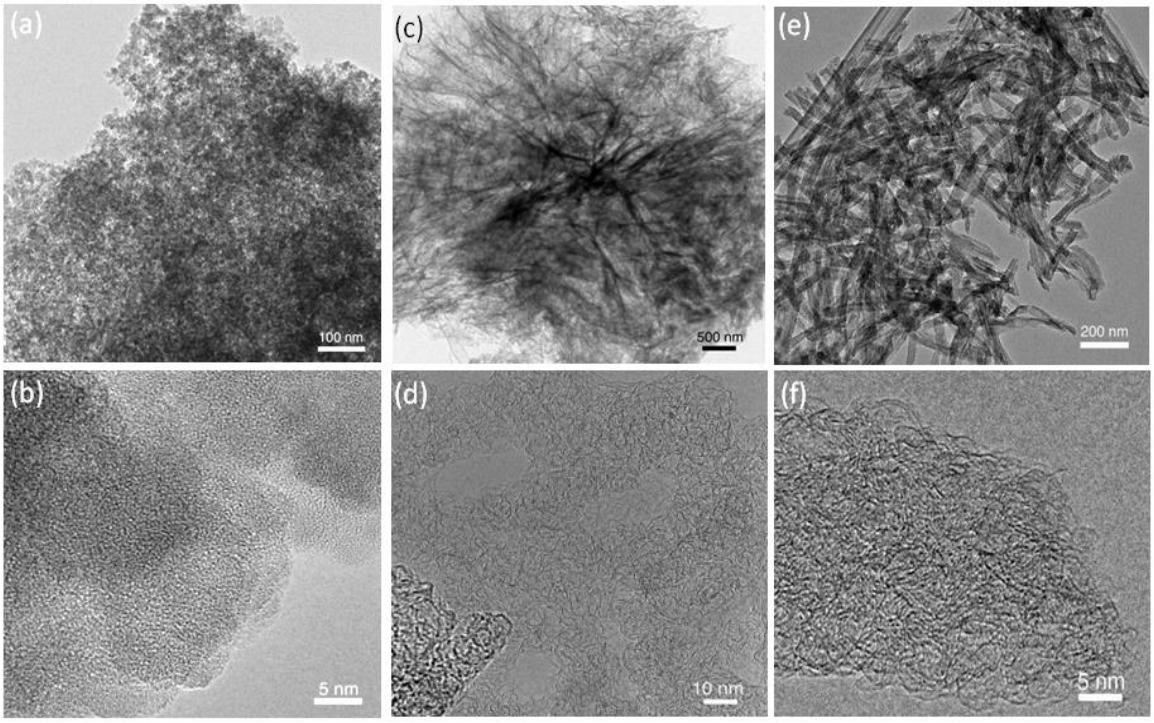

Figure 13: TEM and HRTEM images of the three different activated nanocarbons: (a, b) activated carbon nanoparticles, (c, d) activated carbon nanosheets, and (e, f) activated carbon nanotubes.

XPS was conducted to investigate the functionality of the heteroatoms in the activated nanocarbons. Three major peaks corresponding to C (C 1s), O (O 1s) and N (N 1s) can be clearly seen from the survey spectra (not shown here). However, compared to unactivated carbon nanotubes (CNT), the intensity of N 1s decreased but that of O 1s increased for A-CNT, indicating that the activation had a huge effect on the doped heteroatoms. Specifically, the N/C atomic ratio dropped from 1.6% to 0.1%, while the O/C ratio increased from 3.2% to 6.7%

after activation. As compared to CNT, the predominant C 1s peak of A-CNT shifts slightly to a lower binding energy and its full width at half maximum become narrower, suggesting an increased degree of graphitization in the A-CNT (not shown here).[186, 187] This is further supported by the comparison of the Raman spectroscopy between CNT and A-CNT, where the G band becomes much shaper in the A-CNT and the intensity ratio of the G band to the D band increases from 0.869 (CNT) to 0.893 (A-CNT) after the activation (not shown here). The high resolution C 1s spectrum of CNT and A-CNT (Figure 3.14a) can be fitted with seven components, located at 284.5 eV, 285.2 eV, 285.8 eV, 286.6 eV, 288.0 eV, 289.3 eV, and 290.8 eV corresponding to the C=C (sp^2 hybridized), C–C (sp^3 hybridized), C=N (sp^2 hybridized), C–O–C/C–OH (epoxy and hydroxyl), C=O (carbonyl) and C-N (sp^3 hybridized), O=C–OH (carboxyl) groups, epoxy groups to the π–π* shake-up satellite structure characteristic of conjugated systems respectively.[188-190] The decrease of the percentage of graphitic carbon and nitrogen-containing surface functional groups corresponds to the increase of the oxygen-containing surface functional groups due to the KOH activation, which further indicates the pronounced selective impact of the activation on the functional groups of the nanocarbons. Furthermore, the N 1s high resolution XPS spectrum of CNT and A-CNT (Figure 3.14b) can be fitted using five components that are assigned to pyridinic N (398.1-398.6 eV) N1, nitrile functional group (C≡N) (~399.4 eV) N2 or/and pyrrole-like nitrogen, graphite-like structure (quarternary N) (400.4-400.8 eV) N3, the pyridinic N-oxide

(~402.0 eV) N4 and chemisorbed nitrogen oxide species (404.0 – 406 eV) N5.[191-195] It is noticed that the concentration of pyridinic nitrogen group decreased significantly from 23.2% to 5.3% after activation, while the other nitrogen containing groups increased with different percentages. This is most probably due to the transformation of pyridinic nitrogen atoms into pyrrole-like nitrogen atoms (from 9.8% to 17.7%), graphite-like nitrogen atoms (from 43.7% to 44.3%), pyridinic nitrogen-oxygen atoms (from 11.7% to 19.9%) and chemisorbed nitrogen-oxide atoms (from 11.6% to 12.8%) that caused by the high temperature activation process.[187] The combination of the highly graphitic degree of the activated nanocarbons and the increased percentage of pyrrole-like nitrogen, graphite-like nitrogen, pyridinic nitrogen-oxygen and chemisorbed nitrogen-oxide groups mentioned above are believed to contribute to the significantly increased electrochemical activity of the activated nanocarbons as were also found in previous studies.[186, 187, 196]

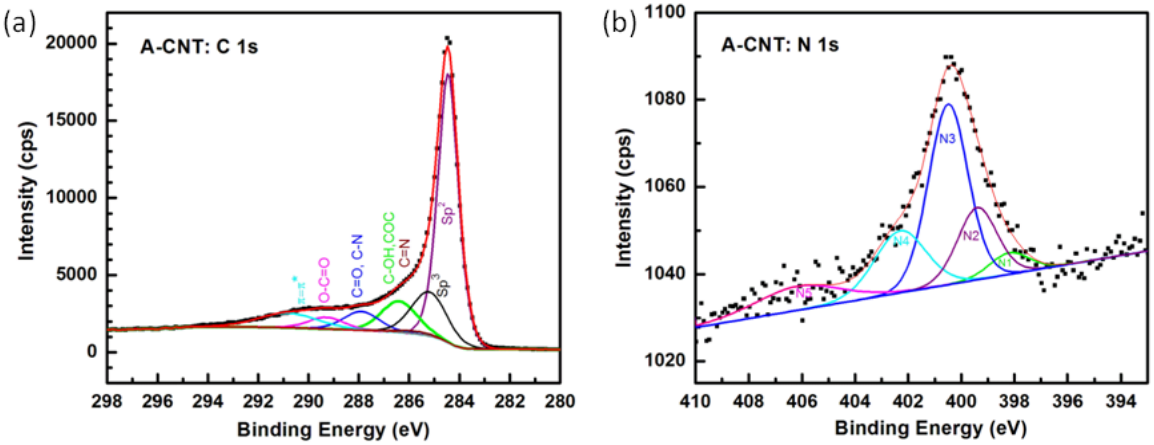

Figure 0.14: XPS curves of A-CNT. High resolution XPS of the deconvoluted (a) C 1s and (b) N 1s peaks.

We further conducted physisorption technique to measure the specific surface area and the pore size distribution of the nanocarbons. Figure 3.15a is the nitrogen adsorption-desorption isotherms of the three different activated nanocarbons. The calculated BET surface area of the activated nanocarbons (A-CNP: 1332.4 $m^2 g^{-1}$; A-CNS: 1957 $m^2 g^{-1}$; A-CNT: 2005.9 $m^2 g^{-1}$) are much higher than that of their unactivated nanocarbon counterparts (Figure S5a, CNP: 17.9 $m^2 g^{-1}$; CNS: 345.8 $m^2 g^{-1}$; CNT: 379.9 $m^2 g^{-1}$), indicating the dramatic enhancement of surface area after activation. The pore size distribution of the activated nanocarbons (Figure 3.15b) shows that the majority of the pores are in the range of micropores, with only a small portion in the range of mesorpores. The micropore area of A-CNT obtained by the t-plot model is as high as 1104.3 $m^2 g^{-1}$, while the value for A-CNS is 687.3 $m^2 g^{-1}$. This agrees with the observation of the pore size by the HRTEM, where some mesopores can be

clearly identified on the A-CNS. However, the pore size distributions of the activated nanocarbons are different from that of the unactivated carbons, where most of the pores of the unactivated nanocarbons are located in the range of mesopores (not shown here). The high surface area and the uniform pore size of our activated nanocarbons are expected to contribute to the enhanced physisportion of the electrolyte ions onto the surface of the materials, and hence increase the energy storage density.

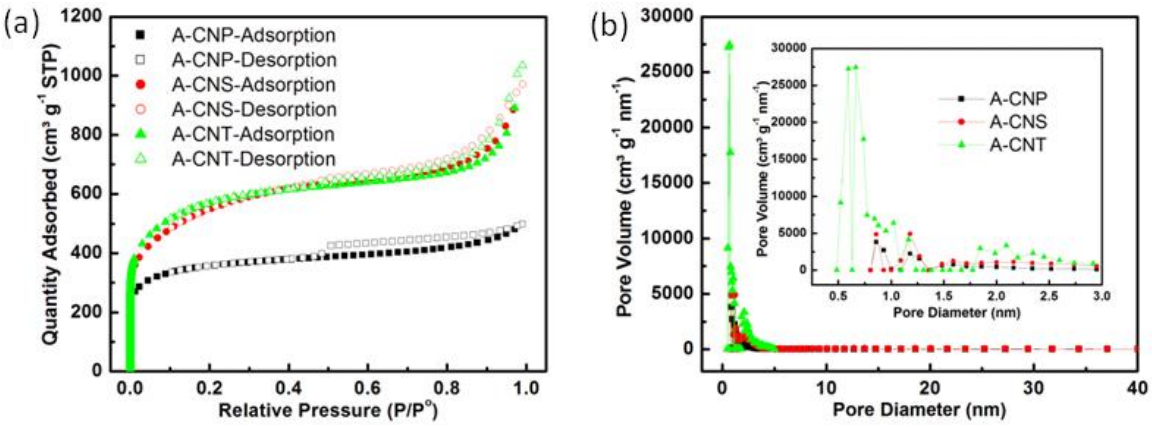

Figure 0.15: (a) Nitrogen adsorption and desorption isotherm and (b) pore size distribution curves of the three different activated nanocarbons: A-CNP, A-CNS, and A-CNT.

3.2.4 Electrochemical Performance of the Nanocarbons in Aqueous Electrolyte

The electrochemical performance of the nanocarbons was firstly studied using three-electrode configuration. We chose to study the A-CNT and CNT as an example to show the different electrochemical behaviors between activated

and unactivated nanocarbons. Figure 3.16a shows a comparison of CD curves between the CNT and A-CNT. It is clearly shown that the electrochemical performance of the A-CNT as supercapacitor electrode material is much better than that of the CNT. This conclusion is supported by the longer charge-discharge period under the same current density (Figure 3.16a). When comparing the electrochemical behaviors of the three different morphologies of activated nanocarbons by CV and CD, we found that the A-CNS and A-CNT have very similar behaviors, which are much better than that of A-CNP. As shown in Figure 3.16b, the CV curves of A-CNS and A-CNT are almost overlapped, but their areas are much larger than that of the A-CNP. Similarly, the charge and discharge process of A-CNT is slightly longer than that of the A-CNS, but both are much longer than that of the A-CNP (Figure 3.16c). These indicate that much higher capacitance can be obtained from A-CNS and A-CNT than that of A-CNP. Figure 3.16d is a summary of the specific capacitance with the change of current density to all the carbon materials. It is found that the specific capacitances of activated carbons are much higher than that of the unactivated carbon counterparts. For example, a high capacitance of 319 F g^{-1} is obtained from the A-CNT based electrode, which is much higher than that of 227 F g^{-1} from the CNT electrode at the same current density of 1 A g^{-1}. The specific capacitance of A-CNT is slightly higher than that of A-CNS (315 F g^{-1} at 1 A g^{-1}), which is consistent with the values of the specific surface area. However, the specific capacitance of A-CNP is much lower than that of the unactivated CNS

and CNT, although its surface area is much higher. This is probably caused by the limited electrolyte diffusion through the highly condensed materials of A-CNP. The high specific capacitances of A-CNT (319 F g^{-1} at 1 A g^{-1}) and A-CNS (315 F g^{-1} at 1 A g^{-1}) are among the best reported values for carbon based supercapacitors, which are higher than that of the reported carbon nanotube (283 F g^{-1}), graphene nanosheets (164 F g^{-1} at 10 mV s^{-1}) and graphene/carbon nanotube hybrid (120 F g^{-1}), but lower than that of the 3D carbon nanotube/graphene sandwich structure (385 F g^{-1} at 10 mV s^{-1}).[119, 197-199] Even at the high current density of 30 A g^{-1}, the specific capacitances are still as high as 154 F g^{-1} for A-CNT and 145 F g^{-1} for A-CNS. The superior electrochemical behaviors of the activated nanocarbons probably benefit from (1) highly activated porous structures, which allow fast diffusion of the electrolyte ions to the whole material surfaces for the formation of electrochemical double layers; (2) excellent electrical conductivity of the activated nanocarbons, which facilitate the fast electron transportation in the electrodes; (3) large surface area and desirable porosity of the activated nanocarbons, which allows the electrolyte ions to be easily adsorbed on the surface of the materials; (4) relatively low level of oxygen doping, which helps in improving the electrochemical activity and the electrode-electrolyte double layer formation.

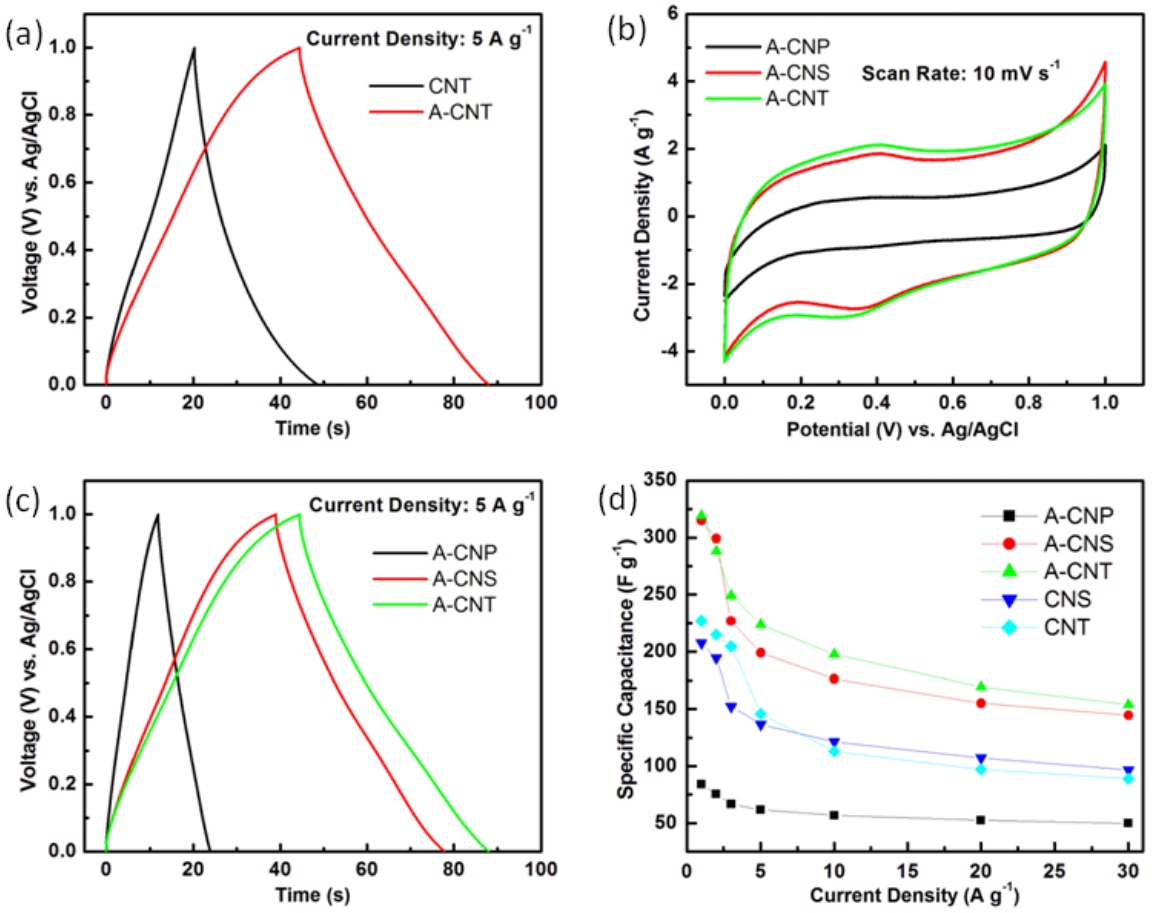

Figure 0.16: Electrochemical performance of the nanocarbons in three-electrode tests in aqueous electrolyte. (a) Comparison of galvanostatic charge-discharge curves between CNT and A-CNT at a current density of 5 A g^{-1}; Comparison of (b) CV at the same scan rate of 10 mV s^{-1} and (c) CD at the same current density of 5 A g^{-1} for the three activated nanocarbons; (d) The change of the specific capacitance with the current density.

We then focused on studying the three activated nanocarbons as active materials in the classical two-electrode configuration, which is considered as the

best practical method to determining the materials' performance for supercapacitor devices.[29] Figure 3.17 shows the CV curves at different scan rates and CD curves at different current densities for all the activated nanocarbons as supercapacitor materials (including A-CNP, A-CNS and A-CNT). The CV curves exhibit ideal rectangular shapes at relatively low scan rates (5-100 mV s^{-1}), and they gradually changed to quasi-rectangular at very high scan rates (1000-2000 mV s^{-1}). The CD curves show perfect symmetrical charge and discharge curves with very small voltage drops even at high current densities. These behaviors indicate excellent electrochemical performance of the activated nanocarbons in the aqueous electrolyte.

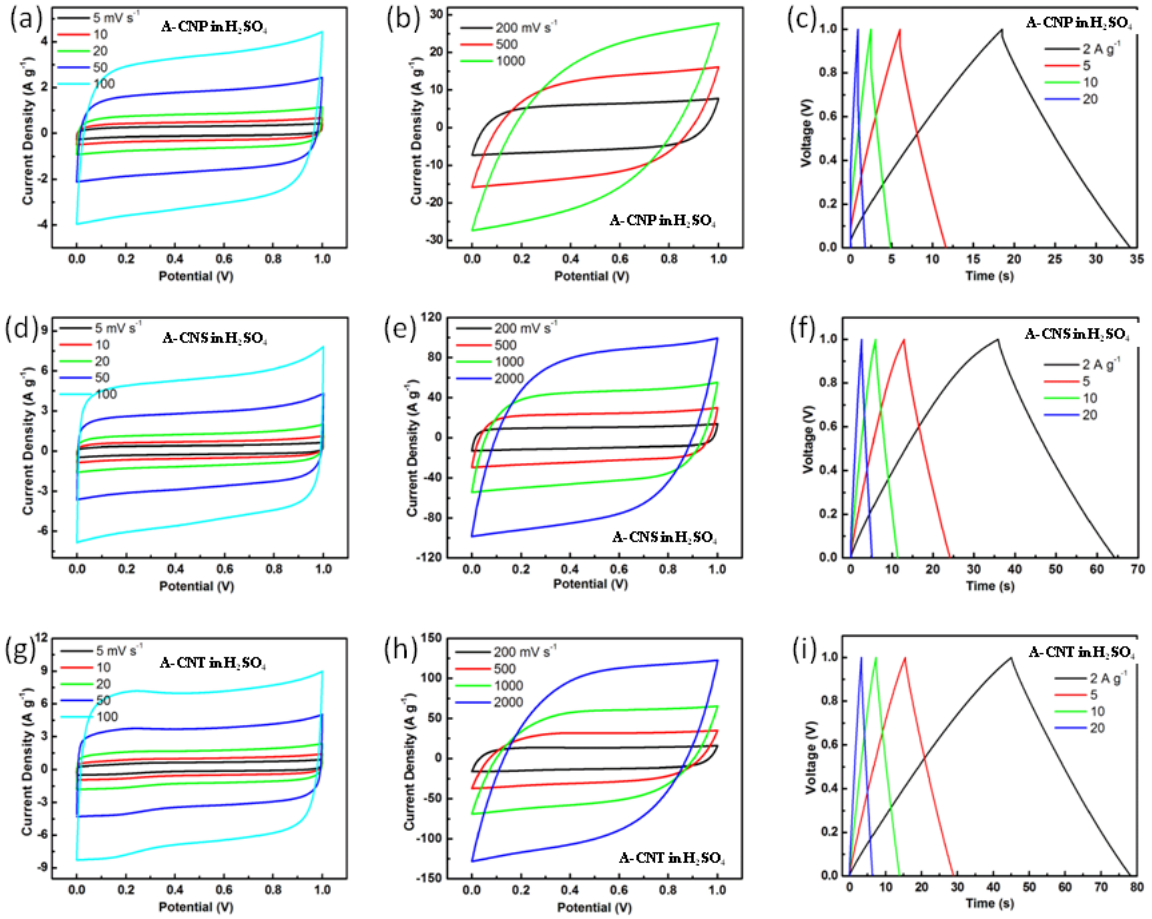

Figure 0.17: Electrochemical performance of the activated nanocarbons in the two-electrode tests in aqueous electrolyte. CV curves at different scan rates and CD curves under different current densities for (a-c) A-CNP, (d-f) A-CNS, and (g-i) A-CNT.

The comparison of the electrochemical properties among the three different nanocarbons reveals that the energy storage capacity is in the order of A-CNP<A-CNS<A-CNT, as demonstrated by the increased CV loop areas at the same scan rate as well as the increased charge-discharge periods at the same

current density (Figure 3.18a). Specifically, the capacitance of the A-CNS is almost doubled that of the A-CNP, while both are lower than the capacitance of A-CNT as shown in Figure 3.18b. The specific capacitance of A-CNT is as high as 145 F g^{-1} at current density of 1 A g^{-1}, higher than 120 F g^{-1} for A-CNS and 65 F g^{-1} for A-CNP at 1 A g^{-1}. Even at a high current density of 30 A g^{-1}, the specific capacitance of A-CNT (125 F g^{-1}) is still higher than that of A-CNS (104 F g^{-1}) and A-CNP (49 F g^{-1}). Moreover, the rate capability of A-CNT (86.2%) and A-CNS (86.6%) is better than that of A-CNP (75.3%), indicating the superior energy storage capacity of A-CNT and A-CNS even within very limited charge times. The electrochemical impedance spectroscopy (EIS) demonstrates the conductivity of the supercapacitor devices. As shown in Figure 3.18c, the EIS of the three nanocarbons shows nearly ideal impedance behaviors of the supercapacitors, highlighting by the small ESR at high frequency range, low charge transfer resistance and the nearly ideal capacitive behaviors demonstrated by the vertical lines at low frequency range. The conductivity of the supercapacitor devices is in the order of A-CNP<A-CNS<A-CNT, indicating by the lower ESR of A-CNT than that of A-CNS and A-CNP (Inset of Figure 3.18c). The high conductivity of the activated nanocarbons will greatly contribute to the electrochemical energy storage capacity of the supercapacitors. As one of the most important parameters to determine the overall performance of the supercapacitors, the electrochemical stability of our activated nanocarbons based devices were cycled at a current density of 10 A g^{-1} for 20000 cycles (Figure 3.18d). It is demonstrated

that our supercapacitors are remarkably stable in the aqueous electrolyte. The A-CNS cell underwent almost no loss on capacitance (retention of 99.8%) even after 20000 fast charge and discharge cycles. Meanwhile, the A-CNT supercapacitor retained 97.1% of its initial capacity, and the A-CNP cell retained 92.6% of the capacity after 20000 cycles. The superb cycling stability further demonstrates the high performance of our supercapacitor devices.

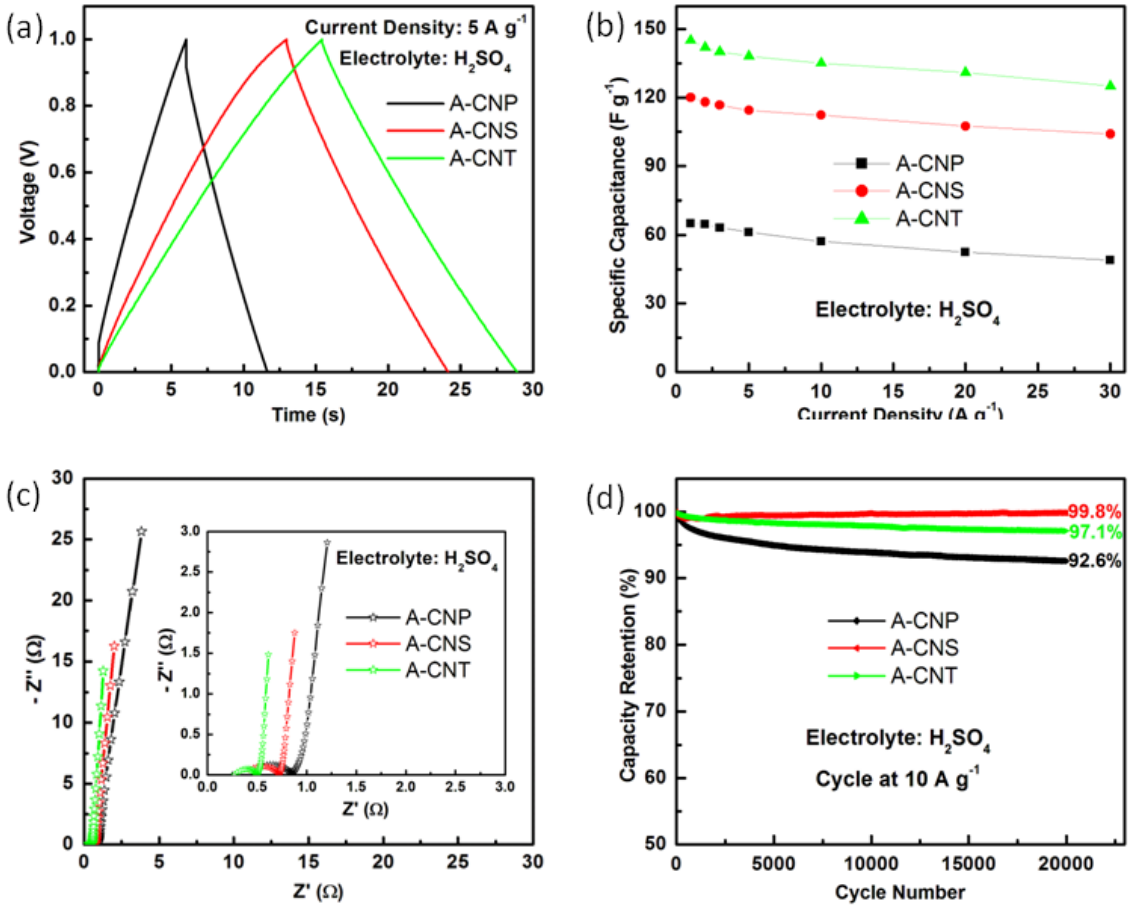

Figure 0.18: Comparison of electrochemical performance of the three activated nanocarbons in two-electrode tests in aqueous electrolyte. (a) CD curves at current density of 5 A g^{-1}; (b) The change of the specific capacitance with the

current density; (c) Electrochemical impedance spectroscopy; (d) Electrochemical cycling stability at current density of 10 A g^{-1} for 20000 cycles.

3.2.5 Electrochemical Performance of the Nanocarbons in Ionic Liquid

The electrochemical voltage window can be increased greatly by using organic or ionic liquid electrolytes. The voltage window increase results in higher energy storage capacity of the devices, as the energy density is proportional to the voltage square ($E=0.5CV^2$).[200] We achieved this by replacing of the aqueous electrolyte with the ion liquid electrolyte in the supercapacitors. 1-Ethyl-3-methylimidazolium tetrafluoroborate ($EMIMBF_4$) was selected as the electrolyte because it is one of the most commonly used ionic liquids for supercapacitors with excellent properties (e.g., low viscosity, high ionic conductivity, and wide working electrochemical window).[201] Compared to a voltage window of 1V in the aqueous electrolyte, the ionic liquid can have a voltage window of 3.5 V. As presented in Figure 3.19, the supercapacitors based on the activated nanocarbons in $EMIMBF_4$ exhibit good electrochemical performance, with rectangular shapes of CV curve over a large range of the scan rates (5-3000 mV s^{-1}) and highly symmetrical charge-discharge curves over different current densities (1-50 A g^{-1}).

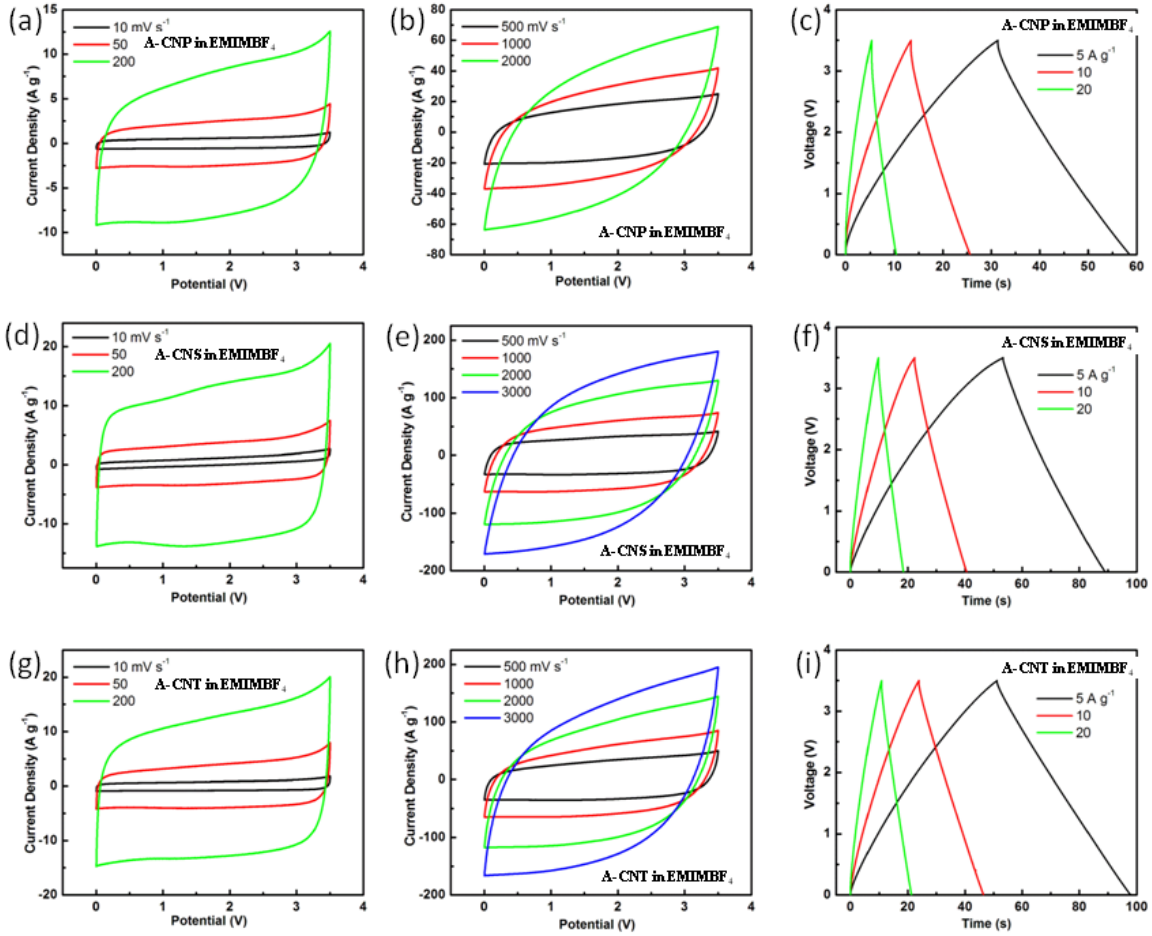

Figure 0.19: Electrochemical performance of the activated nanocarbons in the two-electrode tests in ionic liquid electrolyte. CV curves at different scan rates and CD curves under different current densities for (a-c) A-CNP, (d-f) A-CNS, and (g-i) A-CNT.

When putting together the same electrochemical curves of the three different nanocarbons for comparison, it is found that the electrochemical energy storage capacity is in the order of A-CNP<A-CNS<A-CNT, as revealed by the increased CV areas and longer charge-discharge periods from A-CNP to A-CNS

and then A-CNT (Figure 3.20a). This is consistent with the behavior of the supercapacitors in the aqueous electrolyte. Figure 3.20b is the summary of the specific capacitance at different current densities. It is shown that the specific capacitance of the supercapacitors is in the order of A-CNP<A-CNS<A-CNT, agrees well with the behaviors of the CV and CD. Specifically, the A-CNT based supercapacitor show a high specific capacitance of 140 F g^{-1} at current density of 1 A g^{-1}, much higher than that of the A-CNS based cell (110 F g^{-1} at 1 A g^{-1}) and the A-CNP cell (83.5 F g^{-1} at 1 A g^{-1}). Even at a high current density of 50 A g^{-1}, the specific capacitance of the A-CNT supercapacitor (105.9 F g^{-1} at 1 A g^{-1}) is still much superior to that of the A-CNS cell (95.6 F g^{-1} at 1 A g^{-1}) and the A-CNP cell (44.2 F g^{-1} at 1 A g^{-1}). The high values of the nanocarbons supercapacitors in ionic liquid electrolyte we achieved are among the best capacitances for the carbon based devices, which are higher than that of activated carbon supercapacitor (111 F g^{-1}), multiwalled carbon nanotube supercapacitor (41 F g^{-1}), but lower than the activated graphene reported by Zhu et al. (166 F g^{-1} at 5.7 A g^{-1}).[14, 202, 203] The difference of the capacitance between A-CNT and A-CNS is smaller at higher current density, while the difference between A-CNS and A-CNP becomes larger with the increased current density. This results in better rate capabilities (capacitance ratio of supercapacitor at 50 A g^{-1} to 1 A g^{-1}) of the A-CNS (86.9%) and A-CNT (75.6%) than that of the A-CNP (53%). The EIS in Figure 3.20c shows good conductivity with relatively small resistance, indicating the supercapacitor devices with fast charge rate and excellent power density.

The conductivity values for the three activated nanocarbons based supercapacitors are also in the order of A-CNP<A-CNS<A-CNT, consistent with their electrochemical behaviors.

As two of the most primary parameters to show the energy storage capability of the supercapacitors, the energy and power density of our supercapacitors were included in the Ragone plot (Figure 3.20d). It is clearly seen that the energy and power density of the activated nanocarbons based supercapacitor in ionic liquid electrolyte are much higher than that in the aqueous electrolyte. For example, the energy density of 56.6 Wh kg^{-1} with power density of 4.4 kW kg^{-1} are obtained from A-CNT based supercapacitor in ionic liquid electrolyte, which is higher than that in aqueous electrolyte with energy density of 4.7 Wh kg^{-1} and power density of 1.3 kW kg^{-1}. The supercapacitors also shows the morphology dependent energy storage capacity in the order of A-CNP<A-CNS<A-CNT. In the same ionic liquid electrolyte, the A-CNP based supercapacitors can obtain energy density of 32.8 Wh kg^{-1}, while these values for A-CNS and A-CNT based cells are as high as 44.8 Wh kg^{-1} and 56.6 Wh kg^{-1} respectively. Most importantly, the high energy of 50.5 Wh kg^{-1} and power density of 17.4 kW kg^{-1} (with charge time of 10.5 s) provided by the A-CNT based supercapacitors are among some of the highest reported values for the carbon based supercapacitors.[10, 14, 134, 204-206] It is conclusively demonstrated that our activated nanocarbons are good materials for high performance supercapacitors.

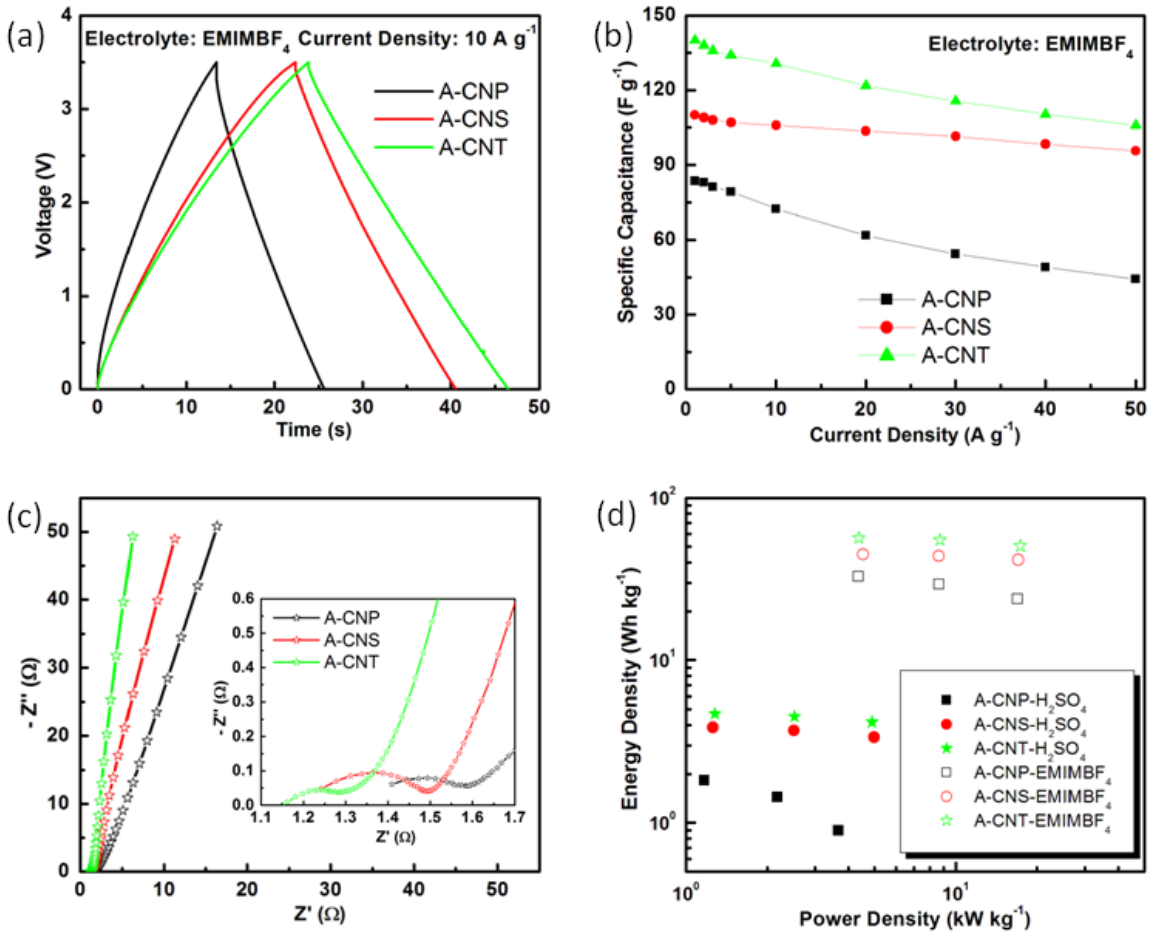

Figure 0.20: Comparison of electrochemical performance of the three activated nanocarbons in two-electrode tests in ionic liquid electrolyte. (a) CD curves at current density of 10 A g^{-1}; (b) The change of the specific capacitance with the current density; (c) Electrochemical impedance spectroscopy; (d) Ragone plot (energy vs. power density) of the nanocarbons in both aqueous and ionic liquid electrolytes.

In summary, we have demonstrated a general chemical route for the preparation of porous activated nanocarbons with controlled dimensionality and morphology for high performance supercapacitor applications. Three different activated nanocarbons (*i.e.* 0D activated carbon nanoparticles, 1D activated carbon nanotubes and 2D activated carbon nanosheets) were derived successfully from different polyaniline nanostructures by a facile carbonization and activation process. The resulting activated nanocarbons with large specific surface area (1332-2005 m^2 g^{-1}), good conductivity, highly porous nanoarchitectures and some levels of heteroatoms doping showed excellent electrochemical performance as electrode materials for supercapacitive energy storage applications. The A-CNT based supercapacitors are capable of delivering a high energy density of 50.5 Wh kg^{-1} and power density of 17.4 kW kg^{-1} with charge time of ~ 10 s, highlighting the good electrochemical performance of these materials as supercapacitor electrodes.

3.3 Summary

In this chapter, we have investigated the use of sacrificial MnO_2 templates to engineer the morphology and nanostructure of the conducting polymers and activated nanocarbons as supercapacitor materials with excellent energy storage performance. The fabrication of different polyaniline and activated carbon nanostructures offers a general chemical route toward the preparation of different

conducting polymers and porous nanocarbons with desirable morphologies, structures and properties. The approaches discussed in this chapter provide a new opportunity for better design of high-performance supercapacitors for energy storage applications.

Chapter 4

Conclusions and Future Work

4.1 Conclusions of the Dissertation

In this dissertation, we have evaluated MnO_2 nanostructured electrodes for supercapacitor energy storage applications. The following results have been obtained.

1. A systematic study was conducted on the preparation of varying morphology MnO_2 nanostructures from nanosheets to nanofibers and nanotubes by controlling the hydrothermal reaction conditions. The growth mechanism of the morphology-dependent MnO_2 nanostructures was investigated by SEM, TEM and 3D electron tomography. The electrochemical performance of MnO_2 supercapacitors was revealed to be highly correlated to their surface area, determined by their morphology and crystallinity, as well as their cycling performance, determined by their defects formation during cycling. The often observed unusual increase in specific capacitance with cycling was studied and correlated not only with MnO_2 electrode morphology, but also with its structural and chemical state, including the formation of defective regions on the materials and the interaction of the materials with the electrolyte.

2. MnO_2 based nanocomposite electrodes were designed for high performance supercapacitor devices. Binary nanocomposites of MnO_2-CNC and MnO_2-graphene showed better electrochemical performance than that of the MnO_2, mainly due to the improved electrode conductivity. Ternary nanocomposite of MnO_2-CNT-graphene exhibited further improvement of electrochemical performance compared to the binary nanocomposites. The MnO_2 grown on CNT acts as an effective spacer for graphene nanosheets to avoid their restacking and agglomeration, while the graphene nanosheets separated in between the MnO_2-CNT contribute to the good electrical conductivity of the composite. The supercapacitors based on the novel electrodes of MnO_2-CNT-textile and MnO_2-CNT-sponge showed excellent electrochemical performance with high energy and power density, due to the rational design of the electrodes and the inherent advantage of the structures.

3. A general chemical route has been developed to synthesize conducting polymers and porous activated nanocarbons with well-controlled morphology and microstructures by taking the transition metal oxides as the reactive templates. As long as the oxidation potentials of the corresponding monomers are lower than the electrochemical potential of the metal oxides, different conducting polymers can be easily polymerized by treating the metal oxides with different morphologies as both the oxidants and templates. The obtained conducting polymers highly mimic the morphologies of the metal oxides, producing conducting polymers with different morphologies that some of them are difficult to

obtain by other methods. Taking polyaniline as an example, we have successfully prepared polyaniline nanospheres, nanotubes and nanofibers by using the corresponding MnO_2 nanostructures as the reactive templates. The further carbonization and activation of the conducting polymers produced different activated nanocarbons with high surface area, good electrical conductivity and highly porous nanostructures. Their electrochemical performance as supercapacitor materials demonstrated the morphology-dependent enhancement of the capacitance with excellent energy and power densities, suggesting the importance of the morphological optimization for supercapacitor materials with the best electrochemical performance.

Overall, the work presented in this dissertation largely enhanced the energy storage performance of the MnO_2 based supercapacitors by solving the conductivity issue of the MnO_2. Compared to the reported literature, our supercapacitors showed very promising electrochemical performance with much improved energy and power densities as summarized in the Ragone plot in Figure 4.1.

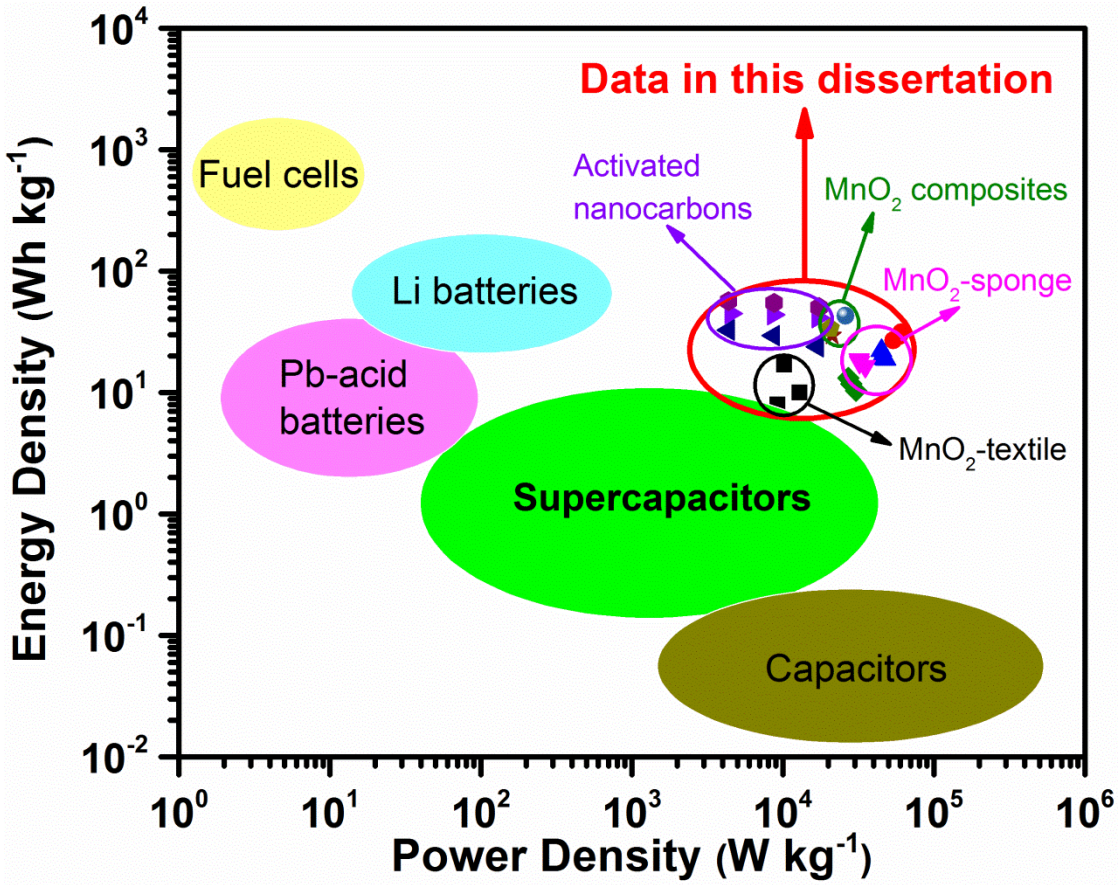

Figure 21 Ragone plot shows the achieved energy and power densities of our MnO_2 based supercapacitors, including the supercapacitors of MnO_2 binary and ternary nanocomposites, MnO_2-CNT-textile and MnO_2-CNT-sponge in aqueous electrolytes, as well as activated nanocarbons in ionic liquid electrolyte. All data are obtained from full cell supercapacitors.

4.2 Future Work and Investigations

In order to further improve the energy storage capacity and fully exploit the potential of MnO_2 based supercapacitors, the following directions are believed to be taken into account.

1. It is noted that the aqueous electrolytes are widely used for MnO_2 based supercapacitors, where two major problems should be solved from the electrolyte point of view: (1) the strictly limited voltage range of the supercapacitor device due to the decomposition of the aqueous electrolytes; (2) the limited capacitance that can be obtained from the existing electrolytes. It is important to explore non-aqueous electrolytes that can be used properly for MnO_2 based supercapacitors with higher voltage range and good electrochemical performance. One approach is to fabricate asymmetric supercapacitor by extending the voltage window while maintaining good electrochemical performance of both positive and negative electrodes, which will discuss further in the next section. Another approach is to utilize organic or ionic liquid electrolytes for MnO_2 based supercapacitors with higher energy density and good electrochemical stability. The third approach is to exploit the so called redox-active electrolytes that may largely improve the capacitance of the MnO_2 based supercapacitors, which was shown recently in carbon and conducting polymer based supercapacitors.[162, 207]

2. The fabrication of MnO_2 based asymmetric supercapacitors can not only extend the voltage window (1.5-2 V in asymmetric supercapacitors vs. 0.8-1 V in symmetric supercapacitors in aqueous electrolytes), but also benefit to the enhancement of electrochemical performance of both positive and negative electrodes. When incorporating the MnO_2 based positive electrode with some other metal oxides (SnO_2, Fe_3O_4, V_2O_5, MoO_3, etc.) or carbons (activated carbons, carbon nanotubes, graphene, etc.) based negative electrodes in proper ways, the asymmetric devices will generate greatly improved electrochemical properties due to the integrated effects from both electrode materials. Under such circumstances, the total capacitance of the asymmetric devices will be enhanced significantly. Therefore, the energy and power density of the devices will also be improved accordingly.

3. The fundamental understanding of the surface redox reactions dominated energy storage mechanism of the MnO_2 supercapacitors is extremely important for the better preparation and development of MnO_2 materials in the future. On the one hand, the theoretical models based on the energy storage process of the MnO_2 supercapacitor electrodes will be very useful for the prediction of the electrochemical behaviors of MnO_2. On the other hand, the direct observation of the charge and discharge process and the associated evolution of the MnO_2 electrodes by some in-situ techniques such as TEM, XRD, XPS and Raman spectroscopies will open a new area towards the fundamental

studies of supercapacitors, as much work has been conducted recently in the field of battery.[208-211]

4. The exploration and discovery of other Mn based electrode materials is important to the future supercapacitor development. For example, Mn based sulfides would be also good candidates for supercapacitor materials as compared to Mn based oxides. In addition, the Mn based ternary oxides and sulfides (such as $CoMnO_x$ or $CoMnS_x$, $NiMnO_x$ or $NiMnS_x$, $MnVO_x$ or $MnVS_x$, etc.) would become a class of excellent materials for supercapacitor energy storage systems in the near future. Furthermore, the Mn based layered intercalation compounds such as Li_xMnO_2, Na_xMnO_2, etc. will improve the energy storage capacity of the supercapacitors significantly, due to their faster ionic diffusion with enhanced redox reactions than the conventional MnO_2 electrode materials.[212]

REFERENCES

1. Conway, B. E. *Electrochemical Supercapacitors: Scientific Fundamentals and Technological Applications*. Kluwer Academic/Plenum: New York, 1999.

2. Simon, P.; Gogotsi, Y. Materials for electrochemical capacitors. *Nature Materials* 2008, 7, 845-854.

3. Winter, M.; Brodd, R. J. What are batteries, fuel cells, and supercapacitors? (vol 104, pg 4245, 2003). *Chemical Reviews* 2005, 105, 1021-1021.

4. Zhang, L. L.; Zhao, X. S. Carbon-based materials as supercapacitor electrodes. *Chem. Soc. Rev.* 2009, 38, 2520-2531.

5. Arico, A. S.; Bruce, P.; Scrosati, B.; Tarascon, J. M.; Van Schalkwijk, W. Nanostructured materials for advanced energy conversion and storage devices. *Nature Materials* 2005, 4, 366-377.

6. Stoller, M. D.; Park, S. J.; Zhu, Y. W.; An, J. H.; Ruoff, R. S. Graphene-Based Ultracapacitors. *Nano Letters* 2008, 8, 3498-3502.

7. Frackowiak, E.; Beguin, F. Carbon materials for the electrochemical storage of energy in capacitors. *Carbon* 2001, 39, 937-950.

8. Pandolfo, A. G.; Hollenkamp, A. F. Carbon properties and their role in supercapacitors. *Journal of Power Sources* 2006, 157, 11-27.

9. Niu, C. M.; Sichel, E. K.; Hoch, R.; Moy, D.; Tennent, H. High power electrochemical capacitors based on carbon nanotube electrodes. *Applied Physics Letters* 1997, 70, 1480-1482.

10. An, K. H.; Kim, W. S.; Park, Y. S.; Moon, J. M.; Bae, D. J.; Lim, S. C.; Lee, Y. S.; Lee, Y. H. Electrochemical properties of high-power supercapacitors using single-walled carbon nanotube electrodes. *Advanced Functional Materials* 2001, 11, 387-392.

11. Wang, Q.; Wen, Z.; Li, J. A hybrid supercapacitor fabricated with a carbon nanotube cathode and a TiO2-B nanowire anode. *Advanced Functional Materials* 2006, 16, 2141-2146.

12. Reddy, A. L. M.; Ramaprabhu, S. Nanocrystalline metal oxides dispersed multiwalled carbon nanotubes as supercapacitor electrodes. *Journal of Physical Chemistry C* 2007, 111, 7727-7734.

13. Henstridge, M. C.; Dickinson, E. J. F.; Compton, R. G. On the estimation of the diffuse double layer of carbon nanotubes using classical theory: Curvature effects on the Gouy-Chapman limit. *Chemical Physics Letters* 2010, 485, 167-170.

14. Zhu, Y. W.; Murali, S.; Stoller, M. D.; Ganesh, K. J.; Cai, W. W.; Ferreira, P. J.; Pirkle, A.; Wallace, R. M.; Cychosz, K. A.; Thommes, M.; Su, D.; Stach, E. A.; Ruoff, R. S. Carbon-Based Supercapacitors Produced by Activation of Graphene. *Science* 2011, 332, 1537-1541.

15. Jayalakshmi, M.; Balasubramanian, K. Simple Capacitors to Supercapacitors - An Overview. *International Journal of Electrochemical Science* 2008, 3, 1196-1217.

16. Chen, S.; Zhu, J.; Wu, X.; Han, Q.; Wang, X. Graphene Oxide-MnO2 Nanocomposites for Supercapacitors. *ACS Nano* 2010, 4, 2822-2830.

17. Wu, Z.-S.; Ren, W.; Wang, D.-W.; Li, F.; Liu, B.; Cheng, H.-M. High-Energy MnO2 Nanowire/Graphene and Graphene Asymmetric Electrochemical Capacitors. *ACS Nano* 2010, 4, 5835-5842.

18. Yan, J.; Khoo, E.; Sumboja, A.; Lee, P. S. Facile Coating of Manganese Oxide on Tin Oxide Nanowires with High-Performance Capacitive Behavior. *ACS Nano* 2010, 4, 4247-4255.

19. Toupin, M.; Brousse, T.; Belanger, D. Charge storage mechanism of MnO2 electrode used in aqueous electrochemical capacitor. *Chemistry of Materials* 2004, 16, 3184-3190.

20. Yan, J.; Fan, Z.; Wei, T.; Qian, W.; Zhang, M.; Wei, F. Fast and reversible surface redox reaction of graphene-MnO2 composites as supercapacitor electrodes. *Carbon* 2010, 48, 3825-3833.

21. Chen, W.; Rakhi, R. B.; Hu, L.; Xie, X.; Cui, Y.; Alshareef, H. N. High-Performance Nanostructured Supercapacitors on a Sponge. *Nano Letters* 2011, 11, 5165-5172.

22. Liu, J. W.; Essner, J.; Li, J. Hybrid Supercapacitor Based on Coaxially Coated Manganese Oxide on Vertically Aligned Carbon Nanofiber Arrays. *Chemistry of Materials* 2010, 22, 5022-5030.

23. Reddy, A. L. M.; Shaijumon, M. M.; Gowda, S. R.; Ajayan, P. M. Multisegmented Au-MnO2/Carbon Nanotube Hybrid Coaxial Arrays for High-Power Supercapacitor Applications. *Journal of Physical Chemistry C* 2010, 114, 658-663.

24. Mai, L.-Q.; Yang, F.; Zhao, Y.-L.; Xu, X.; Xu, L.; Luo, Y.-Z. Hierarchical MnMoO4/CoMoO4 heterostructured nanowires with enhanced supercapacitor performance. *Nat Commun* 2011, 2, 381.

25. Rakhi, R. B.; Cha, D.; Chen, W.; Alshareef, H. N. Electrochemical Energy Storage Devices Using Electrodes Incorporating Carbon Nanocoils and Metal Oxides Nanoparticles. *The Journal of Physical Chemistry C* 2011, 115, 14392-14399.

26. Chen, S.; Zhu, J.; Wu, X.; Han, Q.; Wang, X. Graphene Oxide−MnO2 Nanocomposites for Supercapacitors. *ACS Nano* 2010, 4, 2822-2830.

27. Chen, S.; Zhu, J. W.; Wu, X. D.; Han, Q. F.; Wang, X. Graphene Oxide-MnO2 Nanocomposites for Supercapacitors. *Acs Nano* 2010, 4, 2822-2830.

28. Hou, Y.; Cheng, Y. W.; Hobson, T.; Liu, J. Design and Synthesis of Hierarchical MnO2 Nanospheres/Carbon Nanotubes/Conducting Polymer Ternary Composite for High Performance Electrochemical Electrodes. *Nano Letters* 2010, 10, 2727-2733.

29. Stoller, M. D.; Ruoff, R. S. Best practice methods for determining an electrode material's performance for ultracapacitors. *Energy Environ. Sci.* 2010, 3, 1294-1301.

30. Taberna, P.-L.; Simon, P. Electrochemical Techniques. In *Supercapacitors*, Wiley-VCH Verlag GmbH & Co. KGaA: 2013; pp 111-130.

31. Lee, H. Y.; Goodenough, J. B. Supercapacitor Behavior with KCl Electrolyte. *Journal of Solid State Chemistry* 1999, 144, 220-223.

32. Wei, W. F.; Cui, X. W.; Chen, W. X.; Ivey, D. G. Manganese oxide-based materials as electrochemical supercapacitor electrodes. *Chemical Society Reviews* 2011, 40, 1697-1721.

33. Brousse, T.; Toupin, M.; Dugas, R.; Athouel, L.; Crosnier, O.; Belanger, D. Crystalline MnO2 as possible alternatives to amorphous compounds in electrochemical supercapacitors. *Journal of the Electrochemical Society* 2006, 153, A2171-A2180.

34. Truong, T. T.; Liu, Y. Z.; Ren, Y.; Trahey, L.; Sun, Y. G. Morphological and Crystalline Evolution of Nanostructured MnO2 and Its Application in Lithium-Air Batteries. *Acs Nano* 2012, 6, 8067-8077.

35. Fu, X.; Feng, J.; Wang, H.; Ng, K. M. Room temperature synthesis of a novel gamma-MnO2 hollow structure for aerobic oxidation of benzyl alcohol. *Nanotechnology* 2009, 20.

36. Subramanian, V.; Zhu, H.; Vajtai, R.; Ajayan, P. M.; Wei, B. Hydrothermal Synthesis and Pseudocapacitance Properties of MnO2 Nanostructures. *The Journal of Physical Chemistry B* 2005, 109, 20207-20214.

37. Tang, N.; Tian, X.; Yang, C.; Pi, Z. Facile synthesis of α-MnO2 nanostructures for supercapacitors. *Materials Research Bulletin* 2009, 44, 2062-2067.

38. Yan, J.; Wei, T.; Cheng, J.; Fan, Z.; Zhang, M. Preparation and electrochemical properties of lamellar MnO2 for supercapacitors. *Materials Research Bulletin* 2010, 45, 210-215.

39. Qu, Q.; Zhang, P.; Wang, B.; Chen, Y.; Tian, S.; Wu, Y.; Holze, R. Electrochemical Performance of MnO2 Nanorods in Neutral Aqueous Electrolytes as a Cathode for Asymmetric Supercapacitors. *The Journal of Physical Chemistry C* 2009, 113, 14020-14027.

40. Beaudrouet, E.; Le Gal La Salle, A.; Guyomard, D. Nanostructured manganese dioxides: Synthesis and properties as supercapacitor electrode materials. *Electrochimica Acta* 2009, 54, 1240-1248.

41. Wang, X.; Yuan, A.; Wang, Y. Supercapacitive behaviors and their temperature dependence of sol–gel synthesized nanostructured manganese dioxide in lithium hydroxide electrolyte. *Journal of Power Sources* 2007, 172, 1007-1011.

42. Yu, P.; Zhang, X.; Chen, Y.; Ma, Y. Solution-combustion synthesis of ε-MnO2 for supercapacitors. *Materials Letters* 2010, 64, 61-64.

43. Hu, C.-C.; Tsou, T.-W. Ideal capacitive behavior of hydrous manganese oxide prepared by anodic deposition. *Electrochemistry Communications* 2002, 4, 105-109.

44. Chen, Y.-S.; Hu, C.-C. Capacitive Characteristics of Binary Manganese-Nickel Oxides Prepared by Anodic Deposition. *Electrochemical and Solid-State Letters* 2003, 6, A210-A213.

45. Rajendra Prasad, K.; Miura, N. Electrochemically synthesized MnO2-based mixed oxides for high performance redox supercapacitors. *Electrochemistry Communications* 2004, 6, 1004-1008.

46. Nakayama, M.; Tanaka, A.; Sato, Y.; Tonosaki, T.; Ogura, K. Electrodeposition of Manganese and Molybdenum Mixed Oxide Thin Films and Their Charge Storage Properties. *Langmuir* 2005, 21, 5907-5913.

47. Wen, J.; Ruan, X.; Zhou, Z. Preparation and electrochemical performance of novel ruthenium–manganese oxide electrode materials for electrochemical capacitors. *Journal of Physics and Chemistry of Solids* 2009, 70, 816-820.

48. Yang, D. F. Pulsed laser deposition of cobalt-doped manganese oxide thin films for supercapacitor applications. *Journal of Power Sources* 2012, 198, 416-422.

49. Dubal, D. P.; Kim, W. B.; Lokhande, C. D. Galvanostatically deposited Fe: MnO2 electrodes for supercapacitor application. *Journal of Physics and Chemistry of Solids* 2012, 73, 18-24.

50. Pang, X.; Ma, Z. Q.; Zuo, L. Sn Doped MnO2 Electrode Material for Supercapacitors. *Acta Physico-Chimica Sinica* 2009, 25, 2433-2437.

51. Wang, Y. H.; Zhitomirsky, I. Cathodic electrodeposition of Ag-doped manganese dioxide films for electrodes of electrochemical supercapacitors. *Materials Letters* 2011, 65, 1759-1761.

52. Jianli, K.; Hirata, A.; Lijing, K.; Xianmin, Z.; Ying, H.; Luyang, C.; Cheng, L.; Fujita, T.; Akagi, K.; Mingwei, C. Enhanced supercapacitor performance of MnO 2 by atomic doping. *Angew. Chem. Int. Ed.* 2013, 52, 1664-1667.

53. Wang, G.-X.; Zhang, B.-L.; Yu, Z.-L.; Qu, M.-Z. Manganese oxide/MWNTs composite electrodes for supercapacitors. *Solid State Ionics* 2005, 176, 1169-1174.

54. Raymundo-Piñero, E.; Khomenko, V.; Frackowiak, E.; Béguin, F. Performance of Manganese Oxide/CNTs Composites as Electrode Materials for Electrochemical Capacitors. *Journal of The Electrochemical Society* 2005, 152, A229-A235.

55. Cheng, Q.; Tang, J.; Ma, J.; Zhang, H.; Shinya, N.; Qin, L. C. Graphene and nanostructured MnO2 composite electrodes for supercapacitors. *Carbon* 2011, 49, 2917-2925.

56. Fan, Z. J.; Yan, J.; Wei, T.; Zhi, L. J.; Ning, G. Q.; Li, T. Y.; Wei, F. Asymmetric Supercapacitors Based on Graphene/MnO2 and Activated Carbon Nanofiber Electrodes with High Power and Energy Density. *Advanced Functional Materials* 2011, 21, 2366-2375.

57. Liu, R.; Lee, S. B. MnO2/Poly(3,4-ethylenedioxythiophene) coaxial nanowires by one-step coelectrodeposition for electrochemical energy storage. *Journal of the American Chemical Society* 2008, 130, 2942-2943.

58. Thackeray, M. M. Manganese oxides for lithium batteries. *Progress in Solid State Chemistry* 1997, 25, 1-71.

59. Cheng, F.; Zhao, J.; Song, W.; Li, C.; Ma, H.; Chen, J.; Shen, P. Facile Controlled Synthesis of MnO2 Nanostructures of Novel Shapes and Their Application in Batteries. *Inorganic Chemistry* 2006, 45, 2038-2044.

60. Débart, A.; Paterson, A. J.; Bao, J.; Bruce, P. G. α-MnO2 Nanowires: A Catalyst for the O2 Electrode in Rechargeable Lithium Batteries. *Angewandte Chemie International Edition* 2008, 47, 4521-4524.

61. Toupin, M.; Brousse, T.; Bélanger, D. Influence of Microstucture on the Charge Storage Properties of Chemically Synthesized Manganese Dioxide. *Chem. Mater.* 2002, 14, 3946-3952.

62. Miller, J. R.; Simon, P. Electrochemical Capacitors for Energy Management. *Science* 2008, 321, 651-652.

63. Brousse, T.; Toupin, M.; Dugas, R.; Athouël, L.; Crosnier, O.; Bélanger, D. Crystalline MnO2 as Possible Alternatives to Amorphous Compounds in Electrochemical Supercapacitors. *J. Electrochem. Soc.* 2006, 153, A2171-A2180.

64. Li, W. N.; Yuan, J.; Shen, X. F.; Gomez-Mower, S.; Xu, L. P.; Sithambaram, S.; Aindow, M.; Suib, S. L. Hydrothermal Synthesis of Structure- and Shape-Controlled Manganese Oxide Octahedral Molecular Sieve Nanomaterials. *Advanced Functional Materials* 2006, 16, 1247-1253.

65. Hu, L.; Chen, W.; Xie, X.; Liu, N.; Yang, Y.; Wu, H.; Yao, Y.; Pasta, M.; Alshareef, H. N.; Cui, Y. Symmetrical MnO2–Carbon Nanotube–Textile Nanostructures for Wearable Pseudocapacitors with High Mass Loading. *ACS Nano* 2011, 5, 8904-8913.

66. Zhao, J.; Tao, Z.; Liang, J.; Chen, J. Facile Synthesis of Nanoporous γ-MnO2 Structures and Their Application in Rechargeable Li-Ion Batteries. *Crystal Growth & Design* 2008, 8, 2799-2805.

67. Xiao, W.; Wang, D.; Lou, X. W. Shape-Controlled Synthesis of MnO2 Nanostructures with Enhanced Electrocatalytic Activity for Oxygen Reduction. *J. Phys. Chem. C* 2009, 114, 1694-1700.

68. Wang, X.; Li, Y. Selected-Control Hydrothermal Synthesis of α- and β-MnO2 Single Crystal Nanowires. *Journal of the American Chemical Society* 2002, 124, 2880-2881.

69. Cheng, F.; Su, Y.; Liang, J.; Tao, Z.; Chen, J. MnO2-Based Nanostructures as Catalysts for Electrochemical Oxygen Reduction in Alkaline Media†. *Chem. Mater.* 2009, 22, 898-905.

70. Truong, T. T.; Liu, Y.; Ren, Y.; Trahey, L.; Sun, Y. Morphological and Crystalline Evolution of Nanostructured MnO2 and Its Application in Lithium–Air Batteries. *ACS Nano* 2012, 6, 8067-8077.

71. Ni, J.; Lu, W.; Zhang, L.; Yue, B.; Shang, X.; Lv, Y. Low-Temperature Synthesis of Monodisperse 3D Manganese Oxide Nanoflowers and Their Pseudocapacitance Properties. *J. Phys. Chem. C* 2008, 113, 54-60.

72. Toupin, M.; Brousse, T.; Bélanger, D. Charge Storage Mechanism of MnO2 Electrode Used in Aqueous Electrochemical Capacitor. *Chemistry of Materials* 2004, 16, 3184-3190.

73. Yeager, M.; Du, W.; Si, R.; Su, D.; Marinković, N.; Teng, X. Highly Efficient K0.15MnO2 Birnessite Nanosheets for Stable Pseudocapacitive Cathodes. *J. Phys. Chem. C* 2012, 116, 20173-20181.

74. Luo, J.; Zhu, H. T.; Fan, H. M.; Liang, J. K.; Shi, H. L.; Rao, G. H.; Li, J. B.; Du, Z. M.; Shen, Z. X. Synthesis of Single-Crystal Tetragonal α-MnO2 Nanotubes. *J. Phys. Chem. C* 2008, 112, 12594-12598.

75. Pennycook, S. J. N., P. D. *Scanning Transmission Electron Microscopy Imaging and Analysis*. Springer: New York, 2011.

76. Midgley, P. A.; Dunin-Borkowski, R. E. Electron tomography and holography in materials science. *Nat Mater* 2009, 8, 271-280.

77. Wang, X.; Li, Y. Synthesis and Formation Mechanism of Manganese Dioxide Nanowires/Nanorods. *Chemistry – A European Journal* 2003, 9, 300-306.

78. Li, Y.; Wang, J.; Zhang, Y.; Banis, M. N.; Liu, J.; Geng, D.; Li, R.; Sun, X. Facile controlled synthesis and growth mechanisms of flower-like and tubular

MnO2 nanostructures by microwave-assisted hydrothermal method. *Journal of Colloid and Interface Science* 2012, 369, 123-128.

79. Wang, Y.-T.; Lu, A.-H.; Zhang, H.-L.; Li, W.-C. Synthesis of Nanostructured Mesoporous Manganese Oxides with Three-Dimensional Frameworks and Their Application in Supercapacitors. *J. Phys. Chem. C* 2011, 115, 5413-5421.

80. Chmiola, J.; Yushin, G.; Dash, R.; Gogotsi, Y. Effect of pore size and surface area of carbide derived carbons on specific capacitance. *J. Power Sources* 2006, 158, 765-772.

81. Roberts, A. J.; Slade, R. C. T. Effect of specific surface area on capacitance in asymmetric carbon/α-MnO2 supercapacitors. *Electrochim. Acta* 2010, 55, 7460-7469.

82. Lee, S. W.; Kim, J.; Chen, S.; Hammond, P. T.; Shao-Horn, Y. Carbon Nanotube/Manganese Oxide Ultrathin Film Electrodes for Electrochemical Capacitors. *ACS Nano* 2010, 4, 3889-3896.

83. Ma, S.-B.; Ahn, K.-Y.; Lee, E.-S.; Oh, K.-H.; Kim, K.-B. Synthesis and characterization of manganese dioxide spontaneously coated on carbon nanotubes. *Carbon* 2007, 45, 375-382.

84. Bao, L.; Zang, J.; Li, X. Flexible Zn2SnO4/MnO2 Core/Shell Nanocable−Carbon Microfiber Hybrid Composites for High-Performance Supercapacitor Electrodes. *Nano Letters* 2011, 11, 1215-1220.

85. Xu, M.; Kong, L.; Zhou, W.; Li, H. Hydrothermal Synthesis and Pseudocapacitance Properties of α-MnO2 Hollow Spheres and Hollow Urchins. *J. Phys. Chem. C* 2007, 111, 19141-19147.

86. Yu, P.; Zhang, X.; Wang, D.; Wang, L.; Ma, Y. Shape-Controlled Synthesis of 3D Hierarchical MnO2 Nanostructures for Electrochemical Supercapacitors. *Crystal Growth & Design* 2008, 9, 528-533.

87. Devaraj, S.; Munichandraiah, N. Effect of Crystallographic Structure of MnO2 on Its Electrochemical Capacitance Properties. *J. Phys. Chem. C* 2008, 112, 4406-4417.

88. Athouel, L.; Moser, F.; Dugas, R.; Crosnier, O.; Belanger, D.; Brousse, T. Variation of the MnO2 Birnessite Structure upon Charge/Discharge in an Electrochemical Supercapacitor Electrode in Aqueous Na2SO4 Electrolyte. *The Journal of Physical Chemistry C* 2008, 112, 7270-7277.

89. Sung, D.-Y.; Kim, I. Y.; Kim, T. W.; Song, M.-S.; Hwang, S.-J. Room Temperature Synthesis Routes to the 2D Nanoplates and 1D Nanowires/Nanorods of Manganese Oxides with Highly Stable Pseudocapacitance Behaviors. *The Journal of Physical Chemistry C* 2011, 115, 13171-13179.

90. Ghodbane, O.; Pascal, J.-L.; Favier, F. d. r. Microstructural Effects on Charge-Storage Properties in MnO2-Based Electrochemical Supercapacitors. *ACS Applied Materials & Interfaces* 2009, 1, 1130-1139.

91. Peng, C.; Zhang, S. W.; Jewell, D.; Chen, G. Z. Carbon nanotube and conducting polymer composites for supercapacitors. *Progress in Natural Science* 2008, 18, 777-788.

92. Wu, F.; Xu, B. Progress on the application of carbon nanotubes in supercapacitors. *New Carbon Materials* 2006, 21, 176-184.

93. Lee, B. J.; Sivakkumar, S. R.; Ko, J. M.; Kim, J. H.; Jo, S. M.; Kim, D. Y. Carbon nanofibre/hydrous RuO2 nanocomposite electrodes for supercapacitors. *Journal of Power Sources* 2007, 168, 546-552.

94. Wang, Y.; Shi, Z. Q.; Huang, Y.; Ma, Y. F.; Wang, C. Y.; Chen, M. M.; Chen, Y. S. Supercapacitor Devices Based on Graphene Materials. *Journal of Physical Chemistry C* 2009, 113, 13103-13107.

95. Inagaki, M.; Konno, H.; Tanaike, O. Carbon materials for electrochemical capacitors. *Journal of Power Sources* 2010, 195, 7880-7903.

96. Celorrio, V.; Calvillo, L.; Martinez-Huerta, M. V.; Moliner, R.; Lazaro, M. J. Study of the Synthesis Conditions of Carbon Nanocoils for Energetic Applications. *Energy & Fuels* 2010, 24, 3361-3365.

97. Yu, L. Y.; Qin, Y.; Cui, Z. L. Synthesis of coiled carbon nanofibers by Cu-Ni alloy nanoparticles catalyzed decomposition of acetylene at the low temperature of 241 degrees C. *Materials Letters* 2005, 59, 459-462.

98. Jian, X. A.; Jiang, M.; Zhou, Z. W.; Yang, M. L.; Lu, J.; Hu, S. C.; Wang, Y.; Hui, D. Preparation of high purity helical carbon nanofibers by the catalytic decomposition of acetylene and their growth mechanism. *Carbon* 2010, 48, 4535-4541.

99. Davis, W. R.; Slawson, R. J.; Rigby, G. R. AN UNUSUAL FORM OF CARBON. *Nature* 1953, 171, 756-756.

100. Nujiang Tang, W. K., Chienchung Jeng, Liyuan Wang, Kuanjiuh Lin,and Youwei Du. Coil-in-Coil Carbon Nanocoils: 11 Gram- Scale Synthesis, Single Nanocoil Electrical Properties, and Electrical Contact Improvement. *Acs Nano* 2010, 4, 781-788.

101. Woo Yong Sung, J. G. O., Wal Jun Kim, Seung Min Lee, Soon Chang Yeon, Ho Young Lee and Yong Hyup Kim. Synthesis and field emission characteristics of carbon nanocoils with a high aspect ratio supported by copper micro-tips. *Nanotechnology* 2007, 18, 245603 (5pp).

102. Xinqi Chen, S. Z., Dmitriy A. Dikin, Weiqiang Ding, and Rodney S. Ruoff. Mechanics of a Carbon Nanocoil. *Nano Letters* 2003, 3, 1299-1304.

103. Wang, L. J.; Li, C. Z.; Gu, F.; Zhang, C. X. Facile flame synthesis and electrochemical properties of carbon nanocoils. *Journal of Alloys and Compounds* 2009, 473, 351-355.

104. Wang, L. J., Chun Zhong, Gu Feng, Xiao Jia-zhil Effects of purification and activation on morphology and electrochemical capacity of carbon nanocoils. *journal of china university of petroleum (Edition of Natural Science)* 2009, 02.

105. Horng, Y.-Y.; Lu, Y.-C.; Hsu, Y.-K.; Chen, C.-C.; Chen, L.-C.; Chen, K.-H. Flexible supercapacitor based on polyaniline nanowires/carbon cloth with both high gravimetric and area-normalized capacitance. *Journal of Power Sources* 2010, 195, 4418-4422.

106. Wang, L.; Li, C.; Gu, F.; Zhang, C. Facile flame synthesis and electrochemical properties of carbon nanocoils. *Journal of Alloys and Compounds* 2009, 473, 351-355.

107. Xia, H.; Xiao, W.; Lai, M.; Lu, L. Facile Synthesis of Novel Nanostructured MnO2Thin Films and Their Application in Supercapacitors. *Nanoscale Research Letters* 2009, 4, 1035 - 1040.

108. Li, L.; Qin, Z.-Y.; Wang, L.-F.; Liu, H.-J.; Zhu, M.-F. Anchoring alpha-manganese oxide nanocrystallites on multi-walled carbon nanotubes as electrode materials for supercapacitor. *J Nanopart Res* 2010, 12, 2349-2353.

109. Vivekchand, S. R. C.; Rout, C. S.; Subrahmanyam, K. S.; Govindaraj, A.; Rao, C. N. R. Graphene-based electrochemical supercapacitors. *Journal of Chemical Sciences* 2008, 120, 9-13.

110. Pumera, M. Graphene-based nanomaterials for energy storage. *Energy & Environmental Science* 2011, 4, 668-674.

111. Liu, C. G.; Yu, Z. N.; Neff, D.; Zhamu, A.; Jang, B. Z. Graphene-Based Supercapacitor with an Ultrahigh Energy Density. *Nano Letters* 2010, 10, 4863-4868.

112. Wu, Z. S.; Wang, D. W.; Ren, W.; Zhao, J.; Zhou, G.; Li, F.; Cheng, H. M. Anchoring Hydrous RuO2 on Graphene Sheets for High-Performance Electrochemical Capacitors. *Advanced Functional Materials* 2010, 20, 3595-3602.

113. Qian, Y.; Lu, S. B.; Gao, F. L. Preparation of MnO2/graphene composite as electrode material for supercapacitors. *Journal of Materials Science* 2011, 46, 3517-3522.

114. Rakhi, R. B.; Alshareef, H. N. Enhancement of the energy storage properties of supercapacitors using graphene nanosheets dispersed with metal oxide-loaded carbon nanotubes. *Journal of Power Sources* 2011, doi:10.1016/j.jpowsour.2011.06.038.

115. Yan, J.; Wei, T.; Qiao, W. M.; Shao, B.; Zhao, Q. K.; Zhang, L. J.; Fan, Z. J. Rapid microwave-assisted synthesis of graphene nanosheet/Co3O4 composite for supercapacitors. *Electrochimica Acta* 2010, 55, 6973-6978.

116. Yan, J.; Fan, Z. J.; Wei, T.; Qian, W. Z.; Zhang, M. L.; Wei, F. Fast and reversible surface redox reaction of graphene-MnO2 composites as supercapacitor electrodes. *Carbon* 2010, 48, 3825-3833.

117. Rakhi, R. B.; Chen, W.; Cha, D.; Alshareef, H. N. High performance supercapacitors using metal oxide anchored graphene nanosheet electrodes. *Journal of Materials Chemistry* 2011, 21, 16197-16204.

118. Stoller, M. D.; Park, S.; Zhu, Y.; An, J.; Ruoff, R. S. Graphene-Based Ultracapacitors. *Nano Letters* 2008, 8, 3498-3502.

119. Chen, Y.; Zhang, X.; Yu, P.; Ma, Y. Electrophoretic deposition of graphene nanosheets on nickel foams for electrochemical capacitors. *Journal of Power Sources* 2010, 195, 3031-3035.

120. Yan, J.; Wei, T.; Shao, B.; Ma, F.; Fan, Z.; Zhang, M.; Zheng, C.; Shang, Y.; Qian, W.; Wei, F. Electrochemical properties of graphene nanosheet/carbon black composites as electrodes for supercapacitors. *Carbon* 2010, 48, 1731-1737.

121. Yan, J.; Wei, T.; Shao, B.; Fan, Z.; Qian, W.; Zhang, M.; Wei, F. Preparation of a graphene nanosheet/polyaniline composite with high specific capacitance. *Carbon* 2010, 48, 487-493.

122. Yan, J.; Wei, T.; Fan, Z.; Qian, W.; Zhang, M.; Shen, X.; Wei, F. Preparation of graphene nanosheet/carbon nanotube/polyaniline composite as electrode material for supercapacitors. *Journal of Power Sources* 2010, 195, 3041-3045.

123. Li, F.; Song, J.; Yang, H.; Gan, S.; Zhang, Q.; Han, D.; Ivaska, A.; Niu, L. One-step synthesis of graphene/SnO2 nanocomposites and its application in electrochemical supercapacitors. *Nanotechnology* 2009, 20.

124. Wu, Z.-S.; Wang, D.-W.; Ren, W.; Zhao, J.; Zhou, G.; Li, F.; Cheng, H.-M. Anchoring Hydrous RuO2 on Graphene Sheets for High-Performance Electrochemical Capacitors. *Advanced Functional Materials* 2010, 20, 3595-3602.

125. Yu, D.; Dai, L. Self-Assembled Graphene/Carbon Nanotube Hybrid Films for Supercapacitors. *Journal of Physical Chemistry Letters* 2010, 1, 467-470.

126. Wu, C.; Xie, W.; Zhang, M.; Bai, L.; Yang, J.; Xie, Y. Environmentally Friendly gamma-MnO2 Hexagon-Based Nanoarchitectures: Structural Understanding and Their Energy-Saving Applications. *Chemistry-a European Journal* 2009, 15, 492-500.

127. Dewolff, P. M. INTERPRETATION OF SOME GAMMA-MNO2 DIFFRACTION PATTERNS. *Acta Crystallographica* 1959, 12, 341-&.

128. Reddy, A. L. M.; Shaijumon, M. M.; Gowda, S. R.; Ajayan, P. M. Coaxial MnO2/Carbon Nanotube Array Electrodes for High-Performance Lithium Batteries. *Nano Letters* 2009, 9, 1002-1006.

129. Xia, H.; Lai, M.; Lu, L. Nanoflaky MnO2/carbon nanotube nanocomposites as anode materials for lithium-ion batteries. *Journal of Materials Chemistry* 2010, 20, 6896-6902.

130. Meher, S. K.; Justin, P.; Rao, G. R. Nanoscale morphology dependent pseudocapacitance of NiO: Influence of intercalating anions during synthesis. *Nanoscale* 2011, 3, 683-692.

131. Lu, T.; Zhang, Y.; Li, H.; Pan, L.; Li, Y.; Sun, Z. Electrochemical behaviors of graphene-ZnO and graphene-SnO2 composite films for supercapacitors. *Electrochimica Acta* 2010, 55, 4170-4173.

132. Li, X.; Rong, J.; Wei, B. Electrochemical Behavior of Single-Walled Carbon Nanotube Supercapacitors under Compressive Stress. *ACS Nano* 2010, 4, 6039-6049.

133. Hsieh, Y.-C.; Lee, K.-T.; Lin, Y.-P.; Wu, N.-L.; Donne, S. W. Investigation on capacity fading of aqueous MnO2 center dot nH(2)O electrochemical capacitor. *Journal of Power Sources* 2008, 177, 660-664.

134. Liu, C.; Yu, Z.; Neff, D.; Zhamu, A.; Jang, B. Z. Graphene-Based Supercapacitor with an Ultrahigh Energy Density. *Nano Letters* 2010, 10, 4863-4868.

135. Rakhi, R. B.; Chen, W.; Cha, D.; Alshareef, H. N. Nanostructured Ternary Electrodes for Energy-Storage Applications. *Advanced Energy Materials* 2012, 2, 381-389.

136. Hu, L. B.; Chen, W.; Xie, X.; Liu, N. A.; Yang, Y.; Wu, H.; Yao, Y.; Pasta, M.; Alshareef, H. N.; Cui, Y. Symmetrical MnO2-Carbon Nanotube-Textile Nanostructures for Wearable Pseudocapacitors with High Mass Loading. *ACS Nano* 2011, 5, 8904-8913.

137. Hu, L.; Pasta, M.; La Mantia, F.; Cui, L.; Jeong, S.; Deshazer, H. D.; Choi, J. W.; Han, S. M.; Cui, Y. Stretchable, Porous, and Conductive Energy Textiles. *Nano Letters* 2010, 10, 708-714.

138. Zhang, G.; Sun, S.; Yang, D.; Dodelet, J.-P.; Sacher, E. The surface analytical characterization of carbon fibers functionalized by H2SO4/HNO3 treatment. *Carbon* 2008, 46, 196-205.

139. Sivakkumar, S. R.; Ko, J. M.; Kim, D. Y.; Kim, B. C.; Wallace, G. G. Performance evaluation of CNT/polypyrrole/MnO2 composite electrodes for electrochemical capacitors. *Electrochimica Acta* 2007, 52, 7377-7385.

140. Chou, S.-L.; Wang, J.-Z.; Chew, S.-Y.; Liu, H.-K.; Dou, S.-X. Electrodeposition of MnO2 nanowires on carbon nanotube paper as free-standing, flexible electrode for supercapacitors. *Electrochemistry Communications* 2008, 10, 1724-1727.

141. Hu, L.; Pasta, M.; Mantia, F. L.; Cui, L.; Jeong, S.; Deshazer, H. D.; Choi, J. W.; Han, S. M.; Cui, Y. Stretchable, Porous, and Conductive Energy Textiles. *Nano Letters* 2010, 10, 708-714.

142. Yu, G.; Hu, L.; Vosgueritchian, M.; Wang, H.; Xie, X.; McDonough, J. R.; Cui, X.; Cui, Y.; Bao, Z. Solution-Processed Graphene/MnO2 Nanostructured Textiles for High-Performance Electrochemical Capacitors. *Nano Letters* 2011, 11, 2905-2911.

143. Pech, D.; Brunet, M.; Durou, H.; Huang, P. H.; Mochalin, V.; Gogotsi, Y.; Taberna, P. L.; Simon, P. Ultrahigh-power micrometre-sized supercapacitors based on onion-like carbon. *Nature Nanotechnology* 2010, 5, 651-654.

144. Pech, D.; Brunet, M.; Taberna, P. L.; Simon, P.; Fabre, N.; Mesnilgrente, F.; Conedera, V.; Durou, H. Elaboration of a microstructured inkjet-printed carbon electrochemical capacitor. *Journal of Power Sources* 2010, 195, 1266-1269.

145. Stoller, M. D.; Stoller, S. A.; Quarles, N.; Suk, J. W.; Murali, S.; Zhu, Y. W.; Zhu, X. J.; Ruoff, R. S. Using coin cells for ultracapacitor electrode material testing. *Journal of Applied Electrochemistry* 2011, 41, 681-686.

146. Bao, L. H.; Zang, J. F.; Li, X. D. Flexible Zn2SnO4/MnO2 Core/Shell Nanocable-Carbon Microfiber Hybrid Composites for High-Performance Supercapacitor Electrodes. *Nano Letters* 2011, 11, 1215-1220.

147. Lei, Z. B.; Christov, N.; Zhao, X. S. Intercalation of mesoporous carbon spheres between reduced graphene oxide sheets for preparing high-rate supercapacitor electrodes. *Energy & Environmental Science* 2011, 4, 1866-1873.

148. Yan, J. A.; Khoo, E.; Sumboja, A.; Lee, P. S. Facile Coating of Manganese Oxide on Tin Oxide Nanowires with High-Performance Capacitive Behavior. *Acs Nano* 2010, 4, 4247-4255.

149. Lang, X. Y.; Hirata, A.; Fujita, T.; Chen, M. W. Nanoporous metal/oxide hybrid electrodes for electrochemical supercapacitors. *Nature Nanotechnology* 2011, 6, 232-236.

150. Wu, Z. S.; Ren, W. C.; Wang, D. W.; Li, F.; Liu, B. L.; Cheng, H. M. High-Energy MnO2 Nanowire/Graphene and Graphene Asymmetric Electrochemical Capacitors. *ACS Nano* 2010, 4, 5835-5842.

151. Cottineau, T.; Toupin, M.; Delahaye, T.; Brousse, T.; Belanger, D. Nanostructured transition metal oxides for aqueous hybrid electrochemical supercapacitors. *Applied Physics a-Materials Science & Processing* 2006, 82, 599-606.

152. Zhou, C. F.; Kumar, S.; Doyle, C. D.; Tour, J. M. Functionalized single wall carbon nanotubes treated with pyrrole for electrochemical supercapacitor membranes. *Chemistry of Materials* 2005, 17, 1997-2002.

153. Donne, S. W. General Principles of Electrochemistry. In *Supercapacitors*, Wiley-VCH Verlag GmbH & Co. KGaA: 2013; pp 1-68.

154. Frackowiak, E.; Khomenko, V.; Jurewicz, K.; Lota, K.; Beguin, F. Supercapacitors based on conducting polymers/nanotubes composites. *Journal of Power Sources* 2006, 153, 413-418.

155. Snook, G. A.; Kao, P.; Best, A. S. Conducting-polymer-based supercapacitor devices and electrodes. *J. Power Sources* 2011, 196, 1-12.

156. Li, H.; Wang, J.; Chu, Q.; Wang, Z.; Zhang, F.; Wang, S. Theoretical and experimental specific capacitance of polyaniline in sulfuric acid. *J. Power Sources* 2009, 190, 578-586.

157. Li, D.; Huang, J.; Kaner, R. B. Polyaniline Nanofibers: A Unique Polymer Nanostructure for Versatile Applications. *Accounts of Chemical Research* 2008, 42, 135-145.

158. Li, G.-R.; Feng, Z.-P.; Zhong, J.-H.; Wang, Z.-L.; Tong, Y.-X. Electrochemical Synthesis of Polyaniline Nanobelts with Predominant Electrochemical Performances. *Macromolecules* 2010, 43, 2178-2183.

159. Wu, Q.; Xu, Y.; Yao, Z.; Liu, A.; Shi, G. Supercapacitors Based on Flexible Graphene/Polyaniline Nanofiber Composite Films. *ACS Nano* 2010, 4, 1963-1970.

160. Rakhi, R. B.; Chen, W.; Alshareef, H. N. Conducting polymer/carbon nanocoil composite electrodes for efficient supercapacitors. *Journal of Materials Chemistry* 2012, 22, 5177-5183.

161. Park, H.-W.; Kim, T.; Huh, J.; Kang, M.; Lee, J. E.; Yoon, H. Anisotropic Growth Control of Polyaniline Nanostructures and Their Morphology-Dependent Electrochemical Characteristics. *ACS Nano* 2012, 6, 7624-7633.

162. Chen, W.; Rakhi, R. B.; Alshareef, H. N. Morphology-Dependent Enhancement of the Pseudocapacitance of Template-Guided Tunable Polyaniline Nanostructures. *The Journal of Physical Chemistry C* 2013, 117, 15009-15019.

163. Pan, L. J.; Pu, L.; Shi, Y.; Song, S. Y.; Xu, Z.; Zhang, R.; Zheng, Y. D. Synthesis of Polyaniline Nanotubes with a Reactive Template of Manganese Oxide. *Adv. Mater.* 2007, 19, 461-464.

164. Chen, W.; Rakhi, R. B.; Alshareef, H. N. Facile synthesis of polyaniline nanotubes using reactive oxide templates for high energy density pseudocapacitors. *Journal of Materials Chemistry A* 2013, 1, 3315-3324.

165. Pan, L.; Yu, G.; Zhai, D.; Lee, H. R.; Zhao, W.; Liu, N.; Wang, H.; Tee, B. C.-K.; Shi, Y.; Cui, Y.; Bao, Z. Hierarchical nanostructured conducting polymer hydrogel with high electrochemical activity. *Proceedings of the National Academy of Sciences* 2012, 109, 9287-9292.

166. Giri, G.; Verploegen, E.; Mannsfeld, S. C. B.; Atahan-Evrenk, S.; Kim, D. H.; Lee, S. Y.; Becerril, H. A.; Aspuru-Guzik, A.; Toney, M. F.; Bao, Z. Tuning charge transport in solution-sheared organic semiconductors using lattice strain. *Nature* 2011, 480, 504-508.

167. Zhang, Z.; Wan, M.; Wei, Y. Highly Crystalline Polyaniline Nanostructures Doped with Dicarboxylic Acids. *Advanced Functional Materials* 2006, 16, 1100-1104.

168. Tagowska, M.; Pałys, B.; Jackowska, K. Polyaniline nanotubules—anion effect on conformation and oxidation state of polyaniline studied by Raman spectroscopy. *Synthetic Met.* 2004, 142, 223-229.

169. Ohira, M.; Sakai, T.; Takeuchi, M.; Kobayashi, Y.; Tsuji, M. Raman and infrared spectra of polyaniline. *Synthetic Met.* 1987, 18, 347-352.

170. Baibarac, M.; Baltog, I.; Godon, C.; Lefrant, S.; Chauvet, O. Covalent functionalization of single-walled carbon nanotubes by aniline electrochemical polymerization. *Carbon* 2004, 42, 3143-3152.

171. Huang, J.; Kaner, R. B. A General Chemical Route to Polyaniline Nanofibers. *Journal of the American Chemical Society* 2003, 126, 851-855.

172. Qin, Q.; Tao, J.; Yang, Y.; Dong, X. In situ oxidative polymerization of polyaniline counter electrode on ITO conductive glass substrate. *Polymer Engineering & Science* 2011, 51, 663-669.

173. Sheng, Y.; Chen, J. D.; Zhu, D. Q.; Carrot, C.; Guillet, J. Synthesis of conductive polyaniline via oxidation by MnO2. *Chin. J. Polym. Sci.* 2004, 22, 269-277.

174. Ryu, K. S.; Kim, K. M.; Park, N.-G.; Park, Y. J.; Chang, S. H. Symmetric redox supercapacitor with conducting polyaniline electrodes. *J. Power Sources* 2002, 103, 305-309.

175. Meng, C.; Liu, C.; Chen, L.; Hu, C.; Fan, S. Highly Flexible and All-Solid-State Paperlike Polymer Supercapacitors. *Nano Lett.* 2010, 10, 4025-4031.

176. Lota, G.; Fic, K.; Frackowiak, E. Carbon nanotubes and their composites in electrochemical applications. *Energy & Environmental Science* 2011, 4, 1592-1605.

177. Hall, P. J.; Mirzaeian, M.; Fletcher, S. I.; Sillars, F. B.; Rennie, A. J. R.; Shitta-Bey, G. O.; Wilson, G.; Cruden, A.; Carter, R. Energy storage in electrochemical capacitors: designing functional materials to improve performance. *Energy & Environmental Science* 2010, 3, 1238-1251.

178. An, K. H.; Kim, W. S.; Park, Y. S.; Choi, Y. C.; Lee, S. M.; Chung, D. C.; Bae, D. J.; Lim, S. C.; Lee, Y. H. Supercapacitors using single-walled carbon nanotube electrodes. *Advanced Materials* 2001, 13, 497-+.

179. Arico, A. S.; Bruce, P.; Scrosati, B.; Tarascon, J.-M.; van Schalkwijk, W. Nanostructured materials for advanced energy conversion and storage devices. *Nat Mater* 2005, 4, 366-377.

180. Futaba, D. N.; Hata, K.; Yamada, T.; Hiraoka, T.; Hayamizu, Y.; Kakudate, Y.; Tanaike, O.; Hatori, H.; Yumura, M.; Iijima, S. Shape-engineerable and highly densely packed single-walled carbon nanotubes and their application as super-capacitor electrodes. *Nat Mater* 2006, 5, 987-994.

181. Carriazo, D.; Pico, F.; Gutierrez, M. C.; Rubio, F.; Rojo, J. M.; del Monte, F. Block-Copolymer assisted synthesis of hierarchical carbon monoliths suitable as supercapacitor electrodes. *Journal of Materials Chemistry* 2010, 20, 773-780.

182. Frackowiak, E.; Beguin, F. Electrochemical storage of energy in carbon nanotubes and nanostructured carbons. *Carbon* 2002, 40, 1775-1787.

183. Frackowiak, E. Carbon materials for supercapacitor application. *Physical Chemistry Chemical Physics* 2007, 9, 1774-1785.

184. Barranco, V.; Lillo-Rodenas, M. A.; Linares-Solano, A.; Oya, A.; Pico, F.; Ibanez, J.; Agullo-Rueda, F.; Amarilla, J. M.; Rojo, J. M. Amorphous Carbon Nanofibers and Their Activated Carbon Nanofibers as Supercapacitor Electrodes. *Journal of Physical Chemistry C* 2010, 114, 10302-10307.

185. Wang, J. C.; Kaskel, S. KOH activation of carbon-based materials for energy storage. *Journal of Materials Chemistry* 2012, 22, 23710-23725.

186. Liu, R.; Wu, D.; Feng, X.; Müllen, K. Nitrogen-Doped Ordered Mesoporous Graphitic Arrays with High Electrocatalytic Activity for Oxygen Reduction. *Angewandte Chemie International Edition* 2010, 49, 2565-2569.

187. Yang, S.; Feng, X.; Wang, X.; Müllen, K. Graphene-Based Carbon Nitride Nanosheets as Efficient Metal-Free Electrocatalysts for Oxygen Reduction Reactions. *Angewandte Chemie International Edition* 2011, 50, 5339-5343.

188. Haubner, K.; Murawski, J.; Olk, P.; Eng, L. M.; Ziegler, C.; Adolphi, B.; Jaehne, E. The Route to Functional Graphene Oxide. *Chemphyschem* 2010, 11, 2131-2139.

189. Zhang, J. L.; Yang, H. J.; Shen, G. X.; Cheng, P.; Zhang, J. Y.; Guo, S. W. Reduction of graphene oxide via L-ascorbic acid. *Chemical Communications* 2010, 46, 1112-1114.

190. Fan, X. B.; Peng, W. C.; Li, Y.; Li, X. Y.; Wang, S. L.; Zhang, G. L.; Zhang, F. B. Deoxygenation of Exfoliated Graphite Oxide under Alkaline Conditions: A Green Route to Graphene Preparation. *Advanced Materials* 2008, 20, 4490-4493.

191. Sheng, Z.-H.; Shao, L.; Chen, J.-J.; Bao, W.-J.; Wang, F.-B.; Xia, X.-H. Catalyst-Free Synthesis of Nitrogen-Doped Graphene via Thermal Annealing Graphite Oxide with Melamine and Its Excellent Electrocatalysis. *ACS Nano* 2011, 5, 4350-4358.

192. Kumar, A.; Ganguly, A.; Papakonstantinou, P. Thermal stability study of nitrogen functionalities in a graphene network. *Journal of Physics-Condensed Matter* 2012, 24.

193. Li, X. L.; Wang, H. L.; Robinson, J. T.; Sanchez, H.; Diankov, G.; Dai, H. J. Simultaneous Nitrogen Doping and Reduction of Graphene Oxide. *Journal of the American Chemical Society* 2009, 131, 15939-15944.

194. Kundu, S.; Nagaiah, T. C.; Xia, W.; Wang, Y.; Dommele, S. V.; Bitter, J. H.; Santa, M.; Grundmeier, G.; Bron, M.; Schuhmann, W.; Muhler, M. Electrocatalytic Activity and Stability of Nitrogen-Containing Carbon Nanotubes in the Oxygen Reduction Reaction. *The Journal of Physical Chemistry C* 2009, 113, 14302-14310.

195. Zhong, Y.; Jaidann, M.; Zhang, Y.; Zhang, G.; Liu, H.; Ioan Ionescu, M.; Li, R.; Sun, X.; Abou-Rachid, H.; Lussier, L.-S. Synthesis of high nitrogen doping of carbon nanotubes and modeling the stabilization of filled DAATO@CNTs (10,10) for nanoenergetic materials. *Journal of Physics and Chemistry of Solids* 2010, 71, 134-139.

196. Yu, D.; Zhang, Q.; Dai, L. Highly Efficient Metal-Free Growth of Nitrogen-Doped Single-Walled Carbon Nanotubes on Plasma-Etched Substrates for

Oxygen Reduction. *Journal of the American Chemical Society* 2010, 132, 15127-15129.

197. Liu, C. y.; Bard, A. J.; Wudl, F.; Weitz, I.; Heath, J. R. Electrochemical Characterization of Films of Single‐Walled Carbon Nanotubes and Their Possible Application in Supercapacitors. *Electrochemical and Solid-State Letters* 1999, 2, 577-578.

198. Yu, D.; Dai, L. Self-Assembled Graphene/Carbon Nanotube Hybrid Films for Supercapacitors. *The Journal of Physical Chemistry Letters* 2009, 1, 467-470.

199. Fan, Z.; Yan, J.; Zhi, L.; Zhang, Q.; Wei, T.; Feng, J.; Zhang, M.; Qian, W.; Wei, F. A Three-Dimensional Carbon Nanotube/Graphene Sandwich and Its Application as Electrode in Supercapacitors. *Advanced Materials* 2010, 22, 3723-3728.

200. Zhang, J.; Zhao, X. S. On the Configuration of Supercapacitors for Maximizing Electrochemical Performance. *Chemsuschem* 2012, 5, 818-841.

201. Armand, M.; Endres, F.; MacFarlane, D. R.; Ohno, H.; Scrosati, B. Ionic-liquid materials for the electrochemical challenges of the future. *Nat Mater* 2009, 8, 621-629.

202. Denshchikov, K. K.; Izmaylova, M. Y.; Zhuk, A. Z.; Vygodskii, Y. S.; Novikov, V. T.; Gerasimov, A. F. 1-Methyl-3-butylimidazolium tetraflouroborate with activated carbon for electrochemical double layer supercapacitors. *Electrochimica Acta* 2010, 55, 7506-7510.

203. Pandey, G. P.; Hashmi, S. A.; Kumar, Y. Multiwalled Carbon Nanotube Electrodes for Electrical Double Layer Capacitors with Ionic Liquid Based Gel Polymer Electrolytes. *Journal of The Electrochemical Society* 2010, 157, A105-A114.

204. Cheng, Q.; Tang, J.; Ma, J.; Zhang, H.; Shinya, N.; Qin, L. C. Graphene and carbon nanotube composite electrodes for supercapacitors with ultra-high energy density. *Physical Chemistry Chemical Physics* 2011, 13, 17615-17624.

205. Kim, T. Y.; Lee, H. W.; Stoller, M.; Dreyer, D. R.; Bielawski, C. W.; Ruoff, R. S.; Suh, K. S. High-Performance Supercapacitors Based on Poly(ionic liquid)-Modified Graphene Electrodes. *ACS Nano* 2010, 5, 436-442.

206. Kaempgen, M.; Chan, C. K.; Ma, J.; Cui, Y.; Gruner, G. Printable Thin Film Supercapacitors Using Single-Walled Carbon Nanotubes. *Nano Letters* 2009, 9, 1872-1876.

207. Roldan, S.; Blanco, C.; Granda, M.; Menendez, R.; Santamaria, R. Towards a Further Generation of High-Energy Carbon-Based Capacitors by Using Redox-Active Electrolytes. *Angewandte Chemie-International Edition* 2011, 50, 1699-1701.

208. Huang, J. Y.; Zhong, L.; Wang, C. M.; Sullivan, J. P.; Xu, W.; Zhang, L. Q.; Mao, S. X.; Hudak, N. S.; Liu, X. H.; Subramanian, A.; Fan, H.; Qi, L.; Kushima, A.; Li, J. In Situ Observation of the Electrochemical Lithiation of a Single SnO2 Nanowire Electrode. *Science* 2010, 330, 1515-1520.

209. Hatchard, T. D.; Dahn, J. R. In situ XRD and electrochemical study of the reaction of lithium with amorphous silicon. *Journal of the Electrochemical Society* 2004, 151, A838-A842.

210. Tonisoo, A.; Kruusma, J.; Parna, R.; Kikas, A.; Hirsimaki, M.; Nommiste, E.; Lust, E. In Situ XPS Studies of Electrochemically Negatively Polarized Molybdenum Carbide Derived Carbon Double Layer Capacitor Electrode. *Journal of the Electrochemical Society* 2013, 160, A1084-A1093.

211. Baddour-Hadjean, R.; Pereira-Ramos, J. P. Raman Microspectrometry Applied to the Study of Electrode Materials for Lithium Batteries. *Chemical Reviews* 2010, 110, 1278-1319.

212. Mai, L.; Li, H.; Zhao, Y.; Xu, L.; Xu, X.; Luo, Y.; Zhang, Z.; Ke, W.; Niu, C.; Zhang, Q. Fast Ionic Diffusion-Enabled Nanoflake Electrode by Spontaneous Electrochemical Pre-Intercalation for High-Performance Supercapacitor. *Sci. Rep.* 2013, 3.

LIST OF PUBLICATIONS

1. **Chen, W.**; Rakhi, R. B.; Hu, L.; Xie, X.; Cui, Y.; Alshareef, H. N., High-Performance Nanostructured Supercapacitors on a Sponge. *Nano Letters* 2011, 11, 5165-5172.

2. Hu, L.[*]; **Chen, W.**[*]; Xie, X.; Liu, N.; Yang, Y.; Wu, H.; Yao, Y.; Pasta, M.; Alshareef, H. N.; Cui, Y., Symmetrical MnO_2–Carbon Nanotube–Textile Nanostructures for Wearable Pseudocapacitors with High Mass Loading. *ACS Nano* 2011, 5, 8904-8913. ([*] equal contribution)

3. **Chen, W.**; Rakhi, R. B.; Alshareef, H. N., High energy density supercapacitors using macroporous kitchen sponges. *Journal of Materials Chemistry* 2012, 22, 14394-14402.

4. **Chen, W.**; Rakhi, R. B.; Alshareef, H. N., Capacitance enhancement of polyaniline coated curved-graphene supercapacitors in a redox-active electrolyte. *Nanoscale* 2013, 5, 4134-4138.

5. **Chen, W.**; Rakhi, R. B.; Alshareef, H. N., Facile synthesis of polyaniline nanotubes using reactive oxide templates for high energy density pseudocapacitors. *Journal of Materials Chemistry A* 2013, 1, 3315-3324.

6. **Chen, W.**; Rakhi, R. B.; Alshareef, H. N., Morphology-Dependent Enhancement of the Pseudocapacitance of Oxide Template-Guided Tunable Polyaniline Nanostructures. *The Journal of Physical Chemistry C* 2013, 117, 15009-15019.

7. **Chen, W.**; Rakhi, R. B.; Wang, Q.; Hedhili, M. N.; Alshareef, H. N., Morphological and Electrochemical Cycling Effects in MnO_2 Nanostructures by 3D Electron Tomography. *Adv. Funt. Mater.* (under review)

8. **Chen, W.**; Rakhi, R. B.; Hedhili, M. N.; Alshareef, H. N., Shape-Controlled Porous Nanocarbons for High Performance Supercapacitors. *Small* (under review)

9. **Chen, W.**; Rakhi, R. B.; Bai, Y.; Alshareef, H. N., A General Approach Toward High Performance Supercapacitor Incorporating Graphene Electrode With Redox-Active Electrolytes. (In preparation)

10. **Chen, W.;** Xia, C.; Rakhi, R. B.; Alshareef, H. N., A General Approach Toward Enhancement of Pseudocapacitive Performance of Conducting Polymers in Redox-Active Electrolytes. (In preparation)

11. Rakhi, R. B.; **Chen, W.**; Cha, D.; Alshareef, H. N., Substrate Dependent Self-Organization of Mesoporous Cobalt Oxide Nanowires with Remarkable Pseudocapacitance. *Nano Letters* 2012, 12, 2559-2567.

12. Rakhi, R. B.; **Chen, W.**; Cha, D.; Alshareef, H. N., Nanostructured Ternary Electrodes for Energy-Storage Applications. *Advanced Energy Materials* 2012, 2, 381-389.

13. Rakhi, R. B.; **Chen, W.**; Alshareef, H. N., Conducting polymer/carbon nanocoil composite electrodes for efficient supercapacitors. *Journal of Materials Chemistry* 2012, 22, 5177-5183.

14. Rakhi, R. B.; **Chen, W.**; Cha, D.; Alshareef, H. N., High performance supercapacitors using metal oxide anchored graphene nanosheet electrodes. *Journal of Materials Chemistry* 2011, 21, 16197-16204.

15. Rakhi, R. B.; Cha, D. K.; **Chen, W.**; Alshareef, H. N., Electrochemical Energy Storage Devices Using Electrodes Incorporating Carbon Nanocoils and Metal Oxides Nanoparticles. *Journal of Physical Chemistry C* 2011, 115, 14392-14399.

16. Xie, X.; Ye, M.; Hu, L.; Liu, N.; McDonough, J. R.; **Chen, W.**; Alshareef, H. N.; Criddle, C. S.; Cui, Y., Carbon nanotube-coated macroporous sponge for microbial fuel cell electrodes. *Energy & Environmental Science* 2012, 5, 5265-5270.

17. Bai, Y.; Rakhi, R. B.; **Chen, W.**; Alshareef, H. N., Effect of pH-induced chemical modification of hydrothermally reduced graphene oxide on supercapacitor performance. *Journal of Power Sources* 2013, 233, 313-319.

18. Rakhi, R. B.; **Chen, W.;** Cha, D.; Alshareef, H. N., Influence of Calcination Temperature on the Morphology and Energy Storage Properties of Cobalt Oxide Nanostructures Directly Grown Over Carbon Cloth Substrates, *Materials for Renewable and Sustainable Energy* 2013, 2 (3-4), 1-13.

19*.* Rakhi, R. B.; **Chen, W.;** Hedhili, M. N.; Cha, D.; Alshareef, H. N., RuO_2-decorated, mesoporous cobalt oxide nanosheets on flexible carbon substrate as electrodes for high rate supercapacitors, *Journal of Physical Chemistry C* (Under review)